Investigation of the unusual magnetic properties of Fe and Co on MgO with high spatial, energy and temporal resolution

Inauguraldissertation
zur
Erlangung der Würde eines Doktors der Philosophie
vorgelegt der
Philosophisch-Naturwissenschafftlichen Fakultät
der Universität Basel

von

Susanne Baumann
aus Berneck, St. Gallen

Basel, 2015

Genehmigt von der Philosophisch-Naturwissenschaftlichen Fakultät

auf Antrag von

Prof. Dr. Ernst Meyer, Fakultätsverantwortlicher
Dr. Andreas J. Heinrich, Dissertationsleiter
Prof. Dr. Martino Poggio, Korreferent

Basel, den 19. Mai 2015

Prof. Dr. Jörg Schibler, Dekan

Abstract

Nanometer-sized magnets are used as magnetic bits in data storage devices to hold information. As such devices are further miniaturized, the control of magnetism at the atomic scale becomes essential. One of the critical parameters to realize nanoscopic magnets is a large magnetic anisotropy. Magnetic anisotropy gives its magnetization a preferred axis and thus its directionality. At the atomic scale, magnetic anisotropy originates from anisotropy in the orbital angular momentum and the spin-orbit coupling that connects the spin moment of a magnetic atom to the spatial symmetry of its ligand field environment. Thus far, the magnetic anisotropy energy per atom in single-molecule magnets and ferromagnetic films remains typically one to two orders of magnitude below the theoretical limit imposed by the atomic spin-orbit interaction. Here we investigate the magnetic properties of individual magnetic atoms on thin magnesium oxide (MgO) films. We find highly unusual magnetic behavior for Fe and Co on the oxygen binding site of MgO. By coordinating a single Co atom to this binding site we can even realized the maximum magnetic anisotropy for a $3d$ transition metal atom.

At the heart of this work we combine scanning tunneling microscopy and X-ray absorption spectroscopy experiments and we find striking agreement between these experimental techniques. Scanning tunneling spectroscopy reveals a record-high zero-field splitting of 58 millielectron volts for Co as well as 14 millielectron volts for Fe on the oxygen binding site. This behavior originates from the dominating axial ligand field of this adsorption site,

which leads to out-of-plane uniaxial anisotropy combined with large orbital moment, as observed by X-ray magnetic circular dichroism. The bonding geometry and electronic configuration are calculated by density functional theory, a multiplet analysis and a model developed here, that uses a point-charge calculation combined with Stevens operator equivalents. Scanning tunneling microscopy also allows the tuning of the magnetic anisotropy and spin-polarized measurements that confirm the applied model by revealing further transitions and by allowing the measurement of magnetic moments on single atoms.

A further critical parameter for obtaining miniaturized magnets, for applications in data storage devices, is the magnetic stability, the ability of magnets to retain their magnetic orientation despite external influences. The magnetic stability of larger magnets is determined by a thermal barrier, which scales with the magnetic anisotropy. At the atomic scale, magnetization reversal is often dominated by quantum tunneling of the magnetization. Quantum tunneling allows transitions between states without having to overcome the anisotropy barrier. This is for example caused by mixing between different states, induced by the ligand symmetry. Here we use an all-electrical pump-probe scheme to determine the lifetimes of Co and Fe on MgO and we show how such tunneling can be sufficiently suppressed by careful design of the bonding geometry and by reducing the atom's interaction with the environment. With this approach, we show the longest lifetimes seen so far for $3d$ transition metal atoms: a lifetime of 200 microseconds for Co and of 10 milliseconds for Fe.

The research described in this thesis demonstrates how the complementary use of several experimental and theoretical techniques allows a detailed determination of the character and properties of the magnetic states at the atomic level. These results offer a strategy, based on symmetry arguments and careful tailoring of the interaction with the environment, for the rational design of nanoscopic permanent magnets and single atom magnets.

Contents

Abstract **1**

1 Introduction **8**
1.1 Origins of magnetism at the atomic scale 8
1.2 Materials and techniques 10
1.3 Thesis outline 12

2 Design and use of a molecular beam epitaxy chamber **14**
2.1 Molecular beam epitaxy 14
2.2 Design of a new MBE chamber 15
2.2.1 Design basics 15
2.2.2 Major design steps 15
2.2.3 Detailed description of the chamber capabilities 17
2.3 Sample preparation throughout this work 19
2.4 Summary on MBE 19

3 Probing the spin states of single atoms **20**
3.1 Scanning tunneling microscopy 20
3.2 Spin-excitation spectroscopy 21
3.3 Introduction to the effective spin Hamiltonian 23
3.4 Spin-excitation spectroscopy methods 25
3.5 Spin-excitation spectroscopy on magnetic atoms on MgO . . . 26

3.5.1 Fe on MgO 31
3.5.2 Co on MgO 34
3.6 Summary on spin-excitations on MgO 36

4 Probing the magnetization direction and total moment of single atoms 37
4.1 X-ray absorption spectroscopy and X-ray magnetic circular dichroism 37
4.2 X-ray absorption methods 40
4.3 XMCD results on Fe and Co on MgO 42
4.4 Magnetization curves on Fe and Co on MgO 44
4.5 Summary on XAS and XMCD results 45

5 Insight into the origin of magnetic properties 46
5.1 Multiplet calculations 46
5.2 Specifics for full multiplet calculations on Fe and Co on MgO 50
5.2.1 Fe on MgO 51
5.2.2 Co on MgO 53
5.3 Multiplet calculation based on a point charge model 56
5.3.1 Anti-symmetrized wave functions 57
5.3.2 Surrounding ligands described as point charges 61
5.3.3 The full point charge model 73
5.3.4 Comparison between the multiplet and the point charge calculation 79
5.3.5 Optimized point charge model 82
5.4 From extended point charge model to a simplified Hamiltonian with Stevens operator equivalents 83
5.5 Back to an effective spin Hamiltonian 86
5.6 Summary on multiplet calculations and other models for magnetic systems 89

6 Tuning the energy levels of single atoms **90**
6.1 Anisotropy tuning 90
6.2 Experimental observation of energy tuning 92
6.3 Model to explain the changes 94
6.4 Summary on energy tuning 99

7 Observing additional orbital states **100**
7.1 Observing additional transitions gives a more complete picture of the magnetic properties 100
7.2 Selection rules and transition intensities 101
7.2.1 Possible excitations due to tunneling electrons 103
7.2.2 Calculated transition intensities for Fe and Co on MgO 104
7.3 Spin-polarized tunneling 106
7.4 Master rate equation to determine the occupation of states . . . 108
7.5 Spin-polarized tunneling methods 110
7.6 Spin-polarized probing of additional states 111
7.6.1 Transitions to the higher spin-multiplet in Fe 111
7.6.2 Transitions to a different orbital state in Co 116
7.7 Summary on observation of additional orbital states 119

8 Measuring spin lifetimes **120**
8.1 Spin lifetimes 120
8.2 Probing fast spin lifetimes in STM 124
8.2.1 Lifetime broadening 124
8.2.2 Spin-pumping 124
8.3 Fast relaxations for both Fe and Co on MgO 125
8.4 Probing slow spin lifetimes in STM 128
8.4.1 Pump-probe 128
8.4.2 Two-state-noise 130
8.5 Pump-probe on Co on MgO 131
8.5.1 Long lifetime 131
8.5.2 Measuring the magnetic moment 135

8.5.3 Magnetic field dependence 139
8.6 Extremely long lived states of Fe on MgO 143
8.6.1 Two-state-noise 143
8.6.2 Different MgO thickness 145
8.7 Summary on spin lifetimes 147

9 Further projects **148**
9.1 Stable anti-ferromagnetic Fe chains 149
9.2 Measurement of the MgO thickness 154
9.3 Chiral molecule recognition and manipulation 161
9.4 The worlds smallest movie - made with atoms 162

10 Conclusions **163**

Acknowledgments **167**

Curriculum Vitae **169**

Appendices **172**

A Molecular beam epitaxy chamber **173**

B Scanning tunneling spectroscopy fit **177**

C List of free atom wave functions **179**
C.1 Wave functions of the d^2/d^8-configuration 179
C.2 Wave functions of the d^3/d^7-configuration 183
C.3 Wave functions of the d^4/d^6-configuration 184
C.4 Wave functions of the d^5-configuration 185

D Matrix elements for four-fold symmetric ligand field **186**
D.1 Single electron matrix elements 186
D.2 Multi-electron matrix elements for a four-fold symmetric ligand field 191

D.2.1 Multi-electron matrix elements for Ni 191
D.2.2 Multi-electron matrix elements for Co 193
D.2.3 Multi-electron matrix elements for Fe 195

E Stevens operator equivalents **197**
E.1 List of the relevant Stevens operator equivalents 197
E.2 Transformation to Stevens operator equivalents 198

F Tabulated values for point charge model calculation of 3d transition metal atoms **202**
F.1 Radial matrix elements 202
F.2 Spin-orbit coupling constants 203
F.3 Element-specific Stevens prefactors 203
F.4 Formulas 204
F.4.1 Gamma 204
F.4.2 Stevens prefactors 205
F.4.3 Stevens operator equivalents 205
F.4.4 Full Stevens Hamiltonian 205

G Energy changes due to atom movements **206**
G.1 Energy change due to Fe movement 206
G.2 Energy change due to Co movement 209

H Master rate equation **210**
H.1 Rate equations 210
H.2 Using the rate equations to fit lifetimes 212

References **215**

Chapter 1

Introduction

1.1 Origins of magnetism at the atomic scale

Motivated by ever shrinking data storage technology it becomes essential to understand and control magnetism on the atomic scale. For the design of magnets there are two important factors to consider: One, the magnetic anisotropy, which gives the magnetic moment its directionality and stability, and two, the size of the magnetic moment itself. Stable magnetism arises due to an energy barrier between two magnetic states with opposite alignment. One has to overcome this energy barrier, the so called anisotropy barrier, to switch the direction of such a magnet. However, as magnets become smaller and approach the atomic scale, quantum effects, such as quantum tunneling of the magnetization (*1*,*2*), come into play that can significantly destabilize the states with oppositely aligned magnetic moments. Rather than having to overcome the full anisotropy barrier, quantum tunneling of the magnetization can effectively lower the energy barrier for the magnetization reversal. Thus one of the questions we want to explore in this thesis is *how quantum effects and magnetic stability coexist on the scale of single atoms.*

To answer this question we need to have a *detailed knowledge on the origin*

of magnetism at the atomic scale. In the next paragraphs we would like to introduce the basics of the origin of magnetism and then give detailed descriptions with specific examples throughout this thesis.

On the atomic scale, the magnetic moment consists of contributions of both orbital and spin angular momentum ($\vec{L}$ and $\vec{S}$). The microscopic origin of the magnetic anisotropy is the combined effect of the anisotropy in the atom's orbital angular momentum, together with the interaction between $\vec{L}$ and $\vec{S}$. This interaction is given by the spin-orbit-coupling.

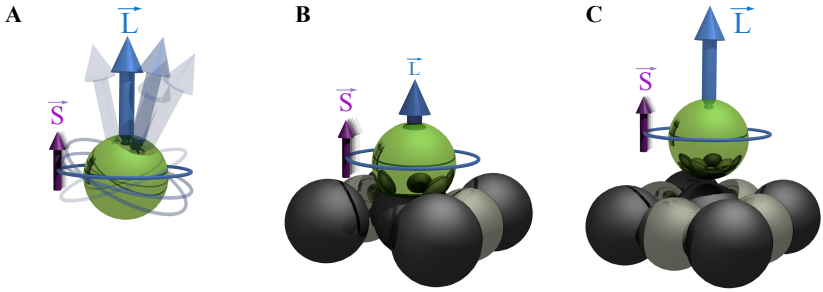

Figure 1.1: Magnetic moment on the atomic scale. (**A**) In a free atom the magnetic moment, consisting of orbital angular momentum $\vec{L}$ (blue) and spin angular momentum $\vec{S}$ (purple), has no preferred direction. (**B**) When such a magnetic atom is placed on a surface or in a molecule, $\vec{L}$ tends to align along specific symmetry directions, given by neighboring atoms, and gets strongly diminished. (**C**) However, bonding geometries can be designed that retain a large orbital moment despite its strong interaction with the surface.

In a free atom there is no preferred axis and consequently there is no anisotropy. The magnetic moment, comprised of $\vec{L}$ and $\vec{S}$ can be oriented in any spatial direction (see Figure 1.1 A). In solids and molecules however, $\vec{L}$ tends to align along specific symmetry directions, set by the spatial location of surrounding atoms. The potential of these surrounding atoms, the ligand field,

also causes the orbital moment to be quenched or strongly diminished (*3*). In those situations, the magnetic moment is primarily due to spin (see Figure 1.1 B). However, the small orbital moment still governs the directionality of the spin via spin-orbit coupling.

Between a free atom and the solid, there is an interesting regime where a single atom keeps its large orbital moment despite its strong interaction with a surface (see Figure 1.1 C). Having the magnetic atom on a surface further allows electrical access to the atom and, by retaining only some of the free atom's orbital degeneracies, provides directionality to the orientation of its magnetic moment.

1.2 Materials and techniques

In this thesis, we study single atoms on surfaces and explore the regime between a free atom and an atom fully incorporated into a solid. Despite its strong interaction with the surface we can retain almost free atom-like orbital moments by appropriate design of the ligand field. The most promising strategy to preserve a large orbital moment while inducing uniaxial anisotropy is to use low-coordination geometries, as shown for atoms deposited on the three-fold coordinated site of a (111) surface (*4*,*5*), and molecular complexes and crystals with two-coordinate metal species (*6–9*). This strategy can be brought to its limit by coordinating one magnetic atom to a single substrate atom.

We will show that one can achieve this extreme by placing single magnetic $3d$ transition metal atoms, such as Co and Fe, on a thin film of magnesium oxide (MgO) (see Figure 1.2). MgO forms a checkerboard pattern of alternating magnesium and oxygen atoms (see Figure 2.2) (*10*,*11*). This substrate provides the desired one-fold coordination site, as most atoms adsorb on top of a single oxygen atom.

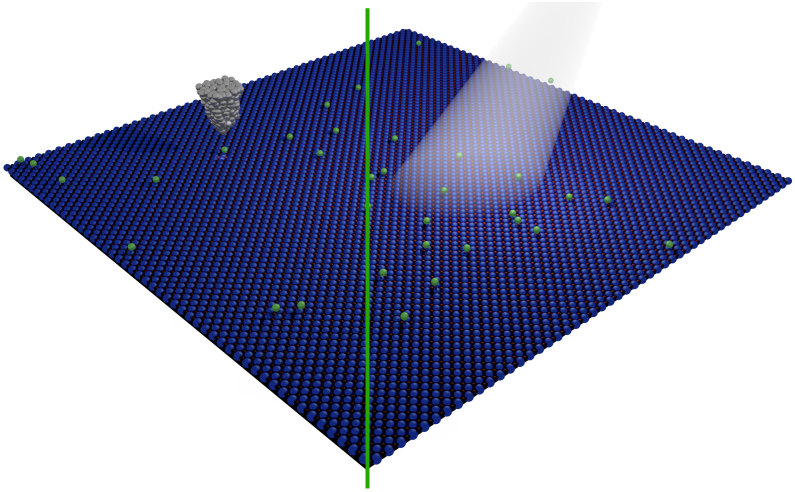

Figure 1.2: Throughout this work we use a combination of scanning tunneling microscopy and X-ray magnetic circular dichroism on the same type of sample. (However, the two techniques were never employed on exactly the same sample as the two tools are located in different labs, one at the IBM Almaden Research Center, United States, and the other at the Swiss Light Source, Switzerland.)

We mainly work with two experimental techniques to investigate these large orbital moments: we use scanning tunneling microscopy (STM) and X-ray circular dichroism (XMCD) (see Figure 1.2) (*12*). Additionally, theoretical calculations, such as density functional theory (DFT) and multiplet calculations as a fit to the X-ray results, are used to support the experimental findings. A STM uses tunneling of electrons between two nearby metal electrodes, consisting of a sharp metal tip and a metal substrate (in our case we use a silver single crystal substrate underneath the MgO layer), to probe, for example, energy levels or lifetimes of atomic-scale objects (left side of Figure 1.2). XMCD on the other hand is an element specific technique that uses differently polarized X-ray light to resolve the spin and orbital moments

of an ensemble of atoms (right side of Figure 1.2). The two experimental techniques complement each other extremely well: XMCD and the multiplet calculations show the character of the magnetic states, while STM gives a direct measurement of specific transitions and the state's lifetime.

1.3 Thesis outline

Using this combination of STM and XMCD and some theoretical calculations, this thesis aims at addressing the following questions:
- *What are the origins of magnetism at the atomic scale?*
- *Is it possible to obtain stable magnetism in a single atom?*
- *Can we use what we learn about the origins of magnetism to design such stable magnets?*

Each chapter endeavors to provide answers to these questions. At the beginning of each chapter, a single sentence explains the importance of the result presented therein with regard to the understanding of magnetism at the atom scale, and for the attainment of stable magnetism in single atoms.

First, we will introduce the sample preparation procedure in Chapter 2. In addition, this chapter gives some detail on the design and building of a molecular beam epitaxy system for an entirely new STM.

Quantum mechanical effects cause discrete energy levels in single atoms and in Chapter 3, we explain how to measure specific transitions between such magnetic energy levels in a STM.

Along with a large anisotropy barrier, the magnitude of the total magnetic moment is an important property in the design of magnets. In Chapter 4 we therefore introduce how XMCD probes the total magnetic moment and its

magnetization direction.

As a fit to the X-ray results, multiplet calculations then give further insight into the character and magnetic properties, such as orbital and spin moments, of the magnetic states that are probed by both experimental techniques (Chapter 5). In that chapter we additionally introduce a simplified version of such calculations that, rather than relying on a fit to the X-ray results, uses DFT results to calculate the magnetic energy levels of the low energy states.

With the insights into the origins of magnetism acquired in the previous chapters, we explain in Chapter 6, how the STM tip can be used to increase the anisotropy barrier by tuning the energy levels of single atoms.

We introduce spin-polarized tunneling in a STM in Chapter 7. We show how the spin-polarization can serve as a sensitive probe to observe changes in the occupation of the different magnetic states, which is a prerequisite to the observation of spin lifetimes.

In Chapter 8 we explore the long lifetimes of the $3d$ transition metal atoms on MgO. We introduce several available timescales in STM measurements and investigate the stability of single magnetic atoms, using Co and Fe on MgO.

A short summary on other interesting projects I was involved in during my PhD is given in Chapter 9, and in Chapter 10 we finish with some concluding remarks.

Overall, this thesis presents some insights into the origins of magnetism and the ingredients necessary for long spin lifetimes or even stable magnetism at the atomic scale. We will present experimental evidence for the largest possible anisotropy barrier for $3d$ transition metal atoms and show the longest lifetimes for single transition metal atoms on surfaces reported so far.

Chapter 2

Design and use of a molecular beam epitaxy chamber

Preparing atomically clean samples is a prerequisite for the ability to measure single atoms on surfaces.

2.1 Molecular beam epitaxy

Molecular beam epitaxy (MBE) is a deposition technique that takes place in an ultra-high vacuum (UHV) environment and achieves high purity films (*13*). In MBE, the to-be-deposited, pure materials are heated slowly until they sublime. In gas form these elements then condense on the substrate. Once on the substrate the materials might react with other materials on the surface, e.g. magnesium (Mg) and oxygen (O) will form a magnesium oxide (MgO) layer on the substrate surface. MBE can be used to fabricate layered structures when different source-materials are deposited in sequence and it is thus a technique that is frequently used in manufacturing semiconductor devices.

In our experiments MBE is used to deposit thin films of insulating material in

order to decouple single atoms from the metallic substrate. We used a single monolayer of MgO as decoupling layer from a silver substrate in most of the experiments discussed here.

2.2 Design of a new MBE chamber

Apart from the experimental advances presented in this thesis, we also worked on designing a new STM system with additional capabilities compared to the two current STMs at the IBM Almaden Research Center (*14*,*15*). A key advantage over the existing microscopes lays in a separate sample preparation chamber, which we will focus on in the following as this was a major part of my PhD work. Separating this chamber from the rest of the STM system allows for more possibilities in terms of materials and techniques for the sample preparation. In the next sections, we will show details on the design of this chamber and its current and possible future capabilities.

2.2.1 Design basics

All design work was done with the 3D CAD software SolidWorks (*16*). The design included for the sample preparation to be carried out in UHV and to allow sample transfer to the main chamber and STM without removal of the sample from the UHV environment. The designed chamber and some additional flanges or custom parts were fabricated by MDC (*17*), while other (often smaller) custom parts were manufactured in IBM's internal model shop.

2.2.2 Major design steps

The main goal of this chamber was to achieve independent sample preparation capabilities, while still being able to easily transfer samples between this

preparation chamber and the main STM chamber. Thus in the design process for the MBE chamber we considered the following points:

1. Easy connection to the rest of the system (STM part):
   We ensured this connection by collaborating closely with MDC on the design of a bi-directional horizontal transfer arm.

2. Ports for all essential preparation tools:
   We consider tools such as pumps for the UHV environment, the deposition sources, the sputter gun for sample cleaning, a heater for annealing and the Auger electron spectrometer for characterization, as the essential tools in this system.

3. Integration of other (more flexible) essentials:
   Also important for a thin film deposition chamber are an ion gauge for pressure read out, a quartz microbalance to monitor film growth, and multiple view ports, as well as mounting brackets for earthquake safety. All of these features are not necessarily bound to specific locations within the chamber and leave thus more flexibility in the design.

4. Additional features for future use:
   This step includes tools that might be important for preparation procedures in the future but are not essential at this point, we consider a RHEED spectrometer as one of these tools. For future freedom in design we tried to fit as many additional ports on the chamber as possible.

For a list of all available ports see Appendix A and for a 3-dimensional model of the final design of the chamber with most tools attached see Figure 2.1 A.

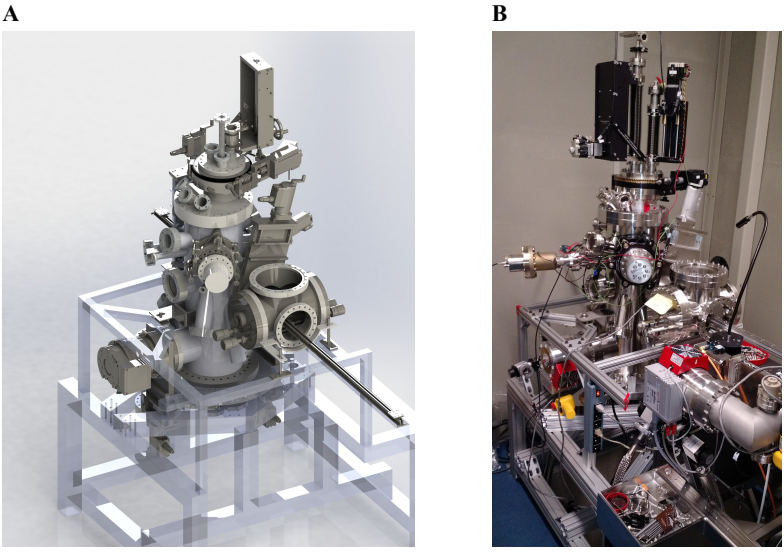

Figure 2.1: Designed molecular beam epitaxy chamber. (**A**) 3-dimensional model of the whole assembly, created in SolidWorks. (**B**) Photograph of the real system as assembled (April 2015).

2.2.3 Detailed description of the chamber capabilities

The main capabilities of the designed MBE chamber include standard sample cleaning and preparation tools such as a sputter gun (port # 10, see Appendix A) or an electron-beam heater (top flange # B). These tools are used for sputtering and annealing cycles of the single crystal substrates. Additionally, there are some standard analysis tools on the chamber such as an Auger electron spectrometer (# 8) and a mass spectrometer (# 20–24). Apart from the standard cleaning and characterization capabilities, the full potential of the preparation chamber lays in its deposition possibilities: The design allows for 5 different 4.5 inch deposition sources (e.g. Knudsen cells) at the bottom of the vacuum chamber (bottom flange # A) that have a mechanical shutter (# 19)

to allow heating the source before deposition on the sample. Additionally, there are some non-shuttered flanges for potential deposition sources (4.5 in # 12–13, 2.75 inch # 14–15), which would also allow for a plasma source to be installed in the future. Multiple other flanges allow for gas inlets (using leak valves) to expand the possibilities in depositing films even more. Deposition rates can be monitored by a quartz microbalance (# 11) either at the sample position or next to the sample, allowing the measurement of the rate during deposition. The chamber is held under ultra-high-vacuum conditions provided by four different independent pumping systems: a turbo pump (# 7), an ion getter pump (# 5) as well as a combined titanium sublimation and cryo-pump (# 6).

The sample is held in place by a rotatable sample stage (# 9) which allows the sample to be in a vertical or in a horizontal position. In the vertical position, the sample faces the Auger electron spectrometer and the sputter gun, in order to monitor the cleaning progress or to allow for sample transfer by the vertical manipulator arm. The horizontal position allows the sample to face towards the bottom of the chamber, ensuring an even deposition of materials over the entire sample surface. In the horizontal position, the sample can be heated and sputtered (or any combination of them together with the deposition). The sample stage can be partially blocked from the deposition sources by a deposition mask (# 27).

In order to give the chamber flexibility for future needs, several additional ports are available with no specifically dedicated use yet (these ports include # 12–15, 20–24 and 26). Additionally, the chamber has available ports for a RHEED spectrometer (# 3–4).

2.3 Sample preparation throughout this work

The sample preparation for all experiments shown in this thesis used MBE for the reactive growth of MgO films. The samples were prepared according to the same recipe in both the STM and XMCD experiments. First, the sample was cleaned by repeated sputter and annealing cycles of the Ag(001) single crystal in UHV, until a high-purity metal surface was achieved. Second, the Mg was evaporated from a crucible in an O_2 atmosphere of $p_{O_2} = 10^{-6}$ mbar. We used growth rates of approximately 1 monolayer (ML) per minute at a sample temperature of typically 310° C. The sample with the thin MgO films on Ag were then transferred through UHV into a low-temperature STM. The single magnetic atoms (mainly Fe or Co) were deposited at about 5–10 K. A schematic representation of the final films is shown in Figure 2.2.

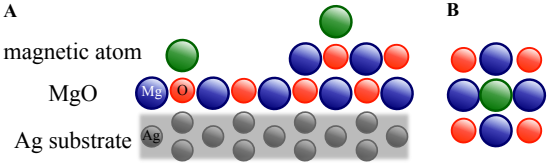

Figure 2.2: Schematic drawing of the sample system used throughout this work. (**A**) Side view of single atoms on thin magnesium oxide films on top of a silver (001) crystal. Here a single monolayer and two layers of MgO are depicted. (**B**) Top view of magnetic atoms on top of a MgO film. The two atoms Fe and Co adsorb on the oxygen binding site.

2.4 Summary on MBE

In this chapter we have introduced the sample preparation procedure used throughout this work. In addition, we have outlined the design and construction process of an entirely new molecular beam epitaxy chamber, which will be available for future experiments at the IBM Almaden Research Center.

Chapter 3

Probing the spin states of single atoms

Understanding the discrete energy levels that arise due to quantum mechanical effects is essential in achieving magnetism at the atomic scale.

The results on Co presented in this chapter are published in: Rau, I.G., Baumann, S. *et al.* Reaching the magnetic anisotropy limit of a 3d metal atom. *Science* **344**, 988–992 (2014). For the Fe measurements the manuscript is in preparation: Baumann, S. *et al.* Spin and orbital magnetism of Fe atoms on MgO.

3.1 Scanning tunneling microscopy

A scanning tunneling microscope (STM) uses the quantum mechanical tunneling effect as the local interaction between two metallic electrodes, an atomically sharp probe tip and the sample surface (*18*). When the tip is brought to within a few atomic diameters of the conducting substrate and a bias voltage is applied, an electrical current flows between them. The

current through this tunnel junction depends exponentially on the width of the energy barrier formed by the vacuum gap. Therefore, STM can be an excellent tool for high resolution imaging in cases where the probe tip is rastered over a sample. STMs also allow for precise atom manipulation on surfaces (*14*), which enables the possibility to build and study atomic-scale structures (*19*,*20*). Due to its excellent spatial resolution, a scanning tunneling microscope has the ability to measure conductance through an individual atom and probe inelastic excitations within single atoms or molecules (*15*,*21*). Furthermore, it is possible to use a magnetic probe tip as a type of spin-filter (spin-polarized STM) (*22*,*23*), acting as a magnetic tunnel junction in which the tip-sample conductance differs according to the relative alignment of the surface and tip magnetic moments. We will first focus on probing magnetic excitations of single atoms and will in later chapters introduce magnetic tips.

3.2 Spin-excitation spectroscopy

The tunneling of electrons in the junction of a STM can occur elastically or inelastically. In the inelastic tunneling process the electrons interact with their environment and they exchange energy and potentially spin angular momentum. These interactions can be observed as sharp steps in the differential conductance ($\mathrm{d}I/\mathrm{d}V$) at certain well defined voltages (*24*) (see schematics in Figure 3.1 B). This technique is known as inelastic electron tunneling spectroscopy. The steps correspond to an excitation, which can be of vibrational or magnetic nature. Since 1998, STMs have been successfully used in many cases on single molecules or even single atoms to detect such excitations (*15*,*21*).

Both the vibrational and magnetic inelastic excitations consist of a measurable change in conductance due to an excitation of an atom, molecule or nanostructure under the tip of a STM. In this case, the tunneling current is both the exciting and the measuring probe. When the tip-sample bias is larger than the

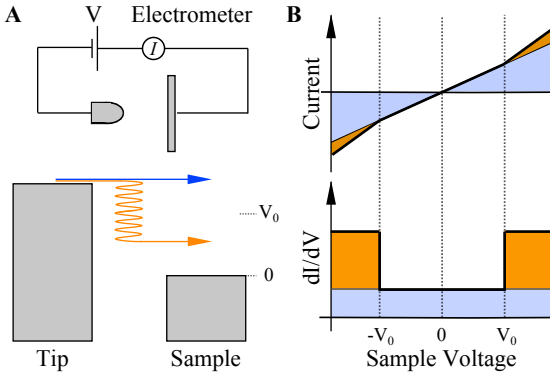

Figure 3.1: Inelastic tunneling spectroscopy schematics. (**A**) STM setup (top panel) together with schematic drawing of elastic (blue) and inelastic tunneling (orange) at an applied bias (V) that is larger than the excitation threshold V_0. (**B**) Current trace (top panel) and the corresponding differential conductance dI/dV (bottom panel) as a function of applied voltage. The inelastic current (orange) shows up as a sharp step in conductance at V_0.

excitation energy the tunneling electron can give up part of its energy and still tunnel into a state above the Fermi energy of the corresponding electrode (see Figure 3.1 A, orange). This inelastic process also contributes to the tunneling current. Below a certain threshold the tunneling current is formed of only elastic electrons, but at the excitation threshold the tunneling current increases as it contains inelastic electrons in addition to the elastic electrons, which leads to the characteristic stepwise increase in the differential conductance that is symmetric around zero bias (Figure 3.1 B).

In our experiments, we are particularly interested in the magnetic properties of single atoms (*25*,*26*) or artificially assembled structures of atoms on surfaces (*19*). We therefore focus on magnetic excitations and use magnetic inelastic electron tunneling spectroscopy, spin-excitation spectroscopy (SES), to obtain information about the magnetic energy levels in our systems and to

probe the various spin states.

3.3 Introduction to the effective spin Hamiltonian

The measured spin states in STM experiments are often described by an effective spin Hamiltonian (*2*,*25*). This simplification of using an effective Hamiltonian has performed well in many systems (*20*,*25*,*27–29*) and is also frequently used in molecular magnets (*2*,*30*). This approach allows the interpretation of spectra without using fundamental theories.

In an effective spin Hamiltonian one replaces the individual contributions of orbital and spin moments by an effective spin moment, which has symmetry properties given by the ligands and the spin of the system. As the central approximation one uses the fact that the orbital moment of magnetic centers is most of the time essentially quenched (*2*,*31*). However, this approximation is not always valid as we will show for the case of Co on MgO.

A system with n unpaired electrons is described by an effective spin $S_{\text{eff}} = n/2$ (we refer to S_{eff} as S from now on to simplify the description), in an effective spin Hamiltonian, which results in $(2S+1)$ effective spin levels associated with it. The energy levels in such a systems are split by low-symmetry components (equivalent to a ligand field acting on orbital moments) as well as by an applied magnetic field. Therefore, the Hamiltonian is:

$$H_{\text{eff}} = H_{\text{CF}} + H_{\text{Z}}. \tag{3.1}$$

Here the crystal field Hamiltonian H_{CF} describes the effect of ligands, which determine the spatial symmetry of the magnetic system. It is most convenient to use operators similar to the so-called Stevens operator equivalents (*32*) to describe the crystal field (see more details on Stevens operator equivalents and

their proper use in Chapter 5):

$$H_{\mathrm{CF}} = \sum_{N,k} B_N^k \hat{O}_N^k \tag{3.2}$$

B_N^k are prefactors and $\hat{O}_N^k$ are the Stevens operators (*32*). N is limited to even integer values smaller than $2S$ ($N = 2, 4, 6, ..., 2S$, all other values vanish). The index k is usually limited by the actual symmetry of the system and can take values between $0 \leq k \leq N$. For example, on a four-fold symmetric surface (see schematic in Figure 3.2, left hand side), only terms with k = 0 and 4 are included. Placing an atom on a surface strongly breaks the symmetry and results in an axial component, which is accounted for by including all terms with k = 0. In addition, for an atom on the oxygen binding site of MgO, its four Mg neighbors lead to terms with k = 4.

Rather than writing out the full Stevens operators for the terms in the crystal field it is common to simplify the Hamiltonian further by subtracting constant terms from the Stevens operators and multiplying any factors into the prefactor, the anisotropy parameter. For the four-fold symmetric case, e.g. a magnetic atom on MgO, the following effective Hamiltonian can describe the spin states:

$$H_{\mathrm{CF}} = D \cdot \hat{S}_z^2 + D' \cdot \hat{S}_z^4 + C \cdot (\hat{S}_+^4 + \hat{S}_-^4) \tag{3.3}$$

where D, D' and C are the anisotropy parameters and $\hat{S}_z$ is the z-axis (surface normal) component of the atom's spin operator $\hat{S}$, and ($\hat{S}_+$, $\hat{S}_-$) are the z-axis ladder operators. In this case, C consists of a multiplicative factor times the B_4^4 of the Stevens operator form. The first two terms, the axial components, change the energy separation between levels with different spin quantum number $|M_S|$. The term due to the four-fold symmetry of the binding site couples states differing by $\pm$ 4 in M_S, which physically introduces an anisotropy in the xy-plane according to which the x- and y-axis are equivalent

but different from the diagonals (see Figure 3.2, left hand side).

The Zeeman Hamiltonian can be written as:

$$H_{\mathrm{Z}} = g^* \mu_{\mathrm{B}} \vec{S} \cdot \vec{B} \tag{3.4}$$

where μ_{B} is the Bohr magneton, g^* is a prefactor (or, more generally, a tensor) connecting the magnetic field and the effective spin vector and $\vec{B}$ is the applied magnetic field.

We use this effective Hamiltonian to simplify the description of Fe on MgO. However, for Co on MgO this approach has to be replaced by a more extensive model as described in detail in Chapter 5.

3.4 Spin-excitation spectroscopy methods

All STM measurements were performed at the IBM Almaden Research Center in a low-temperature ultra-high vacuum system (*15*). The spin-excitation experiments used a DC voltage between the STM tip (positioned over the magnetic atom) and the sample, while measuring conductance with a lock-in technique with an AC excitation of 70 to 150 μV, at 806 Hz. The differential conductance measurements were recorded at 0.6 K, unless otherwise specified. The setup allows to apply magnetic fields of up to 7 T in-plane as well as out-of-plane. If in the following the direction of the magnetic field is not specified it was applied in the out-of-plane direction. The fitting of the SES steps is described in Appendix B. The spin-excitation spectra of different atoms of the same element vary by a few per cent. This effect is most likely due to variations in the local environment of the atoms, for example due to strain at island edges.

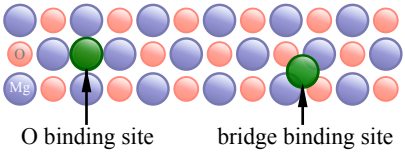

Figure 3.2: Schematic drawing of two possible binding sites on MgO. Most atoms (Co, Fe, Mn_A and Ni) prefer, according to DFT calculations, the oxygen binding site (left hand side). Mn_B seems to prefer the bridge binding site (right hand side).

3.5 Spin-excitation spectroscopy on magnetic atoms on MgO

We deposited four different $3d$ transition metal elements on the flat MgO surface and examined their properties. Figure 3.3 C shows an image with iron, cobalt and nickel atoms on 1 ML of MgO, while Figure 3.4 A shows manganese, iron and cobalt. There are two different kinds of Mn species, Mn_A (upper image) and Mn_B (lower image), more frequently we find the kind associated with the Mn_A atom. Fe, Co and Mn_A (Mn_B) appear as protrusions of 0.18 nm, 0.17 nm and 0.20 nm (0.15 nm) respectively. Interestingly, Ni appears as a depression of 0.04 nm indicating a nearly unchanged density of states around the Fermi energy. Figure 3.3 C additionally contains a Co dimer which appears as a 0.23 nm protrusion. Fe, Co and Ni seem to all prefer the

Figure 3.3 *(following page)*: Overview of different species of transition metal atoms on a single monolayer of MgO. (**A**) SES spectrum of two Co atoms with a clear stepwise increase in conductance at about 60 mV. In (**B**) the spectra of two Fe atoms are depicted, which have a conductance step at roughly 15 mV. (**C**) STM topograph of two Co, two Fe and five Ni atoms and one Co dimer. (V = 100 mV, I = 50 pA). (**D**) Ni appears as a depression and does not have any spectral features up to energies of about $\pm$400 mV (see inset). (**E**) The Co dimer shows a sharp conductance change at about 10 mV. (V = 100 mV, I = 1 nA, B = 0 T, T = 1.2 K).

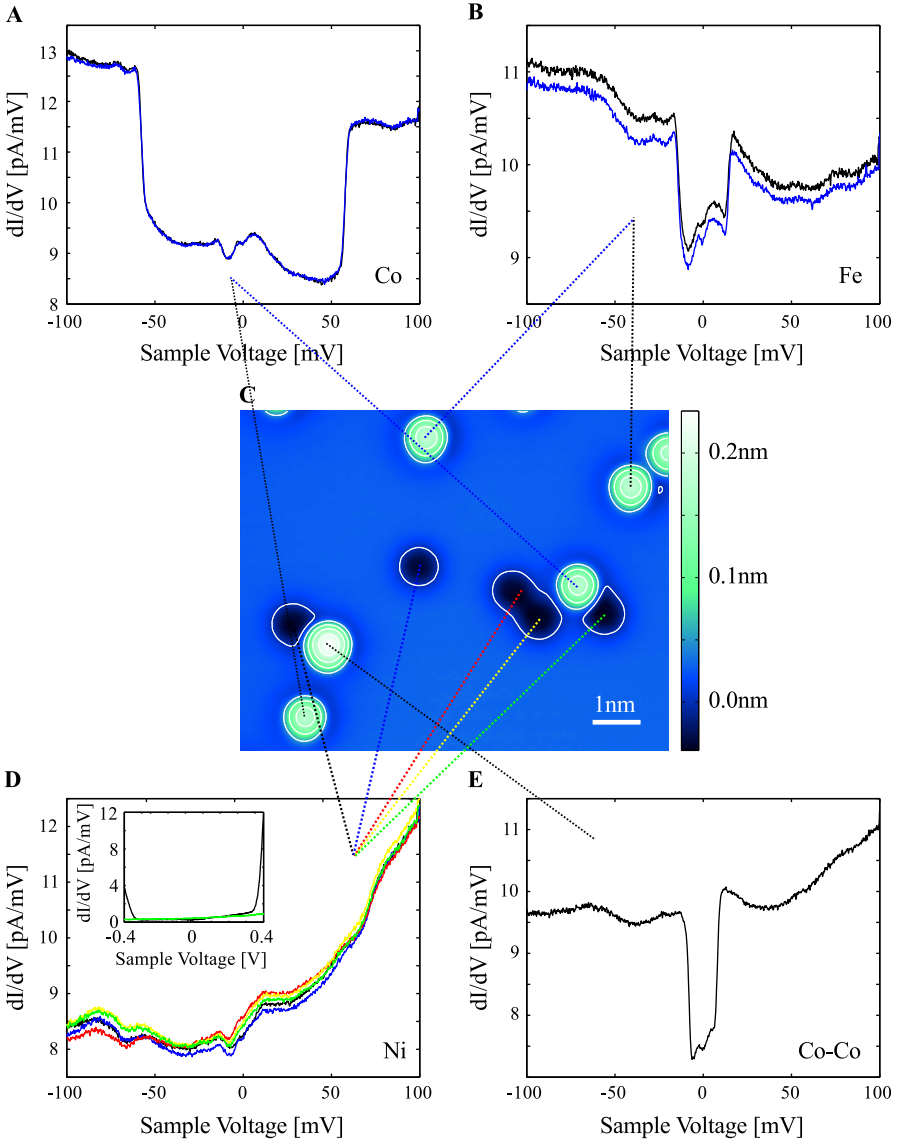
A
dI/dV [pA/mV]
Co
Sample Voltage [mV]
B
dI/dV [pA/mV]
Fe
Sample Voltage [mV]
C
0.2nm
0.1nm
0.0nm
1nm
D
dI/dV [pA/mV]
Ni
Sample Voltage [mV]
dI/dV [pA/mV]
Sample Voltage [V]
E
dI/dV [pA/mV]
Co-Co
Sample Voltage [mV]

same binding site which according to DFT calculations is on top of an oxygen atom (see schematic in Figure 3.2) (*26*,*33*). The two different Mn species appear to adsorb on two different binding sites, Mn_A is found on the same binding site as the other atoms, while Mn_B seems to sit on the bridge site between two oxygen as well as two magnesium atoms (right side of Figure 3.2).

In addition to their different appearance in STM images, the spectral features of the Mn_A and Mn_B atoms are extremely different. Figure 3.3 shows the SES spectra of three magnetic atoms and the one of the Co dimer. Both Co (Figure 3.3 A) and Fe (3.3 B) show a clear step-wise increase symmetric around zero bias. For the Fe atoms this change in conductance is at $\sim$15 mV and for Co at $\sim$60 mV. Both of these so-called zero-field splittings are much larger than any previously observed splitting for atoms on insulating layers (*25*,*28*,*34*) or metal surfaces (*35*,*36*). These characteristic spectra are consistently observed over several different sample preparations.

The spectra for Ni (Figure 3.3 D) however resemble the spectra taken on the bare MgO surface up to energies of at least 100 mV. Only when the bias range is extended up to 400 mV do large changes in conductance start appearing (see inset). After increasing the voltage above $\sim$500 mV the atoms dissociate from the surface. Thus these high voltage features of Ni are not studied further

Figure 3.4 *(following page)*: Overview of different species of transition metal atoms on a single monolayer of MgO. (**A**) Two images of a single monolayer of MgO with two Mn_A, one Co and one Fe atom (upper image) and one Mn_B and one Fe atom (lower image). (V = 100 mV, I = 50 pA). (**B**) The SES spectrum on Mn_A shows no distinct features and looks similar to the background spectrum in the other spectra (C,E). (**C**,**E**) The Co and Fe spectra have an excitation at $\sim$60 mV and $\sim$15 mV, as shown in Figure 3.3. (**D**) Mn_B shows a sharp symmetric step around zero bias of about 0.5 – 2 mV (depending on the atom probed). For comparison the inset in (**E**) shows the same energy window on the Fe atom. (V = 100 mV, I = 2.5 nA (B,C,E) and I = 2 nA (D), B = 1.5 T, T = 1.2 K).

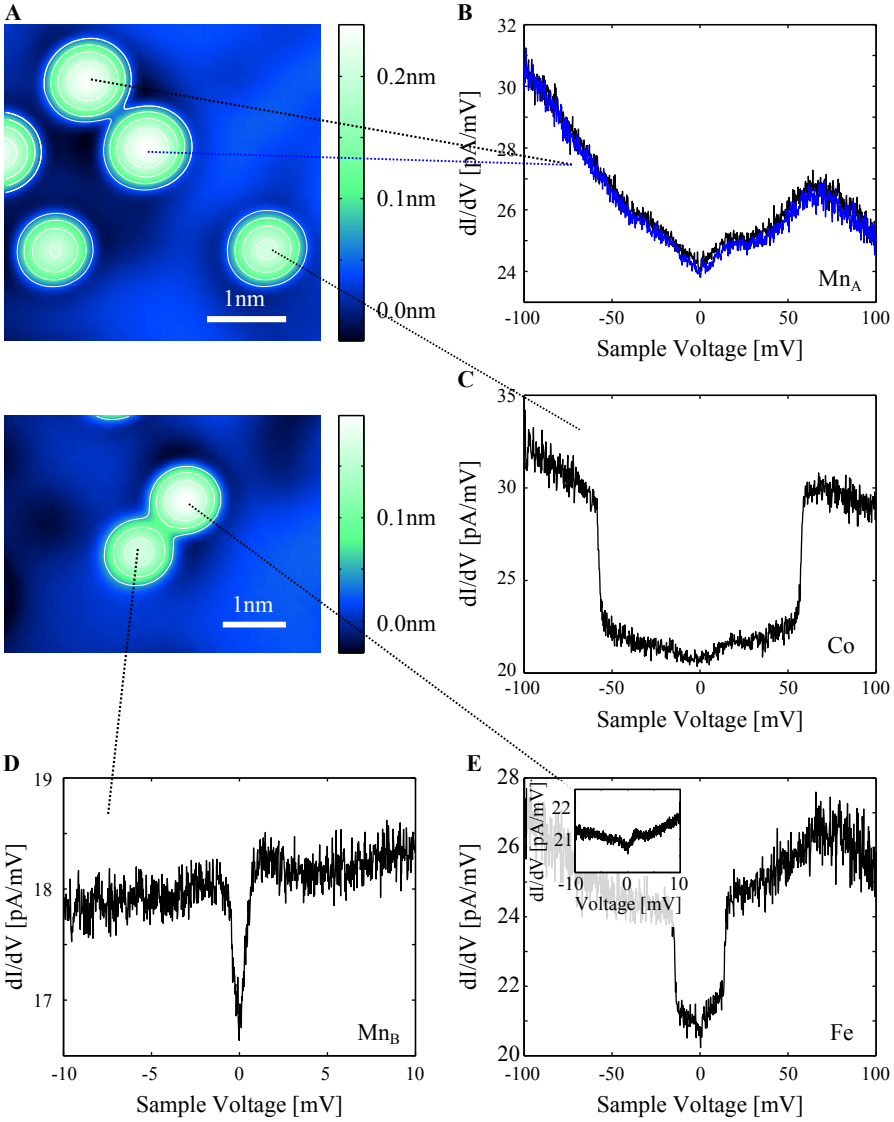
A
0.2nm
0.1nm
0.0nm
1nm
B
dI/dV [pA/mV]
Mn$_A$
Sample Voltage [mV]
C
0.1nm
0.0nm
1nm
Co
Sample Voltage [mV]
D
dI/dV [pA/mV]
Mn$_B$
Sample Voltage [mV]
E
dI/dV [pA/mV]
Voltage [mV]
Fe
Sample Voltage [mV]

in this thesis.

The Co dimer shows a clear step-wise increase in conductance at $\sim$10 mV (3.3 E). This excitation is very different from the Co single atom spectrum indicating a dramatic change in the magnetic properties when several atoms are coupled together, as it has been observed before for chains of Mn atoms (*37*). The dimer imaged and examined here was found as-is on the MgO surface. However, in general only very few dimers (of any atom species) are formed during low temperature deposition. We ensured that these features are indeed related to Co dimers by purposefully building them with atom manipulation. The protocols for this manipulation are still under investigation and no hetero-dimers or longer chains of coupled atoms of any kind were build on MgO so far.

As mentioned above, Mn seems to adsorb on two different binding sites, which results in two very different spectra. Mn_A has, similar to Ni, no spectral features (Figure 3.4 B). Mn_B however has a sharp step at about $0.5-2$ mV (3.4 D). This feature has a strong variation in energy depending on the specific atom probed. Note that this feature could not be reproduced when Mn_A was moved to the same binding site as Mn_B, with STM atom manipulation. This suggests that the feature of Mn_B might therefore be a feature due to a defect in MgO and it is not further investigated in this thesis. The fact that the more frequent Mn_A spectra do not show any SES steps is surprising, as for previous results on other insulating surfaces clear spin-excitations were visible for Mn (*15*,*38*). We speculate that the higher symmetry compared to the previous results as well as the very different chemical environment influences this magnetic behavior significantly.

For the rest of this thesis, the main focus is on single Fe and Co atoms on MgO. Thus, in the next sections we will elaborate the details of their single atom spectra and we will for example show the dependence of the SES steps on a changing magnetic field. The STM experiments on both of these atoms

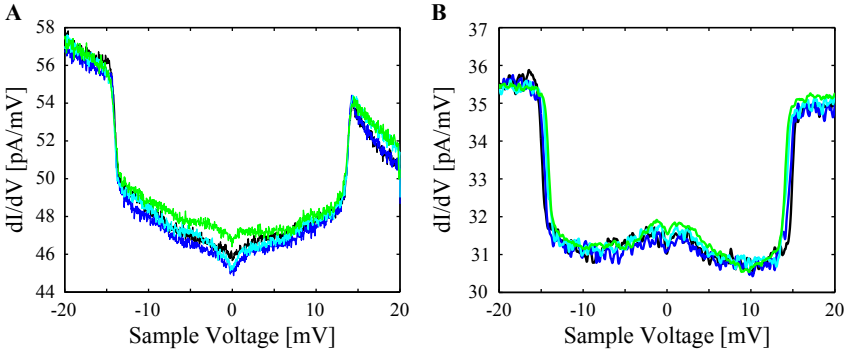

Figure 3.5: Magnetic field dependence of the Fe on MgO in an in-plane (**A**) and out-of-plane (**B**) magnetic field (green: 0 T, cyan: 2 T, blue: 4 T and black: 6 T). The steps change their position only with the out-of-plane field indicating a uniaxial anisotropy in the out-of-plane (perpendicular to the surface) direction.

were additionally supported by XMCD measurements and detailed theoretical calculations, which will be discussed in the following chapters. The results on Mn, Ni and the Co dimer will not be further discussed.

3.5.1 Fe on MgO

The spin-excitation spectrum of an iron atom on MgO in zero magnetic field shows a single step-wise increase in conductance at 14.0 mV (variations between different atoms of ± 0.3 mV were observed), symmetric around zero bias (Figure 3.5). From the comparison of the in-plane (Figure 3.5 A) and out-of-plane (B) magnetic field spectra, we can determine the easy axis of the system to be perpendicular to the surface, because the step energy only varies when the magnetic field is applied along this out-of-plane direction. A zoom-in on the SES step and its magnetic field dependence when the magnetic field is applied out-of-plane is shown in Figure 3.6 A. In a magnetic field the conductance step splits into two distinct steps.

From DFT calculations we know that the spin of the system is close to S = 2. A spin of S = 2 results in five spin levels (see inset in Figure 3.6 B). We label the states consecutively from the ground state, as state 0, to the highest excited state, as state 4. Therefore, the two transitions we see as distinct steps in Figure 3.6 A are the transitions $0 \rightarrow 2$ and $1 \rightarrow 3$ (V_{02} and V_{13}). The two steps shift according to Zeeman energy, which results in a well resolved splitting of 1.9±0.3 mV at 6 T, where the transition $0 \rightarrow 2$ shifts up in energy and the $1 \rightarrow 3$ transition shifts down.

The presence of the V_{13} transition at finite magnetic field is surprising because at low temperature ($k_{\mathrm{B}}T \ll eV_{01}$, where k_{B} is the Boltzman constant and T is temperature) and at low applied bias voltage ($V_{\mathrm{bias}} < V_{02}$) one would expect only state 0 (the ground state) to be occupied for an appreciable fraction of time. The observation of the $1 \rightarrow 3$ transition for Fe on MgO is an indication that the excited state 1 has a lifetime above 1 ns (the mean tunneling time between electrons at the measured currents) (see Chapter 8 for more details on the lifetime).

Fe on MgO is well described by an effective spin Hamiltonian with multiplicity of 5, i.e. effective spin of S_{eff} = 2 (for simplicity only referred to as S in the following), containing a four-fold crystal field with the easy axis along the surface normal and a Zeeman term in the z-direction.

$$H_{\mathrm{eff}} = D \cdot \hat{S}_z^2 + C \cdot (\hat{S}_+^4 + \hat{S}_-^4) + g^* \mu_{\mathrm{B}} \hat{S}_z \cdot B_z \tag{3.5}$$

The magnetic anisotropy parameters are $D = -4.67 \pm 0.05$ meV and $C < 2$ μ eV, and the effective g-value is $g^* = 2.57 \pm 0.06$. The fourth-order term couples the $M_S = \pm 2$ states together, which allows the transition from state 0 to 1 and that in turn allows the V_{13} transition to be visible (if the lifetime in state 1 is long enough). However, if the fourth-order coupling term C is sufficiently small, the splitting will be too small, and the transition intensity

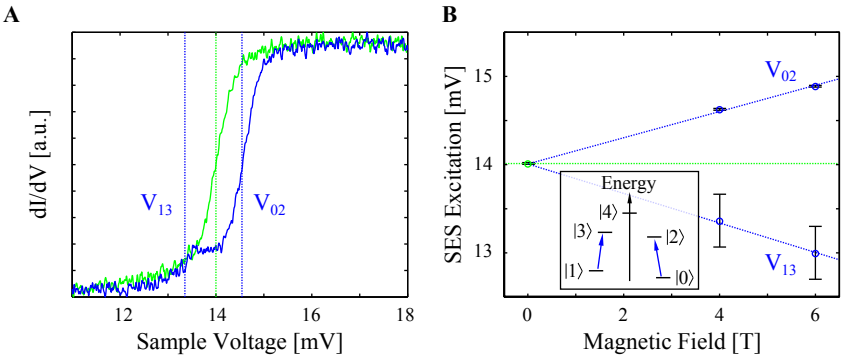

Figure 3.6: SES step energy of Fe on MgO. (**A**) Zoom-in on the step energy at 0 T (green) and 4 T (blue), with the magnetic field applied out-of-plane (normalized in amplitude). The SES step splits into two steps V_{02} and V_{13} in a magnetic field. (V = 30 mV, I = 1 nA). (**B**) Magnetic field dependence of the two SES steps. The two steps split according to Zeeman energy to a splitting of 1.9±0.3 mV at 6 T. The inset shows a schematic drawing of the five energy levels labeled from state 0 to 4.

between 0 and 1 too low, to cause a visible transition in the SES spectra. For simplicity we disregard the term proportional to $\hat{S}_z^4$, as this term has a similar effect on the energy levels as the term with $\hat{S}_z^2$ and neglecting it reduces the number of fitting parameters. For this effective spin Hamiltonian we derived the g^* value from the slope of the B-field dependence shown in Figure 3.6 B (*15*).

Fe on MgO is thus a system that is well described by an effective spin Hamiltonian. The magnetic anisotropy for Fe on MgO is 18.7 meV (= $D\hat{S}_z^2$), which is significantly larger than for Fe atoms on other surfaces (*25*,*36*), but not quite as large as the maximal reported value for the anisotropy of a 3d transition metal atom of about 60 mV, as discussed in the following (*26*). Furthermore, the results presented so far indicate a long lifetime for the first excited state, which we will discuss in more detail in Chapter 8.

3.5.2 Co on MgO

At zero magnetic field, Co on MgO also has only a single visible transition. As shown in Figure 3.7 A, this excitation occurs at 57.7 mV (*26*) which is a much larger zero-field splitting than the couple of meV typical to single atoms on surfaces (*25*,*28*,*34*). This large splitting indicates an exceptionally high magnetic anisotropy for Co on MgO. In Chapter 5 we will demonstrate that this is actually the maximal splitting possible for 3d transition metal atoms. The observed step is again magnetic in origin and splits into two in an applied magnetic field.

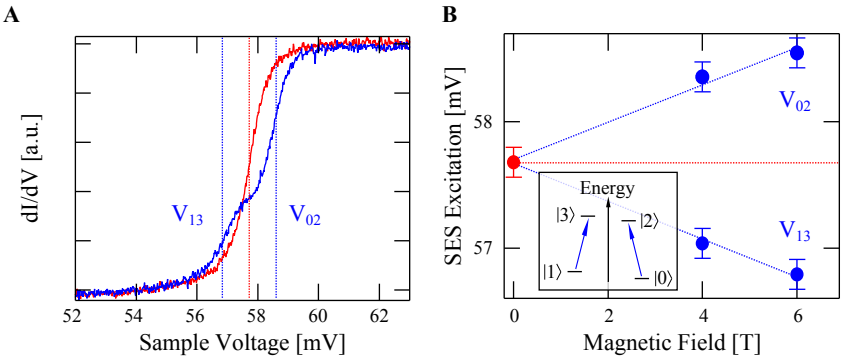

Figure 3.7: SES step energy of Co on MgO. (**A**) Zoom-in on the SES step at 0 T (red) and 6 T (blue), with the magnetic field applied out-of-plane (normalized in amplitude). The SES step splits into two steps V_{02} and V_{13} in a magnetic field. (V = 100 mV, I = 5 nA). (**B**) Magnetic field dependence of the two SES steps. The two steps split with Zeeman energy to a splitting of 1.8±0.2 mV at 6 T. The inset shows a schematic drawing of the Co's four lowest energy levels labeled from state 0 to 3.[1]

The DFT calculations suggest a spin of $S = \frac{3}{2}$ for the Co atoms adsorbed on the oxygen binding site of the MgO surface (resulting in a four-level

[1] From Rau, I. G., Baumann, S. *et al.* Reaching the magnetic anisotropy limit of a 3d metal atom. *Science* **344**, 988–992 (2014). Reprinted with permission from AAAS.

system, see inset in Figure 3.7 B). For ease of discussion we will approximate the magnetic states by a system with uniaxial anisotropy and a spin $S = \frac{3}{2}$ (meaning $D < 0$ in the effective spin Hamiltonian picture). We assign the observed excitations to transitions between the ground ($M_S = \pm\frac{3}{2}$, labeled as states 0 and 1 in Figure 3.7 B, inset) and excited states ($M_S = \pm\frac{1}{2}$, labeled as states 2 and 3). At zero magnetic field, the states 0 and 1, as well as 2 and 3, are degenerate. This yields identical excitation voltages ($V_{02} = V_{13}$). The two steps shift in accordance to the Zeeman energies, with the $0 \rightarrow 2$ transition shifting up and the $1 \rightarrow 3$ transition shifting down with increasing magnetic field, resulting in a well resolved splitting of 1.8 ± 0.2 mV at 6 T.

Similar to the behavior of the Fe atom on MgO, this observation of both transitions in magnetic field (V_{02} and V_{13}), is an indication that the lifetime of state 1 is above 1 ns (the mean tunneling time between electrons at the measured currents). It shows that state 1 is occupied an appreciable fraction of time, despite the low temperature ($k_{\mathrm{B}}T \ll eV_{01}$) and a low applied bias voltage ($V_{\mathrm{bias}} < V_{02}$). For more details on the lifetime see Chapter 8.

The described four level system could be approximated with an effective spin Hamiltonian:

$$H_{\mathrm{eff}} = D\hat{S}_z^2 + g^*\mu_{\mathrm{B}}\hat{S}_z \cdot B_z \tag{3.6}$$

where $D = -28.85$ meV and $g^* = 2.6$. The fourth-order term will not affect the states of a system with spin smaller than 2. Hence, no mixing between the two lowest lying states 0 and 1 will occur. Assuming that the terms in this effective Hamiltonian are only driven by the substrate symmetry, this strongly contradicts the observation of the transition between state 1 and 3. Therefore, a spin Hamiltonian based on the geometry of the substrate cannot accurately describe Co on MgO and we have to rely on more detailed calculations to understand the nature of the observed energy levels (see Chapter 5).

3.6 Summary on spin-excitations on MgO

In this chapter we introduced spin-excitation spectroscopy (SES) which is a powerful technique to resolve magnetic energy levels of individual atoms in STM. We showed the spectroscopic features of four different 3d transition metal atoms, namely Co, Fe, Mn and Ni, on MgO. The main focus is on Co and Fe, which showed clear zero-field excitations at 58 mV and 14 mV, respectively. Such transitions can in most cases be described by an effective spin Hamiltonian, as has been successfully demonstrated in many STM experiments, and is confirmed here, for the case of single Fe atoms on MgO. However, there are systems, such as Co on MgO, where the description with the simplified model of an effective spin Hamiltonian breaks down and where more extensive modeling becomes necessary to accurately describe the states.

Chapter 4

Probing the magnetization direction and total moment of single atoms

Along with a large anisotropy barrier, the magnitude of the total magnetic moment is essential in suppressing spontaneous magnetization reversal.

The XMCD measurements on Co presented in this chapter are published in: Rau, I.G., Baumann, S. *et al.* Reaching the magnetic anisotropy limit of a 3d metal atom. *Science* **344**, 988–992 (2014). For the results on Fe the manuscript is in preparation: Baumann, S. *et al.* Spin and orbital magnetism of Fe atoms on MgO.

4.1 X-ray absorption spectroscopy and X-ray magnetic circular dichroism

X-rays with energies in a range of several 100 eV can be absorbed by single atoms and cause transitions of electrons from core to valence shells. Such

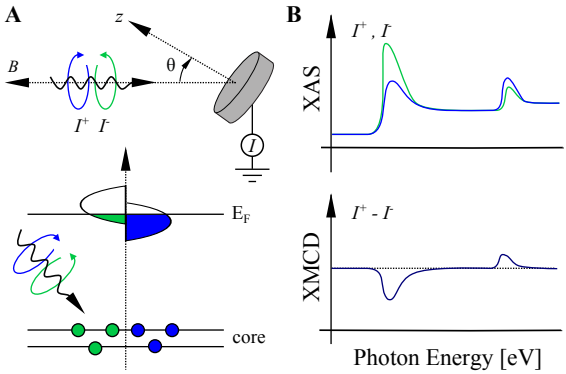

Figure 4.1: X-ray absorption spectroscopy (XAS) and X-ray magnetic circular dichroism (XMCD) schematics. (**A**) X-ray measurement setup (top panel) in which the circularly polarized light (I^+ and I^-) is incident at an angle θ to the surface normal (z) and parallel to the applied magnetic field B. We measure the current on the sample at the absorption energies as a consequence of replenishing the photo-emitted electrons. Absorption occurs whenever the photon energy is large enough to cause transitions of core electrons to the valence band, at the Fermi-energy E_F (lower panel). The different colors indicate different spin directions. The incident circular polarized light can cause $\Delta l = \pm 1$ transitions but does not change the spin. (**B**) The absorption spectra are different between the different circular polarizations of the light (when a magnetic field is applied) (top panel). The difference of the two absorption spectra is the XMCD spectrum which carries information about the spin and orbital moments of the measured system (bottom panel).

transitions occur at a different energy spacings in all elements, making X-ray absorption spectroscopy (XAS) an element specific technique. The absorption is measured by the electron current required to keep the sample at constant electric potential (ground) (see Figure 4.1 A). Electrons removed by X-ray excitations must be refilled from the substrate (more current flows), leading to a peak in the absorption spectrum (see Figure 4.1 B). The most intense absorption features observed are electric-dipole allowed transitions ($\Delta l = \pm 1$, $\Delta s = 0$) to unoccupied final states. The name of the so-called absorption

edge depends on the specific core electron that is excited in that process, the principal quantum number n = 1,2,3 corresponds to the K-,L- and M-edge, respectively. In our experiments we only used $3d$ transition metal atoms and the main excitations are those of $2p$ electrons to the $3d$ unoccupied states, in the L-edge. In the schematic shown in Figure 5.1 (next chapter) we indicate how the induced transitions actually cause a configuration change, for example for Ni from $2p^6 4s^2 3d^8$ to $2p^5 4s^2 3d^9$.

X-ray light can have different polarization directions, such as linear or circular polarization. For probing magnetic properties, circular polarized light is particularly interesting as it carries an angular momentum of $\pm\hbar$. The incident photon of a certain circular polarization can transfer its orbital angular momentum to the excited electron with the selection rule $\Delta l = \pm 1$, while the spin angular momentum remains the same. X-ray magnetic circular dichroism (XMCD) is a difference spectrum of two absorption spectra taken in a magnetic field, one taken with left circular polarized light, one with right circular polarized light (see Figure 4.1 B). Because $3d$ states are the origin of the atomic magnetism ($3d$ transition metals), and we are probing absorption from a $2p$ state to a $3d$ state, this absorption contains information about the magnetic properties. The absorption is spin-dependent insofar that the photoelectrons created from the $2p$ level carry spin angular momentum (induced by spin-orbit coupling in the p-shell), which they use to probe the empty d-states. Indeed, the XMCD spectra allow identification of the magnetization direction and strength of a given element, as well as the quantitative estimation of spin and orbital moment, by means of the so-called XMCD sum rules (*39–41*). Thus, X-ray absorption is an element-specific technique that has the ability to quantitatively separate and determine the spin and orbital magnetic moment and their anisotropy. The relative strength of the XAS features are additionally a fingerprint of the chemical state of a given atom. Due to the surface sensitivity and element specificity, X-ray techniques can resolve features down to a coverage of 0.002 monolayers of a given element and can thus be used on ensembles of single atoms (*42*).

In our experiments we are particularly interested in the comparison of the X-ray results to the the SES result from STM. We focused the measurements on the Fe and Co atoms on MgO, where we already have information about magnetic excitations out of the ground state from the SES spectra. However, we will show that because the sum rules are not well established for single atoms on surfaces we rather have to rely on the the best-fit multiplet calculations to the XAS and XMCD spectra to obtain information about the orbital and spin moment in our atoms (see Chapter 5).

4.2 X-ray absorption methods

The X-ray experiments were performed at the X-Treme beam line of the Swiss Light Source (SLS) (*43*) using circularly polarized light at a temperature of 3.0±0.5 K and in magnetic fields up to ±6.8 T. Different samples with Fe and Co coverage of 0.03 to 0.1 monolayers were measured. The magnetic atoms were deposited on 2 to 4 monolayers of MgO on Ag(001).

The X-ray absorption spectra (XAS) were recorded in the total electron yield mode and normalized by the intensity of the X-ray beam measured on a metallic grid placed upstream from the sample. To probe both out-of-plane and in-plane moments, the sample was rotated with respect to the magnetic field and the X-ray beam by an angle θ from 0° (normal incidence) to 60° (grazing incidence) (see Figure 4.1 A). Measurements were taken over the L_3 and L_2 absorption edge of Fe and Co on MgO, corresponding to excitations of core $2p$ electrons into empty $3d4s$ states.

The XMCD signal is the difference of XAS recorded for parallel (I^+) and anti-parallel (I^-) alignment of the photon helicity with the applied magnetic field. Due to the small coverage, the Co and Fe absorption intensities are small and superimposed on a large background signal originating mostly from the excitation of the Ag-M-edges (see inset in Figure 4.2 B, gray curve). This background was measured prior to the deposition of Co and Fe and

subsequently subtracted from the XAS in order to facilitate the analysis of the multiplet features and compare it with the calculated spectra.

XAS measurements of metal atoms on thin insulating layers presents technical challenges related to the low concentration of the atoms to be probed as well as to the X-ray induced desorption of the adatoms. We found that the XAS intensity quickly changed as a function of time due to exposure to the X-ray beam. Whereas the spectral shape remained mostly unchanged, the absolute absorption intensity was strongly decreasing, by about 20% in 120 s, which is the time required to measure a single absorption scan. Note that the change in the absorption intensity was not reversible, which was verified by temporarily switching off the X-ray beam and recording a spectrum again after a few minutes. Because the spectral line shape remains the same, we exclude that this effect is due to a change of coordination of the magnetic atoms induced by diffusion and aggregation, which would imply significant broadening and changes of the XAS multiplet features (*44*). Therefore, the intensity reduction with exposure time must be attributed to a decrease of atom coverage due to photon induced adatom desorption, as was already observed for Co monomers deposited on Al_2O_3 (*45*). For this reason, every X-ray absorption spectrum was measured on a different region of the sample using a defocused X-ray beam spot size of 1.5 mm x 0.8 mm. The XAS shown in the next section are averages of two (I^+) and two (I^-) spectra recorded over four different regions of the sample. Although the single atom coverage is homogenous on the dimensions of the substrate, this procedure severely limits the acquisition time for each sample and introduces errors in the determination of the absolute XAS intensity required to extract the magnetic moments using the XMCD sum rules (*39*,*40*).

Magnetization curves versus applied field were measured at normal incidence by saturating the magnetic moment at $\pm$6.8 T and recording a pair of spectra (I^+) and (I^-), with each spectrum taken on a different sample position. Because of the need to measure spectra at different points and the larger footprint

of the X-ray beam at $\theta = 60°$, it was not possible to measure the magnetization versus field at grazing incidence.

4.3 XMCD results on Fe and Co on MgO

By measuring the excitation cross-section for $2p$ to $3d$ transitions, L-edge X-ray absorption spectra provide a probe of the magnetic properties of transition metal ions (*46*) that is highly complementary to SES. Spectra obtained at the L-edge with circularly polarized light are shown for both Fe and Co in Figure 4.2. The XAS line shape, for example for the Co, differs from that of atoms adsorbed on metal substrates (*4*,*42*) as well as from typical CoO phases (*39*), showing that the bonding is specific to the MgO surface.

The X-ray magnetic circular dichroism intensity measured at normal incidence (red) is larger for both atoms than the one at grazing incidence (blue) (Figure 4.2 C and D), which implies that the magnetic moment has an out-of-plane easy axis. This out-of-plane easy axis agrees with our previous assessment by SES.

Rather than using the sum rules, we determine the electronic ground state and the structure of the lowest lying magnetic states by simulating the X-ray experimental results using multiplet ligand field theory (see Chapter 5) (*46*). The simulated spectra of both atoms are shown together with the respective experimental spectra in Figure 4.2. We will explain the details of these calculations and their results in the next chapter. Nevertheless, one can directly see from the XMCD spectra for both atoms, Fe and Co, that they must have a large orbital contribution to the total moment due to the fact that in the normal incidence spectra (Figure 4.2 C and D (red curves)), both absorption peaks are negative. Conceptually, a large orbital moment is equivalent to a half filled d-shell in one spin direction (while the other spin orientation is either completely empty or fully filled). If such a half filled valence band is present, the absorption on both L-edges will predominantly occur with one circular polarization (because the

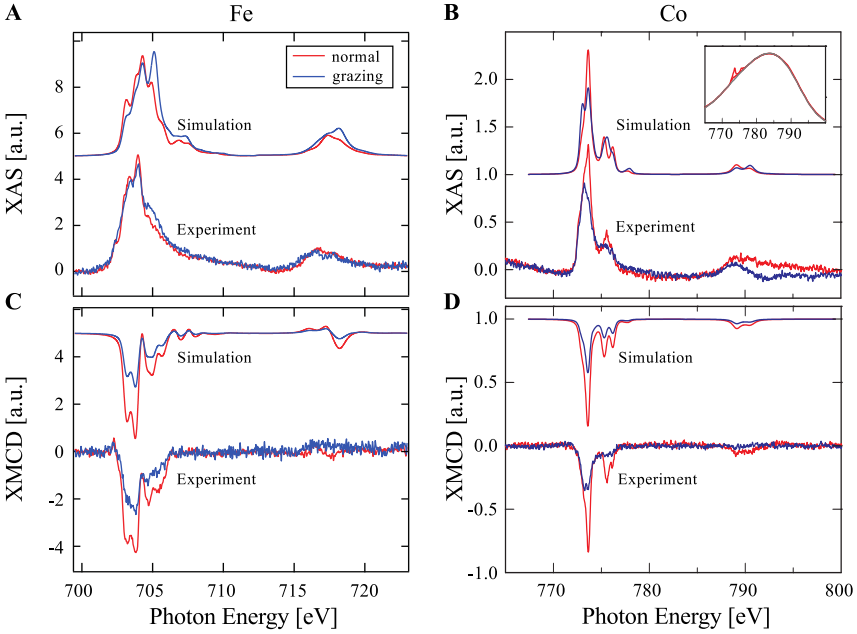

Figure 4.2: Measured and simulated XAS and XMCD over the L_3 and L_2 edges of both Fe and Co. (**A**) XAS spectrum of Fe, and (**B**) of Co[1], at a concentration of 0.03 ML. Normal (red, $\theta = 0°$) and grazing (blue, $\theta = 60°$) incidence of X-ray beam (and magnetic field) to surface normal. The spectra are the sum of positive and negative circular polarization ($I^+ + I^-$). The inset in (B) shows the XAS spectra without background subtraction, the L-edges of both atoms lie on top of the M-absorption edge of the Ag substrate. (**C**) XMCD ($I^+ - I^-$) spectrum of Fe, and (**D**) of Co[1]. (B = 6.8 T, T = 3.0±0.5 K).

spin orientation of the photo-electron is coupled to the incident X-ray light by the spin-orbit coupling of the core level). This leads to a difference spectrum where both L-edges have a negative signal as a strong indication of large orbital moment.

[1] From Rau, I. G., Baumann, S. *et al.* Reaching the magnetic anisotropy limit of a 3d metal atom. *Science* **344**, 988–992 (2014). Reprinted with permission from AAAS.

4.4 Magnetization curves on Fe and Co on MgO

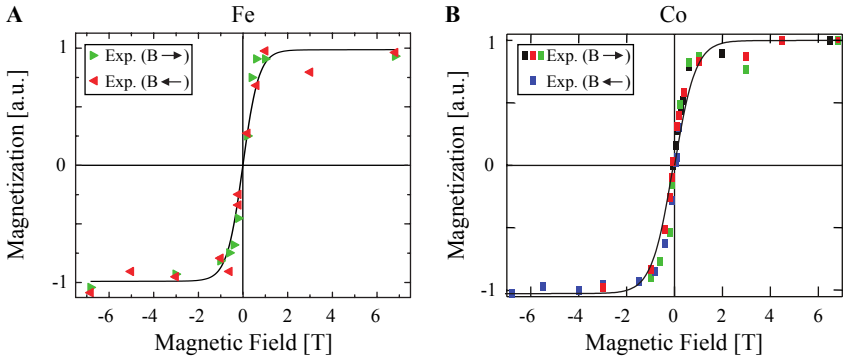

Figure 4.3: Out-of-plane magnetization versus field for both Fe (**A**) and Co (**B**)[1]. (**A**) measured by saturating the sample at 6.8 T (red) and −6.8 T (green) at each point. (**B**) measured by saturating the field at 6.8 T (black, red and green) and −6.8 T (blue). Different colors refer to different samples. The solid line represents the expectation value of $\langle \mu_z \rangle \approx 6\ \mu_B$ (for both atoms). (T = 3.0±0.5 K).

The substantial orbital contribution can also be seen quantitatively in the magnetization curves measured by XMCD as a function of applied field, which indicates a local moment of $\sim 6\mu_B$ per atom for both Fe and Co (Figure 4.3) (where μ_B is the Bohr magneton). This result is in agreement with the magnetization $\langle \mu_z \rangle = \langle L_z \rangle + \langle 2S_z \rangle$ calculated by using the wave functions and energy levels obtained from the multiplet simulations (see next chapter). Both experimental and theoretical curves saturate very fast, as expected for strong magnetic anisotropy.

At low magnetic fields, the measured values remain above the calculated values, which could be the result of slow relaxation effects or induced magnetic

[1] From Rau, I. G., Baumann, S. *et al.* Reaching the magnetic anisotropy limit of a 3*d* metal atom. *Science* **344**, 988–992 (2014). Reprinted with permission from AAAS.

moment contributions from the substrate atoms. Due to the indication of long lifetimes in the SES measurements (observation of a second step (V_{13}) in an applied magnetic field) we specifically tried to see, if the lifetimes of the first excited states could be long enough, to be observable as hysteresis in the magnetization curve. However, such a measurement occurs at a time scale of up to one minute, which would be incredibly long given that the the longest lifetimes for $3d$ transition metal atoms on metals or thin insulators have so far been less than a nanosecond (*35*,*36*,*38*). Thus the magnetization curves give an upper bound on the lifetimes for our atoms (lifetime $<$ min). More information on the lifetimes of Fe and Co will follow in Chapter 8.

4.5 Summary on XAS and XMCD results

In this chapter we showed how X-ray absorption techniques are a powerful complement to the STM measurements as they are able to gain information about local anisotropy of the magnetic moment. We focused our measurements on the transition metal atoms Fe and Co and showed that the easy axis for both atoms is the out-of-plane direction. We additionally showed that both atoms have a total magnetic moment of the ground state close to $\sim 6\mu_B$ and that they both showed clear signs of exceptionally large orbital moment on the MgO surface.

The XAS and XMCD results can be further elaborated using ligand field multiplet calculations. These will reveal details about the electronic structure of the ground state as it is probed by STM and are the subject of the next chapter.

Chapter 5

Insight into the origin of magnetic properties

The magnetic character of different energy states, described by orbital and spin moments, governs their properties in terms of for example their energy separation.

The multiplet calculation on Co presented in this chapter is published in: Rau, I.G., Baumann, S. *et al.* Reaching the magnetic anisotropy limit of a 3*d* metal atom. *Science* **344**, 988–992 (2014). For the calculations on Fe the manuscript is in preparation: Baumann, S. *et al.* Spin and orbital magnetism of Fe atoms on MgO. For the point charge model calculation another manuscript is in preparation: Baumann, S. *et al.* Anisotropy tuning explained by a point charge model.

5.1 Multiplet calculations

In an X-ray absorption experiment an electron from the core electronic shell of an atom gets excited into a valence state, which creates an excited state with

a core hole and an additional electron in the valence shell (see Figure 5.1 A). The overlap of the core and valence wave function creates so-called multiplet effects that can represent themselves as multiple peaks in the absorption spectra (*47*). These multiplet effects are often especially visible in the spectra of $3d$ transition metals at their L_3 and L_2 edges (see e.g. Figure 4.2). They also become more prominent in X-ray experiments on single atoms or low density clusters (*42*,*45*). Simulating and fitting these transitions is the basis of the so-called multiplet calculations.

Multiplet calculations describe a set of calculations that start with the Hamiltonian for the free atom and later add perturbations such as ligands surrounding the atom and spin-orbit coupling of the valence electrons. We will show the effects of the surrounding ligands and the spin-orbit coupling later in this chapter, as they occur at energy scales much smaller than the electrostatic interactions (in the case of $3d$ transition metal atoms). The initial Schrödinger equation of a free atom contains the kinetic energy of the electron (H_{kin}), the electrostatic interaction of the electron with the nucleus (H_{coul}) and the electron-electron repulsion ($H_{\text{e-e}}$):

$$\begin{aligned} H &= H_{\text{kin}} + H_{\text{coul}} + H_{\text{e-e}} \\ &= \sum_N \frac{p_i^2}{2m} + \sum_N \frac{-Ze^2}{\vec{r}_i} + \sum_{\text{pairs}} \frac{e^2}{\vec{r}_{ji}} \end{aligned} \tag{5.1}$$

where N is the number of electrons in the atom, m is the mass of the electron, p_i describes the momentum of each electron, Z is the number of protons in the nucleus and e the elementary charge. $\vec{r}_i$ describes the position of each electron with respect to the nucleus, while $\vec{r}_{ji}$ is the distance between two individual electrons.

One can define an average energy for each configuration (e.g. the $3d^N$ or $2p^5 3d^{N+1}$ configurations, that are used in our X-ray experiments) by

taking those terms of the Hamiltonian that are the identical for all states in the same configuration (first two terms plus the spherical part of the electron-electron interaction). The remaining term in the Hamiltonian, i.e. the modified (non-spherical) electron-electron interaction, then determine the energy separation of the different atomic multiplets within each configuration. The atomic multiplets are labeled by their orbital moment L and spin moment S with a so-called term symbol ${}^{2S+1}X$, where X equals S, P, D and F for L = 0,1,2 and 3. In the absence of spin-orbit coupling, all wave functions with the same L and S are degenerate, giving a $(2L+1)(2S+1)$-fold degenerate energy level for each such term (or atomic multiplet) of a configuration.

Based on experimental observations, Friedrich Hund defined three rules to determine which term symbol is lowest in energy for a partially filled shell (*48*):

1. The states with the largest possible spin have the lowest energy.

2. Among those states, the one with the maximal orbital moment are lowest in energy.

3. If spin-orbit coupling is large, the lowest term has total angular momentum $J = |L - S|$ if the shell is less than half full and $J = |L + S|$ if the shell is more than half full. (Note that this rule does not apply for the $3d$ metal atoms on MgO, as treated later in this chapter, because in our case the ligand field is a stronger perturbation on the energy eigenstates than the spin-orbit coupling.)

To summarize: A term has the lowest energy if the electrons are as far apart as possible, because the Hund's rules are a direct consequence of Coulomb repulsion. This for example results in the ${}^5D$ term as lowest 25-fold degenerate energy level for a d^6 atom such as Fe, or the ${}^3F$ as lowest term for a d^7 atom such as Co.

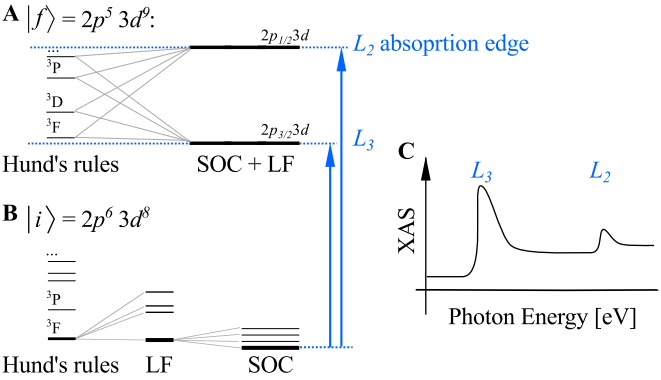

Figure 5.1: Schematics on transition intensity calculations for X-ray absorption spectroscopy. Transitions are calculated from an initial state $|i\rangle$ (**B**) to all possible final states $|f\rangle$ (**A**). The obtained transition intensities are then broadened in order to simulate the XAS and XMCD spectra (**C**). Here, the states of a Ni atom are shown, as a representative transition metal species. (**B**) The eigenstates of the initial state are separated by the free atom Hamiltonian (according to Hund's rules), the ligand field (LF) and spin-orbit coupling (SOC). From this initial state all final states can be reached (given the selection rules are followed). The final states (**A**) are also separated by the free atom Hamiltonian, as well as spin-orbit coupling and ligand field. (**C**) The sum over all possible transitions at the L_3 and L_2 absorption edge then gives the XAS spectrum (as shown before in Figures 4.1 and 4.2).

We will in the following show the results of an extended calculation as a best-fit to the experimental results of XAS and XMCD. The calculation was performed by Dr. Sebastian Stepanow, in the group of Prof. Pietro Gambardella, at the ETH Zürich. In a full multiplet calculation for the XAS analysis, the average energy for each configuration is calculated for the initial and final state configurations (configurations without and with a hole in the core, see Figure 5.1 B and A) and the spacing between the different multiplets (terms) is then determined using so-called Slater-Condon integrals (*47*). In order to model X-ray absorption spectra the average energy of all possible configurations has to be calculated. In Dr. Sebastian Stepanow's calculation,

he in fact calculated the average energies of the initial and final configurations and determined transition intensities between the obtained eigenstates. In the next section we will give some more detail on these calculations and the results on Fe and Co, as shown in Figure 4.2. Later in this chapter, we will introduce our own, simplified version of these calculations. Since for the STM results we are only interested in the ground state configuration, which is the initial state of the X-ray absorption experiments, the calculations can be simplified by only considering that initial state (initial configuration). We limited the calculation further by only calculating the lowest lying atomic multiplet (lowest term). However, both calculations start with the fully anti-symmetrized multi-electron wave functions (Slater determinants), and they both add ligand field effects as well as spin-orbit coupling as perturbations on these initial wave functions (see later in this chapter).

5.2 Specifics for full multiplet calculations on Fe and Co on MgO

We used multiplet ligand field theory (*46*) as a fit to the experimental XAS and XMCD spectra to determine the electronic ground state and the structure of the lowest lying magnetic states. These calculations include charge transfer (σ-donation) via the d_{z^2} orbital and take the mixing between d^N and $d^{N+1}l$ configurations into account, where l describes a ligand hole on the O site. As shown in the previous chapter in Figure 4.2, there is excellent agreement between the simulated and experimental XAS and XMCD spectra for both Fe and Co.

The agreement between calculated and experimental X-ray absorption spectra is considered to be satisfactory when the simulations correctly reproduce: the number and position of the multiplet features, the relative intensity of the spectra measured at normal and grazing incidence and the XMCD intensity.

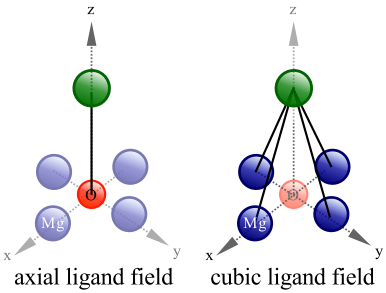

Figure 5.2: Schematic drawing of the different ligand field contributions on MgO. The oxygen atom underneath the magnetic atom causes an axial ligand field (left hand side) and the four next-nearest neighbor magnesium atoms form the cubic ligand field (right hand side).

From the simulations, we obtain the many electron wave functions and corresponding energies for the initial and final states. Only the initial state properties are relevant to determine the magnetic behavior of the system and to compare XAS and STM data. Thus in the following we will show the effects of surrounding ligands and spin-orbit coupling on the initial states of both Fe and Co on MgO. The multiplet model for the magnetic atoms on MgO includes charge transfer to the oxygen, configuration mixing with the O ligand, the axial ligand field due to the nearest neighbor O atom (see Figure 5.2, left side), as well as the cubic ligand field due to the four next-nearest neighbor Mg atoms (see Figure 5.2, right side), the spin-orbit coupling (SOC), and an externally applied magnetic field of 7 T, applied perpendicular to the surface (*47*).

5.2.1 Fe on MgO

The evolution of the energy states of Fe as a function of ligand field, SOC and magnetic field is shown in Figure 5.3 A. The left edge of the figure starts with

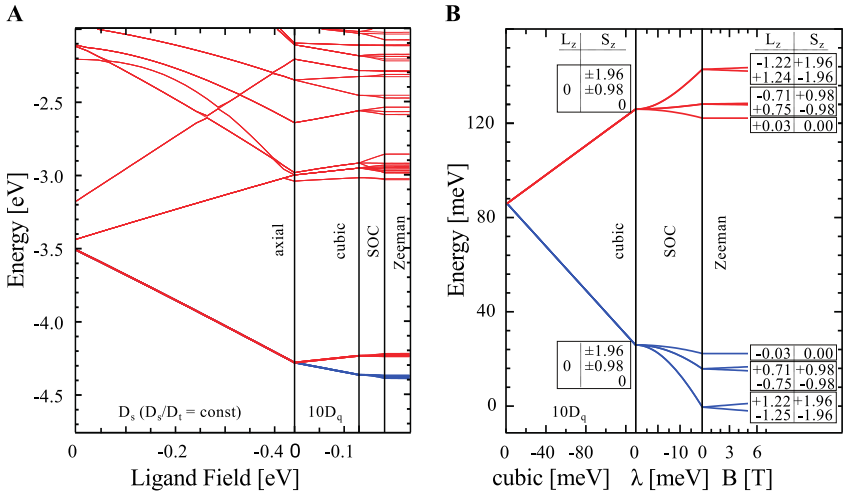

Figure 5.3: The evolution of states according to the full multiplet calculation as a fit to the XAS and XMCD data for Fe on MgO (see also Figure 4.2 A and C). (**A**) Energies of all different states as a function of axial and cubic crystal field, spin-orbit coupling and an applied external magnetic field, starting from the configuration-mixed states ($d^6 + d^7l$) at the left edge of the plot. The ligand field is separated into an axial contribution along the surface normal and a weaker cubic distortion. (**B**) shows a zoom-in on those two lowest lying spin-multiplets. L_z and S_z represent expectation values, shown here for the states after the cubic ligand field, as well as for the final states at an applied magnetic field of 7 T. The higher energy orbital singlet state (∼100 meV above ground state, red) has anti-aligned orbital and spin moments.

the mixed $d^6 + d^7l$ configuration (90% d^6, 10% d^7l) of the Fe atom, where l refers to a ligand hole in the O atom underneath the Fe. This configuration mixing causes a splitting between the $(2L + 1)(2S + 1)$ levels of the ^5D term ($L = 2$, $S = 2$) and results in a 10-fold degenerate lowest energy level, with $\langle L_z \rangle = \pm 2 \otimes \langle S_z \rangle = \pm 1.93, \pm 0.97, 0$, where the spin moment is slightly reduced compared to the free atom value due to the configuration mixing (here, $\langle L_z \rangle$ and $\langle S_z \rangle$ represent the expectation values along the surface

normal).

The axial ligand field due to the O atom underneath the Fe separates these levels further, with the degenerate in-plane orbitals $M_L = \pm 2$ (i.e. $\langle L_z \rangle = \pm 2$) lowest in energy. The cubic ligand field due to the four Mg neighbors lifts this orbital degeneracy and splits the orbital states by $\sim$100 meV into two five-fold degenerate orbital singlets (left edge of Figure 5.3 B). The lowest energy level is then a quintuplet with the orbital moment fully quenched ($\langle L_z \rangle = 0 \otimes \langle S_z \rangle = \pm 1.93, \pm 0.97, 0$). Finally, more than half of the free atom orbital moment is restored by inclusion of the spin-orbit coupling, which couples the two lowest orbital levels (blue and red) in a mostly second-order perturbation (*49*). The SOC consequently gives an energy splitting of the five spin states of the lowest-energy quintuplet. At zero magnetic field, the ground state is (to within 5 μeV) two-fold degenerate with $\langle L_z \rangle = \pm 1.25 \otimes \langle S_z \rangle = \pm 1.96$, i.e. most of the free atom spin and orbital moment is present in the magnetic ground states.

The calculated properties of the lowest spin-multiplet, as determined by the fit to the X-ray spectra (Figure 5.3) can be compared directly to the STM spectra. The zero-field splitting ($V_{02} = V_{13}$) is 13 meV, in good quantitative agreement with SES (14 meV). The effective value g^* in the SES analysis can be viewed simply as the difference in z-axis magnetic moment between the ground state 0 and state 2, which is $\Delta \langle \mu_z \rangle / \mu_B = \Delta \langle L_z \rangle + 2\Delta \langle S_z \rangle = 2.46$, which also agrees well with SES ($g^* = 2.57$). This agreement is remarkable given the markedly different energy scales of the STM and X-ray measurement techniques.

5.2.2 Co on MgO

The evolution of the calculated Co states as a function of ligand field splitting and spin-orbit interaction is shown in Figure 5.4. The lowest energy level (Fig-

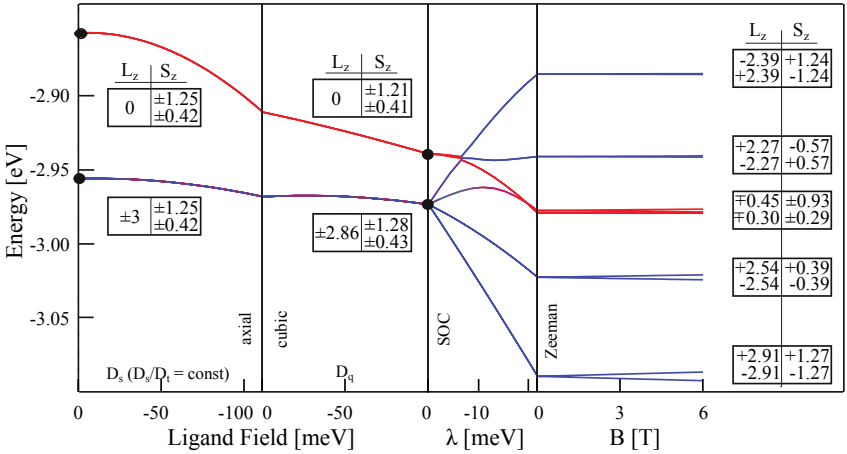

Figure 5.4: The evolution of states according to the full multiplet calculation for Co on MgO. The energies of the different states are shown as a function of axial and cubic ligand field, spin-orbit coupling and an applied external magnetic field. L_z and S_z are the expectation values, shown here for the states marked with black dots, as well as for the final states at an applied magnetic field of 7 T. [1]

ure 5.4, left edge) is an octuplet (blue) with $\langle L_z \rangle = \pm 3 \otimes \langle S_z \rangle = \pm 1.25, \pm 0.42$ ($\langle L_z \rangle$ and $\langle S_z \rangle$ are again the expectation values along the surface normal). The reduced spin moments, compared to the free atom value of $S = \frac{3}{2}$, are a result of the mixing of the spin quadruplet and triplet from the ground state's ${}^4F$ and ${}^3F$ terms of the d^7 (60%) and d^8 (40%) configuration, respectively. The orbital moment however, is not quenched and has the same magnitude as in the free atom case.

The axial ligand field has little effect on the separation between the lowest lying orbital energy levels, since it mostly resembles the configuration mixing

[1] From Rau, I. G., Baumann, S. *et al.* Reaching the magnetic anisotropy limit of a 3d metal atom. *Science* **344**, 988–992 (2014). Reprinted with permission from AAAS.

(which is also aligned along the surface normal). The cubic ligand field term does not significantly change the energy levels of the lowest energy state either, but it lifts the degeneracy between the in-plane orbitals due to a small overlap with empty Mg orbitals, which again mainly effects higher excited states. Nevertheless, the orbital moment is slightly quenched even for the ground state octuplet but it remains high ($\langle L_z \rangle$ = 2.86). Importantly, before spin-orbit coupling is introduced the orbital state is two-fold degenerate.

Finally, spin-orbit coupling leads to a rather strong splitting of the energy levels and to a crossing with the excited state quadruplet ($\langle L_z \rangle$ = 0-orbital, blue). The resulting ground state doublet is essentially made up of $\langle L_z \rangle = \pm 3$ $\otimes$ $\langle S_z \rangle = \pm\frac{3}{2}$ states. What is most unusual about the resulting spin doublet ground state is the fact that it is composed of a mixture of states dominated by $\langle L_z \rangle = \pm 3$ and thus has an orbital moment near the free atom limit. This is mainly due to the fact that a cubic ligand field is not able to lift the degeneracy between $\langle L_z \rangle = \pm 3$, which shows that Co on a four-fold substrate is the best suited $3d$ transition metal ion to obtain large orbital moments.

The multiplet energy diagram in Figure 5.4, derived from the model fit to the XAS data, provides a detailed interpretation of the SES spectra. The calculated energy separation between the ground state spin doublet (states 0 and 1) and the first excited spin doublet (states 2 and 3) at zero field is 55 meV, which closely matches the energy of the conductance step measured with the STM ($V_{02} = V_{13}$ = 57.7 mV, see Figure 3.6). Thus, the multiplet results establish that the separation of the first two spin doublets at 0 T is the zero-field splitting seen in SES spectra and explain its magnitude. A key observation of the multiplet analysis is the nearly unquenched orbital moment of the lowest energy levels, which allows the $\langle S_z \rangle = \pm\frac{3}{2}$ states to be maximally split from the $\langle S_z \rangle = \pm\frac{1}{2}$ states by the spin-orbit interaction. In this case, the zero-field splitting is equal to $\lambda L \Delta M_S$, which for Co (with $L = 3$ and $\Delta M_S = \pm 1$) gives $\lambda L \approx 60$ meV, reaching up to the full magnitude of the spin-orbit coupling energy intrinsic to a Co atom. This

value is much higher than usually observed for transition metal systems, in which $\langle L_z \rangle$ arises as a perturbative effect because of spin-orbit coupling, and the zero-field splitting has a second-order dependence on λ, as discussed in Section 5.2.1 for the Fe atom on the same binding site (*49*,*50*). The ground state found here is robust for a broad range of ligand field values and the separation of the first two spin doublets is always on the order of $\sim$60 meV.

Additionally, one can see in the Co atom that there is a close-by orbital state with $\langle L_z \rangle$ = 0, or in fact M_L = 0 (red). We will discuss this in more detail in later chapters.

5.3 Multiplet calculation based on a point charge model

For STM experiments only the ground state configuration influences the result, the calculation can thus be simplified by only considering a single configuration (e.g. only $3d^N$, no need to calculate the $2p^5 3d^{N+1}$ multiplets). In contrast to the calculations shown in the previous sections, we make a further approximation by not including configuration mixing in these simplified calculations. We start the calculation by using Slater determinants to find the fully anti-symmetrized multi-electron wave functions of each atomic multiplet term in the configuration. In our calculations we use the geometry and the partial charges provided by the DFT calculations to define the ligand field surrounding the transition metal atom under investigation. The calculations presented here do only consider the lowest energy term, such as ^5D for the Fe and ^3F for the Co, and include both the ligand field and spin-orbit coupling perturbations.

In the following we will show step-by-step how such a calculation is build up. First we introduce how to find the wave functions that are the eigenstates

of the free atom Hamiltonian (Section 5.3.1), then we will show how the DFT serves as the basis for the ligand field calculation (Section 5.3.2) and in the last step, we include spin-orbit coupling and the magnetic field (Section 5.3.3). We will summarize these calculations and compare them to the multiplet calculations that were done as a best fit to the X-ray results. Furthermore, we will introduce a way to use the point charge model with Stevens operator equivalents, which will give the possibility to do similar calculations of a whole multiplet without having to build the full free atom wave functions with Slater determinants. Finally, we will try to draw a connection between these calculations and the effective spin Hamiltonian approach used in Chapter 3.

5.3.1 Anti-symmetrized wave functions

In this section we will give a detailed example on how to obtain the free atom wave functions for each multiplet in a configuration. We start with unperturbed wave functions, so-called Slater determinants, which have the symmetry properties of the single electron wave functions. Rather than solving the free atom Hamiltonian (Equation 5.1) we use the fact that the free atom wave functions are eigenstates of the $\hat{L}^2$ and $\hat{S}^2$ operators, to find those free atom wave functions (this approach works, because H and $\hat{L}^2$, $\hat{S}^2$ commute with each other).

Obtaining free atom wave functions using projection operators

The example given here uses the d^2-configuration, with all lower shells full and follows the procedure explained in Chapter 20.3, II (*51*). We will start with a set of unperturbed wave functions and use projection operators to eliminate all terms except a desired one.

The unperturbed wave functions are labeled with their m_{l_i} and m_{s_i} quantum numbers: e.g. $(0^+, 1^-)$ represents the Slater determinant (fully anti-symmetrized wave function) with the first electron having $m_{l_1} = 0$ and $m_{s_1} = +\frac{1}{2} = +$ while the second electron has $m_{l_2} = 1$ and $m_{s_2} = -\frac{1}{2} = -$.

Both electrons are in a d-state so their m_{l_i} quantum numbers can take the values: $2, 1, ..., -2$, m_{s_i} can be $+$ or $-$. In this example the resulting total quantum numbers are $M_L = 1$ and $M_S = 0$.

When using the projection operators it is convenient to start with the states having the M_L and M_S quantum numbers equal zero, since this combination appears in every multiplet of the configuration. The possible multiplets for a d^2-configuration are: ^3F, ^3P, ^1G, ^1D and ^1S. The five possible Slater determinants, having $M_L = 0$ and $M_S = 0$, and their representation in a single electron picture are the following:

$\Psi_1 = (2^+, -2^-)$

$\Psi_2 = (2^-, -2^+)$

$\Psi_3 = (1^+, -1^-)$

$\Psi_4 = (1^-, -1^+)$

$\Psi_5 = (0^+,\ 0^-)$

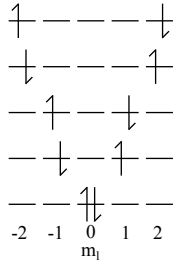

The resulting wave functions are linear combinations of these determinants and they have to be eigenfunctions of the $\hat{S}^2$ and $\hat{L}^2$ operators, because these operators both commute with the free atom Hamiltonian. Using the projection operator for the spin, one can annihilate the three spin-singlet states (^1G, ^1D and ^1S) (using Appendix 24, II (*51*)). The remaining multiplets will be spin-triplet states.

For example, we annihilate the S = 0 states, using $\hat{S}^2 = \hat{S}_+\hat{S}_- + \hat{S}_z^2 - \hat{S}_z$ (where each total spin S operator is a sum of single electron spin operators) and $\hat{S}^2\Phi(^1G) = S(S+1)\Phi(^1G) = 0\Phi(^1G)$, without including normalization factors yet:

$$
\begin{aligned}
(\hat{S}^2 - 0)\Psi_1 =& \hat{S}^2(2^+, -2^-) \\
=& \hat{S}_+\hat{S}_-(2^+, -2^-) + \hat{S}_z^2(2^+, -2^-) - \hat{S}_z(2^+, -2^-) \\
=& \hat{S}_+(2^-, -2^-) + 0 - 0 \\
=& (2^+, -2^-) + (2^-, -2^+) = \Psi_1 + \Psi_2
\end{aligned} \tag{5.2}
$$

This leaves $(\Psi_1 + \Psi_2)$ as part of the wave functions having non-zero spin. The only two multiplets with a non-zero spin state are the ^3F and ^3P terms. Using the projection operator on the orbital part one can then annihilate the ^3P state which results in the wave functions of the ^3F state. With $\hat{L}^2\,\Phi(^3P)$ $= L(L+1)\,\Phi(^3P) = 1 \cdot 2\,\Phi(^3P)$:

$$
\begin{aligned}
(\hat{L}^2 - 1 \cdot 2)(\Psi_1 + \Psi_2) =& (\hat{L}^2\Psi_1 + \hat{L^2}\Psi_2) - 2(\Psi_1 + \Psi_2) \\
=& 2\Psi_1 + 2\Psi_2 + 4\Psi_3 + 4\Psi_4
\end{aligned} \tag{5.3}
$$

Thus, the free atom wave function of the M_L = 0, M_S = 0 state in the ^3F multiplet is (when normalized):

$$
\Phi(^3F, M_L = 0, M_S = 0) = \frac{1}{\sqrt{10}}(\Psi_1 + \Psi_2 + 2\Psi_3 + 2\Psi_4) \tag{5.4}
$$

There are several checks to prove that this is indeed a wave function with $L = 3$ and $S = 1$ as expected for the ^3F multiplet:

$$
\begin{aligned}
\hat{L^2}\Phi =& \frac{1}{\sqrt{10}}((4\Psi_1 + 4\Psi_3) + (4\Psi_2 + 4\Psi_4) + 2(4\Psi_1 + 10\Psi_3 + 6\Psi_5) \\
& + 2(4\Psi_2 + 10\Psi_4 - 6\Psi_5)) \\
=& \frac{1}{\sqrt{10}}(12\Psi_1 + 12\Psi_2 + 24\Psi_3 + 24\Psi_4) \\
=& 12\Phi = 3 \cdot 4\Phi = L(L+1)\Phi
\end{aligned} \tag{5.5}
$$

Therefore $L = 3$, which confirms the assigned F term.

$$\begin{aligned}\hat{S}^2\Phi =& \frac{1}{\sqrt{10}}((\Psi_1 + \Psi_2) + (\Psi_1 + \Psi_2) + 2(\Psi_3 + \Psi_4) + 2(\Psi_3 + \Psi_4)) \\ =& \frac{1}{\sqrt{10}}(2\Psi_1 + 2\Psi_2 + 4\Psi_3 + 4\Psi_4) = 2\Phi = 1 \cdot 2\Phi = S(S+1)\Phi \quad (5.6)\end{aligned}$$

Therefore $S = 1$, confirming that this is a indeed spin-triplet state and therefore a member of the ${}^3F$ multiplet. Similarly to the procedure just demonstrated, the wave functions of all other multiplets can be determined in a straightforward way.

Using step-up and step-down operators to obtain the remaining wave functions of each term

Step-up and step-down (ladder) operators are operators such as $\hat{L}_+$ or $\hat{S}_-$ which change the M quantum number by $\pm$ 1. As an example we apply the step-up orbital operator on the same ${}^3F$ state, with $M_L = 0$ and $M_S = 0$ (Equation 5.4), of the d^2-configuration. For simplicity, we neglect all normalization factors and normalize the wave function later.

$$\begin{aligned}\Phi({}^3F, M_L = 1, M_S = 0) = \hat{L}_+ \ \Phi({}^3F, M_L = 0, M_S = 0) \\ =& (2^+, -1^-) + (2^-, -1^+) + 2(1^+, 0^-) + 2(2^+, -1^-) \\ &+ 2(1^-, 0^+) + 2(2^-, -1^+) \\ =& 3(2^+, -1^-) + 3(2^-, -1^+) + 2(1^+, 0^-) + 2(1^-, 0^+) \quad (5.7)\end{aligned}$$

Thus, the free atom wave function of the M_L = 1, M_S = 0 state in the ${}^3F$ multiplet is (when normalized):

$$\begin{aligned}&\Phi({}^3F, M_L = 1, M_S = 0) \\ &= \frac{1}{\sqrt{10}}(\sqrt{3}(2^+, -1^-) + \sqrt{3}(2^-, -1^+) + \sqrt{2}(1^+, 0^-) + \sqrt{2}(1^-, 0^+))\end{aligned}$$

(5.8)

Similarly, all other free atom wave functions can be obtained. For example, the M_L = 3, M_S = 1 wave function of the ^3F multiplet can be found by applying $\hat{L}_+^2$ and $\hat{S}_+$ to the $M_L = 1$, $M_S = 0$ wave function in Equation 5.8:

$$\begin{aligned}\Phi(^3F, M_L = 3, M_S = 1) = \hat{S}_+\hat{L}_+^2\ \Phi(^3F, M_L = 1, M_S = 0)\\ =(2^+, 1^+)\end{aligned} \tag{5.9}$$

With this set of tools one can therefore determine all wave functions of the different multiplets. When calculating the wave functions with more than two electrons one can use a further tool called *fractional parentage* for their determination (*51*). All wave functions as shown here are already anti-symmetrized (they are determinants). See the Appendix C for tables with all wave functions of the lowest-lying multiplets for each d^N-configuration.

In our point charge model calculations we add the ligand field and the spin-orbit coupling as perturbations on these free atom wave functions. In the following, we will only consider the lowest-lying multiplet of each configuration, as it can be seen in the full multiplet model that the next higher multiplets for both Fe and Co on MgO are sufficiently separated in energy from the lowest energy states (see Figures 5.3 and 5.4), and thus their influence on these states can be neglected. We therefore do not need to calculate the energy differences between the different multiplets (*51*). Thus, in the next step of the calculation we can already consider the effect of the surrounding ligands on the $(2L + 1)(2S + 1)$-fold degenerate level of the lowest energy multiplet.

5.3.2 Surrounding ligands described as point charges

In this section we will explain how to calculated the ligand field Hamiltonian (as a perturbation on the free atom wave functions) due to point charges

surrounding the magnetic atom. We base the point charge calculation on the results obtained by DFT calculations, because DFT is a technique that is able to accurately calculate the ligand positions as well as the charges associated with the ligands.

Starting point: DFT calculation

In order to calculate the effects of surrounding ligands on a single magnetic atom we used the optimized geometry obtained from density functional theory calculations (DFT). These calculations were performed by Dr. Shruba Gangopadhyay and Oliver R. Albertini, in the team of Dr. Barbara A. Jones, at the IBM Almaden Research Center.

To model the periodic 2D slab geometry, we used spin-polarized DFT with a plane wave basis set, as implemented in Quantum ESPRESSO (*52*) and WIEN2k (*53*). We used the generalized gradient approximation (GGA) for the exchange correlation interaction. In Quantum ESPRESSO, we optimized the geometry of a slab of six atomic layers of Ag, in which the lower three are kept fixed at bulk Ag values. On top of the Ag layers we added a layer of MgO where the O atoms are on top of the Ag atoms as found by previous DFT calculations (*26*,*54*). We added the magnetic atoms on three possible adatom sites on the MgO surface (on top of O, on top of Mg and on a bridge site between two O and two Mg atoms) and optimized the whole Fe/MgO/Ag or Co/MgO/Ag system. Our calculations suggest that Fe and Co prefer to bind to the O top site over other adatom position. For the calculation we implemented eight effective atomic (Ag) layers of vacuum above the slab. This structure is repeated periodically in all three spatial direction. The WIEN2k calculations were carried out with an inversion symmetric seven layer structure, which includes five layers of Ag, and a top and bottom layer of MgO. The slab was set up with eight layers of vacuum between the top and bottom adatoms.

Because a naïve application of DFT on d-electron materials generally does

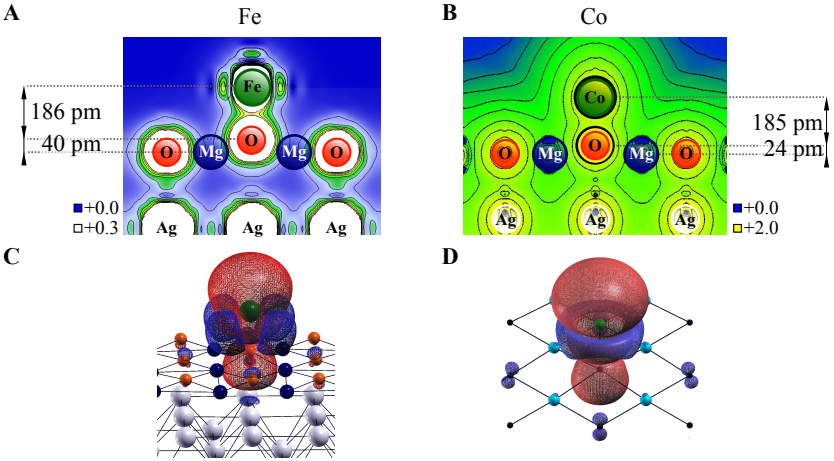

Figure 5.5: Charge- and spin-density plot as calculated in DFT+U for both Fe (**A**, **C**) and Co (**B**, **D**)[1]. (**A**, **B**) The color bar is in atomic units (e/a_0^3, where e is the elementary charge and a_0 is the Bohr radius). The distances in z-direction are indicated in the structure of the single magnetic atom on top of its preferred oxygen binding site of a single MgO layer on a silver substrate. (**C**, **D**) The spin-density of Fe clearly reflects the four-fold symmetry of the substrate, while for Co the spin-density is almost fully cylindrical, which is in great agreement with the results from the multiplet calculation.

not get either the d-electron energy or many aspects of the magnetization correct, we used an on-site Coulomb interaction (U = 3.2 eV for Fe and U = 6.9 eV for Co) for the d-states of the magnetic atoms. U is obtained using a linear response approach implemented in Quantum ESPRESSO for both Fe and Co (*55*). With this approach we find for Fe a spin of S = 1.85 μ_B and for Co S = 1.51 μ_B.

Figure 5.5 A and B show the charge-density calculation as well as the geometry of the two transition metal atoms Fe and Co on MgO. The charge density

[1] From Rau, I. G., Baumann, S. *et al.* Reaching the magnetic anisotropy limit of a 3d metal atom. *Science* **344**, 988–992 (2014). Reprinted with permission from AAAS.

	distance ion to O $d_{\text{M-O}}$	distance ion to Mg $d_{\text{M-Mg}}$	charge ion q_{M}	charge O q_{O}	charge Mg q_{Mg}	angle to $z-$axis θ_{Mg}
Fe	186 pm	3.11 pm	$+6.44\,e$	$-1.50\,e$	$+1.72\,e$	$136.66°$
Co	185 pm	3.00 pm	$+7.09\,e$	$-1.59\,e$	$+1.70\,e$	$134.10°$

Table 5.1: Geometry and total charges as determined from DFT+U calculations on Fe and Co on top of MgO/Ag(001). e is the elementary charge.

plots for both atoms reveal a strong interaction between the magnetic atom and the O underneath it. To a lesser degree, there is some interaction between the magnetic atom and the four Mg atoms. This also shows up in the spin-density, as shown in Figure 5.5 C and D. The analysis shows an overall additional positive charge of ($+0.44\ e$) on Fe and of ($+0.09\ e$) for Co. The charges on the surrounding O and Mg atoms are shown in Table 5.1.

The obtained optimized geometry shows that the Fe atom stays 186 pm above the O atom while the oxygen atom gets slightly pulled up from the MgO plane by 40 pm (see Figure 5.5 A). Similarly, the Co atom is 185 pm above the O atom, which itself is pulled up from the MgO plane by 24 pm (B). All the resulting structure and the charges are listed in Table 5.1. The magnetic atom (Fe or Co) is referred to as ion, or M. The parameters that are needed later are: $d_{\text{M-Mg}}$, $d_{\text{M-O}}$, q_{M}, q_{Mg}, q_{O} as well as θ_{Mg} (see schematics in Figure 5.6).

Ligand field potential

When using point charges to calculate the ligand field it is easiest to express the potential in spherical harmonics (*56*). We show this procedure here for a single atom on MgO, where the point charges in the x- and y-direction are identical with two Mg atoms in each direction while the z-direction has only one charge,

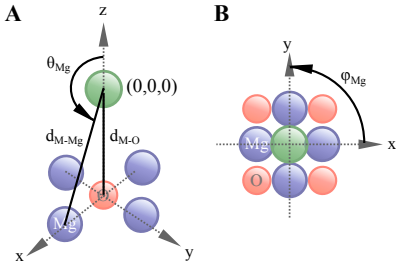

Figure 5.6: 3-dimensional (**A**) and top view (**B**) of the atom arrangement for a single magnetic atom on a four-fold surface, such as MgO. Indicated are those parameters that are needed for the point charge model calculation.

the O atom underneath the magnetic atom. As introduced in the last paragraph we determine the positions of these point charges and their actual charge by DFT calculations (see Figure 5.5 and Table 5.1).

The potential at a an arbitrary point (r, θ, ϕ), when expressed in polar coordinates about the magnetic atom and summed over all J neighboring ions, is:

$$V(r,\theta,\phi) = -\frac{1}{4\pi\epsilon_0}\sum_{j=1}^{J}\frac{q_j}{\left|\vec{R}_j - \vec{r}\right|} \tag{5.10}$$

where ϵ_0 is the electric constant. The sum is over all J ligands, where q_j is the charge on the ligand (in units of electric charge) and $|\vec{R}_j - \vec{r}|$ is the distance between point $\vec{r}$ and the ligand at position $\vec{R}_j$ from the origin (from the magnetic atom). The ligand field Hamiltonian is then written as the potential acting on all N electrons of the magnetic atom. The electrons of the magnetic atom are at positions (r_i, θ_i, ϕ_i) and each carry a fraction of the total charge calculated by DFT: q_{M}/N. Thus the ligand field Hamiltonian, for an atom

with N electrons and J neighboring ions, is:

$$H_{\mathrm{LF}} = \sum_{i=1}^{N} q_i V(r_i, \theta_i, \phi_i) = -\frac{1}{4\pi\epsilon_0} \sum_{i=1}^{N} \sum_{j=1}^{J} \frac{q_j}{\left|\vec{R}_j - \vec{r_i}\right|} \cdot \frac{q_M}{N} \tag{5.11}$$

The distance between the individual electrons at the magnetic atom and the surrounding ligands, $|\vec{R}_j - \vec{r_i}|$ can be expressed in terms of spherical harmonics (Y_l^m) by using the associated Legendre functions (P_n^0). If we define ω as the angle between the two vectors $\vec{r_i}$ and $\vec{R}_j$, then:

$$\frac{1}{\left|\vec{R}_j - \vec{r_i}\right|} = \sum_{n=0}^{\infty} \frac{r_i^n}{R_j^{(n+1)}} P_n^0(cos(\omega)), \tag{5.12}$$

if $\vec{R}_j > \vec{r_i}$ (which is always true here, because $\vec{r_i}$ describes the electrons of the magnetic atom, while $\vec{R}_j$ describes the ligands surrounding the atom). By expressing the angle ω in terms of the polar angles of the electrons (θ_i, ϕ_i) and the ligands (θ_j, ϕ_j), we can write the Legendre function in terms of spherical harmonics:

$$P_n^0(cos(\omega)) = \frac{4\pi}{(2n+1)} \sum_{m=-n}^{n} (-1)^m Y_n^{-m}(\theta_j, \phi_j) Y_n^m(\theta_i, \phi_i) \tag{5.13}$$

The ligand field potential $V(r_i, \theta_i, \phi_i)$ for each electron of the magnetic atom can therefore be expressed as:

$$\begin{aligned} V(r_i, \theta_i, \phi_i) &= -\frac{1}{4\pi\epsilon_0} \sum_{j=1}^{J} \frac{q_j}{\left|\vec{R}_j - \vec{r_i}\right|} \\ &= -\frac{1}{4\pi\epsilon_0} \sum_{j=1}^{J} q_j \sum_{n=0}^{\infty} \frac{r_i^n}{R_j^{(n+1)}} \frac{4\pi}{(2n+1)} \sum_{m=-n}^{n} (-1)^m Y_n^{-m}(\theta_j, \phi_j) Y_n^m(\theta_i, \phi_i) \\ &= -\frac{1}{4\pi\epsilon_0} \sum_{n=0}^{\infty} \sum_{m=-n}^{n} r_i^n \gamma_{nm} Y_n^m(\theta_i, \phi_i) \end{aligned}$$

(5.14)

where

$$\gamma_{nm} = \sum_{j=1}^{J} \frac{4\pi}{(2n+1)} \frac{q_j}{R_j^{(n+1)}} (-1)^m Y_n^{-m}(\theta_j, \phi_j) \tag{5.15}$$

As shown before the relevant point charges for an atom on MgO are at the following positions with respect to the magnetic atom at $(0,0,0)$ (in polar coordinates) (see schematics in Figure 5.6): O: $(d_{\text{M-O}}, \pi, 0)$, Mg: $(d_{\text{M-Mg}}, \theta_{\text{Mg}}, 0)$, $(d_{\text{M-Mg}}, \theta_{\text{Mg}}, \pi/2)$, $(d_{\text{M-Mg}}, \theta_{\text{Mg}}, \pi)$ and $(d_{\text{M-Mg}}, \theta_{\text{Mg}}, 3\pi/2)$. This results in a potential for each electron of the following form (only showing the non-zero terms, all other terms vanish in the Hamiltonian):

$$\begin{aligned} V(r_i, \theta_i, \phi_i) &= -\frac{1}{4\pi\epsilon_0}(\gamma_{00} Y_0^0(\theta_i, \phi_i) + r_i^2 \gamma_{20} Y_2^0(\theta_i, \phi_i) + r_i^4 \gamma_{40} Y_4^0(\theta_i, \phi_i) \\ &\qquad + r_i^4 \gamma_{44}(Y_4^4(\theta_i, \phi_i) + Y_4^{-4}(\theta_i, \phi_i))) \\ &= -\frac{1}{4\pi\epsilon_0}(V_0^0(\vec{r}_i) + V_2^0(\vec{r}_i) + V_4^0(\vec{r}_i) + V_4^4(\vec{r}_i)) \end{aligned} \tag{5.16}$$

This potential can be separated into its different symmetry contributions. For example, the $V_4^4(\vec{r}_i)$ part of the potential is caused by the four Mg neighbors (see next paragraph). The different contributions are explicitly:

$$\begin{aligned} V_0^0(\vec{r}_i) &= \gamma_{00} \frac{1}{2} \sqrt{\frac{1}{\pi}} \\ V_2^0(\vec{r}_i) &= r_i^2 \gamma_{20} \frac{1}{4} \sqrt{\frac{5}{\pi}} (3cos^2(\theta_i) - 1) \\ V_4^0(\vec{r}_i) &= r_i^4 \gamma_{40} \frac{3}{16} \sqrt{\frac{1}{\pi}} (35cos^4(\theta_i) - 30cos^2(\theta_i) + 3) \\ V_4^4(\vec{r}_i) &= r_i^4 \gamma_{44} \frac{3}{16} \sqrt{\frac{35}{2\pi}} sin^4(\theta_i) 2cos(4\phi_i) \end{aligned} \tag{5.17}$$

with a list of the γ_{nm} prefactors, here specifically for a magnetic atom on the four-fold oxygen binding site of the MgO surface:

$$\begin{aligned}
\gamma_{00} &= \sum_j \frac{4\pi}{1}\frac{q_j}{R_j}Y_0^0(\theta_j,\phi_j) = 2\sqrt{\pi}\left(\frac{4q_{\text{Mg}}}{d_{\text{M-Mg}}} + \frac{q_{\text{O}}}{d_{\text{M-O}}}\right) \\
\gamma_{20} &= \sum_j \frac{4\pi}{5}\frac{q_j}{R_j^3}Y_2^0(\theta_j,\phi_j) = 4\sqrt{\frac{\pi}{5}}\left(\frac{(3cos^2(\theta_{\text{Mg}})-1)q_{\text{Mg}}}{d_{\text{M-Mg}}^3} - \frac{q_{\text{O}}}{d_{\text{M-O}}^3}\right) \\
\gamma_{40} &= \sum_j \frac{4\pi}{9}\frac{q_j}{R_j^5}Y_4^0(\theta_j,\phi_j) \\
&= \frac{\sqrt{\pi}}{12}\left(\frac{q_{\text{Mg}}}{d_{\text{M-Mg}}^5}(35cos^4(\theta_{\text{Mg}}) - 30cos^2(\theta_{\text{Mg}}) + 3) + \frac{8q_{\text{O}}}{d_{\text{M-O}}^5}\right) \\
\gamma_{44} &= \sum_j \frac{4\pi}{9}\frac{q_j}{R_j^5}Y_4^{-4}(\theta_j,\phi_j) = \frac{q_{\text{Mg}}}{12}\sqrt{\frac{35\pi}{2}}\frac{4sin^4(\theta_{\text{Mg}})}{d_{\text{M-Mg}}^5}
\end{aligned} \tag{5.18}$$

Each magnetic atom on MgO has a slightly different geometry, e.g. different distance from the oxygen atom ($d_{\text{M-O}}$). These differences are reflected in the different γ_{nm} prefactors of the potential. However, for all $3d$ transition metal atoms on MgO the same four potential terms (V_0^0, V_2^0, V_4^0 and V_4^4) will affect the energy eigenstates.

The ligand field Hamiltonian for an atom on an oxygen binding site of the MgO surface can thus be written as:

$$H_{\text{LF}} = \sum_{i=1}^{N} q_i V(\vec{r}_i) = -\frac{q_M}{4\pi\epsilon_0}\sum_{i=1}^{N}\left((V_0^0(\vec{r}_i) + V_2^0(\vec{r}_i) + V_4^0(\vec{r}_i) + V_4^4(\vec{r}_i)\right) \tag{5.19}$$

which includes the explicit single electron potentials (Equation 5.17) with the specific γ_{nm} prefactors for the MgO surface (Equation 5.18). In the following we will neglect the V_0^0 potential as it changes all energy levels equally and thus has no effect on the resulting energy differences.

From single electron to multi-electron potential

In the last paragraphs we introduced the ligand field Hamiltonian as a sum of single electron potentials. The H_{LF} Hamiltonian depends on the position of each electron in space, thus direct integration over the spatial extend of each electron's wave function is necessary. In this paragraph, we will show how to determine the energy eigenstates of the ligand field Hamiltonian by direct integration over each electron's wave functions. First, we will show how to determine all single electron matrix elements. Second, we will show that when summing over the single electron matrix elements, we can determine all multi-electron matrix elements in a straightforward way.

The energy eigenstates for a single electron (or single electron matrix elements) of a certain ligand field potential $V_n^m(\vec{r}_i)$ can be determined by direct integration over the individual wave functions. For the integral, both the single electron wave functions and the ligand field potential are represented as products with spherical harmonics (see above). The energy eigenstates E_i of a single $3d$ electron are equivalent to the eigenstates of a d^1-configuration with the wave functions $\Psi_i(\vec{r}_i) = R_{n_i}(r_i)Y_{l_i}^{m_{l_i}}(\theta_i, \phi_i)$. (Note that n_i, l_i and m_{l_i} are the quantum numbers of the electron, while n, m represent the symmetry of the system.) For a single symmetry term, the energy eigenstates are:

$$
\begin{aligned}
E_i(n,m) &= -\frac{1}{4\pi\epsilon_0}\ \langle\Psi_i|q_i V_n^m(\vec{r}_i)|\Psi_i\rangle \\
&= -\frac{q_i}{4\pi\epsilon_0}\int_0^{2\pi}\int_0^{\pi}\int_0^{\infty} \Psi_i^*(\vec{r}_i)\, r_i^n \gamma_{nm} Y_n^m(\theta_i,\phi_i)\, \Psi_i(\vec{r}_i)\ r_i^2 sin(\theta_i)\ dr_i\, d\theta_i\, d\phi_i
\end{aligned}
$$

l_i, m_{l_i}	2,−2	2,−1	2, 0	2, 1	2, 2
2,−2	$\frac{-1}{7}\sqrt{\frac{5}{\pi}}$				
2,−1		$\frac{1}{14}\sqrt{\frac{5}{\pi}}$			
2, 0			$\frac{1}{7}\sqrt{\frac{5}{\pi}}$		
2, 1				$\frac{1}{14}\sqrt{\frac{5}{\pi}}$	
2, 2					$\frac{-1}{7}\sqrt{\frac{5}{\pi}}$

Table 5.2: Table shows the single electron matrix elements for a $3d$ electron (l = 2) in the V_2^0 potential ($\int_0^{2\pi}\int_0^{\pi} Y_{l_i}^{m_{l_i}*}\, Y_2^0\, Y_{l_i}^{m_{l_i}}\, sin(\theta_i)\, d\theta_i\, d\phi_i$). In order to obtain the actual energy eigenstates these values have to be multiplied by $-\frac{q_M}{4\pi\epsilon_0} \cdot \langle r^n \rangle\, \gamma_{nm}$, where γ_{nm} can be calculated as shown in the previous section and $\langle r^n \rangle$ is tabulated in Appendix D, Table D.1.

(5.20)

The radial and the angular parts of this integral can be separated. The radial part is often not accurately known and it is thus used as an element-specific parameter $\langle r^n \rangle = \int_0^{\infty} R_{n_i}(r_i)^2 r_i^n r_i^2 dr_i$. This parameter is given in several tables, e.g. by Abragam and Bleaney (*31*) (see Table D.1 in the Appendix D). The separation of the radial part leaves the integration over the spherical harmonics when determining the matrix elements of a single electron wave function.

In our case we only consider the valence electrons of $3d$-elements, then l_i = 2 and $-2 \leq m_{l_i} \leq 2$ in $Y_{l_i}^{m_{l_i}}$. In Table 5.2 the resulting matrix elements for the single electron wave function in the V_2^0 potential are shown. The elements in the table only represent the angular integral, all prefactors, such as $-\frac{q_M}{4\pi\epsilon_0}$, $\langle r^n \rangle$ and γ_{nm}, are omitted.

All additional single electron matrix elements for $3d$-electrons in a four-fold

potential are tabulated in Appendix D. We will now use these single electron matrix elements to determine the energy eigenstates of multi-electron wave functions, for example for atoms in a d^2-configuration in a four-fold symmetric ligand field.

We have shown earlier that the ligand field Hamiltonian is a sum of single electron Hamiltonians (see Equation 5.19). For example for a d^2-configuration $H_{\mathrm{LF}} = q_1 V(\vec{r}_1) + q_2 V(\vec{r}_2)$, there are no terms involving both $\vec{r}_1$ and $\vec{r}_2$. In addition, the multi-electron wave functions can be written as Slater determinants (as linear combinations of products of single electron wave functions): thus $\Phi = \frac{1}{\sqrt{2}}(\Psi_a(\vec{r}_1)\Psi_b(\vec{r}_2) - \Psi_a(\vec{r}_2)\Psi_b(\vec{r}_1))$, or as linear combinations of such Slater determinants (see Section 5.3.1). The multi-electron matrix elements can then be determined as sums of single electron matrix elements:

$$\begin{aligned}
&\langle\Phi|H_{\mathrm{LF}}|\Phi\rangle = \langle\Phi|(q_1 V(\vec{r_1}) + q_2 V(\vec{r_2}))|\Phi\rangle \\
&= \langle\Phi|q_1 V(\vec{r_1})|\Phi\rangle + \langle\Phi|q_2 V(\vec{r_2})|\Phi\rangle
\end{aligned} \tag{5.21}$$

As an explicit example we derive the matrix elements for one of the wave functions of the ${}^3F$ multiplet in the d^2-configuration (as determined earlier, see Equation 5.9).

$$\begin{aligned}
&\left\langle\Phi({}^3F, M_L = 3, M_S = 1)\,|\,(q_1 V(\vec{r}_1) + q_2 V(\vec{r}_2))\,|\,\Phi\right\rangle \\
&= \left\langle(2^+, 1^+)|\,(q_1 V(\vec{r}_1) + q_2 V(\vec{r}_2))\,|(2^+, 1^+)\right\rangle \\
&= \frac{1}{\sqrt{2}}(\langle\Psi_{2^+}(\vec{r_1})\Psi_{1^+}(\vec{r_2})|(q_1 V(\vec{r}_1) + q_2 V(\vec{r}_2))|\Psi_{2^+}(\vec{r_1})\Psi_{1^+}(\vec{r_2})\rangle \\
&\quad - \langle\Psi_{2^+}(\vec{r}_1)\Psi_{1^+}(\vec{r}_2)\,|(q_1 V(\vec{r}_1) + q_2 V(\vec{r}_2))|\,\Psi_{2^+}(\vec{r}_2)\Psi_{1^+}(\vec{r}_1)\rangle \\
&\quad - \langle\Psi_{2^+}(\vec{r}_2)\Psi_{1^+}(\vec{r}_1)\,|(q_1 V(\vec{r}_1) + q_2 V(\vec{r}_2))|\,\Psi_{2^+}(\vec{r}_1)\Psi_{1^+}(\vec{r}_2)\rangle \\
&\quad + \langle\Psi_{2^+}(\vec{r}_2)\Psi_{1^+}(\vec{r}_1)\,|(q_1 V(\vec{r}_1) + q_2 V(\vec{r}_2))|\,\Psi_{2^+}(\vec{r}_2)\Psi_{1^+}(\vec{r}_1)\rangle)
\end{aligned} \tag{5.22}$$

In this example only the first and last term are non-zero and since

$q_1 = q_2 = q_M/2$, we can write the resulting matrix element as:

$$\begin{aligned}\left\langle \Phi(^3F, M_L = 3, M_S = 1) \right| \left(q_1 V(\vec{r}_1) + q_2 V(\vec{r}_2) \right) \left| \Phi \right\rangle \\ = \; q_M \; \left(\left\langle \Psi_{2^+} \right| V(\vec{r}_i) \left| \Psi_{2^+} \right\rangle + \left\langle \Psi_{1^+} \right| V(\vec{r}_i) \left| \Psi_{1^+} \right\rangle \right)\end{aligned} \tag{5.23}$$

Using Table 5.2 and Equation 5.20 we can therefore find the energy eigenstate of the multi-electron wave function with M_L = 3 and M_S = 1 (^3F term of the d^2-configuration) in a V_2^0 ligand field potential:

$$\begin{aligned}E(^3F, M_L = 3, M_S = 1) &= -\frac{q_M}{4\pi\epsilon_0} \left\langle r^2 \right\rangle \gamma_{20} \left(-\frac{1}{7}\sqrt{\frac{5}{\pi}} + \frac{1}{14}\sqrt{\frac{5}{\pi}} \right) \\ &= -\frac{q_M}{4\pi\epsilon_0} \left\langle r^2 \right\rangle \gamma_{20} \left(-\frac{1}{14}\sqrt{\frac{5}{\pi}} \right)\end{aligned} \tag{5.24}$$

Thus the matrix element for this wave function of the d^2-configuration is $-\frac{1}{14}\sqrt{\frac{5}{\pi}}$. The matrix elements for all multi-electron wave functions are tabulated in Appendix D. We will in the following simplify the discussion by limiting the prefactor to $\langle r^n \rangle \gamma_{nm}$, where it is implied that $-\frac{q_M}{4\pi\epsilon_0}$ is included in the prefactor.

Note that the energy eigenstates in any ligand field only depend on the orbital quantum number.

Using the matrix elements and $\langle r^n \rangle$ as tabulated in Appendix D, and the γ_{nm} prefactors as calculated from the formulas in the previous section, we can calculate the evolution of states due to the surrounding ligands for both Fe and Co on the MgO surface (Figure 5.7). As seen before, Co has a doubly degenerate lowest-lying state with $\langle L_z \rangle = \pm 3$, meaning that the Co's orbital moment remains free-atom-like after consideration of the ligand field. On the

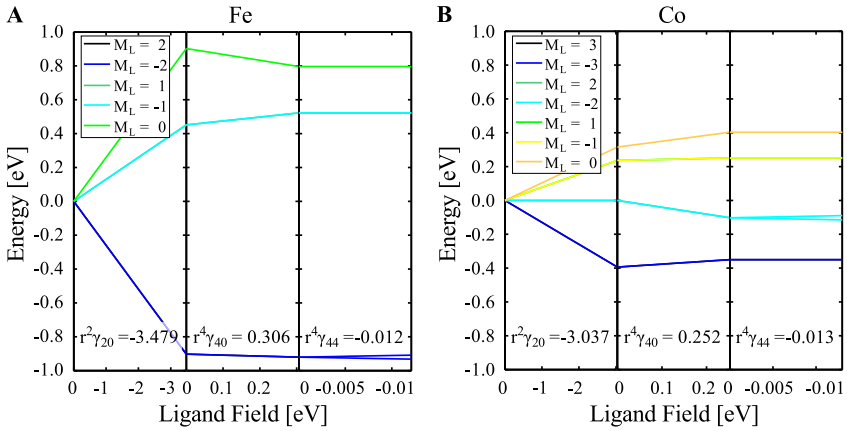

Figure 5.7: Ligand field calculated with the point charge model for Fe (**A**) and Co (**B**) on the four-fold MgO surface. Shown is the evolution of states for the different terms in the ligand field potential. The prefactors shown include the radial matrix element $\langle r^n \rangle$ (tabulated in Appendix D, for simplicity we only write r^n in this figure), as well as γ_{nm} (including $-\frac{q_M}{4\pi\epsilon_0}$), as calculated in Section 5.3.

other hand, Fe has a fully quenched orbital moment with the lowest-lying state being a singlet with $\langle L_z \rangle = 0$ (in fact a mixture of $M_L = \pm 2$) (right hand side of the corresponding plots) (for a zoom-in on the V_4^4 potential see Figure 5.9).

5.3.3 The full point charge model

In the previous section we have calculated the change in energy levels due to the ligand field contribution. In this section, we will now include all remaining contributions to the total Hamiltonian, i.e. the spin-orbit coupling and an external magnetic field.

In the case of $3d$-transition metal atoms on MgO the spin-orbit coupling in-

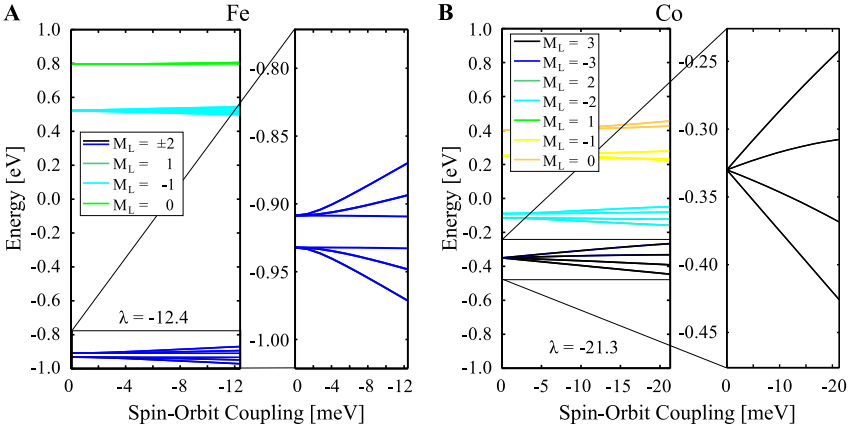

Figure 5.8: Spin-orbit coupling calculated with the point charge model for Fe (**A**) and Co (**B**). The left side of both plots shows the evolution of all states as a function of increasing coupling starting from the last points of the ligand field calculation, see Figure 5.7. The right hand side shows a zoom-in on the lowest two spin-multiplets.

duces smaller energy changes than the ligand field, thus considering spin-orbit coupling after the ligand field contribution is appropriate. Spin-orbit coupling aligns the spin along the orbital moment and is thus part of the origin of the magnetism of a single atom. The spin-orbit coupling Hamiltonian is:

$$\begin{aligned} H_{\mathrm{SOC}} &= \lambda \vec{L} \cdot \vec{S} = \lambda(\hat{L}_x \hat{S}_x + \hat{L}_y \hat{S}_y + \hat{L}_z \hat{S}_z) \\ &= \lambda(\frac{1}{2}(\hat{L}_+ \hat{S}_- + \hat{L}_- \hat{S}_+) + \hat{L}_z \hat{S}_z) \end{aligned} \tag{5.25}$$

λ is the spin-orbit coupling constant, which is -12.4 meV for Fe and -21.3 meV for Co (*31*). We can calculate the eigenenergy and the eigenstates

of the spin-orbit coupling Hamiltonian as follows:

$$\begin{aligned} E_{\text{SOC}}|\Phi\rangle &= H_{\text{SOC}}|\Phi\rangle \\ &= \lambda \left(\frac{1}{2}(\hat{L}_+\hat{S}_- + \hat{L}_-\hat{S}_+) + \hat{L}_z\hat{S}_z\right)|\Phi\rangle \end{aligned} \tag{5.26}$$

As an example, we again use the wave function of the ^3F multiplet in the d^2-configuration with M_L = 3 and M_S = 1 (as determined earlier, see Equation 5.9). Under the influence of the ligand field Hamiltonian the eigenenergy of this wave function changed, but it remained an eigenstate of the Hamiltonian (no mixing to other states occurred). Using e.g. $\hat{S}_z|+\rangle = M_S|+\rangle = \frac{1}{2}|+\rangle$ and $\hat{L}_\pm|M_L\rangle = \sqrt{(L(L+1) - M_L(M_L \pm 1)}|M_{L\pm1}\rangle$ we can determine the change in eigenenergy and the eigenstate of this wave function due H_{SOC}:

$$\begin{aligned} E\ &\left|\Phi(^3F, M_L = 3, M_S = 1)\right\rangle = H_{\text{SOC}}\ \left|\Phi(^3F, M_L = 3, M_S = 1)\right\rangle \\ =&\lambda \left(\frac{1}{2}(\hat{L}_+\hat{S}_- + \hat{L}_-\hat{S}_+) + \hat{L}_z\hat{S}_z\right)\ \left|(2^+, 1^+)\right\rangle \\ =&\lambda \left(\frac{1}{2}\left(\hat{L}_+\sqrt{2}\left(\left|(2^-, 1^+)\right\rangle + \left|(2^+, 1^-)\right\rangle\right) + 0\right) + \hat{L}_z \cdot 1\ \left|(2^+, 1^+)\right\rangle\right) \\ =&\lambda \left(0 + 3 \cdot 1\ \left|(2^+, 1^+)\right\rangle\right) \\ =&3\,\lambda\ \left|(2^+, 1^+)\right\rangle \end{aligned} \tag{5.27}$$

The resulting eigenenergy is therefore $3\,\lambda$ and the eigenstate remains unchanged. Thus this eigenstate retains its free atom wave function under the influence of the ligand field and spin-orbit coupling.

The evolution of states for Fe and Co under the influence of spin-orbit coupling, starting from the states after inclusion of the ligand field potential are reported in Figure 5.8. The results show the same qualitative behavior as seen in the more extended model introduced previously (Figures 5.3 and 5.4). The

Fe has a more quadratic dependence on the spin-orbit coupling constant λ, while Co has a linear dependence. The difference between the quadratic versus linear dependence can be seen in terms of perturbation theory: Fe has a non-degenerate level, so second order perturbation theory dominates, while for Co, with the degenerate level as a starting point, the first order perturbation term is non-zero (note though that we did not use perturbation theory to find the eigenenergies and eigenstates of the Hamiltonian).

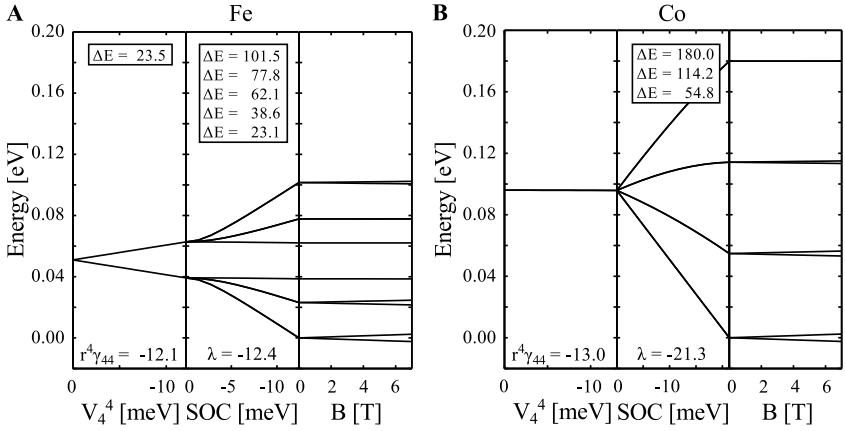

Figure 5.9: The point charge model for Fe (**A**) and Co (**B**), beginning at the V_4^4-ligand field potential. The left side of both plots shows the evolution of two lowest-lying orbital states as a function the ligand field, spin-orbit coupling (middle plot) and external applied magnetic field (right side). The energy differences noted in the plot are with respect to the lowest energy level.

In the calculations shown here we used an externally applied magnetic field as the last term in the Hamiltonian:

$$H_Z = \vec{\mu_0}\mu_B\vec{B} = (\vec{L} + 2\vec{S})\mu_B\vec{B} \tag{5.28}$$

A zoom-in on the evolution of the lowest-energy states starting from the cubic ligand field term V_4^4, including spin-orbit coupling and external magnetic field is shown in Figure 5.9 for both Fe and Co.

The full Hamiltonian for the system consists of the ligand field term (H_{LF}), the spin-orbit coupling (H_{SOC}) and the external magnetic field (H_{Z}):

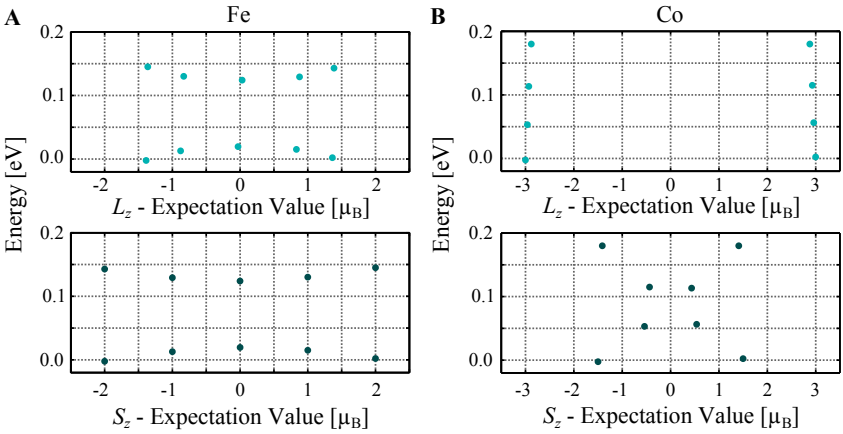

Figure 5.10: Orbital $\langle L_z \rangle$ and spin $\langle S_z \rangle$ expectation value in the out-of-plane (easy-axis) direction calculated with the point charge model for Fe (**A**) and Co (**B**). The values shown are for a 7 T external magnetic field along the z-axis. In all plots the $2\,(2S+1)$ lowest energy states are shown. For Fe, both the spin and orbital moments are close to zero for the intermediate states, while Co keeps almost its full free atom orbital moment for all states shown. (Here the optimized model for Fe is shown, see Section 5.3.5.)

$$H = H_{\mathrm{LF}} + H_{\mathrm{SOC}} + H_{\mathrm{Z}} \tag{5.29}$$

In Figure 5.10 we show the orbital $\langle L_z \rangle$ and spin $\langle S_z \rangle$ expectation value in the z-direction in an applied magnetic field of $B_z = 7$ T for both atoms. For Fe, both the spin and orbital moments of the intermediate states (4 and 5) are

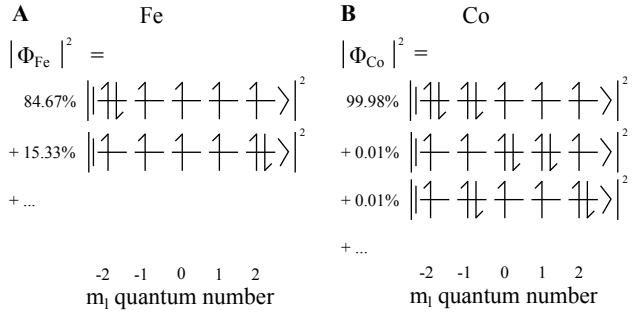

Figure 5.11: Composition of the ground state wave functions in a single electron picture for both Fe (**A**) and Co (**B**) in an applied magnetic field of $B_z = 7$ T. The parts of the wave function shown have an amplitude of $\geq 0.01\%$. For both wave functions there are additional minimal contributions of other states that are not shown. (Here the optimized model for Fe is used, see Section 5.3.5.)

close to zero. Co, on the other hand, keeps almost its full free atom orbital moment for all states shown. The presence of the large orbital moment in all states for the Co atom explains why an effective spin Hamiltonian does not work well for such a system, as no clear barrier for the reversal of the magnetic moment is present. In Fe however, the orbital moment reverses together with the spin moment which allows a description with an effective spin Hamiltonian where the orbital moment is part of the anisotropy parameters (see later in this chapter). (Note that in Figure 5.10 the expectations values of Fe are from the model that has been optimized to fit the STM results (see next Section 5.3.5).)

To clarify the character of the different wave functions we show in Figure 5.11 the ground state wave functions at 7 T in a single electron picture. One can see that Co is almost fully polarized to a single contribution of large M_L and only minor contributions of other wave functions are present in the ground state, which leads to a large orbital moment in the out-of-plane direction ($\langle L_z \rangle$). Also Fe regained a major part (about 2/3) of its orbital moment due to spin-orbit coupling but the orbital moment is not fully restored as seen in the fairly large contributions of a wave function with opposite M_L. (Note that

(a) Fe

	full	PC
$V_{02} \approx V_{13}$	14.3	23.1
V_{04}	20.4	38.6
$V_{06} \approx V_{17}$	154.3	77.8

(b) Co

	full	PC
$V_{02} = V_{13}$	54.9	54.8
$V_{04} = V_{15}$	90.6	114.2
$V_{08} = V_{19}$	121.8	

Table 5.3: Comparison of the energy splitting at 0 T between the two models: *full* for the full multiplet calculation as a best fit to X-ray data, *PC* for point charge model as a simplified version, using the geometry and charges obtained by DFT calculations. For Fe, there is a small energy splitting of 5.8 neV between states 0 and 1 (according to the point charge model) which is why we use two energies V_{02} (V_{06}) and V_{13} (V_{17}) as approximately equal, even though they deviate slightly even at 0 T. All energies are in meV.

for the Fe the wave functions of the optimized model are plotted, see Section 5.3.5.)

5.3.4 Comparison between the multiplet and the point charge calculation

When comparing the multiplet and the point charge calculation to each other, one can see that their calculated evolution of states (Figures 5.3 and 5.4 vs. 5.9) are in good qualitative agreement. Both calculations result in the same order of the energy eigenstates with similar relative energy spacing. In this comparison we use the non-optimized results, as described in Sections 5.3.2 and 5.3.3. We will introduce an optimization of the Fe's calculation in Section 5.3.5.

In Table 5.3, the energies of different transitions at zero external magnetic field and, in Table 5.4, the expectation values of $\langle L_z \rangle$ and $\langle S_z \rangle$ at $B_z = 7$ T are shown for both atoms, Fe and Co, and both calculations.

(a) Fe			(b) Co		
$\|n\rangle$	full $\langle L_z\rangle, \langle S_z\rangle$	PC $\langle L_z\rangle, \langle S_z\rangle$	$\|n\rangle$	full $\langle L_z\rangle, \langle S_z\rangle$	PC $\langle L_z\rangle, \langle S_z\rangle$
0	$-1.25, -1.96$	$-1.95, -2.00$	0	$-2.91, -1.27$	$-2.99, -1.50$
1	$+1.22, +1.96$	$+1.94, +2.00$	1	$+2.91, +1.27$	$+2.99, +1.50$
2	$-0.75, -0.98$	$-1.82, -1.00$	2	$-2.54, -0.39$	$-2.96, -0.54$
3	$+0.71, +0.98$	$+1.79, +1.00$	3	$+2.54, +0.39$	$+2.96, +0.54$
4	$-0.03, +0.00$	$-0.14, -0.00$	4	$-0.30, +0.29$	$-2.93, +0.43$

Table 5.4: Comparison between the $\langle L_z\rangle$ and $\langle S_z\rangle$ expectation values at 7 T between the two models: *full* for the full multiplet calculation as a best fit to X-ray data, *PC* for point charge model as a simplified version, using the geometry and charges obtained by DFT calculations. All values are in μ_B.

We first focus on the comparison of the results for the Fe atom. Both models approximate the energy of the transition visible in the STM measurements to within 10 meV and the ratio between the different energies are comparable. However, the point charge model overestimates the energy splitting V_{02} by more than 50%. Experimentally we are only able to resolve the $V_{02} \approx V_{13}$ transition as 14 meV. The difference between the models amongst each other and to the experiment is mostly due to slight changes in the V_4^4 (cubic) potential.

The spin moments $\langle S_z\rangle$ for Fe are in both models (almost) fully polarized at $B_z = 7$ T. On the other hand, the full model obtains orbital moments $\langle L_z\rangle$ that are reduced by about 35% with respect to the point charge model. The $\langle L_z\rangle$ expectation value is also strongly dependent on the choice of the cubic ligand field as we will point out more in the next chapter. Overall for Fe on MgO, we can conclude, that the two models obtain results that are in good qualitative agreement despite their quantitative differences. We will show in the next section how the point charge model can be optimized by changing the radial

component in the ligand field potential (Section 5.3.5).

The comparison of the Co's energies gives even better agreement for the first excitation at 0 T ($V_{02} = V_{13}$), where the deviation is less than 1%. However, the second excitation seen in the full multiplet model, does not appear at all in the point charge model, which is due to the fact that the full model includes configuration mixing. Due to this mixing additional levels appear close to the ground state (see Figure 5.4, red). Without including such configuration mixing we are not able to model this second transition correctly. (We will see in Chapter 7 that this additional energy level can be made visible by using spin-polarized tunneling.) The second excitation seen in the point charge model has a similar energy as the third excitation of the full model. This confirms that the additional energy level seen in the full multiplet model is due to a part of the calculation that is not considered in the point charge model (the configuration mixing).

The configuration mixing also manifests itself in the reduced spin and orbital moments seen in the full multiplet model as compared to the point charge calculation. Especially, the spin moment of the ground and first excited state deviates strongly between the two models, where the full calculation's $\langle S_z \rangle$ expectation value is reduced by 18% with respect to the point charge model. The expectation values of the orbital moment on the other hand are within 3% of each other.

Thus the two calculations are well comparable, despite their very different approach where one uses a fit to the X-ray data and the other uses DFT calculations as a starting point. However, problems come into play, mostly when a large amount of configuration mixing is present for a single atom, such as for Co on MgO. Nevertheless, the point charge approach is a great approximation for single atoms on surfaces. In some preliminary calculations we could even show that it also gives feasible results for the same atoms on Cu_2N even though the symmetry breaking on that particular surface is a lot stronger than on the

four-fold symmetric MgO surface.

5.3.5 Optimized point charge model

We pointed out in the last section that the results of the point charge model overestimate all the calculated energy splittings of the Fe atom. We believe that this is mainly due to the fact that we used the bulk values for the radial integrals as tabulated by (*31*) but on surfaces the atom's wave functions are less confined in space and can spread out more. Therefore, we suggest a stretching of the radial part $\langle r^n \rangle$ for Fe by a factor determined by comparison to the SES measurements. The Co atom does not need a stretching factor as the nature of its lowest energy states makes it insensitive to changes in the cubic ligand field and thus any factor could be used without significantly changing the results obtained for Co.

We optimized the radial part for Fe by a factor of $(\sqrt{2.11})^n$ to obtain a splitting of 14.02 meV for the V_{02} transition. This results in $\langle L_z \rangle = -1.39$ and $\langle S_z \rangle = -2.00$ as the expectation values for the ground state at $B_z = 7$ T. Thus the $\langle L_z \rangle$ expectation value of this optimized model is within 10% of the results obtained with the full multiplet model. The results presented in the following chapters are all based on the optimized result for Fe, as a better fit to the STM experiments.

We would like to note here as well, that the DFT calculations might not have used a large enough unit cell to obtain zero interaction between neighboring magnetic atoms (due to computational restrictions). Thus increasing the unit cell further might slightly change some of the ligand positions with respect to the values used here (e.g. less buckling of the MgO under the magnetic atom might be possible). However, we believe that the results obtained here are astonishingly close to the experimental values even for Fe on MgO, where the magnetic atom is extremely sensitive to slight changes in its environment.

5.4 From extended point charge model to a simplified Hamiltonian with Stevens operator equivalents

One can eliminate the need to use single electron wave functions by the use of so-called Stevens operator equivalents (*32*). These operator equivalents are designed to describe the ligand field in terms of angular momentum operators rather than with spherical harmonics, as done in Section 5.3.2 above. Thus these operator equivalents act on the orbital angular momentum (as shown here) or the total angular momentum of an atom and describe the effect of surrounding ligands. Nevertheless, they are often applied to the spin angular momentum, even though the spin only indirectly orients itself with the surrounding ligand field via spin-orbit coupling (see next section).

The Stevens operator equivalents Hamiltonian for a four-fold symmetric surface, such as the MgO, has the following form:

$$H_{\mathrm{LF}} = \sum_{n,m} B_n^m \hat{O}_n^m = B_2^0 \hat{O}_2^0 + B_4^0 \hat{O}_4^0 + B_4^4 \hat{O}_4^4 \tag{5.30}$$

where $n = 2, 4, ..., 2L$, and $0 \leq m \leq n$. All other terms vanish, when determining the matrix elements with spherical harmonics (see Section 5.3.2). The B_n^m are prefactors and $\hat{O}_n^m$ are the so-called Stevens operators:

$$\begin{aligned}
\hat{O}_2^0 =& 3\hat{L}_z^2 - L(L+1) \\
\hat{O}_4^0 =& 35\hat{L}_z^4 - (30L(L+1) - 25)\hat{L}_z^2 + 3L^2(L+1)^2 - 6L(L+1) \\
\hat{O}_4^4 =& \frac{1}{2}(\hat{L}_+^4 + \hat{L}_-^4)
\end{aligned} \tag{5.31}$$

In Table 5.5 we show a list of the $\langle r^n \rangle \gamma_{nm}$ prefactors as used with the multi-electron wave functions in the point charge model together with a list of the Stevens operator equivalent prefactors (B_n^m). Note that $\langle r^n \rangle \gamma_{nm}$ is included

(a) Fe

V_n^m	PC $\langle r^n \rangle \gamma_{nm}$	Stevens B_n^m
V_2^0	-7.340 eV	-317.43 meV
V_4^0	1.361 eV	-6.58 meV
V_4^4	-0.054 eV	4.36 meV

(b) Co

V_n^m	PC $\langle r^n \rangle \gamma_{nm}$	Stevens B_n^m
V_2^0	-3.037 eV	-26.27 meV
V_4^0	0.252 eV	0.24 meV
V_4^4	-0.013 eV	-0.21 meV

Table 5.5: Different ligand field prefactors as used in the point charge model (PC) and with Stevens operator equivalents (Stevens). Both of these prefactors give the same result for the ligand field. However, with the Stevens operator equivalent one does not need to know the full multi-electron wave functions, which makes the calculations easier. Note that $-\frac{q_M}{4\pi\epsilon_0}$ is included in these prefactors.

in the corresponding B_n^m, as shown below. We empirically determined transformation factors between the two methods as shown in Equation 5.32. We find that we can use a constant transformation factor for each Stevens prefactor (a, b, c) which needs to be additionally multiplied by a term that is different for each atom and depends on the order of the Stevens term (x_n). A more detailed calculation of these prefactors starting from the multi-electron potentials is shown in Appendix E.2.

$$\begin{aligned} B_2^0 &= \langle r^2 \rangle \gamma_{20} \cdot a \cdot x_2, \quad \text{with} \quad a = \frac{p}{42}\sqrt{\frac{5}{\pi}} \\ B_4^0 &= \langle r^4 \rangle \gamma_{40} \cdot b \cdot x_4, \quad \text{with} \quad b = -\frac{p}{168}\sqrt{\frac{1}{\pi}} \\ B_4^4 &= \langle r^4 \rangle \gamma_{44} \cdot c \cdot x_4, \quad \text{with} \quad c = -\frac{p}{84}\sqrt{\frac{70}{\pi}} \end{aligned} \tag{5.32}$$

where p is the prefactor for the electrostatic potential: $-\frac{1}{4\pi\epsilon_0}$, with ϵ_0 the electric constant, x_2 and x_4 represent factors that are atom-specific (see Appendix E.2), for example $x_2 = x_4 = 1$ for Fe (d^6-configuration, $L = 2$) or

$x_2 = -x_4 = 1/5$ for Co (d^7-configuration, $L = 3$). q_M is included in γ_{nm} in this discussion.

The factors determined here allow a much simpler calculation of the atomic levels within a specific multiplet of a configuration. It allows calculations without knowing any details about the single electron wave functions and thus several steps of the calculations shown previously can be skipped. We note that the factors determined here are identical to those determined by Stevens (*32*) and Bleaney (*57*). In their description, each B_n^m is determined by a factor (α_J,β_J) that depends on L and S of the specific multiplet, as well as an additional constant (see Appendix E for more details) (*56*). In contrast to the Stevens method, we determine a multiplying factor x_2 and x_4 and a constant that is atom independent and does not require any knowledge about the originating spherical harmonic function, nevertheless, the results are the same. It must be noted that it is conventional, that all factors of $\hbar$ are dropped, when using the operator equivalents to evaluate the ligand field matrix elements.
Here we will not demonstrate how to actually transform the potential V into Cartesian coordinates and then do the tedious work of accounting for all commutation relations to get from the potential V to the Stevens operator equivalents, this is done elsewhere in much detail (*32*,*56*). Nevertheless, we would like to mention that the operator equivalent method works because of the Wigner-Eckert theorem. For the lowest $(2L+1)$-fold multiplet the Wigner-Eckert theorem proves that within this subspace, the spherical harmonics can be replaced by the components of the L operator, so that the matrix elements of these equivalent operators are proportional to the matrix elements of the original ligand field potential ($\langle LM_L|Y_n^m|L'M'_L\rangle \propto \langle LM_L|\hat{O}_n^m|L'M'_L\rangle$) (*2*,*31*).

Overall, the total Hamiltonian for using Stevens operator equivalents is the following:

$$\begin{aligned} H_{\text{Stevens}} =& H_{\text{LF}} + H_{\text{SOC}} + H_{\text{Z}} \\ =& B_2^0\hat{O}_2^0 + B_4^0\hat{O}_4^0 + B_4^4\hat{O}_4^4 + \lambda\vec{L}\cdot\vec{S} + (\vec{L} + 2\vec{S})\mu_{\text{B}}\vec{B} \end{aligned} \tag{5.33}$$

In this section we showed how to use Stevens operator equivalents to obtain the same results as when using a calculation with the full multi-electron wave function albeit limited to a single multiplet. In addition, we worked out the relation between the two approaches in a way that is consistent with the results shown by Stevens (*32*,*57*).

In Appendix F one can find a list of all necessary tables and formulas for performing these easy calculations on the basis of the DFT-calculated geometry and the Stevens operator equivalents.

5.5 Back to an effective spin Hamiltonian

In a last step we would like to show how the calculation of a full atomic multiplet is related to the previously introduced effective spin Hamiltonian. Here, we start with the different orbital levels in a ligand field, but before introducing spin-orbit coupling. Thus all orbital levels contain $(2S + 1)$-degenerate spin levels. In the previous calculation, this degeneracy was lifted due to the coupling of the spin to the orbital moment, via the spin-orbit coupling, which for example in the case of Fe on MgO resulted in a 5-level spin-system as the lowest energy spin-multiplet. Exactly these well defined low energy spin-multiplets are subject to a description with an effective spin Hamiltonian as introduced in Section 3.3.

In order to obtain an effective spin Hamiltonian description of the same levels, it is necessary to remove the orbital part from the previous Hamiltonian (H or H_{Stevens}). However, both the spin-orbit coupling term ($H_{\text{SOC}} = \lambda\vec{L}\cdot\vec{S}$) and the Zeeman term ($H_{\text{Z}} = (\vec{L} + 2\vec{S})\mu_{\text{B}}\vec{B}$) contain the orbital angular momentum L. Thus in an effective spin Hamiltonian, the effects of L have to

be absorbed in the effective anisotropy parameters and the effective g^*-value.

For example, since for Fe the levels are split mainly due to second order perturbation theory, we could start by writing the effective Hamiltonian according to perturbation theory (*2*,*31*,*58*):

$$\begin{aligned} H_{\text{eff}}^{(2)} =& -\lambda^2 \sum_{n\neq 0} \frac{\left|\left\langle \Phi_0|\vec{L}\cdot\vec{S}|\Phi_n\right\rangle\right|^2}{E_n - E_0} \\ =& -\lambda^2 \sum_{n\neq 0} \frac{\left|\left\langle \Phi_0|\hat{L}_x\hat{S}_x + \hat{L}_y\hat{S}_y + \hat{L}_z\hat{S}_z|\Phi_n\right\rangle\right|^2}{E_n - E_0} \end{aligned} \tag{5.34}$$

We use the wave functions Φ_n here, to refer to the eigenstates of the magnetic atom after the ligand field contribution (eigenstates of H_{LF}) but before spin-orbit coupling. Since we would like to write this effective Hamiltonian in terms of a spin Hamiltonian where we eliminate L, we can define:

$$\Lambda_{\nu\nu} = \sum_{n\neq 0} \frac{\left|\left\langle \Phi_0|\hat{L}_\nu|\Phi_n\right\rangle\right|^2}{E_n - E_0} \tag{5.35}$$

Therefore the effective Hamiltonian can be rewritten as:

$$\begin{aligned} H_{\text{eff}}^{(2)} =& -\lambda^2(\Lambda_{xx}\hat{S}_x^2 + \Lambda_{yy}\hat{S}_y^2 + \Lambda_{zz}\hat{S}_z^2), \\ & \text{subtract: } -\frac{\lambda^2}{2}(\Lambda_{xx}+\Lambda_{yy})(\hat{S}_x^2+\hat{S}_y^2+\hat{S}_z^2) \\ H_{\text{eff}}^{(2)} =& \lambda^2(\Lambda_{zz} - \frac{1}{2}\Lambda_{xx} - \frac{1}{2}\Lambda_{yy})\hat{S}_z^2 + \frac{1}{2}\lambda^2(\Lambda_{xx}-\Lambda_{yy})(\hat{S}_x^2 - \hat{S}_y^2) \\ =& D\hat{S}_z^2 + E(\hat{S}_x^2 - \hat{S}_y^2) \end{aligned} \tag{5.36}$$

(The physical properties of the Hamiltonian are not changed by subtracting a constant.)

This transformation results in $D = -5.84$ meV and $E = 0$ meV for Fe on MgO. This D value is slightly larger than the one obtained as a fit to the STM results (Section 3.5.1). However, one can easily see that when diagonalizing the spin-orbit coupling Hamiltonian (H_{SOC}), the second order perturbation term will not be the only non-zero term. Thus the treatment in Section 3.5.1 should most likely have been expanded to other terms, i.e. $D'\hat{S}_z^4$, in order for the two results to be comparable.

Note that a similar approach for the Co atom would have to include first order perturbation terms, which would be proportional to the $\hat{S}$ operator. This is also visible in the expectation value plot (Figure 5.10), where $\langle S_z \rangle$ changes linearly with energy but does not result in an effective anisotropy barrier. Perturbation theory starting from degenerate levels is often more complicated than in the case of non-degenerate levels. As a result of this, it is often cited that effective spin Hamiltonians only work when the orbital levels are non-degenerate and the orbital moment is fully quenched before spin-orbit coupling (*2*,*31*,*58*,*59*).

All the additional elements of an effective spin Hamiltonian are obtained by extending the perturbation theory results to higher orders. The connection between the ligand field and the order of perturbation to be consider for an effective Hamiltonian is however not straightforward. The entire expansion to higher orders is thus beyond the scope of this work and unnecessary if the energy levels are already calculated with the point charge model.

5.6 Summary on multiplet calculations and other models for magnetic systems

In this theory-based chapter, we started with explaining the basics of the multiplet calculations performed as a fit to the X-ray results and how these calculations can explain the character and properties of the magnetic energy levels probed previously by STM. We furthermore introduced a calculation based on the DFT-calculated geometry and charge distribution that allows a fairly accurate representation of the magnetic energy levels without any fitting parameters. Finally, we showed how by using Stevens operator equivalents these calculations can be extremely simplified. We believe that the tools presented in this chapter will prove to be very useful in future STM studies.

In a next step, we want to show how understanding the origin of the states for single atoms on surfaces can be a useful tool to understand influences of small perturbations in the environment of these single atoms. We will show how displacing the magnetic atom slightly (changing γ_{nm}) can change the energies of the system and can thus be a tool to tune the effective anisotropy barrier.

Chapter 6

Tuning the energy levels of single atoms

Being able to change the spacing between different energy levels, which in turn can increase the magnetic anisotropy, can be another pathway to obtain slow magnetization reversal.

For the results presented in this chapter the manuscript is in preparation: Baumann, S. *et al.* Anisotropy tuning explained by a point charge model.

6.1 Anisotropy tuning

In the last chapter we introduced a detailed understanding of different perturbations from the free atom description to single atoms on surfaces. Here we want to explore how, under certain circumstances, these perturbations can be tuned (mainly the ligand field) in such a way as to change the energy levels. We show experimentally how the energies can be changed and offer a model, based on the previous calculations, that explains the changes.

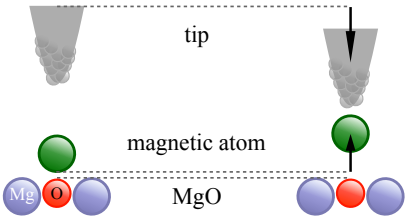

Figure 6.1: The tip proximity can influence the height of the atom above a specific substrate (here, above MgO). As the tip is brought closer to the atom (right panel) the atom is pulled upwards, away from the surface.

In recent years there have been several studies demonstrating some amount of tuning of the energy levels, and with it, the magnetic anisotropy of the system. (Note that in this chapter, we will use anisotropy and magnetic anisotropy interchangeably.) Some research groups used chemical bonding to surface atoms, e.g. oxygenation of a Fe atom in a molecule (*60*), to drastically change the anisotropy and even to switch the easy magnetization axis from in-plane to out-of-plane. In a different approach, nearby spins were used to tune the coupling to a single atom, which also tunes the energy levels of the atom under study (*29*). This study used precise atom manipulation on the Cu_2N surface to change the coupling between the two atoms, which in turn modified the energy levels of both of them. Both of these approaches present a way of tuning the anisotropy. However, rather than in a continuous way they only allow certain values of the anisotropy to be obtained due to e.g. the discrete nature of the surface binding site. In recent years several experiments also demonstrated the continuous tuning of the anisotropy. One example used the piezo-electric properties of ZnO in an ensemble EPR experiment to tune the anisotropy of Mn impurities via electric fields by distorting the ligand field around the magnetic atoms (*61*). Similarly, it was shown in a STM experiment, that for a Fe-molecule on a superconductor the anisotropy of the magnetic center in the molecule can be tuned by tip proximity in a continuous way (*62*). The tuning due to the tip proximity has been assigned

to mechanical deformations caused by the tip, which change the ligand field and that in turn changes the energy levels. Thus the STM tip might provide an easily accessible way to tune the energy levels of a single atom and to tune its magnetic anisotropy (see Figure 6.1).

We will show here how this applies to Fe on MgO and we will explain the observed changes with the point charge model introduced in the proceeding chapter. We will also demonstrate how this anisotropy tuning will only work for atoms in an appropriate symmetry environment: The energy levels of Co, for example, are not subject to tuning under the tip influence on the four-fold symmetric MgO surface.

6.2 Experimental observation of energy tuning

The experiments shown in this chapter were again performed with the scanning tunneling microscope. We measured the energy of the SES transition for Fe and Co as a function of tip proximity which we specify by the tunnel current at which the feedback loop opened (Figure 6.2). The measurements on Fe were performed at B = 0 T (see Sections 3.5.1), where there is only a single SES transition (the V_{02} and V_{13} transitions are equivalent). Co was measured at 6 T (see Section 3.5.2) and only the higher energy transition (V_{02}) is shown.

As seen in Figure 6.2, the two atoms, Fe and Co, react differently to tip proximity. The step energy of the Fe atom grows exponentially as a function of tip proximity, while the Co is almost insensitive to any change in tip height. Far away from the atom, the Fe SES energy is 14.5 mV (for this atom at 0 T). The SES energy increases by about 4% (+0.6 mV), when the tip is moved $\sim$200 pm closer to the atom (increasing setpoint tunnel current by 2 orders of magnitude (50 pA to 5 nA)). Similar changes of SES energies with tip-sample distance have been observed for molecules on Pb (*62*). Co on the other hand exhibits only a 0.1% change in SES step energy when the tip is 100 pm closer.

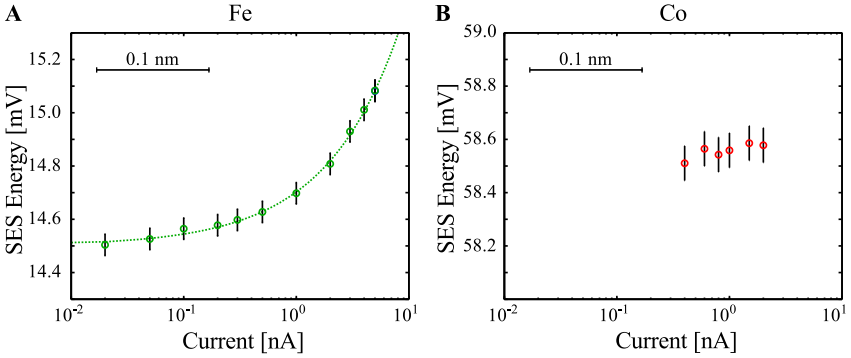

Figure 6.2: Tip height dependence of the SES step. For Fe at 0 T (**A**) there is only a single step ($V_{02} = V_{13}$), while for Co at 6 T (**B**) only the higher energy step V_{02} of the double step is shown. Both plots show an energy range of 1 mV. The line in (A) is a fit to the data. Note that (Setpoint voltage Fe: V = 30 mV, B = 0 T, Co: V = 50 mV, B = 6 T).

Figure 6.2 A shows that for Fe we are able to change the SES energy continuously. Note that the induced change is reversible. The fact that the Fe SES energy seems to grow exponentially with tip proximity, indicates that the interaction that causes this change scales exponentially with tip-atom distance as well (*63*,*64*). The exponential fit tails off at about 14.5 mV, which corresponds to the energy at 20 pA. Thus we can assume that at currents lower than 20 pA the tip-atom distance is large enough so that the tip is not interacting with the atom anymore, or that the interaction is effectively zero at greater distances.

In the next section we will explain these changes in SES energy based on changes in the ligand field as the tip is brought closer to the individual atoms.

6.3 Model to explain the changes

In the previous chapters we showed how the magnetic behavior of Fe on the O binding site of MgO is very different from the Co's. Co retains an orbital degeneracy in the four-fold symmetric ligand field and thus the spin-orbit coupling splits the lowest energy octuplet linearly into four doublets, which gives rise to the maximal zero-field splitting (*26*). Fe on the other hand loses its orbital degeneracy due to the mixing of the $M_L = \pm 2$ states in the same ligand field and the spin-orbit coupling induces an orbital moment by coupling to the excited multiplet (about 100 mV higher in energy). This results in a significantly smaller zero-field splitting (V_{02}) compared to Co. Due to the energetic proximity of the excited spin-multiplet, Fe SES energies are susceptible to small changes in atomic arrangements, whereas Co is about 10 times less sensitive to such changes.

The point charge model allows us to modulate the distance to the different ligands. In particular, we can change the height of the magnetic atom above the MgO layer (see schematics in Figure 6.1). (The MgO layer is not allowed to relax here.) Changing this distance affects both the Fe-O (Co-O) as well as the Fe-Mg (Co-Mg) distance. In Figure 6.3 we show two different magnetic-atom-to-oxygen distances and their influence on the evolution of states. Shown is evolution of the lowest $2\,(2S+1)$ energy states starting with the effect of the cubic ligand field (V_4^4 potential). We show their dependence on the cubic ligand field, the spin-orbit coupling and an externally applied magnetic field. The zero energy is set at zero magnetic field for both atom-oxygen distances. When comparing the two atoms one can easily see that the Co atom is insensitive to the change in distance to its surrounding ligands (the orange and black curves almost lay on top of each other). Fe on the other hand shows strong changes. Those changes are mainly due to the ligand-field splitting between the two lowest orbital states. For example, the splitting between the two lowest orbital states (before considering spin-orbit coupling) is reduced by 10 meV, if the Fe atom is 5 pm farther away from the

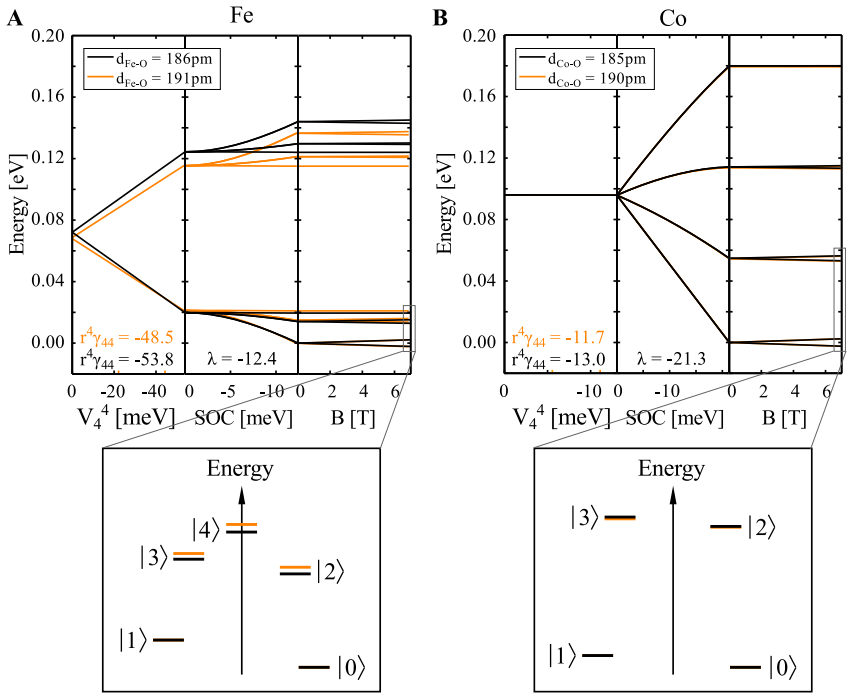

Figure 6.3: Point charge calculation for Fe (**A**) and Co (**B**) with changing distance between the magnetic atom and oxygen ($d_{\text{M-O}}$). The black curves for Co show the same evolution of states as shown in Figure 5.9, while for Fe the black curves show the optimized model (see Section 5.3.5). The orange curves show the evolution of states with 5 pm larger magnetic-atom-to-oxygen distance than the black curves (see schematics in Figure 6.1). The evolution of states shown here starts from the four-fold symmetric ligand field term (left side of both plots) and the black and orange curves are aligned at zero magnetic field to visualize the induced changes of the resulting energies by the cubic ligand field. The bottom panels show level diagrams of the resulting states at 7 T.

surface. As a consequence of the weaker ligand field (atom further away), the energy splitting induced by spin-orbit coupling is larger (especially visible for

the lowest 5 states).

Thus the multiplet model based on point charges lets us understand the changes in SES energy in terms of a slight movement of the magnetic atom. The atom gets pulled towards the STM tip as the tip moves closer (see schematics in 6.1). This movement in the out-of-plane direction changes both the axial as well as the cubic ligand field. The small change in the axial field has no effect on the order of the energy levels (not shown). In particular, for the Fe atom the $M_L = \pm 2$ levels are more than an eV lower in energy than the $M_L = \pm 1$ levels. Thus the final energy levels are not affected by a change in the axial field. The cubic field however, changes the splitting between the two lowest spin-quintuplets, which in turn influences the effect of the spin-orbit coupling. The further the two quintuplets are split (i.e. the larger the cubic ligand field, or the closer the Fe atom to the four Mg atoms), the smaller the coupling between the two quintuplets (levels couple more the closer they are together). This leads to a smaller splitting between the spin states (see Figure 6.3, black vs. orange curve).

We find that by changing the magnetic-atom-to-oxygen-distance we can change the zero-field splitting ($V_{02} = V_{13}$) close to linearly, see Figure 6.4 A, B, in a small range around the relaxed atom distance. For the Fe atom, a 5 pm Fe-O distance change causes a change of about 1 meV in V_{02}. For the Co atom a similar change in Co-O distance has less effect and only causes a change of about 0.2 meV. (In Appendix G we show the energy change when the distance to the oxygen atom is changed by ± 40 pm a large change that would probably only be possible when bonding to the tip occurs, which would change the situation alltogether. Nonetheless, the change over this large range occurs with constant slope indicating that these results are robust against an absolute height offset.)

To better compare the simulated results with the experimental SES change we determine the distance the magnetic atom must move (with respect to the

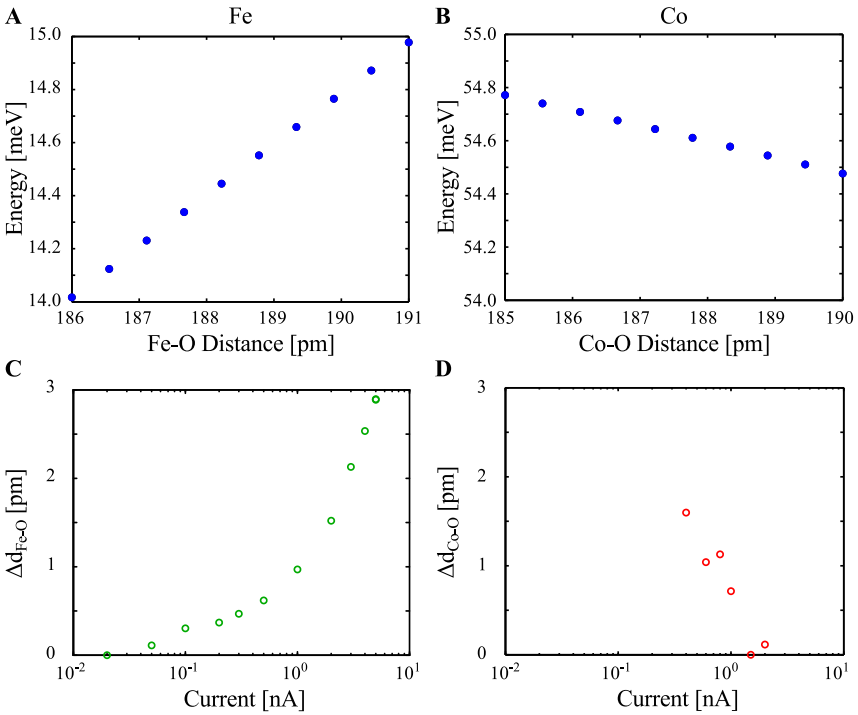

Figure 6.4: Point charge calculation for Fe (**A**) and Co (**B**) with step-wise changed distance between the magnetic atom and the oxygen, starting from the relaxed structure (calculated by DFT) to a 5 pm increased distance. For the Fe (optimized) the resulting change of the V_{02} energy is 1 meV, while for Co it is -0.2 meV. The left and right edges of these plots show the same results as the black and orange curves, respectively, in Figure 6.3. Panels (**C**) and (**D**) use the experimental data of Figure 6.2 matched to an equivalent energy difference in the calculation to determine the movement of the atom vs. the measured current. The change in energy in the Fe atom thus corresponds to an atom movement of roughly 3 pm, and for the Co the observed change is equivalent to a -1.5 pm change in the Co-O distance. ((A), (B) and (C) are calculated at 0 T, (D) is at 6 T to match the data shown in 6.2.)

oxygen atom) in order to reproduce the measured SES energy shift shown in Figure 6.2 (see Figure 6.4 C and D). For the Fe atom, we find that a displacement of only ∼3 pm is required to match the experimentally observed zero-field splitting (see Figure 6.4 C), when the tip is brought ∼200 pm closer to the atom (see Figure 6.2 and schematic 6.1). Thereby, the calculated magnetic anisotropy barrier (equivalent to V_{04}) changes from 21.4 mV to 22.3 mV when the atom moves by 3 pm.

The point charge model calculation for Co indicates a shift of the SES step energy to lower energy as the magnetic-atom-to-oxygen distance is increased (Figure 6.4 B). Experimentally, a shift to slightly higher energy is observed when the tip is moved closer to the atom (Figure 6.2 B). Together, this would suggest that bringing the tip closer to the atom makes the atom-to-oxygen distance smaller (Figure 6.4 D). We find it unlikely that the direction of the atom displacement would be inverted between Co and Fe, as the tip-sample forces causing the relaxation should be attractive in both cases. We rather conclude that the energy shifts for Co (including their sign) are not well approximated by the point charge model.

Note that the model presented here assumes that only the magnetic atom moves under the influence of the tip, in a more elaborate analysis one might find that all ligands move due to tip proximity. Nevertheless, this model illustrates a possible pathways to tune the magnetic anisotropy of a given atom.

We expect a similar movement for other atoms on surfaces when the tip is close enough. However, as seen for Co on MgO, when the lowest lying levels are e.g. the $M_L = \pm 3$, they will not be affected the same way by a change in the cubic ligand field and therefore the observed SES step is expected to be independent of tip-sample distance. Thus the ability to modify the magnetic energy levels by means of the proximity of the tip depends (i) on the magnetic atom itself (e.g. lowest energy term ^5D vs. ^3F) and (ii) on the symmetry the atom is found in (potentially a three-fold symmetric surface would affect the

cobalt's energy levels more than the iron's). Overall, we believe that Fe on MgO is one of the most favorable systems to observe such an effect, as the symmetry and lowest orbital states allow a strong modulation of the individual energy levels.

6.4 Summary on energy tuning

In this chapter we demonstrated a way to continuously tune the energy levels and thus the anisotropy of a single atom on a surface. In particular, we were able to tune the energy levels for Fe on MgO. We explained the tuning as due to a slight movement of the atom as a consequence of tip-sample interaction. We also showed that such a movement of the atom only affects those atoms with appropriate symmetry to induce quenching of the orbital moment and that therefore, the Co atom reacts to to similar tip-sample interactions much less.

Chapter 7

Observing additional orbital states

The transition rates and the resulting occupation of individual states are closely related to their lifetimes.

For the results on Fe presented in this chapter the manuscript is in preparation: Baumann, S. *et al.* Spin and orbital magnetism of Fe atoms on MgO.

7.1 Observing additional transitions gives a more complete picture of the magnetic properties

In the previous chapters we have shown measurements of the lowest-energy spin states in SES spectroscopy and we have introduced a detailed understanding of those states, based on XMCD results and multiplet calculations as a fit to the experimental values, or alternatively by using DFT calculations as the basis of a point charge model. By performing further STM experiments and combining them with such calculations we have seen that the Fe atom on MgO is extremely sensitive to the local environment, especially to its

distance to the neighboring Mg atoms, which is due to the fact that there is a second nearby spin-multiplet. In this chapter, we will show that, when using a spin-polarized tip as a more sensitive probe in STM, we are able to observe transitions to this second spin-multiplet. We will also show, that the spin-polarized tunneling allows us to probe a state in Co that crosses with the lowest multiplet due to the initial configuration mixing. Thus, in this chapter we will introduce spin-polarized tunneling as a means to observe transitions to other orbital states. The understanding of such transitions is based on a set of possible selection rules, where spin angular momentum is exchanged between the surface atom and the tunneling electrons, while explicitly keeping the orbital angular momentum unchanged.

We will show here that the probed additional transitions in STM are consistent with the results obtained by a fit to the XMCD spectra and that in turn shows again how the two techniques are so complementary to each other. We would not be able to interpret these transitions with STM measurements alone as they go beyond the point charge model. However, these STM measurements could potentially also be used to improve the results from the XMCD measurements, especially in systems where the X-ray absorption measurements pose technical challenges due to, for example, beam induced atom desorption. To get a detailed understanding of a system at the atomic scale it is often not enough to just employ one technique and it becomes necessary to use a combination of techniques to probe the atom's properties. The use of STM and XMCD is shown here to be a great example of such a combination.

7.2 Selection rules and transition intensities

As introduced in Chapter 3, the conductance through an atom in a STM junction consists of elastic and inelastic tunneling. In the inelastic process the tunneling electrons are able to exchange energy and spin angular momentum with the local atom, while both those quantities need to be conserved over the

whole process. The orbital moment is often almost fully quenched when an atom is placed on a surface. Therefore, it is not well developed how to model the interaction of the tunneling electrons with the orbital angular momentum. In the following, we assume that the tunneling electrons do not carry orbital angular momentum, thus they can only exchange spin angular momentum with the local spin of the atom on the surface and the atoms orbital moments have to stay unchanged. Then, the transition rate from an initial to a final state has a form given by Fermi's golden rule and depends on the interaction potential of the atoms spin with the spin of the tunneling electron (*25*,*65–67*).

Given that the local spin and the tunneling electron are non-interacting before and after the tunneling event, we can choose the wave function product of the state of the local atom $|\Phi\rangle$ and the state of the tunneling electron $|\sigma\rangle$ as the basis. We then model the interaction between the tunneling electron and the localized spin as an exchange interaction. The transition rate from an initial state $|\Phi_\mathrm{i}, \sigma_\mathrm{i}\rangle$ to a final state $|\Phi_\mathrm{f}, \sigma_\mathrm{f}\rangle$ is then proportional to:

$$Y(\Phi_\mathrm{i}, \sigma_\mathrm{i}, \Phi_\mathrm{f}, \sigma_\mathrm{f}) = \left| \left\langle \Phi_\mathrm{f}, \sigma_\mathrm{f} | \vec{S} \cdot \vec{\sigma} + u | \Phi_\mathrm{i}, \sigma_\mathrm{i} \right\rangle \right|^2 \tag{7.1}$$

where $\vec{S} \cdot \vec{\sigma}$ is the interaction potential, $\vec{S}$ and $\vec{\sigma}$ are spin vector operators for the surface atom and the tunneling electron, respectively. The parameter u is a real constant and accounts for a spin-dependent elastic component in the interaction (*67*). As mentioned above, this rate model implicitly requires that the orbital moments of the atom stay constant, while the tunneling electrons can exchange spin angular momentum with the atom. This exchange of spin angular momentum follows the usual selection rule $\Delta M_S = \pm 1{,}0$ (given by the tunneling electron, see below). The orbital moments stay constant if a part of the initial orbital wave function overlaps with the final orbital wave function, which is for example the case for all lowest $2\,(2S+1)$ states of Fe, as they all have components of both $M_L = +2$ and $M_L = -2$, despite $\langle L_z \rangle$ changing.

The transition intensity function is non-zero for all transitions that obey the spin conservation rule. Elastic tunneling events, that are still spin-dependent, are accounted for when the initial and final states are identical (i = f) (events that are spin-dependent in the sense that the tunneling electron interacts with the local spin). For all other events the local spin state changes (i $\neq$ f) and thus they describe inelastic tunneling processes.

7.2.1 Possible excitations due to tunneling electrons

There are several possible transitions a tunneling electron can undergo when interacting with a magnetic atom on the surface. The tunneling electrons can be in the spin states $|\sigma\rangle = |\pm\frac{1}{2}\rangle$. Thus upon interaction with the local spin on the surface they can potentially exchange one $\hbar$ of angular momentum and change their spin state by $\Delta\sigma = \pm 1$. Figure 7.1 A–C describe all possible inelastic processes, where the spin state of the local atom on the surface ends in an excited state after the interaction with the tunneling electron:

A A tunneling electron can start in state $|\sigma_\mathrm{i}\rangle = |+\frac{1}{2}\rangle$ and end in state $|\sigma_\mathrm{f}\rangle = |-\frac{1}{2}\rangle$ (Figure 7.1 A). In this process it changes its quantum number by $\Delta\sigma = -1$, while the spin of the atom on the surface changes by $\Delta M_S = +1$.

B Inversely, the tunneling electron can start in state $|\sigma_\mathrm{i}\rangle = |-\frac{1}{2}\rangle$ and end in state $|\sigma_\mathrm{f}\rangle = |+\frac{1}{2}\rangle$, changing its spin state by $\Delta\sigma = +1$ and the atom's state by $\Delta M_S = -1$, leaving the atom in an excited state (Figure 7.1 B).

C A further possible inelastic excitation can happen if the tunneling electron can excite the local spin state without exchanging spin angular momentum. These transitions occur for spin-excitations with significant wave function overlap so that transitions with $\Delta M_S = 0$ are possible, while $\Delta\sigma = 0$ (Figure 7.1 C).

Furthermore, Figure 7.1 D describes an elastic tunneling event:

D Neither the atom on the surface nor the tunneling electron change their spin state in an elastic tunneling event (again $\Delta M_S = 0$ and $\Delta\sigma = 0$) (Figure 7.1 D).

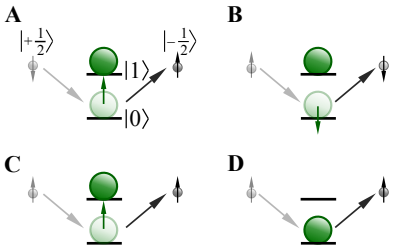

Figure 7.1: Schematics of spin-polarized tunneling processes. (**A**,**B**) In an inelastic excitation the tunneling electron can exchange its angular momentum ($\Delta\sigma = \mp 1$) with the angular momentum of the local spin ($\Delta M_S = \pm 1$). (**C**) An other inelastic process can occur when the atom gets excited, without the exchange of spin-angular momentum ($\Delta\sigma = 0$, $\Delta M_S = 0$). (**D**) Additionally, an elastic process can happens if neither the atom on the surface, nor the tunneling electron change their spin state.

7.2.2 Calculated transition intensities for Fe and Co on MgO

The transition intensities for Fe and Co on MgO are derived from Equation 7.1 as a sum of all the processes mentioned above. For simplicity we used $u = 0$ here (*67*). In the analysis of the spin-excitation spectra only the ratios of the transition intensities are of importance thus we omit any normalization factors (*67*).

Figure 7.2 shows the calculated transition intensities Y for both Fe and Co. All transition intensities larger than 10^{-3} are shown as solid lines, the stronger a transition the wider its line. The blue and black lines depict the most probable transitions, given that the initial states are occupied for a significant amount of time (more about occupation of states below). Additionally, all

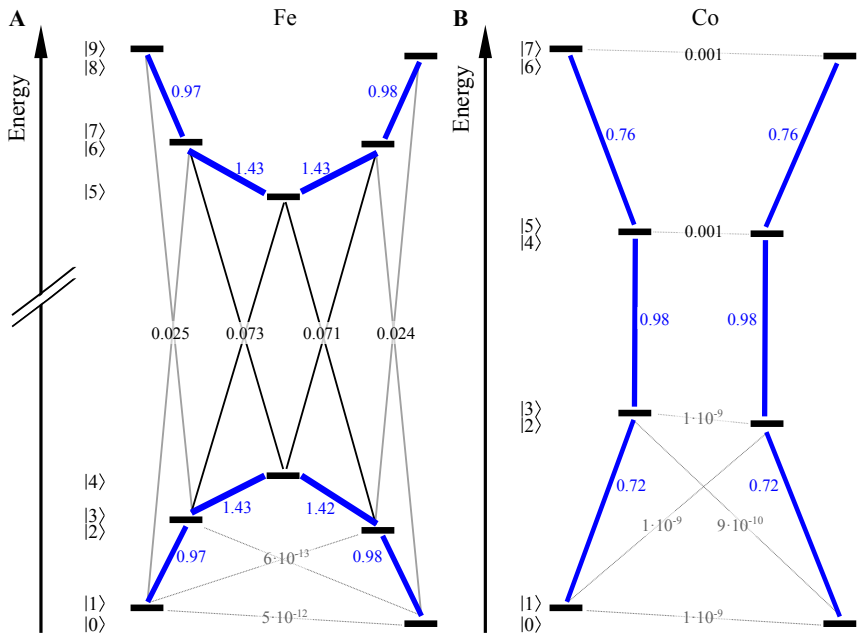

Figure 7.2: Calculated transition intensities for Fe (**A**) and Co (**B**), at $B_z = 6$ T. These transition intensities are calculated from the optimized point charge model for Fe. All transition intensities Y larger than 10^{-3} are shown as solid lines ($u = 0$), the stronger a transition the wider its line and blue and black lines depict the most probable transitions, given that the initial states are occupied. Additionally, all transitions within the lowest $(2S + 1)$ states are shown. (Energies not to scale.)

transitions within the lowest $(2S + 1)$ states are shown even if their intensity is lower than 10^{-3}.

For Fe, the most probable transitions, according to the calculation, are all spin-flip transitions within each of the two spin-multiplets (all blue lines, $Y \approx 1$). The next higher intensity occurs for transitions out of the initial states 2, 3 and 4 into the upper multiplet, although with an order of magnitude

smaller intensity (black lines, $Y \approx 0.07$). Furthermore, a transition out of the ground state to the upper spin-multiplet seems to have a reasonable intensity (gray lines, $Y \approx 0.02$). However, we will show in Section 7.6.1, that the only transitions that we are able to observe in STM, stem from the transitions marked in blue and black. Note that the transition between the ground state 0 and state 1 is extremely rare, indicating a long lifetime from state 1 to 0 (see next chapter).

For the Co atom the main transitions happen between adjacent states (blue lines, $Y \approx 1$). All other transitions are rare. Again, the intensity between state 0 and 1 is very low, indicating a long lifetime of the excited state 1 (see next chapter).

In Sections 7.6.1 and 7.6.2, we will show that some of the rare transitions, such as those marked in black for the Fe atom, are detectable when using a more sensitive probe, i.e. a spin-polarized tip. In the next section, we therefore introduce spin-polarized tunneling.

7.3 Spin-polarized tunneling

Spin-polarized (SP) STM refers to all tunneling processes that use a magnetic tip rather than a normal metal tip (*22*,*23*). For such tunneling, the tip can be coated with a magnetic thin film (*22*,*23*) or, as shown here, it can be built by vertical atom manipulation (*68*) by transferring single magnetic atoms to the STM tip apex (*38*). Having a magnetic tip causes the tunnel junction to behave analogous to a tunneling magneto resistance junction, at the atomic scale, as shown in Figure 7.3. The measured current is high when the magnetic moments of the tip and the surface atom (or thin film) align with each other and is low, when the two magnetic moments are anti-aligned. The example in Figure 7.3 uses a stable anti-ferromagnetic chain of eight Fe atoms to visualize this effect (see more about this experiment in Section 9.1) (*19*). In the next

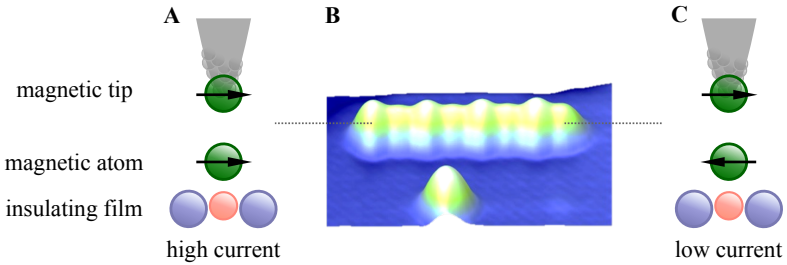

Figure 7.3: Schematics of spin-polarized tunneling. In spin-polarized tunneling a magnetic tip is used to sense the state of the substrate spin. (**A**) When the magnetic moments of tip and surface atom are aligned with each other the current through the tunnel junction is high. (**B**) As it is the case for the left-most atom in the STM topograph of an anti-ferromagnetic chain of eight identical Fe atoms on a Cu_2N surface (*19*)[1]. (These atoms have identical heights when scanned with a non-spin-polarized tip.) (**C**) The current through the tunnel junction is low when the magnetic moments of the tip and surface atom are anti-aligned (e.g. right-most atom in (**B**)).

chapter, we will use this effect to determine spin lifetimes of different states.

Here, we want to focus on conductance ($\mathrm{d}I/\mathrm{d}V$) measurements that use SP tips to probe changes in the occupation of states. The conductance, $\mathrm{d}I/\mathrm{d}V$, not only reflects inelastic spin-excitations (SES with normal (see Chapter 3) and SP tips), but also the change in the occupation of magnetic states (only probed by a SP tip). These conductance contributions are added, leading to extra peaks and troughs at the thresholds of transitions where the occupation of spin states abruptly changes (*38*,*67*). We point out that these spin polarized spectra are current dependent insofar as the tunneling electrons must arrive frequently enough to probe the excited states before their decay (*38*). Changes in occupation toward states that are aligned with the tip spin-polarization contribute to an increased conductance (higher current due to more alignment

[1] From Loth, S. *et al.* Bistability in Atomic-Scale Antiferromagnets. *Science* **335**, 196–199 (2012). Reprinted with permission from AAAS.

of the surface and tip's magnetic moment). Conversely, changes toward oppositely aligned states reduce the conductance. A more detailed description of SP dI/dV thus requires the analysis of the voltage- and current-dependent occupation of the magnetic states.

In the next section, will introduce a set of rate equations of the form of a master equation (*38*), that will allow us to calculate the occupation of states. We will then, later in this chapter, describe the experimental results and compare them to the calculated population of states to find transitions to other orbital states for both Fe and Co on MgO.

7.4 Master rate equation to determine the occupation of states

The occupation of each energy level can be described by considering all excitation and deexcitation rates from and to all other states. The qualitative model described here, is the same as used in (*38*), and has the form of a master rate equation. The change in the occupation $n_i(t)$ of each spin state i is given by the difference of the transition rates into and out of each state.

$$\frac{dn_i(t)}{dt} = \sum_j r_{ij} n_j(t) - r_{ji} n_i(t) \tag{7.2}$$

Here, r_{ji} represents the overall transition rate from spin state i to state j. These transition rates consist of induced excitation, as well as induced and spontaneous deexcitation. We account for four possible contributions in the model (see schematic 7.4):

$t \rightarrow s$: transitions (excitations and deexcitations) due to electrons tunneling from the tip to the sample,

$s \rightarrow t$: transitions (excitations and deexcitations) due to electrons tunneling from the sample to the tip,

$s \rightarrow s$: spontaneous deexcitation due to substrate electrons that tunnel through the MgO, interact with the local spin and tunnel back to the substrate, and

$t \rightarrow t$: spontaneous deexcitation due to tip electrons that tunnel through the vacuum barrier interact with the atom's spin and return to the tip.

All these possible rates are added together to yield the total transition rate:

$$r_{ji} = r_{ji}^{t \rightarrow s} + r_{ji}^{s \rightarrow t} + r_{ji}^{s \rightarrow s} + r_{ji}^{t \rightarrow t} \tag{7.3}$$

The individual transition rates are described by the conventional model for inelastic electron tunneling (*24*) and the transition intensities Y described above. The rates depend on the number of electrons per second that interact with the local atom, which is set by the conductance of the tunnel junction (for $t \rightarrow s$, $s \rightarrow t$ and $t \rightarrow t$) and the conductance through the substrate (for $s \rightarrow s$). We account for the spin-polarization of the tip by letting the density

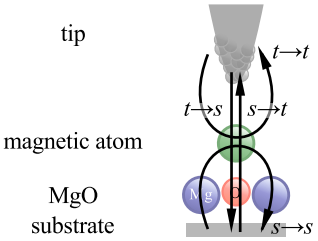

Figure 7.4: Schematics of the different tunneling path. The spin of the magnetic atom can be excited and deexcited by electrons tunneling from the tip to the sample ($t \rightarrow s$) and from the sample to the tip ($s \rightarrow t$). Additionally, electrons tunneling from the substrate (tip) through the atom and back to the substrate (tip) ($s \rightarrow s$, $t \rightarrow t$) can serve as an additional spontaneous deexcitation path.

of spin-up electrons ($|\sigma\rangle = |+\frac{1}{2}\rangle$) be proportional to $\frac{1+\eta}{2}$ (proportional to $\frac{1-\eta}{2}$ for spin-down electrons ($|\sigma\rangle = |-\frac{1}{2}\rangle$)). More details on the rates equations are given in Appendix H.

In order to obtain the population of states at any given voltage we solve these rate equations for their steady-state solution.

7.5 Spin-polarized tunneling methods

We build spin-polarized STM tips by using a reversible transfer of one or several atoms from the sample surface to the tip apex (*38*,*67*). This technique is complementary to the established technique of using magnetically coated STM tips (*22*,*23*). Since different magnetic atoms have a different spectroscopic fingerprint (Chapter 3) we can identify the different adatoms, before transferring them to the tip. We use vertical atom manipulation (*19*,*37*) to pick up individual Fe or Co atoms from the MgO layer to the tip apex. The applied external magnetic field polarizes the tip atom, which results in a net spin-polarization of the density of tip states at the Fermi energy.

For the most successful vertical atom manipulation, we start with a slightly blunt tip, which allows an additional atom to be absorbed at the apex of the tip. On MgO, we start at a typical tunnel junction impedance of 10 GΩ, the tip is then lowered towards the atom until it is close to point contact (about -0.5 nm to -0.7 nm). Subsequently, a voltage pulse of about 0.5 V is applied to the sample with respect to the tip. The tip is then withdrawn while the voltage is still applied before resetting normal imaging conditions (*38*,*67*). Repeating this procedure one or several times results in a spin-polarized tip. We use the long lifetimes of Fe (and Co) to affirm that the tip obtained with this procedure is spin-polarized (see Chapter 8).

We can also reverse this process and drop the magnetic atom from the STM

tip apex. This however, is often less successful than the single atom transfer from the surface to the tip, particularly on the MgO surface. We therefore might have to rely on reconditioning the tip by dipping it into the bare silver substrate. Successful transfers from the tip apex to the surface were obtained by bringing the tip close to point contact with the MgO surface (starting again at 10 GΩ and lowering the tip by about -0.8 nm), while applying a small bias voltage (1 mV).

7.6 Spin-polarized probing of additional states

In this section, we will show the spin-polarized spectra of Fe and Co on MgO. We are particularly interested in the transitions that become visible only when a spin-polarized probe is used and are not observable otherwise.

7.6.1 Transitions to the higher spin-multiplet in Fe

Figure 7.5 A shows the spin-polarized conductance of Fe on MgO. As detailed in Section 7.3, the conductance contributions of the inelastic transitions and of the changes of state occupation are added together. This leads to extra peaks and troughs at the thresholds of transitions, where the occupation of spin states abruptly changes. This is especially visible, when comparing the jagged spin-polarized spectrum shown here to the spectrum taken with a non-spin-polarized tip (see Figure 3.6). The vertical lines in Figure 7.5 A indicate the calculated energies for the V_{01}, V_{02}, V_{13}, V_{04} and V_{14} transitions. Compared to the spectrum with a non-spin-polarized tip, there is a drop in conductance at the V_{01} transition energy. Additionally, there is a faint increase in conductance at the V_{14} transition (marked with blue arrows) which was absent with a non-spin-polarized tip (Figure 3.6 A). (This transition has a finite intensity due to a small tilt in the experimental setup that is not considered in Figure 7.2.) The voltage- and current-dependent changes in the conductance are signatures of spin-pumping (changes in the occupation of

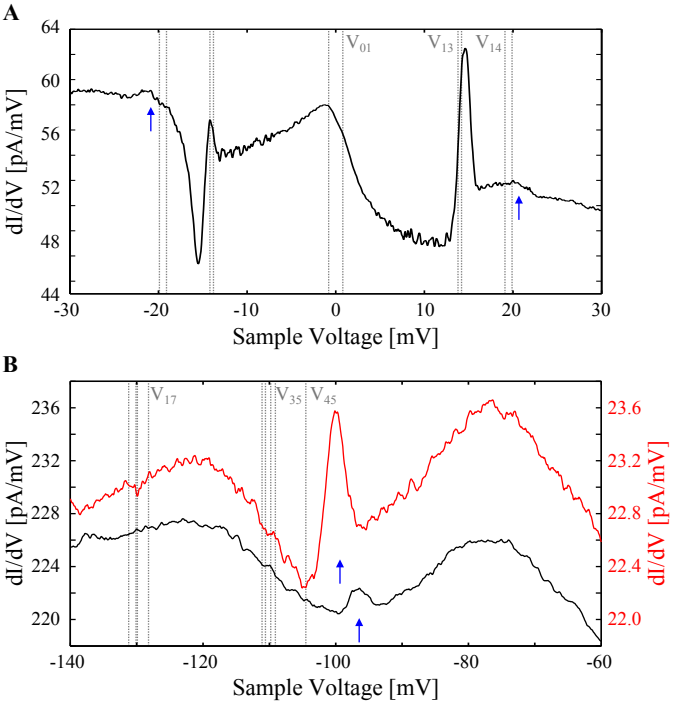

Figure 7.5: Spin-polarized dI/dV spectra of Fe in the range shown before ($\pm$30 mV) (**A**) and around $\sim$100 mV (**B**). (**A**) Spin-polarized spectrum in same energy window as Figure 3.6. (I = 500 pA, V = 10 mV, B = 1.5 T). (**B**) High-energy SES feature (V_{35}) measured with a spin-polarized tip at two different currents, black: I = 5 nA, red: I = 0.5 nA. (V = 30 mV, B = 6 T). All available transitions are indicated with vertical lines in the two panels, the labels correspond to the lowest energy transitions in cases where there are several transitions with similar energies. (T = 1.2 K)

long-lived magnetic states), which will be discussed in more detail in the next chapter.

The spin-polarized STM measurements of dI/dV in the energy range of

transitions from the lower (states 0 – 4) to upper (states 5 – 9) spin-multiplet reveal a change in conductance at $\sim$100 mV (Figure 7.5 B, marked with blue arrows). When using a non-spin-polarized tip, excitations in this energy range were not detectable. In Figure 7.5 B, all transitions energies, as calculated from the point charge model, are marked with gray lines. The additional feature at $\sim$100 mV is lower in energy than all the calculated energies. Despite the slightly different energies between the calculation and the experimental results, we can use the calculated population of states to determine which transition causes the observed additional feature.

In Figure 7.6 we show the calculated voltage-dependent steady-state population of all $2\,(2S+1)$ lowest energy spin states of Fe. The population of each state changes as additional transitions become available. For example, one can see in Figure 7.6 A and C, that the occupation of state 1 (blue curve) slowly increases between about 5–12 mV (both voltage sides). This indicates that state 1 is only populated at voltages larger than the V_{01} threshold. The fact that the population changes only slowly, indicates that the direct transition between states 0 and 1 is rare. At a voltage of $\sim$12 mV the population of state 1 rapidly decreases. This decrease is due to the fact that at 6 T the V_{13} transition becomes available at $\sim$12 mV. At this voltage, the V_{13} transition serves as an additional deexcitation path from state 1 to state 0 via state 3. As a result, the population of state 1 is rapidly decreased. Only at higher voltage, when V_{02} becomes available, does the population of state 1 increase again (via transitions through state 2).

Similarly, the population of other states can be assigned to the available transitions (and their respective intensities) at each specific voltage. In the following, we will focus on the energy range of transitions from the lower (states 0 – 4) to the upper spin-multiplet (states 5 – 9) (Figure 7.6 B). At voltages larger than $\sim$110 mV, the population of all excited states 5 – 9 increases simultaneously. This shows that once the first transition to the upper spin-multiplet is possible, all transitions within that multiplet become

available ($Y \approx 1$ between neighboring states). Thus after the initial transition, all states of the upper spin-multiplet have a non-zero state population. From the simulation, we can conclude that this first available transition is the transition from state 3 to state 5 (V_{35}). Note that the four transitions V_{35}, V_{25}, V_{46} and V_{47} are all nearly equal in energy.

Thus, using the results from the population of states analysis (Figure 7.6 B), we can assign the $\sim$100 mV transition observed in the SP dI/dV spectrum (Figure 7.5 B) to the transition from state 3 to state 5. The energy of the V_{35} transition is calculated as 109 meV at 1.5 T in the point charge model. The transition intensity of this transition is an order of magnitude smaller than the intensity of the V_{02} transition (see Section 7.2). Although this transition intensity would be much too small to readily identify as an inelastic transition with a non-spin-polarized tip, it is evident when detected as a population change with a spin-polarized tip.

Characteristically, the first available transition also reduces the occupation of its initial state (state 3) and distributes this population randomly between all other states. This inherently leads to an increased population of those states that are more aligned with the tip and thus the conductance increases as soon as the voltage is sufficiently large to cause such a transition. Once electrons can be excited to the upper spin-multiplet, they can easily be distributed along all states in that multiplet ($Y \approx 1$ for neighboring states), as discussed above. Thus once a transition to the upper multiplet is possible all other transition from the lower to the upper spin-multiplet become invisible in the experiments, despite, for example, the reasonably high transition intensity of Y = 0.02 between the ground state and state 6.

Note that, consistent with the behavior of the Fe atom under the influence of the STM tip seen in the last chapter, the observed change in occupation of states in the spin-polarized dI/dV in Figure 7.5 B, moves towards lower energies as the tip is brought closer to the Fe atom (as the current increases)

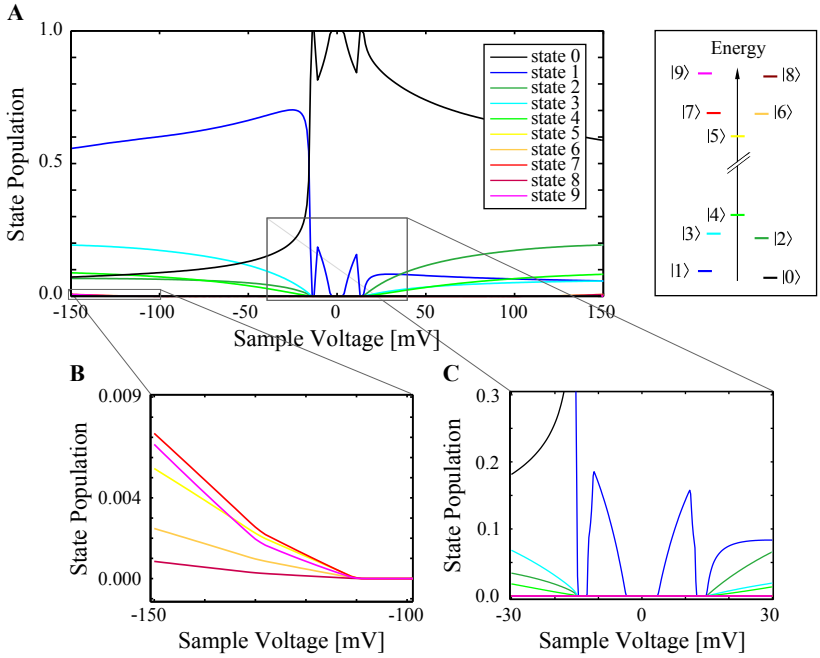

Figure 7.6: Steady-state occupation for states of Fe. Calculated with the master rate equation model, for a junction impedance of V = 10 mV, I = 100 pA. The substrate conductance is set to G_{ss} = 2.5·10^{-5} G_0 (G_0 is the conductance quantum). The tip's spin-polarization is $\eta = -0.3$. (**A**) Steady-state population over a voltage range of $\pm$150 mV. (**B**) Zoom-in to the range of transitions between the lower and upper spin-multiplet. This shows the onset of state occupation in the upper spin-multiplet starting at $\sim$110 mV. (**C**) Occupation of states in the range of the lower spin-multiplet ($\pm$30 mV). (B = 6 T, T = 0.5 K).

(see calculation in Figure G.2). Additionally, the fact that the increase in conductance for the higher current (black curve in Figure 7.5) is smaller than for the low current, indicates that at such high current, the deexcitation due to the tip-to-tip electrons ($t \rightarrow t$) happens at a higher rate than the excitation by

subsequent tunneling electrons.

Transitions between states belonging to different spin-multiplets have been observed in spin chains (e.g. singlet to triplet states) and molecular magnets (*37*,*38*,*69*). Unique to Fe on MgO is the fact that the excitation from the lower to the upper spin-multiplet involves a transition from states where the orbital and spin moments are aligned (lower spin-multiplet) to states where they are anti-aligned (upper spin-multiplet).

7.6.2 Transitions to a different orbital state in Co

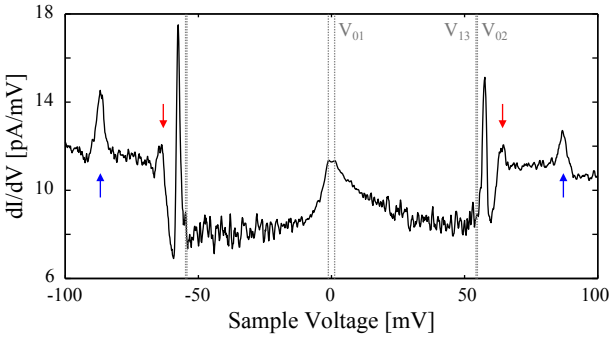

Figure 7.7: Spin-polarized dI/dV spectrum of Co in the same energy window as in Figure 3.7 ($\pm$100 mV). The vertical lines indicate the transitions V_{01}, V_{02} and V_{13} as calculated with the point charge model. Red arrows indicated additional transitions to higher excited states at $\sim$65 mV and the blue arrows indicate transitions to the $\langle L_z \rangle$ = 0 orbital state (see Figure 5.4). (I = 1 nA, V = 100 mV, B = 3 T, T = 1.2 K).

Similarly to Fe, the Co spin-polarized dI/dV spectrum in Figure 7.7 shows multiple conductance changes. Figure 7.7 displays the same energy window as the spectrum recorded with a non-spin-polarized tip shown in Figure 3.7. The known transitions (V_{01}, V_{02} and V_{13}) calculated with the point charge

model are indicated with vertical lines.

In Figure 7.8, we show the calculated occupation of states from the point charge model for Co. Similarly to Fe, additional transitions to even higher excited states can be observed for Co once states 2 and 3 are populated and the voltage is large enough to make the additional transitions possible. Such transitions are, for example, those to states 4 and 5 at ∼65 mV. These changes in the population of states are visible in the spin-polarized dI/dV spectrum (Figure 7.7) as the additional peak-trough combination marked with red arrows.

Strikingly, the spin-polarized spectrum in Figure 7.7 shows additional features at ∼90 mV (marked with blue arrows). Such a transition does not correspond to any transition known in the point charge model (there is no corresponding change in state population at this voltage in Figure 7.8). Nevertheless, the multiplet calculation performed as a fit to the X-ray data clearly showed an additional set of states (red lines in Figure 5.4), with $\langle L_z \rangle = 0$ character. These additional states are roughly at the energies of the observed feature in the spin-polarized spectrum. The observation of these states is quite astounding, as they mainly come into play due to the strong configuration mixing of the Co on the MgO surface. Thus the observation of these states serves as a confirmation that configuration mixing plays indeed an important role for Co on MgO.

Note that the observation of this conductance change around ∼90 mV serves as a further strong confirmation of how well the two experimental techniques, XMCD and STM (together with their theoretical descriptions), agree with each other. Furthermore, tunneling into a state of such different character (meaning a state originating from very different M_L states) is an additional indication on how sensitive a spin-polarized probe can be. The fact that configuration mixing has to be included to explain this change in the occupation of states also shows the limitations of the point charge model as presented so far.

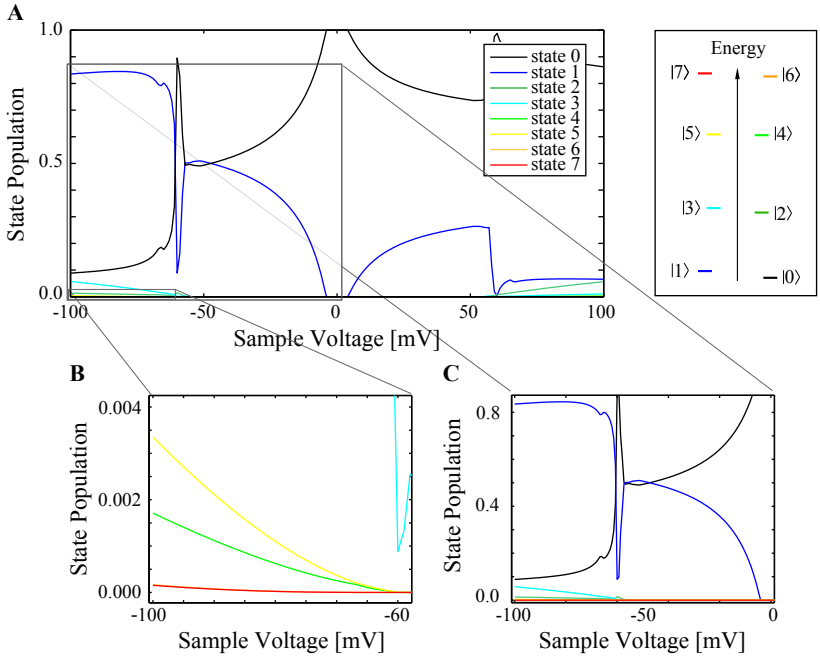

Figure 7.8: Steady-state occupation for states of Co. Calculated with the master rate equation model, for a junction impedance of V = 10 mV, I = 100 pA. The substrate conductance is set to G_{ss} = 2.5·10^{-5} G_0 (G_0 is the conductance quantum, see Section 8.5.1). The tip's spin-polarization is $\eta = -0.3$. (**A**) Steady-state population over the same voltage range as in Figure 7.7. (**B**) Zoom-in to transitions to higher excited states. (**C**) Occupation of states as probed in Figure 8.7 A (Section 8.5.2). (B = 6 T, T = 0.5 K).

Note that in the Co case, the population of states below the zero-field splitting ($V_{02} = V_{13}$) is not symmetric between positive and negative bias. For Fe on the other hand, the population below the zero-field splitting is almost symmetric. This difference stems from the fact that for Fe the transition

between state 0 and state 1 is mainly a ΔM_S = 0 transition while for Co it is a ΔM_S = $\pm$1 transition which is subject to spin-transfer torque (*70*,*71*). We will discuss this effect in more detail in Section 8.5.2.

7.7 Summary on observation of additional orbital states

In this chapter we determined transition intensities for various transitions within the lowest $2\,(2S+1)$ *states of Fe and Co on MgO, using selection rules that only allow the exchange of spin angular momentum between the tunneling electrons and the spin on the surface. We furthermore introduced spin-polarized tunneling and characterized changes in the spin-polarized tunneling spectra as changes in the occupation of states. Using a spin-polarized tip we could identify certain magnetic transitions with much higher sensitivity than with a normal metal tip.*

For the Fe atom, we showed that transitions can be induced from the lower to the upper spin-multiplet, which are transitions from states where the orbital and spin magnetic moments are aligned, to states where they are anti-aligned. In Co, we showed transitions to a set of states that come into play due to the fairly strong configuration mixing (as shown by the XMCD measurements). The observation of the additional transition in Co has two major effects, it serves as a further indication of the striking agreement between STM and XMCD experiments and the multiplet calculation, but it also shows the limitations of the point charge model, which does not include configuration mixing and is thus not able to predict the additional transition.

Chapter 8

Measuring spin lifetimes

In order to achieve stable magnetization of atomic spins for possible applications in electronic devices, it is necessary to reduce their interaction with the environment, while retaining the ability to electrically probe them.

For the results presented in this chapter two manuscripts are in preparation, for Fe: Paul, W., Baumann, S. *et al.* Extremely long lifetimes for single $3d$ transition metal atoms on a surface., and for Co: Baumann, S. *et al.* Controlling the magnetic moment and the lifetime of a single atom by exchange interaction.

8.1 Spin lifetimes

Throughout this thesis we have hinted at the existence of long lifetimes of various excited states for both Fe and Co on MgO. An upper bound of a few minutes for the first excited state was concluded from the magnetization curves in Section 4.4. In this chapter we aim to give a more detailed and thorough description of the different timescales and methods used to probe lifetimes in a scanning tunneling microscope. The lifetime of a magnetic state is defined as the exponential decay time T_1 of a spin starting in an

excited state and relaxing back to thermal equilibrium. In in the limit of small temperature, as in our case, this is almost equivalent to relaxing back to the ground state. In the following we will therefore describe the relaxed state as the ground state rather than as thermal equilibrium. The ability to probe long lifetimes crucially relies on spin-polarized tunneling, which senses the orientation of the surface magnetic moment with respect to the tip moment.

As introduced earlier, achieving stable magnetism on the atomic scale is a long-standing goal motivated by ever-shrinking electronic devices. Sufficiently large magnets have their two oppositely aligned magnetic states well separated by an energy barrier, the anisotropy barrier. In order to change the orientation of such a magnet the energy barrier has to be overcome. However, as magnetic bits (or magnets) become smaller and smaller, quantum mechanical effects, such as tunneling of the magnetization (*1*,*2*), come into play, which can significantly destabilize the states with opposite magnetic moments. Thus to reach the goal of bistability in atomic-scale magnets, quantum tunneling of the magnetization has to be sufficiently suppressed. One successful strategy is to increase the magnetic moment by clustering several spins together. One of the first examples employing this strategy in molecular magnets was Mn-12-acetate (*30*). Another example on a surface is a 5-Fe bi-stable cluster (*20*). A different strategy is to use exchange coupling to stabilize the spins, as shown in the anti-ferromagnetically coupled 12-Fe stable magnetic bit (*19*), see Section 9.1. All three of these examples achieved spin lifetimes of seconds to hours (at cold temperatures). Rather than using several atoms, a different approach to increasing the magnetic moment is to use a single magnetic atom (here we only discuss $3d$ transition metal atoms) and design its ligand symmetry in a manner that retains a large orbital magnetic moment, together with the spin moment. This strategy has so far been used in molecular magnets, e.g. in a linear iron complex (*7*), reaching lifetimes of many milliseconds. Here we have already demonstrated how we can attain large magnetic moments for Fe and Co single atoms on MgO and in this chapter we will now show their long spin lifetimes.

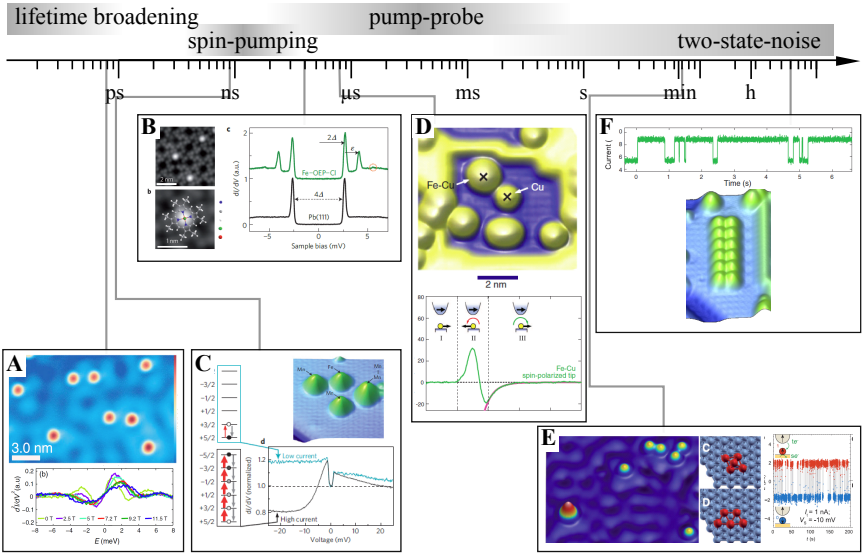

Figure 8.1: Overview over different spin lifetimes and their probing mechanism in STM experiments reported so far for 3*d* transition metal atoms. The images stem from the corresponding papers and their lifetimes are from left to right: (**A**) ∼200 fs, measured by lifetime broadening (*36*)[1], (**B**) 0.5 ns (*38*)[2], (**C**) 10 ns (*62*)[3] both measured by spin-pumping, (**D**) 200 ns (*72*)[4] measured by a pump-probe technique, (**E**) ∼100 s (*20*)[5] and (**F**) several hours (*19*)[6] measured as two-state-noise. (Note that this figure tries to give an overview over some experiments that are possible, it does not attempt to be complete. This figure is based on a slide from Dr. Sebastian Loth, CFEL Hamburg.)

[1] Reprinted figure with permission from Khajetoorians, A. A. *et al.* Itinerant Nature of Atom-Magnetization Excitation by Tunneling Electrons. *Phys. Rev. Lett.* **106**, 37205 (2011). Copyright (2011) by the American Physical Society.

[2] Reprinted by permission from Macmillan Publishers Ltd: Nature Physics (Heinrich, B. W. *et al.* Protection of excited spin states by a superconducting energy gap. *Nat. Phys.* **9**, 765–768 (2013).), copyright (2013)

[3] Reprinted by permission from Macmillan Publishers Ltd: Nature Physics (Loth, S. *et al.* Controlling the state of quantum spins with electric currents. *Nat. Phys.* **6**, 340–344 (2010).), copyright (2010)

The scanning tunneling microscope is an exceptionally powerful tool when it comes to measuring spin lifetimes at the atomic scale. First, it is a tool with outstanding spatial resolution. Secondly, it allows access to timescales over many orders of magnitude (as elaborated below, see Figure 8.1). Thirdly, as we have shown earlier, it allows excitation into specific excited states and thus can probe the relaxation out of known spin states. For many of these time-evolution measurements the STM tip serves as the source of the excitation as well as the probe sensing the decay.

Probing lifetimes larger than milliseconds in a scanning tunneling microscope can be done by directly reading out the variations in tunnel current (two-state-noise), due to the relative alignment of the surface magnetic moment with respect to the tip moment, given that the current is large enough for detection of these variations ($I >$ picoamperes). As the lifetimes decrease and spin dynamics becomes faster, a real-time read-out via the current often becomes impossible because the bandwidth of high-gain current amplifiers, needed for STM, is insufficient to directly access fast relaxations at low tunnel currents. To measure these faster lifetimes in the range of several nanoseconds to milliseconds an all-electrical pump-probe scheme was recently developed at IBM (*72*). As the lifetimes become even shorter than tens of nanoseconds, only indirect measurements such as spin-pumping (*38*) or lifetime broadening of SES transitions (*35*,*36*) are available. See Figure 8.1 for an overview of the different techniques to probe spin dynamics in STM. In the following we will discuss these different measurement techniques for the different time scales in more detail and we will show the lifetimes of Fe and Co on MgO, starting from fast to slow spin lifetimes.

[4] From Loth, S. *et al.* Measurement of Fast Electron Spin Relaxation Times with Atomic Resolution. *Science* **329**, 1628–1630 (2010). Reprinted with permission from AAAS.

[5] From Khajetoorians, A. A. *et al.* Current-Driven Spin Dynamics of Artificially Constructed Quantum Magnets. *Science* **339**, 55–59 (2013). Reprinted with permission from AAAS.

[6] From Loth, S. *et al.* Bistability in Atomic-Scale Antiferromagnets. *Science* **335**, 196–199 (2012). Reprinted with permission from AAAS.

8.2 Probing fast spin lifetimes in STM

8.2.1 Lifetime broadening

The shortest possible lifetimes determined to date in STM experiments are on the order of femtoseconds to picoseconds. On the basis of the Heisenberg uncertainty principle ($\Delta E \Delta t \geq \hbar/2$), the width of the SES excitation becomes broader as its lifetime becomes shorter. Thus lifetime broadening is the first step towards obtaining spin dynamics in STM experiments. The measurement does not require a spin-polarized tip, because the lifetime is determined indirectly via the SES step width. Most of the examples of lifetime broadening involve single magnetic atoms on metal substrates, such as Fe on Cu(111) with $\sim$200 fs (*36*) (see Figure 8.1 A) or Fe on Ag(111) with $\sim$400 fs (*35*).

8.2.2 Spin-pumping

Spin-pumping describes a process where an excited state has sufficiently long lifetime such that it may not have decayed before the arrival of the next tunneling electron. The fact that the state is populated for a significant length of time means that additional transitions to further excited states, as well as the direct sensing of this state's conductance with a spin polarized tip are possible. The process is current-dependent, because the detection is only possible if consecutive tunneling electrons encounter the surface spin in that excited state. At low current the spin has sufficient time to relax back to its ground state and thus no spin-pumping behavior is observable. The onset current for which a change in the excited state population is detected is an indicator of its lifetime. The lifetimes accessible with this technique are in the range of nanoseconds, the typical time between consecutive tunneling electrons at I = 100 pA.

In cases where additional transitions are used to observe the lifetime of an

excited state, spin-polarized tips are not necessary for the detection. Examples of spin-pumping with normal non-spin-polarized tips include a Mn-dimer on Cu_2N (*38*) and paramagnetic Fe-molecules on Pb with a lifetime of $\sim$10 ns (*62*) (see Figure 8.1 B).

However, as shown in the last chapter, the spin-polarized tip can serve as a more sensitive probe for rare transitions by detecting changes in the occupation of states. An example of such spin-pumping measurements that involve additional transitions but use a spin-polarized tip for their detection is shown in the next section.

Lifetimes of excited states as a result of spin-pumping are not always visible as additional transitions, but may be observed as a conductance drop due to current-driven occupation of the excited states. The conductance drop is a consequence of a reduced alignment of the surface magnetic moment with the tip. An example for such spin-pumping behavior was seen for single Mn atoms on Cu_2N with excited state lifetimes on the order of $\sim$0.5 ns (Figure 8.1 C).

8.3 Fast relaxations for both Fe and Co on MgO

Both Fe and Co on MgO, have measurable spin lifetimes at several different time scales. We will show a detailed investigation of the slowest lifetimes, those from state 1 to the ground state, later in this chapter. First, we focus on the observable fast lifetimes, which involve higher excited states (state 2 and above). In Figure 8.2 we show the spin-polarized dI/dV spectra for both Fe and Co in a range of $\pm$200 mV (see also Figures 7.5 and 7.7), with the corresponding level diagram. For both atoms, gray lines at $\sim$4 mV indicate the Zeeman splitting between the ground state and the first excited state and the blue transitions mark the measured SES excitations, V_{13} (and V_{02}) (as seen in Chapter 3). In addition, the orange lines show excitations which occur

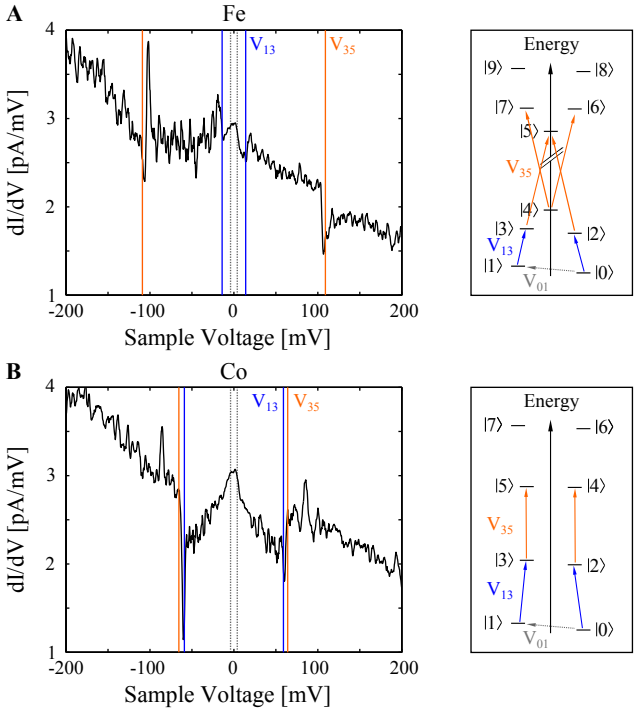

Figure 8.2: Spin-polarized dI/dV spectra and the corresponding schematic drawing of the possible excitations for both Fe (**A**) and Co (**B**). The blue lines mark the SES transitions V_{13} and V_{02}. Orange lines mark those transitions that become available due to spin-pumping (starting from states 2, 3 or 4). Gray lines indicate the transition from the ground state to state 1. We only label the lowest energy transitions (i.e. V_{13} and V_{35}) in the spectra as those are the first observable transitions (see also Sections 7.6.1 and 7.6.2). (V = 100 mV, I = 250 pA, B = 6 T, T = 1.2 K).

out of higher excited states, such as states 2, 3 or 4. We showed in the last chapter that these transitions are only visible with a spin-polarized tip. Their observation is a consequence of spin-pumping and they can only be detected if subsequent tunneling electrons encounter the surface spin in that excited

state. This observation gives a lower bound to the lifetime of the excited state.

The features at $\sim$100 mV (see Figure 8.2 A, orange) for Fe stem from transitions out of one of the excited states, 2, 3 or 4. (In Section 7.6.1, we determined that V_{35} causes the observed change in the population of states.) The energy of these transitions is sufficiently different from, for example, the V_{13} or V_{02} transition energy (blue) to make its detection with spin-polarized tunneling electrons easily distinguishable from other excitations. The observation of these transitions indicates that the lifetime of one or more of the initial states (2, 3, 4) is longer than $\sim$1 ns (the mean time between tunneling electrons at 250 pA) (*38*).

For Co, an additional peak-trough combination at $\sim$65 mV indicates that there are additional transitions out of states 2 or 3, such as V_{35} and V_{24} (see Figure 8.2 B, orange, and Figure 7.7, red arrow), but their energies are too similar to the V_{13} and V_{02} excitation (blue) to resolve their energies reliably (see also Section 7.6.2). Nevertheless, the additional transitions are present, which again means that the lifetime of one or more of its initial states (2 and 3) is longer than $\sim$1 ns. Thus both atoms have excited states with lifetimes longer than 1 ns.

For Fe and Co on MgO we do not observe any examples of lifetime broadened SES transitions, despite the fact that the width of the SES steps is too large to be explained by temperature broadening alone. For example, the fitted step width of the lowest SES transition ($V_{02} = V_{13}$) for Fe at 0 T is 0.7 mV (see Figure 3.6 and Appendix B). A thermally broadened inelastic transition has a width of 5.5 k_BT (*24*), resulting in an effective T = 1.5 K, which is significantly larger than the 0.6 K measurement temperature. On the other hand, lifetime broadening is not expected since the $>$1 ns lifetimes inferred from the spin-pumping measurements imply lifetime broadening of $<$1 μeV. Thus the underlying cause of the broadening is not yet known.

From the spin-polarized spectra, such as Figure 8.2, we can conclude that the lifetimes for some of the higher excited states, such as states 2 and 3, for both atoms, Fe and Co, are in the nanosecond range. These lifetimes are significantly longer than the lifetimes measured for atoms adsorbed directly on metal substrates (*35*,*36*) and they are also longer than the lifetimes of single atoms on other thin insulators seen previously (*38*). The thin MgO layer between the metal substrate and the magnetic atom is thus shown to be a good decoupling film. This is even more evident when measuring the lifetime of the first excited state (1), which we will show in the following.

8.4 Probing slow spin lifetimes in STM

8.4.1 Pump-probe

An all-electrical pump-probe scheme with single-atom resolution has only recently enabled access to the time scales of a few nanoseconds to several hundred milliseconds in STM measurements (*72*). So far, pump-probe experiments in a STM junction have been used to probe the spin lifetime from the first excited state (1) back to the ground state (0). However, a pump-probe scheme could in principle be used to probe the lifetimes of other selected states as well. Examples of pump-probe experiments have shown a lifetime of $\sim$200 ns for a Fe-Cu dimer on Cu_2N (*72*) (Figure 8.1 D) or as shown here, of $\sim$200 μs for Co on MgO (*26*) (see Section 8.5).

The lifetimes from state 1 to state 0 for Fe and Co on MgO were measured with such an all-electrical pump-probe scheme (see Figure 8.3) (*72*). A pump voltage pulse of high enough amplitude (larger than the threshold voltage for spin-excitation) creates a non-equilibrium population in the first excited state 1. Following the pump pulse, the bias voltage is set to zero while the population of states evolves towards equilibrium. After a time delay Δt, a probe pulse of smaller amplitude is used to sense the orientation of the

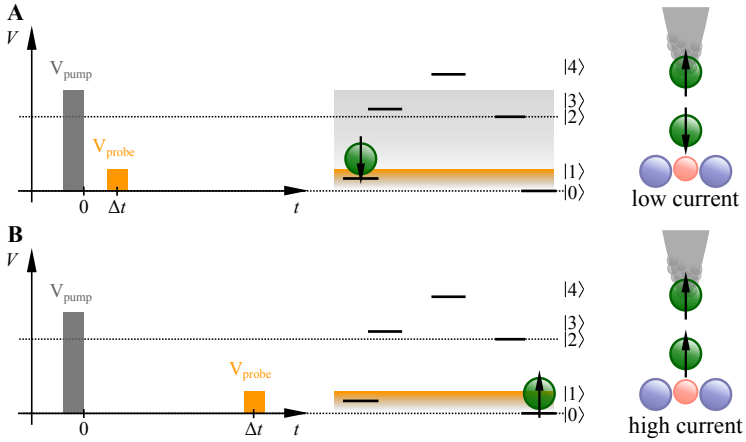

Figure 8.3: Schematic of the pump-probe measurements. (**A**) First, a pump pulse of a voltage larger than the V_{02} threshold is applied, which creates a sufficiently large probability of occupying the first excited state 1 at the end of the pump pulse. Afterward, the voltage is turned off as the spin dynamics proceeds at zero applied voltage. Finally, a probe pulse is applied to sense the state of the system by using a spin-polarized tip. At short time delay Δt most of the population is still in the excited state (anti-aligned with the tip) (**A**). The relaxation process back to the ground state is monitored by repeating these pump-probe cycles with varying time delay of the probe pulse. At long time delay the system is fully relaxed back to the ground state (aligned with the tip) by the time the probe pulse senses the state of the spin (**B**).

magnetic state on the surface. The magnetic state is measured as a function of the delay time Δt between the probe pulse and the preceding pump pulse. These pump and probe cycles are repeated a sufficient number of times at each time delay until an exponential fit to the pump-probe decay signal can be used to determine the lifetime T_1.

The pump-probe signal is modulated at audio frequency ($20 - 900$ Hz) and detected using standard lock-in techniques. For the lifetime data presented

here, a probe-chop technique is used, in which the probe pulses are present at delay time Δt during the first half of each audio cycle, and absent during the second half. We made sure that the measured lifetimes do not depend on variations in the pump or probe voltage, nor on the pump or probe width. However, the setpoint voltage and current (and thus tip proximity) can result in different lifetimes as discussed below.

For the pump-probe amplitude plots, as discussed in Section 8.5.2, a probe-shift technique applies probe pulses at delay Δt during the first half of each audio cycle, and at fixed long delay $\Delta t \gg T_1$ during the second half.

In both cases, the series of pump pulses continues uninterrupted through both halves of the audio cycle and consequently produces no signal at the audio modulation frequency. This way the current due to the pump pulses can be separated from the current due to the probe pulse, which is the desired signal.

8.4.2 Two-state-noise

Spin lifetimes ranging from milliseconds to minutes can be directly detected in the two-state-noise of the tunnel current, when probed with a spin-polarized tip. The surface atom switches between its two oppositely aligned magnetic states slowly enough so that each switching event can be seen as telegraph-noise in the tunnel current. For such measurements a spin-polarized tip is necessary to distinguish between the aligned and anti-aligned magnetic state of the atom with respect to the tip. To determine an quantitative lifetime, many individual switching events have to be recorded to make a histogram of the residence time in each state.

So far there have only been a few examples of small assembled magnets on surfaces that had long enough lifetimes for such two-state-noise behavior to be recorded in STM tunnel junctions. Examples of such systems are

rows of 6 to 12 Fe atoms coupled anti-ferromagnetically to each other on a Cu_2N surface (*19*) (Figure 8.1 F, see also Section 9.1) and clusters of 5 Fe atoms on Cu(111) (Figure 8.1 E). This has to our knowledge not been convincingly shown for single magnetic atoms on surfaces (despite the recent but contested reports on single Ho atoms on Pt(111) (*5*,*73*)). We will show here how a single $3d$ transition metal atom can exhibit such slow switching. Millisecond lifetimes are possible due to the symmetry protected, extremely rare transitions between states 1 and 0 in the case of Fe on MgO.

8.5 Pump-probe on Co on MgO

In this section we will report on the long lifetime of Co atoms on single monolayers of MgO and how the tip proximity can shorten that lifetime significantly. Additionally, we will introduce a way to use the pump-probe scheme to measure the magnetic moment of single atoms on a surface.

8.5.1 Long lifetime

The lifetime T_1 of the Co's excited state 1 is measured with the pump-probe scheme. Two such pump-probe measurements for Co at 3 T are shown in Figure 8.4 for two different setpoint currents. The two traces each show an exponentially changing current over time, which yields the lifetime at that specific tip height. In Figure 8.4 B the tip is 0.2 nm farther away from the Co atom than in A. In these experiments we record the current due to the probe pulse, which we express as the number of electrons per probe pulse. For example, in A the probe voltage is 10 mV with a pump width of 1 μs, which leads to a baseline of 624 electrons per probe pulse when the spin is in the ground state 0 (when the delay time is large). In B the probe pulse is longer to follow the measured lifetime with the tip $\sim$0.2 nm farther away from the

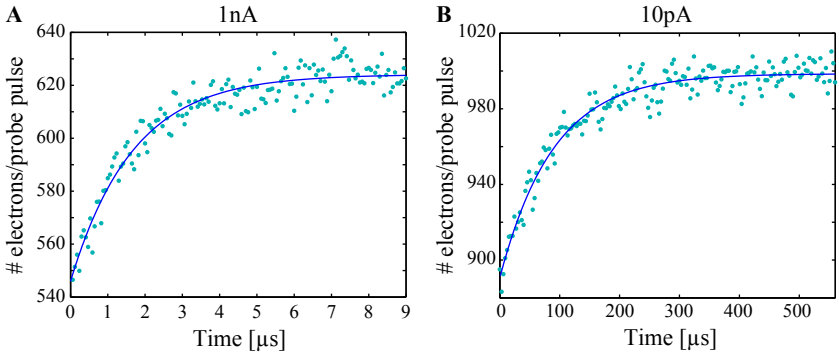

Figure 8.4: Two pump-probe traces of Co at 3 T, at two different tip heights: (**A**) at 1 nA and (**B**) at 10 pA both at 100 mV. The solid line is an exponential fit to the data. The lifetime at 1 nA is 1.7±0.1 μs (**A**) and at 10 pA it is 89.3±3.3 μs (**B**). ($V_{\text{pump}} = -100$ mV, $V_{\text{probe}} = -10$ mV, T = 1.2 K (**A**), 0.6 K (**B**)).

atom, which leads to a different baseline.

The tip at close proximity to the atom leads to a lifetime of 1.7±0.1 μs (A) while the lifetime T_1 for the tip farther away from the atom is 89.3±3.3 μs (B). Thus, in this example, changing the tip height results in a lifetime that changes by almost two orders of magnitude, which means that the STM tip can strongly influence the lifetime from excited state 1 to the ground state 0.

In Figure 8.5 we show the lifetime as a function of applied tunnel junction conductance, i.e. as a function of tip-sample distance. At currents above 100 pA at 100 mV the lifetime rapidly decreases (roughly proportional to $1/I^2$), while at low current the lifetime becomes independent of current. Because the lifetime is independent of external influences such as tip proximity and applied current (at low currents), we conclude that the lifetime in this second regime corresponds to the intrinsic lifetime of the excited state 1. In the following, we will use the term ”intrinsic” only to

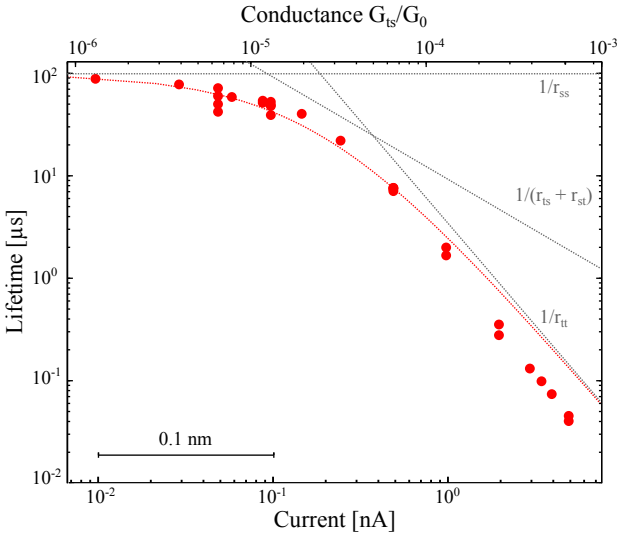

Figure 8.5: Tip height dependence of Co spin lifetime at 3 T. Lifetimes are for zero applied voltage. Setpoint current and voltage are present only to establish the tip height before beginning the measurement. At large tip-atom distance the lifetime is independent of the tip, the lifetime in this regime is therefore the intrinsic lifetime of Co, which is $\sim$90 μs at 3 T. For currents above 100 pA at 100 mV the lifetime rapidly decreases (roughly proportional to $1/I^2$), indicating that the tip electrons become the dominant decay path. Error bars are comparable to symbol size. G_{ts} describes the tunnel junction conductance and G_0 the conductance quantum. (V = 100 mV, V_{pump} = $-$100 mV, V_{probe} = $-$10 mV, T = 0.6–1.2 K).

refer to lifetimes that are independent of the tip height. The intrinsic lifetime for Co on a single monolayer of MgO/Ag(001) is therefore $\sim$90 μs at 3 T.

In the case of magnetic atoms placed near electrodes (here, the Ag substrate and STM tip), spin relaxation can occur through $\Delta M_S = \pm 1,0$ transitions induced by electrons from these electrodes that scatter off the magnetic atom and either tunnel across the junction or return to the original electrode

(see tunneling paths in Section 7.4) (*74*). In the high conductance regime (>100 pA/100 mV), in the example above, the tip-to-tip deexcitation path limits the lifetime. In the model applied here this implies that the decay is proportional to the inverse of the tip-to-tip tunneling rate ($1/r_{tt}$). In the intrinsic lifetime regime on the other hand, the substrate electrons limit the lifetime. Thus the lifetime is equal to the inverse of the substrate-to-substrate tunneling rate $1/r_{ss}$ (we will show later in this chapter an example on how increasing the MgO thickness can change this limit).

We fit the lifetime data as a function of tip-sample conductance G_{ts} (red curve in Figure 8.5), with the following function (a derivation of this function is given in Appendix H.2):

$$\begin{aligned}\tau_{10} &= \frac{1}{r_{ss} + r_{ts} + r_{st} + r_{tt}} \\ &= \frac{1}{\Delta E_{10} \cdot P_{10} \cdot \frac{1}{e^2}\left(G_{ss} + 2\,G_{ts} + \frac{G_{ts}^2}{G_{ss}}\right)}\end{aligned} \tag{8.1}$$

The lifetime depends on the energy difference between states 1 and 0, ΔE_{10}, the normalized transition intensity between these states P_{10}, the conductance through the substrate G_{ss} and e is the elementary charge. At 3 T the energy difference ΔE_{10} is 2.0 meV, as calculated by the point charge model.

Formula 8.1 models the lifetime as a function of current (or tip-sample conductance G_{ts}) with three distinct regimes. At low currents, the lifetime is dominated by the $1/G_{ss} \propto 1/r_{ss}$ conductance and is mostly independent of current. This is the intrinsic lifetime regime. For the opposite extreme, at high currents, the decay is mainly driven by tip-to-tip electrons so the lifetime is proportional to $1/(G_{ts}^2/G_{ss}) \propto 1/r_{tt}$ and is thus inversely proportional to the square of the current (described above as $1/I^2$). The sum of the tip-sample and sample-tip transition rates (proportional to $1/(2\,G_{ts}) \propto 1/(r_{ts} + r_{st})$) only influence the lifetime at intermediate currents. The different tunneling rates balance each other at the intersection between the rates which occurs at

a tip height corresponding to about 130 pA at the given setpoint of 100 mV. We determine the normalized transition intensity P_{10} and the substrate conductance G_{ss} from the fit. The transition intensity from state 0 to state 1 for Co at 3 T as calculated by the point charge model is $0.2{\cdot}10^{-8}$. From the fit we obtain a transition intensity of $(12.7{\pm}2.5){\cdot}10^{-8}$ which is about a factor 50 larger than the calculated value. This agreement is reasonably good given that the point charge model calculation does not include configuration mixing. The conductance G_{ss} obtained from the fit is $(2.5{\pm}0.5){\cdot}10^{-5}$ G_0, where G_0 is the conductance quantum.

Overall, we can conclude that one strategy to increase the spin lifetime of single atoms on surfaces investigated by STM is to decrease the interaction with the tip (until the intrinsic lifetime regime is reached). In Chapter 6 we showed that the magnetic anisotropy of certain single atoms can be increased, when the tip moves closer to the atom. Now we show that, despite the potentially increased magnetic anisotropy, the lifetime of the atom depends more heavily on the quantum tunneling of the magnetization between states 1 and 0 and this quantum tunneling of the magnetization is facilitated by the deexcitation due to tip electrons. Thus, decreasing the interaction of the local spin with the tip increases its spin lifetime.

8.5.2 Measuring the magnetic moment

This section shows how to use the pump-probe scheme to measure the total magnetic moment of an atom in a STM by determining the Zeeman splitting between states 0 and 1. This splitting is not visible directly in SES because the transition intensity between these states is too small.

In Figure 8.6 we show pump-probe traces recorded with two different pump voltage (V_{pump}). Both traces show an identical lifetime of 515±45 ns. Thus the lifetime is independent of the pump voltage, but the pump-probe amplitude

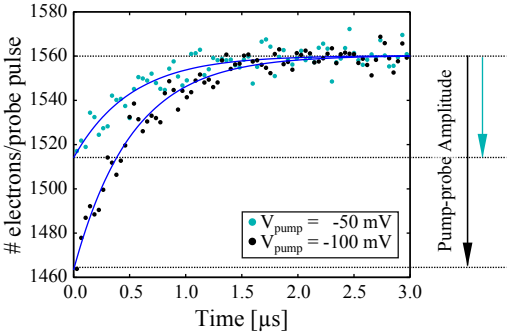

Figure 8.6: Pump-probe traces of Co on a single monolayer of MgO recorded with two different pump voltages (V_{pump}). The lifetimes are almost identical, but the two traces have different pump-probe amplitudes. The lifetime for $V_{\text{pump}} = -100$ mV is 518±21 ns (black curve) and the one for $V_{\text{pump}} = -50$ mV is 512±45 ns (green curve). (I = 5 nA, V = 100 mV, $V_{\text{probe}} = -10$ mV, B = 6 T).

varies between the different traces. Note that the green curve has a pump voltage of -50 mV, which is smaller in magnitude than the SES transition energy of $\sim$60 mV (see Figure 3.7). This is additional evidence that the measured lifetime is indeed the lifetime of state 1 since it cannot involve any higher excited states at this low pump voltage.

To conclusively determine which state gives rise to the long lifetime signals observed here, we measured the amplitude of the pump-probe signal as a function of pump voltage (Figure 8.7), which shows an onset of the signal at -59 ± 2 meV (A) and another sharp onset at 1.9 ± 0.1 meV (B). The first threshold is in good agreement with V_{02} and indicates when state 1 can be reached via state 2. The 1.9 meV threshold corresponds to the direct excitation $0 \rightarrow 1$, which is in agreement with $V_{01} = 2(\langle L_z \rangle + 2\langle S_z \rangle)\mu_{\text{B}} B$ calculated from the multiplet and the point charge model at 3 T, demonstrating that we are indeed measuring the lifetime of state 1. This Zeeman splitting yields a total magnetic moment of 5.5 ± 0.3 $\mu_{\text{B}} B$, which matches the magnetic moment

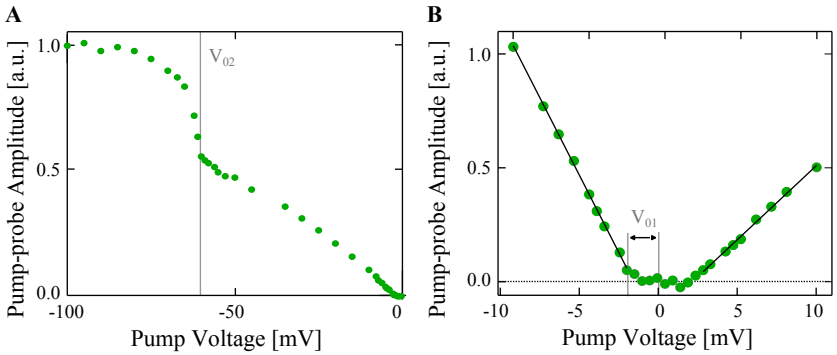

Figure 8.7: Pump-probe signal amplitude at 3 T as a function of pump voltage. The vertical line at -59 mV in (**A**) shows the transition seen in the dI/dV spectra (Figure 3.7). (**B**) Pump-probe amplitude for a smaller range of pump voltages. Linear fits (black lines) extrapolate to -2 ± 0.1 mV and $+1.8\pm0.2$ mV at zero amplitude. Error bars are comparable with symbol size. (I = 500 pA, V = 100 mV, $V_{\text{probe}} = -10$ mV, T_1 = 7.6$\pm$0.1 ms).[1]

determined from the XMCD measurements (Figure 4.3 B), including the large orbital moment.

The 1.9 mV threshold in the pump-probe amplitude proves that direct transitions from state 0 to state 1 are possible if the tunneling electron have sufficient energy. However, the pump-probe amplitude increases slowly with increasing pump voltage indicating that this transition is rare. The small but sufficient mixing of the lowest energy states with other excited states allows the coupling of states 0 and 1 by a $\Delta M_S = \pm 1$ spin-flip transition, which can explain the observed quantum tunneling induced via substrate and tip electrons. We note that the difference in the slope of the signal at positive versus negative pump voltage is due to the spin-polarization of the tip. The spin-polarization

[1] From Rau, I. G., Baumann, S. *et al.* Reaching the magnetic anisotropy limit of a 3d metal atom. *Science* **344**, 988–992 (2014). Reprinted with permission from AAAS.

is a result of an imbalance of spin-up versus spin-down electrons in the density of states of the tip and thus transitions using the majority spins are more likely than their counterparts, due to spin-transfer torque (*70,71*). For example, for Co on MgO the excitation from state 0 to 1 changes the surface spin by $\Delta M_S = -1$, while the spin of the tunneling electron changes by $\Delta\sigma = +1$. If there are more spin-up electrons in the tip such a transition is more likely when tunneling from the sample to the tip (negative voltage side) than when tunneling from the tip to the sample (positive side) (see Figure 8.8).

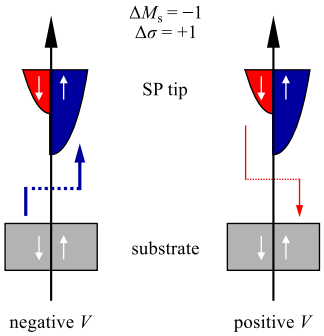

Figure 8.8: Schematic representation of the effects of spin-transfer torque. If the tip is spin-polarized with more spin-up than spin-down electrons, then a $\Delta\sigma = +1$ spin-flip of the tunneling electron is more likely when tunneling from the sample to the tip (negative voltage side) than when tunneling from the tip to the sample (positive voltage side). This explains the different slopes for positive and negative voltage in Figure 8.7 B, since for Co the transition between state 0 and 1 is a $\Delta M_S = -1$ transition (thus $\Delta\sigma = +1$).

We have shown here that we can probe the lifetime of the first excited state, which is true also for pump voltages above the SES transition of ∼60 mV. This also means that the measured pump-probe amplitude, as shown in Figure 8.7, is proportional to the voltage-dependent population of state 1. Thus the amplitudes in Figure 8.7 can be directly compared to the population of state

1 as shown in Figure 7.8 C (blue trace). Here we probe this population after a short time delay which allows all other states to decay back into the two lowest lying states (states 0 and 1).

This technique allows one to measure the magnetic moment of a single atom with the STM. Thus with this method we extend the capabilities of the STM to probe magnetic properties. This can be useful in cases where XMCD measurements are not available, or where high spatial resolution is necessary, e.g. to distinguish the magnetic behavior of atoms on different binding sites or more generally to distinguish individual magnetic nanostructures on a surface.

8.5.3 Magnetic field dependence

In this section we show the influence of an external magnetic field on both the magnetic moment and the lifetime of the excited state 1. First, we demonstrate that the measured Zeeman splitting (V_{01}) changes linearly with magnetic field. Secondly, we will introduce the complex behavior of the Co lifetime as a function of magnetic field.

In Figure 8.9 we show the measured low energy threshold as a function of magnetic field. Measuring the magnetic moment, equivalently the V_{01} threshold, requires small tip-sample distances, due to signal-to-noise reasons, and a sufficiently large energy splitting. Therefore, when determining the threshold as a function of external magnetic field (Figure 8.9 A) we used a current of 3.5 nA at 100 mV. This close tip proximity results in a lifetime of 99$\pm$2 ns at 3 T, meaning that the lifetime is strongly shortened by the influence of the tip.

For such high currents (close proximity of the tip to the atom) the pump-probe signal reverses its sign at low external B-field, see Figure 8.9 B (black curve). The fact that the pump-probe signal becomes positive indicates that

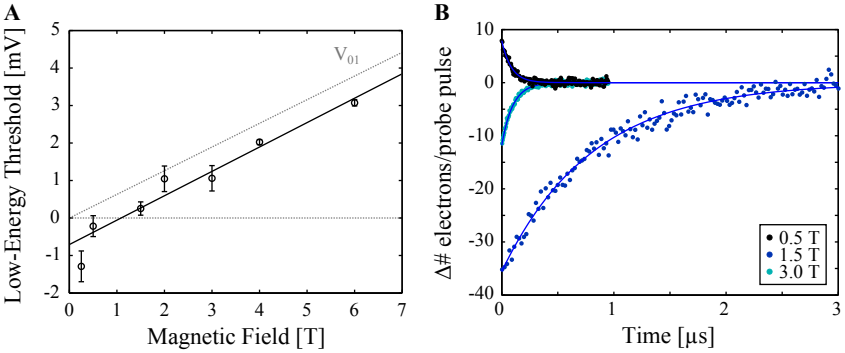

Figure 8.9: Magnetic field dependence of the low-energy threshold (V_{01}) and lifetime, measured at 3.5 nA, 100 mV. (**A**) Threshold as a function of magnetic field. The slope of the fitted line (black) corresponds to $2(\langle L_z\rangle + 2\langle S_z\rangle)\mu_B B$ = 5.6 $\mu_B B$. The gray line indicates the calculated energy $2V_{01}$ as a function of external magnetic field. (**B**) Lifetime for three different magnetic fields. The lifetime is 99±2 ns at 3 T, 808±19 ns at 1.5 T and 85±3 ns at 0.5 T (fitted line in blue). Note that the sign of the pump-probe signal for the lowest B-field is reversed (black curve) and that the longest lifetime is the one at 1.5 T. (V = 100 mV, $V_{\text{pump}} = -100$ mV, $V_{\text{probe}} = -10$ mV, T = 1.2 K).

the measured decay happens from a state that is more aligned with the tip magnetic moment to a state that is less aligned. This suggests a reversal in energy of the two lowest lying states. This reversal is represented in the threshold measurement in Figure 8.9 A, by a negative signal (negative V_{01}) at small external fields (the threshold crosses through zero at about 1 T).

The linear fit in Figure 8.9 A (black line) corresponds to a slope of $2(\langle L_z\rangle + 2\langle S_z\rangle)\mu_B B$ = 5.6 $\mu_B B$, which is similar to the slope for the magnetic moment based on $\langle L_z\rangle$ = 2.91 and $\langle S_z\rangle$ = 1.27 from the multiplet calculation (gray line). The linear fit gives a V_{01} threshold that is zero at ∼1 T. At 1 T we were not able to measure any pump-probe signal for a 3.5 nA current, which further confirms such a cross-over.

An inversion of the pump-probe signal can be observed when the magnetic moments of the atom and the tip are coupled anti-ferromagnetically. Indeed, a similar behavior has been seen very recently for chains of 3 Fe atoms on Cu_2N (*75*). In the three-atom chains the exchange interaction between the tip and the local atom acted analogously to a local magnetic field that could be tuned to several Tesla. In our experiments, the cross-over of the pump-probe signal and the measured V_{01} threshold indicate a similar behavior, where at close tip-sample distance (3.5 nA at 100 mV) the tip acts as an additional local magnetic field of about 1 T, pointing in the opposite direction of the external magnetic field. Note that this is not a real magnetic field, but rather the exchange interaction acting on the atom to give the same effect as a magnetic field.

The offset of the low-energy threshold in magnetic field (Figure 8.9 A) clearly emphasizes the strong effect of the tip on the magnetic atom. It also serves as another indication that the lifetime at such small tip height is expected to be extremely different from the intrinsic lifetime of the system (see Figure 8.5). This is also visible in Figure 8.9 B, where we show three pump-probe curves at different external magnetic fields, all recorded at the same tip height (3.5 nA at 100 mV). It is interesting to note that the lifetime at 1.5 T is an order of magnitude longer than at 3 T. The lifetime is 99 ± 2 ns at 3 T, 808 ± 19 ns at 1.5 T and 85 ± 3 ns at 0.5 T. Thus these lifetimes vary by about a factor of 10. At this point it is not well understood what causes these variations in lifetime as a function of magnetic field.

In Figure 8.10 we show the magnetic field dependence of the lifetime at eight different tip heights (represented as different currents), most of which are in the regime of strong tip interaction. All tip heights are set at 100 mV. The yellow curve corresponds to the current used in the magnetic field-dependent threshold measurement (3.5 nA, see Figure 8.9). The black curve corresponds to a current of 100 pA, which is roughly at the intersection of the intrinsic lifetime regime with the regime where the tip dominates the lifetime. The

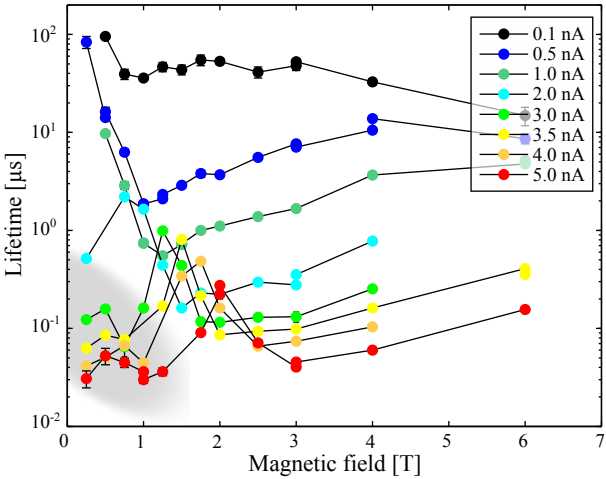

Figure 8.10: Magnetic field dependence of the Co lifetime at eight different tip heights on one monolayer of MgO. The tip height is set by different currents each at 100 mV. All traces where the pump-probe signal is inverted (positive) are marked by a gray area. Error bars are comparable to symbol size. (V = 100 mV, $V_{\text{pump}} = -100$ mV, $V_{\text{probe}} = -10$ mV, T = 1.2 K).

intrinsic lifetime of Co (or here the lifetime at 100 pA and 100 mV) on a single monolayer of MgO on Ag seems more or less constant over a wide range of external magnetic fields. Nevertheless, at low field the lifetime increases. For all other currents one can observe a similar significant peak in lifetime occurring at higher and higher magnetic field as the current increases. At smaller magnetic fields (smaller than the clear maximal lifetime) the pump-probe signal inverts (gray area). We thus assume that the lifetime of Co increases significantly when the effective magnetic field at the atom (combination of external field and field due to the exchange interaction with the tip) is close to zero, meaning that states 0 and 1 are nearly degenerate. This is confirmed by the lifetime at large tip-sample distance (at 10 pA and 100 mV) of 232$\pm$17 μs at 1 T, compared to 89 $\pm$3μs at 3 T (Figure 8.4 B).

Some open questions remain for the magnetic field dependence of the lifetime of Co on MgO especially for the regime of strong tip-atom interaction (e.g. why is the lifetime at 3.5 nA and 100 mV so much longer at 1.5 T than at both at 3 T and 1.25 T). A similar question is why the lifetime at all tip heights seems to get longer at low effective magnetic field. We would like to note that the magnetic field for all results in this chapter is aligned at $\sim 10^{\circ}$ away from the surface normal, i.e. away from the Co atom's easy axis. This tilt might be the cause of some of these processes as more mixing between states can be induced. A more detailed understanding of the decay processes that govern the lifetime of Co is beyond the scope of this thesis.

In summary, we can conclude that increasing the tip-to-atom distance increases the spin lifetime, independent of external magnetic field. This is true up to a certain limit, where the intrinsic lifetime is reached.

8.6 Extremely long lived states of Fe on MgO

In this section we will show that Fe indeed has an extremely long lifetime and also that thicker magnesium oxide decouples the magnetic atoms more from the metallic substrate, which lengthens their spin lifetime.

8.6.1 Two-state-noise

We have noted earlier that observing the switching of small magnetic structures directly in the tunnel current is only possible if the lifetime of the single atom or arrangement of atoms on the surface is long. In Figure 8.11 A we present a current trace of a single Fe atom on two monolayers of MgO at 5 T. In this two-state-noise example the ground state is occupied 91.3% of the time, while the excited state 1 is only occupied for 8.7%, as shown in the histogram of the state occupation in Figure 8.11 B. The analysis of the switching events

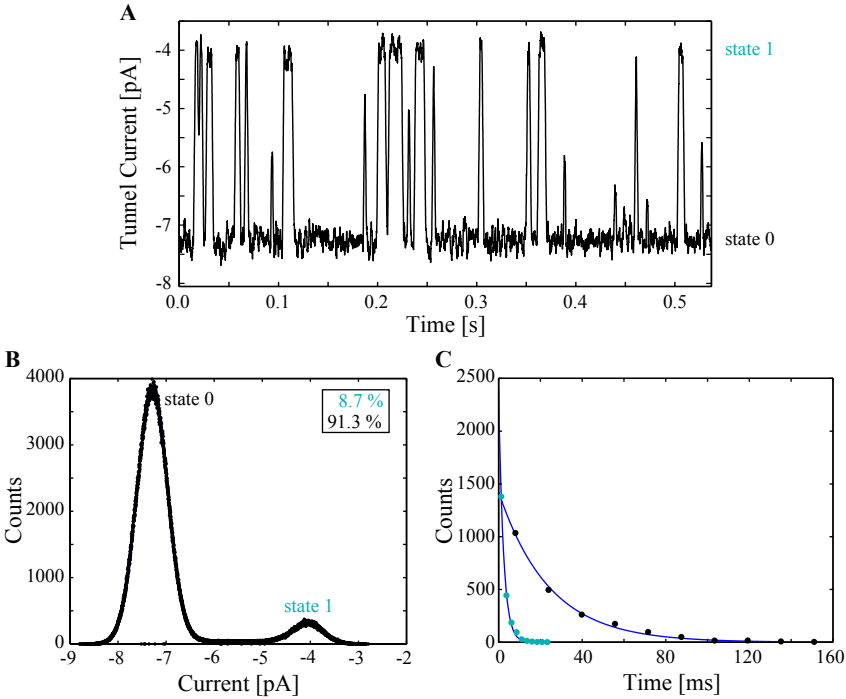

Figure 8.11: Two-state-noise trace on Fe on 2 monolayers MgO. (**A**) Section of a 60 s long recording of telegraph noise on a single Fe atom. Histograms of state occupation (**B**) and time in each state (**C**). At these tunneling conditions the excited state 1 is occupied for only 8.7% of the time. The lifetime of state 1 is 2.30±0.08 ms, while the mean time in the ground state 0 is 24.09±0.92 ms. (V = 10 mV, I = 7.5 pA, B = 5 T, T = 1.2 K).

reveals a lifetime of the excited state of 2.3±0.1 ms at 7.5 pA and 10 mV, while the lifetime of the ground state, the high current state, is 24±1 ms.

Similar to the Co atom, the lifetime of Fe is extremely sensitive to external influences, such as tip proximity and current. Thus the measured lifetimes

vary between several tens of microseconds (at small tip-sample distance) up to several milliseconds. In the following we will limit the discussion to lifetimes in the intrinsic lifetime regime (meaning the plateau seen in Figure 8.5). The lifetimes were primarily determined by pump-probe measurements. The purpose of showing the two-state-noise trace here is to provide a more direct and visual representation of the long lifetime. It also demonstrates that long lifetimes are possible even in the presence of an applied voltage.

8.6.2 Different MgO thickness

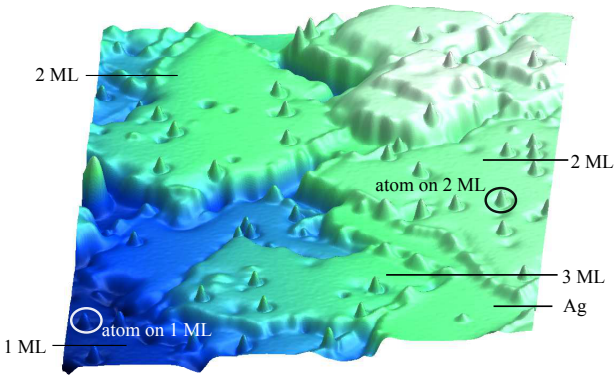

Figure 8.12: STM topograph (31.5 x 46 nm^2) of single Fe atoms on zero to two monolayers of MgO on Ag(001). Different thickness of layers are marked, so are the two atoms used for pump-probe measurements. (V = 150 mV, I = 3 pA, T = 1.2 K).

In Figure 8.12 we show a STM image of an area with MgO thickness varying between zero and three monolayers. The two atoms for the following lifetime comparison are circled.

In Figure 8.13 we show two lifetime traces, on one (Figure 8.13 A) and two

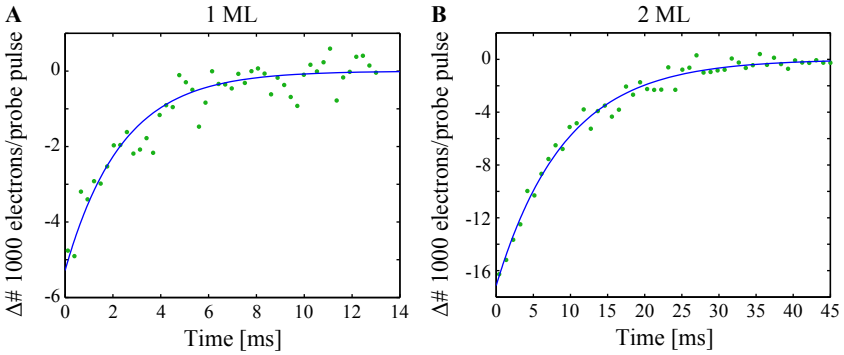

Figure 8.13: Spin lifetime measurement on Fe on 1 and 2 monolayers of MgO. (**A**) The lifetime on one monolayer is 2.87±0.30 ms. (**B**) The lifetime on 2 monolayers is 9.17±0.40 ms. (V = 10 mV, I = 1 pA, V_{pump} = −150 mV, V_{probe} = 10 mV, B = 4 T, T = 1.2 K).

(B) monolayers of MgO. Both lifetimes are recorded at the same tip height (1 pA at 10 mV), which in both cases gives the intrinsic lifetime of Fe, as the tip is far enough away from the atom (despite the fact that in the two monolayer case the tip is actually 0.1 nm closer to the atom due to the added insulating layer). The T_1 time on a single monolayer of Fe is 2.9±0.3 ms, while on two monolayers it is 9.2±0.4 ms. Thus the lifetime increases by roughly a factor of 3 when the coupling to the metallic substrate is reduced by increasing the MgO thickness.

Decreasing the coupling from the substrate also increases the lifetime and is an additional important strategy in the design of future nanometer-sized magnets. However, we note here that the ability to electrically probe these intrinsic single atom lifetimes is difficult to retain as the thickness of the decoupling layer is increased.

8.7 Summary on spin lifetimes

In this chapter we introduced different methods to measure the lifetime of single magnetic atoms and nanostructures with a STM. Using a pump-probe scheme and even direct observation of two-state-switching, we measured the longest lifetimes of single 3d transition metal atoms on a surface observed so far. We found an intrinsic lifetime of ∼2.5 ms for Fe and ∼200 μs for Co, both on a single monolayer of MgO. In this chapter we also offer two different strategies to increase the lifetime of single atoms: first, by reducing the interaction with the tip, and second, by introducing an additional MgO layer to decrease the interaction with the substrate. The second strategy lead to Fe lifetimes of ∼10 ms on two monolayers of MgO. Furthermore, we used the pump-probe scheme to measure the magnetic moment of Co on this surface and found good agreement between the measurement and the theoretical results. This enables the STM to obtain the value of the magnetic moment independent of XMCD measurements.

Whether a spin lifetime of 10 ms is long enough to call it stable magnetism on the atomic scale is left up to the reader, but the results presented here (and throughout this thesis) offer a strategy, based on symmetry arguments and careful tailoring of the interaction with the environment, for the rational design of nanoscopic permanent magnets and single atom magnets.

Chapter 9

Further projects

This thesis has focused on the results on magnetic atoms on MgO, as measured with STM and XMCD and calculated with DFT, a multiplet calculation and a point charge model. In addition, during my PhD there were a couple other projects, apart from the main MgO results, that we want to highlight in the next few paragraphs. Those four additional projects involve:

(i) Stable anti-ferromagnetic chains of Fe atoms on Cu_2N (published in Science 2012 (*19*)),

(ii) Measurement of the MgO thickness with AFM and STM (published in ACSNano 2014 (*10*)),

(iii) Manipulation and sorting of chiral molecules on Cu(111) (under review at NanoLetters (*76*)), and

(iv) A movie made with atoms: '*A Boy and his Atom*' (published 2013 (*77*))

In the following, we will introduce each project with a summary paragraph and will then attach the corresponding papers (if applicable) for a more detailed description of the work.

9.1 Stable anti-ferromagnetic Fe chains

The goal of long lived atomic-scale magnets can not only be achieved by careful design of the symmetry environment of single atoms but it can also be attained by coupling several atoms together. We brought this to an extreme by building arrays of Fe atoms on a Cu_2N surface that are stable for hours at low temperature. The Fe atoms on this surface couple anti-ferromagnetically forming stable Néel states.

An example of a row of 8 Fe atoms is shown in Figure 7.3, where one can see how the anti-ferromagnetic arrangement causes the conductance through such a system to alternate between high and low (aligned and anti-aligned with the tip), when the tip is spin-polarized. The anti-ferromagnetic coupling has the consequence that these structures have no net magnetic moment. However, despite this lack of magnetic moment, we could show that they can serve as stable classical magnets (at low temperature) when only a few atoms are coupled together. Thus for attaining stable magnetism in small structures large magnetic moment is not always necessary, as coupling between atoms can suppress quantum tunneling of the magnetization sufficiently to give the larger structures magnetic bistability. Indeed, for some smaller structures we could observe quantum tunneling of the magnetization (e.g. rows of 6 Fe atoms).

In addition, we showed that we can switch between the stable Néel states by applying small voltage pulses and that these structures remain stable also without an externally applied magnetic field. Furthermore, due to the lack of net magnetic moment these structures can be packed closely together. We even created a byte that can store information for several hours by arranging eight arrays of 2 x 6 Fe atoms, demonstrating that atomic-scale structures could potentially be used in future storage devices.

From Loth, S. *et al.* Bistability in Atomic-Scale Antiferromagnets. *Science* **335**, 196–199 (2012). Reprinted with permission from AAAS.

Bistability in Atomic-Scale Antiferromagnets

Sebastian Loth,[1,2]* Susanne Baumann,[1,3] Christopher P. Lutz,[1] D. M. Eigler,[1] Andreas J. Heinrich[1]*

Control of magnetism on the atomic scale is becoming essential as data storage devices are miniaturized. We show that antiferromagnetic nanostructures, composed of just a few Fe atoms on a surface, exhibit two magnetic states, the Néel states, that are stable for hours at low temperature. For the smallest structures, we observed transitions between Néel states due to quantum tunneling of magnetization. We sensed the magnetic states of the designed structures using spin-polarized tunneling and switched between them electrically with nanosecond speed. Tailoring the properties of neighboring antiferromagnetic nanostructures enables a low-temperature demonstration of dense nonvolatile storage of information.

Nanometer-scale ferromagnets are used as magnetic bits to hold information in mass storage devices. Antiferromagnets have been difficult to switch and sense because of their lack of net magnetic moment, but they offer advantages such as insensitivity to magnetic fields.

In ferromagnetic materials, the magnetic moments of the constituent atoms align, yielding a net magnetic moment. The direction of this magnetization can be changed by the application of a magnetic field or by spin-polarized currents (*1*). As magnetic devices shrink toward atomic dimensions, new tools to fabricate and probe them with atomic resolution are emerging (*2*–*4*). These have revealed magnetic bistability in ferromagnetic islands (*5*, *6*) and chains (*7*), having as few as 30 atoms, as well as in metal-organic molecules (*8*–*10*).

Antiferromagnets have neighboring atoms with counteraligned magnetic moments. The absence of a net magnetic moment makes imaging the magnetic structure of antiferromagnets more difficult. Antiferromagnetic (AFM) domains in thin films have been imaged using x-ray scattering (*11*). On the atomic scale, the spin structure of antiferromagnets has been observed by scanning tunneling microscopy (*12*, *13*) and atomic force microscopy (*14*). So far, controlled switching of antiferromagnets has required the help of nearby ferromagnetic domains (*15*), magnetoelectricity (*16*), or optical pulses (*17*). We investigated the role that AFM nanostructures can play as candidates for magnetic storage and spintronic devices.

We assembled AFM nanostructures with a low-temperature scanning tunneling microscope (STM) by placing Fe atoms in a regular pattern on a surface (Fig. 1A). The spins of neighboring Fe atoms couple antiferromagnetically by an exchange interaction with strength J = 1.2 meV (*18*) (fig. S1). The Fe atoms were placed at a binding site on a Cu_2N surface, for which Fe has a large magnetic anisotropy field that aligns its spin to the resulting easy axis (*19*). A magnetic field of up to 6 T was applied in order to make the microscope's tip spin-sensitive by polarizing its magnetic apex (*18*) and in order to test the effect of magnetic field on the nanostructures.

In assemblies of just a few magnetic atoms, the atomic spins often couple to form quantum superposition states (*20*). For AFM coupling, this results in a singlet ground state, characterized by a wave function in which all spins populate opposing spin states equally (*21*). In contrast, we find that isolated AFM structures with as few as six Fe atoms exhibit stable Néel states, in which the spin orientation alternates between neighboring atoms. These states can be well described by the classical Ising model (*22*), in which the spins always point along one axis. Spin-polarized STM images of a linear eight-atom chain (Fig. 1, B to E) can clearly distinguish the two Néel states. The spin-polarized STM tip forms a magnetic tunnel junction in which the conductance alternates between high (parallel alignment of tip and sample spins) and low (antiparallel alignment) as the tip passes from atom to atom along the chain (*12*, *13*, *23*). Identical chains built from Mn atoms do not show the magnetic bistability and do not exhibit a spin-polarized contrast along the chain (fig. S2). A key difference between Fe and Mn chains is the strength of the magnetic anisotropy, which is ~50 times stronger in Fe than in Mn on this surface (*19*). The strong easy-axis anisotropy of Fe evidently stabilizes the two Néel states as observable magnetic states.

The stability of the magnetic states was not affected by imaging them using an applied voltage of <2 mV, but voltages in excess of ~7 mV caused switching. To intentionally switch the magnetic state of the entire antiferromagnet, the tip was held stationary over any Fe atom of the structure, and tunnel current was passed through it at >7 mV until a step, indicating a change in magnetic state, was observed in the current (Fig. 2A). Subsequently, the voltage was lowered to prevent further switching. Near the 7-mV switching threshold, the Néel state in which the spin of the atom

[1]IBM Research Division, Almaden Research Center, 650 Harry Road, San Jose, CA 95120, USA. [2]Max Planck Research Group–Dynamics of Nanoelectronic Systems, Centre for Free-Electron Laser Science, Hamburg, and Max Planck Institute for Solid State Research, Stuttgart, Germany. [3]Department of Physics, University of Basel, Klingelbergstrasse 82, 4056 Basel, Switzerland.

*To whom correspondence should be addressed. E-mail: heinrich@almaden.ibm.com (A.J.H.); sebastian.loth@mpsd.cfel.de (S.L.).

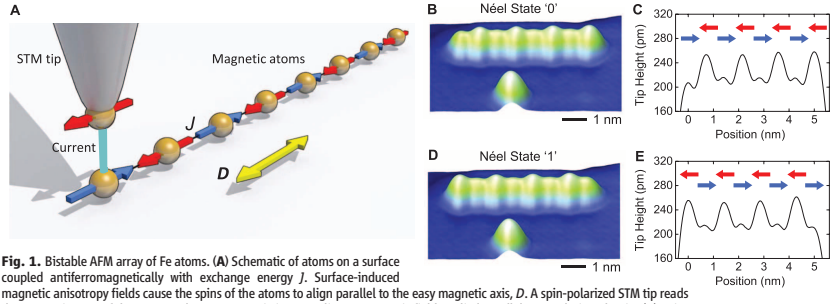

Fig. 1. Bistable AFM array of Fe atoms. (**A**) Schematic of atoms on a surface coupled antiferromagnetically with exchange energy J. Surface-induced magnetic anisotropy fields cause the spins of the atoms to align parallel to the easy magnetic axis, D. A spin-polarized STM tip reads the magnetic state of the structure by magnetoresistive tunneling. A magnetic field applied parallel to D polarizes the tip. (**B**) Spin-polarized STM image of a linear chain of eight Fe atoms assembled on a Cu_2N overlayer on Cu(100). This is a constant-current image using 2 mV and 1 pA. Spins are in Néel state 0. (**C**) Section through center of chain in (B) with the spin orientation of each Fe atom indicated by colored arrows. (**D** and **E**) Same as (B) and (C) but in Néel state 1.

under the tip is aligned with the magnetic field was occupied ~90% of the time (Fig. 2A). This directionality offers a path toward controlled directional switching. An alternative process to switch AFM structures, the use of spin transfer torque (*1*, *5*), has previously been proposed (*24*, *25*).

We found that the state switched most readily when the tip was placed over an end atom of a chain. The switching between magnetic states was found to occur stochastically, with a uniform probability per unit of time, which we characterized by means of a switching rate (*18*) (fig. S3). This rate increased rapidly when the tunneling current was increased.

With increasing voltage, the switching rate exceeded the bandwidth of the STM's current amplifier, so a pulsed-voltage scheme was used to determine the fast switching rates (Fig. 2B). Submicrosecond pulses were applied to the junction (*26*), and each pulse was followed by a low-voltage window in which the resulting magnetic state was detected (*18*). The switching rate increased faster than in proportion to the voltage up the highest voltage tested, with switching times of ~20 ns at 0.5 V (Fig. 2C). This demonstrates electrical switching of the AFM nanostructures at high speeds and femtojoule energies.

To investigate the stability of the Néel states, we examined the thermal switching rates of linear chains of Fe atoms with varying length, (1×*n*), and arrays of two coupled chains, (2×*n*) (Fig. 3). All structures containing eight or more atoms were found to be stable at the lowest temperature, 0.5 K. Spontaneous flipping between the two Néel states sets in with increasing temperature. Structures with more atoms remain stable to higher temperatures (Fig. 3, A to C) (*6*, *27*).

Above ~5 K, the switching rates of the (1×6), (1×8), and (2×6) arrays follow the Arrhenius law with comparable spin reversal barriers, $E_B \sim 7$ to 12 meV, and exponential prefactors, $\rho_0 \sim 10^8\ s^{-1}$ (Fig. 3E and table S1). This prefactor falls in the typical range, 10^7 to 10^{14}, found for ferromagnetic nanoparticles (*5*, *28*) and magnetic molecules (*29*). The values for E_B are comparable to the threshold for voltage-induced switching (Fig. 2C) and to the energy $2\,S^2J = 9.6$ meV ($S = 2$ for Fe) needed to create a single Ising domain wall within one of the chains by flipping one or more consecutive spins at the end of a chain (*22*). This indicates that current- and temperature-induced switching between the two Néel states is accomplished by propagating domain walls along each chain.

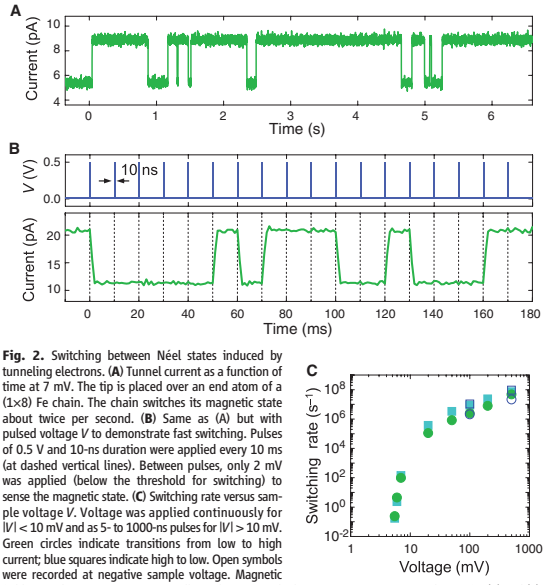

Fig. 2. Switching between Néel states induced by tunneling electrons. **(A)** Tunnel current as a function of time at 7 mV. The tip is placed over an end atom of a (1×8) Fe chain. The chain switches its magnetic state about twice per second. **(B)** Same as (A) but with pulsed voltage *V* to demonstrate fast switching. Pulses of 0.5 V and 10-ns duration were applied every 10 ms (at dashed vertical lines). Between pulses, only 2 mV was applied (below the threshold for switching) to sense the magnetic state. **(C)** Switching rate versus sample voltage *V*. Voltage was applied continuously for $|V| < 10$ mV and as 5- to 1000-ns pulses for $|V| > 10$ mV. Green circles indicate transitions from low to high current; blue squares indicate high to low. Open symbols were recorded at negative sample voltage. Magnetic field 1 T and temperature 0.5 K for all panels. Tip-sample distance was set at 20 pA and 2 mV for (B) and (C).

Below ~5 K, the switching rates of the (1×6) and (1×8) chains become independent of temperature. Such behavior is consistent with quantum tunneling of magnetization (*30*), which is typically observed in few-atom molecular magnets (*8*, *9*) and also occurs in magnetic nanoparticles (*28*). Here, it causes the AFM nanostructures to evolve between the two Néel states, thus limiting their stability even though thermal switching is frozen out. Comparison of the structures of Fig. 3E highlights two avenues to reduce quantum tunneling: First, through increasing the chain length. The addition of two atoms, from (1×6) to (1×8), reduced the tunneling rate 1000-fold. Second, through the coupling of two chains, from (1×6) to (2×6) as shown in Fig. 3D. Even though the spin coupling between chains of $J' = 0.03$ meV per atom (*18*) is much weaker than the exchange coupling within a chain, *J*, it suppresses tunneling markedly. The large difference in the strength of *J* and *J′* is linked to the Cu_2N surface's crystal structure and is evidence of a superexchange-mediated interaction in the Cu_2N molecular network (*18*–*20*) (fig. S1).

A different manifestation of quantum tunneling of magnetization can be found in the (2×4) array, which has a much reduced exponential prefactor and energy barrier, 1.5 meV. This energy is comparable to $4 \times 2\,S^2J' = 1.1$ meV, the energy required to frustrate the weak coupling between the two short chains. This low barrier and the much-reduced exponential prefactor of only $\rho_0 = 5 \times 10^3\ s^{-1}$, indicate a reversal process in which one entire chain switches in a thermally assisted tunneling process (*29*).

The thermal switching rates were found to be independent of magnetic field (fig. S4), and both Néel states were occupied for equal amounts of time (fig. S3), showing that these AFM arrays are fully spin-compensated. The AFM nanostructures are magnetically stable even in the absence of an external magnetic field (fig. S6).

The (2×6) array is highly stable at low temperatures, where switching was observed so rarely that no tunneling rate could be derived. We experimentally determined a lower limit for the stability of these arrays of less than one switching event per 17 hours at 0.5 K.

A challenge to miniaturizing the bits in ferromagnetic storage media is the interaction of neighboring bits because of their dipolar magnetic fields (*31*). This would not be present in AFM storage media. At atomic dimensions, however, exchange interactions can still cause undesired coupling between neighboring bits (*27*). Figure 4A shows an AFM byte, a dense packing of eight (2×6) Fe arrays, with each array representing one bit of information. The structure was engineered to have reduced bit-to-bit exchange interactions. Neighboring bits were staggered in a way that places the atoms of any given bit symmetrically between the atoms of the neighboring bits, resulting in a near-perfect cancellation of bit-to-bit exchange couplings through geometric frustration (Fig. 4B) (*23*).

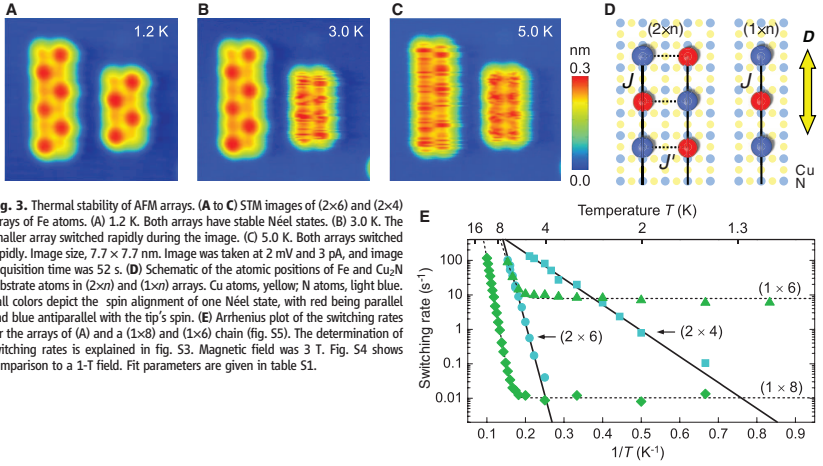

Fig. 3. Thermal stability of AFM arrays. (**A** to **C**) STM images of (2×6) and (2×4) arrays of Fe atoms. (**A**) 1.2 K. Both arrays have stable Néel states. (**B**) 3.0 K. The smaller array switched rapidly during the image. (**C**) 5.0 K. Both arrays switched rapidly. Image size, 7.7 × 7.7 nm. Image was taken at 2 mV and 3 pA, and image acquisition time was 52 s. (**D**) Schematic of the atomic positions of Fe and Cu_2N substrate atoms in (2×*n*) and (1×*n*) arrays. Cu atoms, yellow; N atoms, light blue. Ball colors depict the spin alignment of one Néel state, with red being parallel and blue antiparallel with the tip's spin. (**E**) Arrhenius plot of the switching rates for the arrays of (A) and a (1×8) and (1×6) chain (fig. S5). The determination of switching rates is explained in fig. S3. Magnetic field was 3 T. Fig. S4 shows comparison to a 1-T field. Fit parameters are given in table S1.

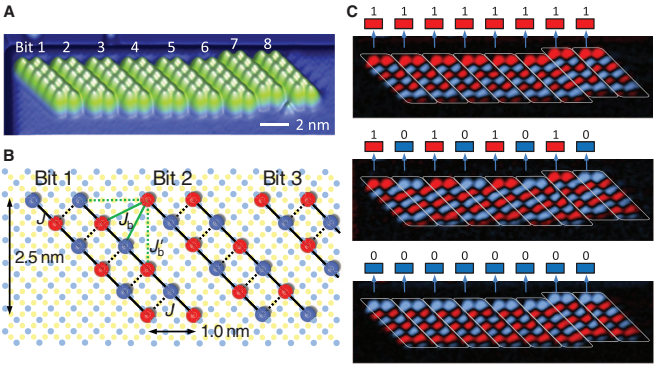

Fig. 4. Ultradense AFM data storage. (**A**) Non–spin-polarized STM image, 24 × 8 nm, of eight (2×6) arrays assembled from Fe atoms. (**B**) Schematic of the bits in (A), with colors as in Fig. 3D. J_b and J_b': pairwise canceling exchange couplings between atoms in neighboring bits. (**C**) Information storage in a magnetic byte. A color-coded difference between spin-polarized and spin-averaged images is shown, with red corresponding to higher tip height and blue to lower tip height in the spin-polarized image. (Top) All eight bits in logic 1 state (as defined by the spin orientation of the top two Fe atoms in each bit). (Middle) Alternating pattern of 1 and 0. (Bottom) All 0. More bit patterns are shown in fig. S7.

Each of the eight bits shown in Fig. 4A can be switched without perturbing the state of the other bits. Figure 4C and fig. S7 show short sequences of test arrangements written into the byte. These configurations are stable over a time scale of hours, and readout was achieved by topographic imaging. Each bit occupies an area of only 9 nm^2.

The arrangement of Fe atoms that form each bit in the byte is a variant on the (2×6) array (compare Fig. 3D and Fig. 4B), in which the ends of each bit are beveled to give the endmost atoms of each bit the same spin orientation. This provides clarity in viewing the state and shows that the exact arrangement of atoms is not critical for magnetic stability.

Our results demonstrate that switchable nanoscale antiferromagnets are candidates for future memory, storage, and spintronic applications.

References and Notes

1. C. Chappert, A. Fert, F. N. Van Dau, *Nat. Mater.* **6**, 813 (2007).
2. R. Wiesendanger, H.-J. Güntherodt, G. Güntherodt, R. J. Gambino, R. Ruf, *Phys. Rev. Lett.* **65**, 247 (1990).
3. J. W. Lau, J. M. Shaw, *J. Phys. D Appl. Phys.* **44**, 303001 (2011).
4. J. V. Barth, G. Costantini, K. Kern, *Nature* **437**, 671 (2005).
5. G. Herzog, S. Krause, R. Wiesendanger, *Appl. Phys. Lett.* **96**, 102505 (2010).
6. S. Krause *et al.*, *Phys. Rev. Lett.* **103**, 127202 (2009).
7. P. Gambardella *et al.*, *Nature* **416**, 301 (2002).
8. J. D. Rinehart, M. Fang, W. J. Evans, J. R. Long, *Nat. Chem.* **3**, 538 (2011).
9. L. Thomas *et al.*, *Nature* **383**, 145 (1996).
10. J. R. Friedman, M. P. Sarachik, J. Tejada, R. Ziolo, *Phys. Rev. Lett.* **76**, 3830 (1996).
11. F. Nolting *et al.*, *Nature* **405**, 767 (2000).
12. S. Heinze *et al.*, *Science* **288**, 1805 (2000).
13. C. L. Gao, W. Wulfhekel, J. Kirschner, *Phys. Rev. Lett.* **101**, 267205 (2008).
14. U. Kaiser, A. Schwarz, R. Wiesendanger, *Nature* **446**, 522 (2007).

15. I. E. T. Iben, in *31st EOS/ESD Symposium* (ESD Association, Rome, NY, 2009), p. 1.
16. X. Chen, A. Hochstrat, P. Borisov, W. Kleemann, *Appl. Phys. Lett.* **89**, 202508 (2006).
17. A. V. Kimel *et al.*, *Nat. Phys.* **5**, 727 (2009).
18. Supporting material is available on *Science* Online.
19. C. F. Hirjibehedin *et al.*, *Science* **317**, 1199 (2007).
20. C. F. Hirjibehedin, C. P. Lutz, A. J. Heinrich, *Science* **312**, 1021 (2006).
21. O. Waldmann, T. Guidi, S. Carretta, C. Mondelli, A. L. Dearden, *Phys. Rev. Lett.* **91**, 237202 (2003).
22. I. Bose, A. K. Pal, *Eur. Phys. J. B* **77**, 139 (2010).
23. A. A. Khajetoorians, J. Wiebe, B. Chilian, R. Wiesendanger, *Science* **332**, 1062 (2011).
24. P. M. Haney, R. A. Duine, A. S. Núñez, A. H. MacDonald, *J. Magn. Magn. Mater.* **320**, 1300 (2008).
25. S. Urazhdin, N. Anthony, *Phys. Rev. Lett.* **99**, 046602 (2007).
26. S. Loth, M. Etzkorn, C. P. Lutz, D. M. Eigler, A. J. Heinrich, *Science* **329**, 1628 (2010).
27. S. Mørup, D. E. Madsen, C. Frandsen, C. R. H. Bahl, M. F. Hansen, *J. Phys. Condens. Matter* **19**, 213202 (2007).
28. W. Wernsdorfer *et al.*, *Phys. Rev. Lett.* **79**, 4014 (1997).
29. D. Gatteschi, R. Sessoli, J. Villain, *Molecular Nanomagnets* (Oxford Univ. Press, New York, 2006).
30. B. Barbara, E. M. Chudnovsky, *Phys. Lett. A* **145**, 205 (1990).
31. E. E. Fullerton *et al.*, *Appl. Phys. Lett.* **77**, 3806 (2000).

Acknowledgments: We acknowledge B. Melior for expert technical assistance. S.L., C.P.L., and A.J.H. thank the Office of Naval Research for financial support. A patent application regarding information storage in antiferromagnetic nanostructures was filed with the U.S. Patent and Trademark Office.

Supporting Online Material

www.sciencemag.org/cgi/content/full/335/6065/196/DC1
Materials and Methods
Figs. S1 to S7
Table S1
References (*32*–*38*)

19 September 2011; accepted 28 November 2011
10.1126/science.1214131

9.2 Measurement of the MgO thickness

We have shown earlier that determining the local thickness of the thin decoupling film, here MgO, is key for the understanding and tuning of the lifetimes of small magnetic structures or single atoms. Here we present two techniques for measuring the MgO thickness on the atomic scale. The first technique uses a combination of atomic force microscopy (AFM) and scanning tunneling microscopy. We scanned the surface in AFM mode (constant cantilever frequency shift), which is equivalent to scanning at constant interaction with the surface (essentially scanning at constant distance from the surface). Simultaneously, the tunnel current was recorded. Since the current decays exponentially in the tunnel barrier formed by the variable-thickness MgO layer, this combination of AFM and STM shows the local thickness of the insulating MgO.

For the second technique we used solely scanning tunneling microscopy. We recorded two images in which, by changing the bias voltage, we selectively tunneled either into the MgO surface or the surface of the metallic substrate. When subtracting the two images from each other we could then determine the local thickness of the oxide film. Note that this technique requires scanning at voltages as high as 2 – 3 V, which means that at least for atoms on MgO this method can not be used at the same time as single metal atoms are adsorbed on the surface, because at such high voltage the atoms are displaced in an uncontrolled fashion.

These techniques can be extremely helpful for determining the local film thickness. We would like to note that as we show in this thesis, for some experiments, it is at least in principle possible to use the lifetime of single atom or molecules to determine the local film thickness. This was demonstrated previously for a different insulator, NaCl, by measuring the lifetime of a Cl-vacancy on 5 – 11 monolayers of NaCl on Cu(111) (*78*).

Measuring the Three-Dimensional Structure of Ultrathin Insulating Films at the Atomic Scale

Susanne Baumann,[†,‡] Ileana G. Rau,[†] Sebastian Loth,[§,⊥] Christopher P. Lutz,[†] and Andreas J. Heinrich[†,*]

[†]IBM Almaden Research Center, 650 Harry Road, San Jose, California 95120, United States, [‡]Department of Physics, University of Basel, Klingelbergstrasse 82, 4056 Basel, Switzerland, [§]Max Planck Institute for the Structure and Dynamics of Matter, 22761 Hamburg, Germany, and [⊥]Max Planck Institute for Solid State Research, 70569 Stuttgart, Germany

ABSTRACT The increasing technological importance of thin insulating layers calls for a thorough understanding of their structure. Here we apply scanning probe methods to investigate the structure of ultrathin magnesium oxide (MgO) which is the insulating material of choice in spintronic applications. A combination of force and current measurements gives high spatial resolution maps of the local three-dimensional insulator structure. When force measurements are not available, a lower spatial resolution can be obtained from tunneling images at different voltages. These broadly applicable techniques reveal a previously unknown complexity in the structure of MgO on Ag(001), such as steps in the insulator−metal interface.

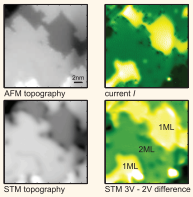

KEYWORDS: magnesium oxide · atomic force microscopy · conductive AFM · scanning tunneling microscopy · thickness determination · thin oxide films · thin insulating films

Ultrathin insulating films provide precise electrostatic coupling and electron tunneling from a conducting substrate to a second electrode or to adsorbed nanostructures.[1] Such films have long served as gate insulators and tunnel junctions,[2] and they are gaining use as tunable catalytic surfaces[3] and substrates for magnetic nanostructures.[4] Magnesium oxide (MgO) films in particular are increasingly used in these roles[5−9] and can be grown epitaxially with monolayer thickness control. The precise film thickness and structure determines the coupling, so techniques to characterize the films at the atomic scale are essential.

Here we show how scanning probe methods can be used not only to determine the exact local film thickness of a thin insulator but also to resolve its three-dimensional structure. We use scanning tunneling microscopy (STM) and conductive atomic force microscopy (AFM), which is a combination of STM and standard AFM,[10−12] to measure the richly varied structure of thin MgO films grown on Ag(001) and to determine the MgO thickness as well as the topography of the buried MgO−Ag interface. In conductive AFM, we record the tunnel current while scanning the tip with constant force interaction over the surface (Figure 1a). This allows us to characterize the full three-dimensional structure of the thin insulator with atomic resolution and reveals the rather complex morphology of MgO on Ag. On the basis of our conductive AFM measurements, we demonstrate a method to determine the structure of the thin insulating film solely based on STM by making use of the electronic properties of MgO films. We show that the latter approach is only feasible in high-quality thin films and results in a lateral resolution of about 2 nm. The two techniques for thickness determination can be adapted in a straightforward way to thin films of other insulating materials on conducting substrates.

Aspects of the structure of different ultrathin films, including MgO, have previously been studied with various scanning probe techniques. In particular, electronic properties of thin MgO films on various metal substrates have been investigated with STM.[13−15] These properties were then applied to determine some aspects of the MgO thickness.[16,17] Atomic-scale spatial resolution with AFM has been demonstrated

* Address correspondence to andreash@us.ibm.com.

Received for review November 27, 2013 and accepted December 30, 2013.

Published online December 30, 2013
10.1021/nn4061034

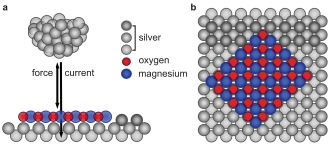

Figure 1. Combined STM and AFM setup. (a) STM tip is mounted on an AFM cantilever to allow simultaneous measurements of the force between the tip and the surface of the insulating film and the current to the underlying Ag substrate. (b) Top view of the MgO film on Ag(001). Oxygen atoms are on top of the Ag atoms and the magnesium atoms in the hollow sites.[25] MgO preferably forms edges along the nonpolar direction, with alternating oxygen and magnesium atoms along the edge.

on cleaved MgO(001) single crystals and MgO thin films.[18,19] The combined use of AFM and STM on MgO has been used to distinguish between different kinds of defects[20] and to determine work function shifts.[21] Here we use the combination of scanning probe techniques to determine the three-dimensional structure of the MgO films and to image the topography of the MgO/Ag interface. Conductive AFM on large areas has been used as a method for the thickness determination on a different material, aluminum oxide on Co, but lacked lateral atomic resolution.[22] Electronic contrasts in STM were used on nickel oxide on Ag to determine the insulator thicknesses locally.[23] Here we show that on MgO a careful thickness determination of the thin insulating films with conductive AFM is needed to properly interpret the varied bias-dependent contrasts observed in STM.

RESULTS AND DISCUSSION

The thin films of MgO on Ag(001) were grown in a room temperature vacuum chamber and transferred in vacuum to the cold scanning probe microscope (see Methods for details). All experiments were performed with a home-built STM/AFM operating at low temperature (6 K) and in ultrahigh vacuum. The microscope has a force sensor with a conductive probe tip.[24] The simultaneous recording of force and tunneling current (Figure 1a) allows the characterization of MgO films with atomic-scale lateral as well as vertical thickness resolution. The force channel maps the topography of the surface and is used to regulate the tip−sample distance, while at the same time, the tunnel current channel maps the thickness of the MgO layer.

In AFM operation, we detect the frequency shift (FM-AFM) of the cantilever due to the tip's interaction with the surface.[26] The cantilever operates at small constant oscillation amplitude (~0.1 nm peak-to-peak) and is sensitive primarily to the force gradient of the atomic-scale junction, rather than to background forces between the larger-scale tip and the surface.[27]

An AFM image of a typical MgO sample recorded at a constant frequency shift of $\Delta f = -25$ Hz is shown

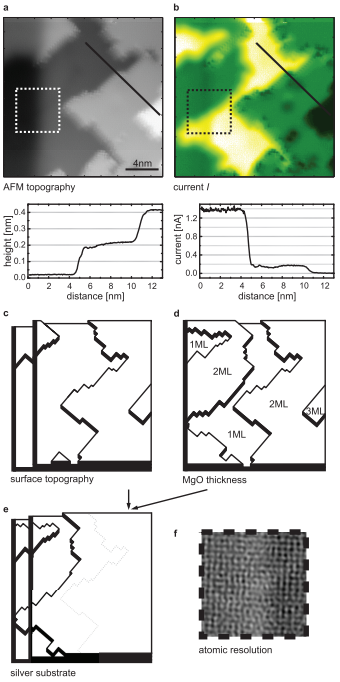

Figure 2. Comparison of AFM and tunnel current measurements over several MgO layers. (a) AFM topography of ~2 ML MgO grown on Ag(001) ($\Delta f = -25$ Hz, $V = -5$ mV, 20 × 20 nm^2). (b) Simultaneously with the AFM topography, the tunnel current is recorded. Changes in the current are due to changes in the thickness of the MgO barrier between the tip and the Ag substrate. The tunnel current image (b) differs significantly from the topography (a), which indicates different local MgO thickness and subsurface Ag steps. This complex sample structure is schematically shown in (c−e). (c) Topography of the top surface of the MgO (schematic drawing of (a)). (d) Thickness of the MgO (without the Ag substrate), which is indicated directly by the current image in (b). (e) Schematic drawing of the underlying Ag topography inferred from (a) and (b) (see text). (The dotted line indicates a MgO thickness change associated with a surface step.) (f) Atomic resolution in an enlarged view of (a) (area indicated in (a,b), 5.6 × 5.6 nm^2). The atomic resolution continues over one and two monolayers of MgO, as well as over an underlying Ag step which is not accompanied by a change in the MgO thickness.

in Figure 2a. This frequency shift corresponds to an attractive interaction with a force gradient of 4 N/m (see Methods), which is about a tenth of the stiffness of a single chemical bond (10−100 N/m). Subject to such strong force interaction, the tip is near mechanical contact with the surface, and the AFM image reveals

the surface topography of the MgO film on Ag(001). We observe ~5 nm wide terraces with a step height of 0.20 ± 0.01 nm between neighboring terraces. This step height agrees well with the bulk MgO atomic layer thickness of 0.21 nm.[28]

While acquiring this AFM image, a small surface-to-tip bias voltage was applied ($V = -5$ mV) and the tunnel current (I) was recorded (Figure 2b). At this low bias, the MgO has no electronic states accessible to tunneling electrons. It acts as an insulating tunneling barrier similar to the vacuum tunnel junction albeit with different barrier height. The tunnel current image (Figure 2b) is remarkably different from the AFM topographic image (Figure 2a): changes in the current often do not coincide with steps in the AFM topograph. In tunnel junctions, the tunnel current is exponentially sensitive to the width of the barrier between the tip and the conducting substrate. Differences in this current thus provide a sensitive measure of the insulating film thickness—the thicker the film, the smaller the tunnel current. We find that the tunnel current decreases by a factor of ~8 for each additional monolayer of MgO. The comparison of Figure 2a,b shows that MgO changes its thickness not only at steps related to the surface topography but also at locations where the surface is smooth, which indicates that there must be additional steps in the underlying substrate. The schematic drawings in Figure 2 illustrate the resulting three-dimensional structure of the thin MgO film by independently showing the topography of the surface—vacuum interface (c), the MgO thickness (d), and the topography of the underlying Ag substrate (e) of the same area.

Magnesium oxide on Ag(001) grows with the oxygen atoms on top of the Ag atoms and the magnesium atoms in the hollow sites (Figure 1a).[25,29,30] Individual atomic layers of MgO are known to terminate preferably along nonpolar edges, in which oxygen and magnesium atoms are alternating along the edge (Figure 1b).[29,30] Figure 2b shows that most changes of the MgO thickness occur by forming such nonpolar edges (45° to the image axes in the figure). Nonpolar MgO edges occur both atop the MgO film and at the buried MgO/Ag interface, where a matching Ag step occurs in order to preserve the crystalline order. In addition to the nonpolar MgO edges, the underlying Ag substrate in Figure 2 also shows a step parallel to a polar MgO direction (vertical feature along left edge in Figure 2a,e). However, Figure 2b shows that the thickness of the MgO film does not change along that Ag edge. A magnified view of the AFM topography above part of this feature (Figure 2f) reveals that MgO layers avoid forming what would be a polar step edge, by using a carpet-like growth mode, in which the film is draped smoothly over the Ag step without introducing any edges in the MgO layers.[31,32] This carpet-like growth appears in both single- and double-layered MgO regions of this figure.

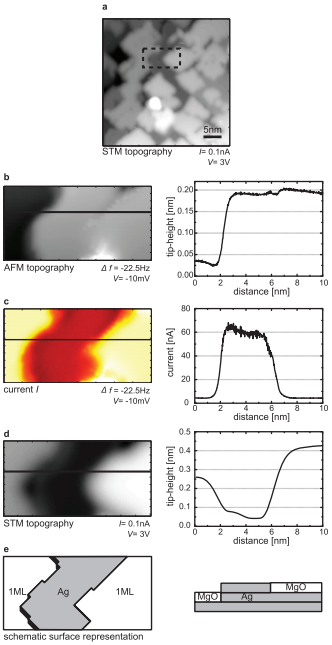

Figure 3. Embedded MgO islands on Ag(001). (a) STM topography shows single monolayer MgO islands (I = 0.1 nA, V = 3 V, 35 × 35 nm^2). (b) AFM topography (constant Δf = −22.5 Hz, so tip is near contact with the surface) shows MgO islands embedded in the Ag substrate. The top surface of the MgO is coplanar with the Ag region (right side of the image, 5 × 10 nm^2) or recessed by one monolayer (left). (c) Tunnel current image obtained simultaneously with the AFM topography (V = −10 mV) distinguishes regions covered by one monolayer of MgO from bare Ag regions. (d) Constant-current STM topography of the same area recorded at high bias in order to tunnel into the surface state of the MgO (I = 0.1 nA, V = 3 V). (e) Schematic cross section of the surface. Comparison between the two topographies (b,d) indicates an apparent height of 0.6 nm for the first monolayer of MgO in STM imaging at 3 V.

Repeated cycles of sputtering and annealing of the silver crystal leave a flat Ag surface with atomically flat terraces of ~100 nm width as verified by STM imaging before MgO film deposition. We therefore conclude that most of the observed steps at the MgO/Ag interface arise during the epitaxial growth of the MgO, which is consistent with the occurrence of mostly nonpolar step edges. For submonolayer MgO, an AFM image and its corresponding tunneling current image are shown in Figure 3b,c. The AFM topography (Figure 3b) and simultaneously acquired tunnel current (Figure 3c) show single monolayer MgO islands

embedded into the Ag substrate. The AFM image shows the two most frequently observed cases: the top surface of the MgO lies in essentially the same plane as the adjacent region of bare Ag(001) (right side of figure), or it lies one monolayer below (left side). The current image (Figure 3c) recorded simultaneously with the AFM topography ($V = -10$ mV) shows clear differences between the MgO islands and the bare Ag substrate. The current decreases by a factor of ~13 when moving the tip from the metal to the first monolayer of MgO. Samples prepared with submonolayer MgO coverage predominantly show areas having only one monolayer of MgO. It therefore appears that MgO starts growing in single layers unlike NaCl, which often occurs in double layers first.[33] The conductance measured on these one monolayer MgO islands closely matches that observed for the lowest MgO thickness seen in the ~2 ML sample of Figure 2b, which corroborates the assignment of 1 ML to those regions. The observed embedded islands indicate that the MgO prefers to terminate its edges at a matching Ag step rather than at the vacuum interface. Such embedded structures have been predicted to be energetically favorable over islands on top of the Ag substrate.[30]

These conductive AFM results reveal a surprising variety in the morphology of MgO films on Ag(001), in which embedded islands are intermixed with on-top islands and carpet-like coverage of some Ag steps. Some of these observed features, such as embedded islands for submonolayer coverage, have been observed previously.[14,16] Here we show how thicker oxide films of MgO also form islands at the MgO/Ag interface, where they terminate at matching Ag steps, rather than forming a continuous first monolayer.

Scanning tunneling microscopy can be used to further investigate the electronic properties of the MgO films. In particular, electronic states close to the surface can be identified with tunneling spectroscopy. The bare Ag substrate shows a flat dz/dV spectrum between 0.5 and 4 V (not shown), while the MgO film shows two prominent dz/dV peaks (Figure 4). These peaks have been previously identified as corresponding to the interface state between the Ag(001) and the MgO at ~2 V and a MgO surface state (or its conduction band edge) at ~2.5 V.[14,29,34,35] Figure 4a shows a continuous line of dz/dV spectra, sweeping the tip laterally over 1−4 monolayers of MgO (Figure 4b,c). This spectral map shows the evolution of the electronic states as the tip passes over a variety of surface features: the MgO/Ag interface state remains roughly constant in magnitude, while the MgO state shows a strong dependence on the film thickness. (For a comparison between dz/dV and previous thickness-dependent spectroscopic STM methods,[14] see Supporting Information.)

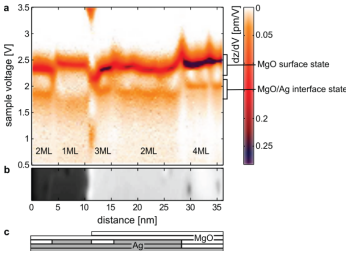

Figure 4. dz/dV spectroscopy over MgO of different thickness. Numerical derivative dz/dV of $z(V)$ spectra in constant-current mode (I = 10 pA). (a) Sequence of dz/dV spectra recorded along a line across the surface. The dz/dV signal is plotted color-coded as a function of lateral position and voltage (white, low signal; dark, high signal). MgO has two characteristic states: an interface state at ~2 V (state at the interface between the Ag and MgO) and a surface state at ~2.5 V.[14] The line of spectra in (a) extends over 1−4 monolayers of magnesium oxide, with changes on the surface as well as in the underlying interface (b,c). (b) STM topograph (V = 3 V, I = 10 pA) shows the top surface of the MgO. (c) Schematic drawing of the same area. The MgO states are perturbed for several nanometers around locations where the MgO thickness changes.

A bias of 3 V or more is commonly used in STM images of MgO thin films.[13,14] This voltage is well above the dz/dV peak associated with the MgO state, so tunneling into the surface of the MgO is allowed. Thus these images resemble the surface topography of the MgO (see Figure 5a, compared to Figure 2a). However, when the bias voltage is below the characteristic MgO state (*e.g.*, 2 V), the electrons can only tunnel into the interface state or into the Ag substrate directly (Figure 5b), which gives a distinctly different image.[13,16,17] The 2 V image contains information about the topography of the metal surface below the thin insulating layer, modulated by the thickness of the film. In Figure 5c, we show the difference of those two scanning voltages, which can be understood as the difference between scanning the top of the MgO and scanning the interface between the oxide and the metal substrate, and thus the "bottom" of the MgO. Such a difference image therefore reveals the thickness of the MgO. Indeed, the STM difference image (Figure 5c) shows the same MgO thickness map as the conductive AFM image (Figure 2b), albeit with reduced spatial resolution. At these voltages, the difference between individual MgO layers appears as a height change of ~0.1 nm (Figure 5d).

These measurements show that thickness determination can be carried out by a STM-only method on scanning probe systems without AFM capability. However, when using STM on a submonolayer coverage of

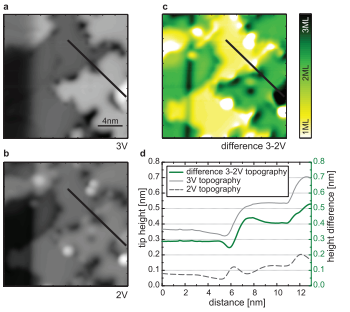

Figure 5. MgO thickness determination with STM. Measurements of the same area as in Figure 2 on ~2 ML MgO/Ag(001). (a) STM image at 3 V, where electrons are tunneling into the surface state (compare to Figure 2a,c), and (b) at 2 V, which corresponds to tunneling into the MgO−Ag interface or the Ag substrate (Figure 2e). (c) Difference between the 3 and 2 V images, which is comparable to Figure 2b,d. This difference is therefore an alternative way to determine the thickness of the MgO. (d) Line cuts of all three images. $I = 0.1$ nA in all images, 20×20 nm^2.

MgO, care should be taken with the STM-only technique since embedded islands, as shown in Figure 3, appear as tall protrusions with respect to the Ag substrate. For example, the MgO island that appears 0.2 nm lower than the Ag substrate in the AFM channel (Figure 3a) appears as a 0.2 nm protrusion in STM imaging (Figure 3d). This thus carries the risk of assigning these apparent 0.2 nm protrusions as MgO islands grown atop the Ag substrate.[16,17] Here we use the AFM channel to unambiguously show that these islands are embedded into the Ag surface.

By comparing the STM and AFM measurements, we can draw two important conclusions. First, as long as the surface is covered with more than a full monolayer of MgO, we find that STM imaging at ~3 V gives an accurate representation of the surface topography (compare the AFM image of Figure 2a with the STM image of Figure 5a). However, for submonolayer coverage of MgO, where some bare Ag regions are exposed, these STM images at high bias do not represent the surface topography as revealed by AFM (Figure 3). The large apparent height in STM (Figure 3d) of the first monolayer is presumably due to the reduced barrier energy (work function) above MgO compared to bare Ag.

Second, Figure 4a shows that the MgO state and the MgO/Ag interface state are clearly resolved only ~2 nm laterally away from any step edges. This is true for both surface and buried MgO steps. This wide border area of the MgO island's electronic structure also becomes visible by comparing the AFM and STM images, where the steps in the STM topography do not appear as sharp edges. Thickness determination with STM-only measurements thus yields an effective spatial resolution of 2 nm and requires samples with sufficiently large insulator terraces.

CONCLUSIONS

The present paper demonstrates measurement of the thickness of a thin insulating film on a metal substrate with high spatial resolution scanning probe methods. Simultaneous AFM and STM measurements are used to give a clear picture of the complex three-dimensional structure of thin magnesium oxide films on Ag(001). We find that thickness changes can occur independently from surface steps revealing embedded islands and carpet-like growth of MgO films. The techniques presented here for the three-dimensional thickness determination should be applicable to other thin insulating films and should thus open new possibilities for thickness-dependent studies such as tuning the decoupling of individual atoms or molecules from their metal substrate or for studying thickness-dependent catalytic reactions on the surface of thin insulators.

METHODS

Sample Preparation. The protocol for growing MgO films on Ag(001) is similar to that used in earlier publications.[14,16,35] The Ag surface was cleaned by repeated cycles of sputtering (Ar^+, $p_{Ar} = 2 \times 10^{-6}$ Torr, 1 keV, 6 min) followed by annealing (680 K, 5 min) to obtain a clean Ag surface. After these cleaning cycles, the impurities were below the detection limit of an Auger electron spectrometer and STM images revealed a clean Ag substrate.

MgO thin films were epitaxially grown on the clean Ag(001) crystal by evaporating Mg onto the ~480 K surface, while exposing the surface to molecular oxygen gas ($p_{O_2} = 1 \times 10^{-6}$ Torr). The magnesium evaporation source was a homemade Knudsen cell kept at ~620 K and mounted 15 cm from the Ag surface to achieve a growth rate of ~1 ML per minute. The film preparation was done in the room temperature vacuum chamber, and the sample was passed through ultrahigh vacuum to the cold STM/AFM directly after the growth.

AFM/STM. The AFM measurements were done using an AFM with the qPlus sensor design having a resonance frequency of $f_0 = 21\,860$ Hz and a spring constant k_0 of ~1800 N m^{-1}.[24] Oscillation amplitude was ~0.1 nm peak-to-peak. The force gradient is well approximated by $k = 2 \times k_0 \times (\Delta f/f_0)$.[27] A metal STM tip made of Ir, likely coated with Ag from the sample, was mounted on the AFM cantilever to allow simultaneous measurements of the current and force gradient.

dz/d*V* Measurements. For the dz/dV measurements, the tip height (z) is recorded while voltage sweeps at constant current (closed feedback loop) are performed and subsequently the numerical derivative of the $z(V)$ curve is calculated. For Figure 4a, the tip was moved laterally by 0.1 nm between each recorded $z(V)$ spectrum. The observed peaks, or states, obtained with dz/dV are systematically shifted with respect to some literature values[14] due to the specific spectroscopy method applied (see Supporting Information).

Conflict of Interest: The authors declare no competing financial interest.

Acknowledgment. The authors thank Bruce Melior for expert technical assistance. C.P.L. and A.J.H. thank the Office of Naval Research for financial support (N00014-11-C-0483).

Supporting Information Available: Comparison between thickness-dependent spectroscopic methods, along with another example of a conductive AFM to STM comparison. This material is available free of charge *via* the Internet at http://pubs.acs.org.

REFERENCES AND NOTES

1. Repp, J.; Meyer, G.; Stojković, S. M.; Gourdon, A.; Joachim, C. Molecules on Insulating Films: Scanning-Tunneling Microscopy Imaging of Individual Molecular Orbitals. *Phys. Rev. Lett.* **2005**, *94*, 026803.
2. Sun, J.; Ralph, D. Magnetoresistance and Spin-Transfer Torque in Magnetic Tunnel Junctions. *J. Magn. Magn. Mater.* **2008**, *320*, 1227–1237.
3. Freund, H.-J.; Pacchioni, G. Oxide Ultra-thin Films on Metals: New Materials for the Design of Supported Metal Catalysts. *Chem. Soc. Rev.* **2008**, *37*, 2224–2242.
4. Loth, S.; Baumann, S.; Lutz, C. P.; Eigler, D. M.; Heinrich, A. J. Bistability in Atomic-Scale Antiferromagnets. *Science* **2012**, *335*, 196–199.
5. Parkin, S. S. P.; Kaiser, C.; Panchula, A.; Rice, P. M.; Hughes, B.; Samant, M.; Yang, S.-H. Giant Tunnelling Magnetoresistance at Room Temperature with MgO(100) Tunnel Barriers. *Nat. Mater.* **2004**, *3*, 862–867.
6. Yuasa, S.; Nagahama, T.; Fukushima, A.; Suzuki, Y.; Ando, K. Giant Room-Temperature Magnetoresistance in Single-Crystal Fe/MgO/Fe Magnetic Tunnel Junctions. *Nat. Mater.* **2004**, *3*, 868–871.
7. Yoon, B.; Häkkinen, H.; Landman, U.; Wörz, A. S.; Antonietti, J.-M.; Abbet, S.; Judai, K.; Heiz, U. Charging Effects on Bonding and Catalyzed Oxidation of CO on Au_8 Clusters on MgO. *Science* **2005**, *307*, 403–407.
8. Harding, C.; Habibpour, V.; Kunz, S.; Farnbacher, A. N.-S.; Heiz, U.; Yoon, B.; Landman, U. Control and Manipulation of Gold Nanocatalysis: Effects of Metal Oxide Support Thickness and Composition. *J. Am. Chem. Soc.* **2009**, *131*, 538–548.
9. Shin, H.-J.; Jung, J.; Motobayashi, K.; Yanagisawa, S.; Morikawa, Y.; Kim, Y.; Kawai, M. State-Selective Dissociation of a Single Water Molecule on an Ultrathin MgO Film. *Nat. Mater.* **2010**, *9*, 442–447.
10. Sawada, D.; Sugimoto, Y.; Morita, K.; Abe, M.; Morita, S. Simultaneous Measurement of Force and Funneling Current at Room Temperature. *Appl. Phys. Lett.* **2009**, *94*, 173117.
11. Polesel-Maris, J.; Lubin, C.; Thoyer, F.; Cousty, J. Combined Dynamic Scanning Tunneling Microscopy and Frequency Modulation Atomic Force Microscopy Investigations on Polythiophene Chains on Graphite with a Tuning Fork Sensor. *J. Appl. Phys.* **2011**, *109*, 074320.
12. Majzik, Z.; Drevniok, B.; Kamiński, W.; Ondráček, M.; McLean, A. B.; Jelínek, P. Room Temperature Discrimination of Adsorbed Molecules and Attachment Sites on the Si(111)-7 × 7 Surface Using a qPlus Sensor. *ACS Nano* **2013**, *7*, 2686–2692.
13. Gallagher, M.; Fyfield, M.; Cowin, J.; Joyce, S. Imaging Insulating Oxides: Scanning Tunneling Microscopy of Ultrathin MgO Films on Mo(001). *Surf. Sci.* **1995**, *339*, L909–L913.
14. Schintke, S.; Messerli, S.; Pivetta, M.; Patthey, F.; Libioulle, L.; Stengel, M.; De Vita, A.; Schneider, W.-D. Insulator at the Ultrathin Limit: MgO on Ag(001). *Phys. Rev. Lett.* **2001**, *87*, 276801.
15. Klaua, M.; Ullmann, D.; Barthel, J.; Wulfhekel, W.; Kirschner, J.; Urban, R.; Monchesky, T. L.; Enders, A.; Cochran, J. F.; Heinrich, B. Growth, Structure, Electronic, and Magnetic Properties of MgO/Fe(001) Bilayers and Fe/MgO/Fe(001) Trilayers. *Phys. Rev. B* **2001**, *64*, 134411.
16. Valeri, S.; Altieri, S.; del Pennino, U.; di Bona, A.; Luches, P.; Rota, A. Scanning Tunnelling Microscopy of MgO Ultrathin Films on Ag(001). *Phys. Rev. B* **2002**, *65*, 245410.
17. Schintke, S.; Schneider, W.-D. Insulators at the Ultrathin Limit: Electronic Structure Studied by Scanning Tunnelling Microscopy and Scanning Tunnelling Spectroscopy. *J. Phys.: Condens. Matter* **2004**, *16*, R49.
18. Barth, C.; Henry, C. R. Atomic Resolution Imaging of the (001) Surface of UHV Cleaved MgO by Dynamic Scanning Force Microscopy. *Phys. Rev. Lett.* **2003**, *91*, 196102.
19. Heyde, M.; Sterrer, M.; Rust, H.-P.; Freund, H.-J. Atomic Resolution on MgO(001) by Atomic Force Microscopy Using a Double Quartz Tuning Fork Sensor at Low-Temperature and Ultrahigh Vacuum. *Appl. Phys. Lett.* **2005**, *87*, 083104.
20. König, T.; Simon, G. H.; Rust, H.-P.; Pacchioni, G.; Heyde, M.; Freund, H.-J. Measuring the Charge State of Point Defects on MgO/Ag(001). *J. Am. Chem. Soc.* **2009**, *131*, 17544–17545.
21. König, T.; Simon, G. H.; Rust, H.-P.; Heyde, M. Work Function Measurements of Thin Oxide Films on Metals—MgO on Ag(001). *J. Phys. Chem. C* **2009**, *113*, 11301–11305.
22. Olbrich, A.; Ebersberger, B.; Boit, C.; Vancea, J.; Hoffmann, H.; Altmann, H.; Gieres, G.; Wecker, J. Oxide Thickness Mapping of Ultrathin Al_2O_3 at Nanometer Scale with Conducting Atomic Force Microscopy. *Appl. Phys. Lett.* **2001**, *78*, 2934–2936.
23. Steurer, W.; Surnev, S.; Fortunelli, A.; Netzer, F. P. Scanning Tunneling Microscopy Imaging of NiO(100)(1 × 1) Islands Embedded in Ag(100). *Surf. Sci.* **2012**, *606*, 803–807.
24. Giessibl, F. J. Atomic Resolution on Si(111)-(7 × 7) by Noncontact Atomic Force Microscopy with a Force Sensor Based on a Quartz Tuning Fork. *Appl. Phys. Lett.* **2000**, *76*, 1470–1472.
25. Sgroi, M.; Pisani, C.; Busso, M. *Ab Initio* Density Functional Simulation of Structural and Electronic Properties of MgO Ultra-thin Adlayers on the (001) Ag Surface. *Thin Solid Films* **2001**, *400*, 64–70.
26. Albrecht, T. R.; Grütter, P.; Horne, D.; Rugar, D. Frequency Modulation Detection Using High-*Q* Cantilevers for Enhanced Force Microscope Sensitivity. *J. Appl. Phys.* **1991**, *69*, 668–673.
27. Ternes, M.; Lutz, C. P.; Hirjibehedin, C. F.; Giessibl, F. J.; Heinrich, A. J. The Force Needed To Move an Atom on a Surface. *Science* **2008**, *319*, 1066–1069.
28. Heinrich, V. E.; Cox, P. A. *The Surface Science of Metal Oxides*; Cambridge University Press: New York, 1994.
29. Kiguchi, M.; Goto, T.; Saiki, K.; Sasaki, T.; Iwasawa, Y.; Koma, A. Atomic and Electronic Structures of MgO/Ag(001) Heterointerface. *Surf. Sci.* **2002**, *512*, 97–106.
30. Ferrari, A. M.; Casassa, S.; Pisani, C. Electronic Structure and Morphology of MgO Submonolayers at the Ag(001) Surface: An *Ab Initio* Model Study. *Phys. Rev. B* **2005**, *71*, 155404.
31. Hebenstreit, W.; Redinger, J.; Horozova, Z.; Schmid, M.; Podloucky, R.; Varga, P. Atomic Resolution by STM on Ultra-thin Films of Alkali Halides: Experiment and Local Density Calculations. *Surf. Sci.* **1999**, *424*, L321–L328.
32. Wintterlin, J.; Bocquet, M.-L. Graphene on Metal Surfaces. *Surf. Sci.* **2009**, *603*, 1841–1852. Special Issue of Surface Science dedicated to Prof. Dr. Dr. h.c. mult. Gerhard Ertl, Nobel-Laureate in Chemistry 2007.
33. Repp, J.; Meyer, G. Scanning Tunneling Microscopy of Adsorbates on Insulating Films. From the Imaging of Individual Molecular Orbitals to the Manipulation of the Charge State. *Appl. Phys. A: Mater. Sci. Process.* **2006**, *85*, 399–406.
34. Altieri, S.; Tjeng, L. H.; Sawatzky, G. A. Electronic Structure and Chemical Reactivity of Oxide−Metal Interfaces: MgO-(100)/Ag(100). *Phys. Rev. B* **2000**, *61*, 16948–16955.
35. Sterrer, M.; Heyde, M.; Novicki, M.; Nilius, N.; Risse, T.; Rust, H.-P.; Pacchioni, G.; Freund, H.-J. Identification of Color Centers on MgO(001) Thin Films with Scanning Tunneling Microscopy. *J. Phys. Chem. B* **2006**, *110*, 46–49.

9.3 Chiral molecule recognition and manipulation

Careful characterization and study of systems at the atomic scale is not only important for small devices with magnetic properties, but also for the development of new materials, for example for catalysis (*79*) and for photonic devices (*80*). Particularly interesting are chiral molecules, i.e. molecules that differ from their mirror image, they exhibit what are called left- and right-handed structures. Chiral molecules are interesting because of their importance for example in optically active materials (materials where chiral molecular crystals are used to polarize light), and their prevalence in biological systems.

Molecules that are shaped like helices are one class of chiral molecules. The way helical molecules interact with each other and assemble into macroscopic structures is still not well understood. The STM lends itself to the investigations of such molecular recognition at the nano-scale, since one can combine the advantages of its imaging capabilities, for the molecular identification, with atom or molecule manipulation, that allows the separation of different molecular species into their left- and right-handed forms (enantiomers).

We use heptahelicene as a model system for the understanding of molecular recognition on a surface. The 7-ring carbohelicene, heptahelicene, is a ring molecule that forms two chiral enantiomers, one with right- and one with left-handedness. We use the STM to study self-assembled dimers of these heptahelicenes on Cu(111) (*81*). After manual separation of the two molecules of a dimer with a molecule-terminated STM tip, we determined their handedness with a metal-atom-terminated tip. We found that the molecules strongly prefer to form hetero-chiral pairs, pairs of one molecule of each chirality (out of 52 dimers only one was found to be homo-chiral). Thus our study shows that single molecule manipulation is a valuable tool to understand intermolecular recognition at surfaces.

9.4 The worlds smallest movie - made with atoms

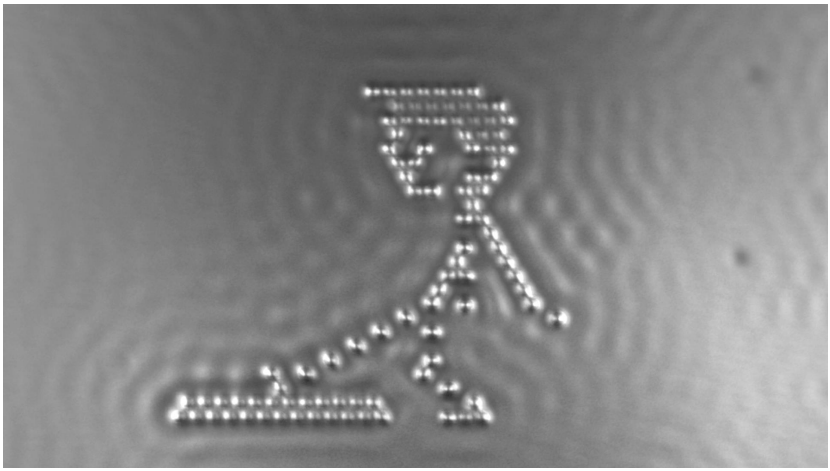

Figure 9.1: One scene from the stop motion movie *A Boy and his Atom* (see the whole movie at (*77*)).

Not long after the invention of the scanning tunneling microscope (*18*), D. M. Eigler showed that this was also a tool that allowed the precise manipulation of single atoms (*14*). Today, we still use atom manipulation on a daily basis to build spin-polarized tips (*26*,*38*) or to build and study structures of atoms and molecules (*19*,*76*). In order to showcase these capabilities, we made a short stop-motion movie using horizontal atom (molecule) manipulation. The movie was made out of 242 still frames 30×25 nm^2 in size and it took 10 days to assemble all frames (without instrument set-up and post-processing).

Once inspired by D. M. Eigler myself, I am now excited to see how kids and adults alike are interested in this project (more than 5 million *youtube* views) and how it is a way of expressing how science can be so much fun, when we get to build and explore new worlds one atom at the time.

Chapter 10

Conclusions

This work elucidates the interplay between the magnetic anisotropy, spin and orbital degrees of freedom in systems at the border of free atoms and the solid state, and highlights the atomistic limits on the miniaturization of magnetic systems. Magnetic anisotropy is a fundamental property of magnetic materials that governs the stability and directionality of their magnetization. At the atomic level, magnetic anisotropy originates from anisotropy in the orbital angular momentum and the spin-orbit coupling that connects the spin moment of a magnetic atom to the spatial symmetry of its ligand field environment. Generally, the ligand field that is necessary for the anisotropy also quenches the orbital moment and reduces the total magnetic moment of the atom to its spin component. However, careful design of the coordination geometry of a single atom can preserve the orbital moment while inducing uniaxial anisotropy. We demonstrate here both of these cases. While the symmetry of Fe on MgO fully quenches its orbital moment before it is partially restored by spin-orbit coupling, for Co on MgO the coordination geometry preserves almost its full orbital moment and spin-orbit coupling then allows extremely large magnetic anisotropy.

Scanning tunneling spectroscopy and X-ray absorption spectroscopy mea-

surements show a zero-field splitting of 14 meV for Fe and 58 meV for Co (the maximal value afforded by the spin-orbit coupling). Multiplet calculations, that fit the X-ray absorption spectra, show that both atoms have a large orbital moment along the out-of-plane direction, $\langle L_z \rangle$ = 1.3 μ_B for Fe and $\langle L_z \rangle$ = 2.9 μ_B for Co. Thus for either atom the measured orbital moment is more than two thirds of the free atom orbital moment, and vastly exceeds the typical values in bulk materials (*41*,*82*). However, the mechanisms that underlie these large orbital moments are fundamentally different for the two atoms. The four-fold symmetric ligand field given by the MgO surface is able to quench the Fe's orbital moment because it can mix the $M_L = \pm 2$ ground state components. In contrast, Co in the same ligand field environment is protected from such mixing by its $M_L = \pm 3$ ground state. In Co, this results in a linear response to the spin-orbit coupling and that in turn leads to the maximal zero-field splitting for 3d-transition metal atoms. Fe on the other hand represents the more common case (*31*), where spin-orbit coupling restores some of the otherwise quenched orbital moment due to mixing with the next-higher orbital state. For Fe, we can even probe transitions to this higher spin-multiplet ($\sim$100 mV) by spin-polarized STM measurements, which reflect a change in the occupation of states.

We emphasize that the two experimental techniques employed here complement each other, and together give a very thorough understanding of the atomic-scale magnetism of Fe and Co on MgO: XMCD and multiplet calculations show the character and properties of the magnetic states while STM gives a direct measurement of specific transitions. The combination of both techniques is extremely powerful in describing the many-body interactions that determine the spin and the orbital degrees of freedom of magnetic atoms on surfaces, going beyond the spin Hamiltonian description successfully used in previous STM studies of nano-sized magnetic structures (*25*,*34*,*73*).

In this thesis, we further introduce a calculation of the lowest atomic multiplet that is based on the results of DFT calculations. This approach

uses the DFT-calculated geometry and charge distribution to accurately reproduce the character and order of the magnetic states of both Fe and Co. The obtained expectation values are within about 30% of values obtained with the full multiplet model. We combine these calculations with Stevens operator equivalents (*32*), which simplifies the calculation significantly. These calculations thus give the combination of STM experiments with DFT calculations an additional tool-set when working with magnetic materials. In this thesis, we use these newly developed calculations to explain an energy shift in the zero-field splitting of Fe by a movement of the magnetic atom under the influence of the STM tip. Due to its nearby orbital state, the Fe atom is extremely sensitive to the four-fold symmetric ligand field environment of the MgO. Thus even small movements of atoms can change the anisotropy of the system significantly and we can continuously tune the anisotropy barrier of the Fe atom by about 1 meV, induced by a $\sim$3 pm movement of the Fe atom in the out-of-plane direction.

Stable magnetism is governed by the ability of a system to overcome its anisotropy barrier and, when the system is small enough that quantum effects are important, the ability to suppress quantum tunneling of the magnetization. Due to the large energy barrier and the large magnetic moment for both Fe and Co demonstrated here, a long lifetime for state 1, the state oppositely aligned to the ground state, is possible. However, quantum tunneling of the magnetization can induce direct transitions between these states and thereby shorten the lifetime of the excited state. Quantum tunneling of the magnetization can be induced by electrons from the substrate or the tip that scatter off the atom. Thus the lifetimes of such small quantum magnets are extremely sensitive to the interactions with their environment. We show how reducing the scattering from tip electrons by increasing the atom-tip distance is an important strategy in suppressing quantum tunneling of the magnetization. Moreover, introducing additional monolayers of MgO further decouples the atoms from the conduction electrons of the substrate, which also increases the spin lifetime. We find T_1 times of $\sim$10 ms for Fe and $\sim$200 μs

for Co on MgO. These are the longest lifetimes reported to date for single $3d$ transition metal atoms on a surface.

This work introduces several strategies on expanding the capabilities of scanning tunneling microscopes in examining quantum magnets. We show new ways to probe rare transitions either by spin-polarized sensing of changes in the occupation of states or by a pump-probe scheme, which gives the ability to measure magnetic moments on single atoms.

The large zero-field splittings and long spin lifetimes measured in this work demonstrate the advantages and impediments intrinsic to size reduction in magnetic materials. Despite the very large magnetic anisotropy, the strong coupling of d-electrons to the environment makes the spin lifetime of transition metal atoms very sensitive to perturbations caused by the ligand field and scattering from conduction electrons. Nonetheless, the large energy and long time scales measured in these experiments indicate that relatively long-lived quantum states are possible for single Fe and Co atoms on MgO surfaces.

The detailed understanding of the origin of magnetism gained by this work can be used to develop strategies for the rational design of long-lived quantum states at the atomic scale. We show here that symmetry is of paramount importance for the stability of a system. Nevertheless, apart from the symmetry the bonding chemistry plays an important role and governs many of the magnetic properties. The effects of bonding are not discussed in this thesis but are extensively studied in single molecular magnets (*1*,*2*). From symmetry arguments the systems presented here are already well optimized. Therefore, in order to push the limits of large anisotropy and long-lived quantum states even further, one might need to switch to rare earth atoms.

Acknowledgments

First, I would like to thank my advisors Dr. Andreas J. Heinrich from the IBM Almaden Research Center, United States, and Prof. Ernst Meyer from the University of Basel, Switzerland, for their support throughout my thesis.

I am deeply thankful for my time at IBM and having the opportunity to work there. Although many people were crucial in producing the results for my PhD, the most important person was Dr. Andreas J. Heinrich. I am incredibly thankful for his constant support and excellent scientific contributions. Furthermore, I would like to thank Christopher P. Lutz for inspiring my scientific curiosity and asking me the questions I needed to hear. I would also like to thank Dr. William Paul for his important scientific contributions as well as his contributions to the design of the MBE chamber and for many great scientific discussions. Furthermore, I want to thank other members of the IBM team for their scientific contributions, namely Dr. Sebastian Loth, Dr. Ileana G. Rau, Dr. Roger M. Macfarlane, Niklas Romming, Kai Yang and Dr. Taeyong Choi. Special thanks goes to Bruce Melior for his excellent technical expertise and for teaching me design skills and how to use SolidWorks. I also want to acknowledge the help provided by the model shop team at IBM. Furthermore, I want to thank Dr. D.M. Eigler; I am deeply grateful for his constant support and excellent advice.

Throughout my thesis we had the chance to collaborate with several groups

in and outside of IBM. I would like to acknowledge a fruitful collaboration with the XMCD- and multiplet calculations-team and the interesting scientific discussions it fostered. First of all, I want to express my gratitude to Prof. Harald Brune, from the EPFL Lausanne, Switzerland, for enabling the measurements at the X-Treme beam line. From the rest of the team, I would like to thank in particular Prof. Pietro Gambardella (ETH Zürich, Switzerland), Dr. Stefano Rusponi, Dr. Fabio Donati, Dr. Luca Gragnaniello (all EPFL Lausanne), Dr. Sebastian Stepanow (ETH Zürich), Dr. Jan Dreiser and Dr. Cinthia Piamonteze (PSI Villigen, Switzerland). Special thanks go to Dr. Stefano Rusponi and Dr. Fabio Donati for analyzing the XMCD data and to Dr. Stebastian Stepanow for performing the multiplet calculations.
For their contributions to this large collaboration on Fe and Co on MgO and for their efforts in providing DFT calculations, I would also like to thank Dr. Barbara A. Jones, Dr. Shruba Gangopadhyay and Oliver R. Albertini (IBM Almaden).

Additionally, I would like to express my thanks to Prof. Karl-Heinz Ernst from EMPA, Switzerland, for the collaboration on chiral molecules.

Finally, I would like to thank, without specifically mentioning names, all the great people I met and worked with during my time in the US, both in and outside IBM, as well as family and friends from Switzerland. Many of them provided essential support throughout my PhD work and for this I am deeply thankful.

Curriculum Vitae

Susanne Baumann

650 Harry Road – San Jose, CA 95120 – USA

Education

IBM Almaden Research Center, San Jose, USA
University of Basel, Switzerland
PhD in Applied Physics, *2011–expected summer 2015*
Work includes probing of spin-states and their lifetimes in single atoms with scanning tunneling microscopy and x-ray absorption techniques, as well as design of a new vacuum chamber for improved sample preparation
Advisors: Dr. Andreas J. Heinrich and Prof. Ernst Meyer

University of Basel, Switzerland
IBM Almaden Research Center, San Jose, USA
Masters of Science in Nanoscience, *2008–2011*
Courses focused on nanophysics
Thesis on how to characterize the thickness of thin insulating films with scanning probe microscopy
Advisors: Dr. Andreas J. Heinrich and Prof. Dominik Zumbühl

Experience

Research

University of Basel, Switzerland
Internship in Molecular Electronics *2009–2009*
Project work on the development of miniaturized monomolecular arrays of gold nanoparticles covered with alkane chains.

University of Basel, Switzerland
Internship in Neurobiology *2008–2009*
The work included the examination of a differentiation protocol of mouse embryonic stem cells into neural cells on a carbon nanotube substrate and the investigation of their electrical activity with electrophysiological methods.

Other

SwissOptic, Heerbrugg, Switzerland
Assistance in Measurement Engineering *2005–2011*
Responsible for quality control of high precision optical parts, mainly over laser interferometry, as well as assistance in other measurement techniques and beam alignment in the optical modules.

Languages

German: native

English: fluent *Cambridge Certificate in Advanced English (CAE)*

French: basic *Diplome d'Etudes en Langues Français (DELF)*

Computer skills

MATLAB: data anlysis, as well as simulations

SolidWorks: 3D CAD design software

Publications

1. Ileana G. Rau*, Susanne Baumann*, Stefano Rusponi, Fabio Donati, Sebastian Stepanow, Luca Gragnaniello, Jan Dreiser, Cinthia Piamonteze, Frithjof Nolting, Shruba Gangopadhyay, Oliver R. Albertini, Roger Macfarlane, Christopher P. Lutz, Barbara A. Jones, Pietro Gambardella, Andreas J. Heinrich and Harald Brune, **Reaching the Magnetic Anisotropy Limit of a 3*d* Metal Atom**, *Science* **344**, 988 (2014).
2. Susanne Baumann, Ileana G. Rau, Sebastian Loth, Christopher P. Lutz and Andreas J. Heinrich, **Measuring the Three-Dimensional Structure of Ultrathin Insulating Films at the Atomic Scale**, *ACS Nano* **8** (2), 1739 (2014).
3. Sebastian Loth, Susanne Baumann, Christopher P. Lutz, D. M. Eigler and Andreas J. Heinrich, **Bistability in Atomic-Scale Antiferromagnets**, *Science* **335**, 196 (2012).

Manuscripts in preparation

4. Karl-Heinz Ernst, Susanne Baumann, Christopher P. Lutz, Johannes Seibel, Laura Zoppi and Andreas J. Heinrich, **Pasteurs experiment performed at the nanoscale: manual separation of chiral molecules one by one**. *Nano Letters* (under review).
5. Susanne Baumann *et al.* **Spin and orbital magnetism of Fe atoms on MgO**.
6. William Paul, Susanne Baumann *et al.* **Extremely long lifetimes for single 3*d* transition metal atoms on a surface**.
7. Susanne Baumann *et al.* **Anisotropy tuning explained by a point charge model**.
8. Susanne Baumann *et al.* **Controlling the magnetic moment and the lifetime of a single atom by exchange interaction**.

Talks

ICNT Vail 2014: invited talk

Nanomanipulation Workshop Mulhouse 2014: invited talk

MMM conference Denver 2013: invited talk, winning of a student travel award

several seminar talks at renowned institutions: such as UC Berkeley, University of Oxford, University of Hamburg, Max-Planck-Institute Hamburg and Stuttgart, IBM Zürich and others

Other Contributions

A Boy and his Atom: Production and publication of the world's smallest movie 'A Boy and his Atom', www.ibm.com/madewithatoms

INASCON 2009: Organisation committee of the International Nanoscience Students Conference 2009, taking place from August 20 to 23, 2009, www.inascon.eu

References

Available upon request

Appendices

Appendix A

Molecular beam epitaxy chamber

The following table contains information about all flanges (ports) and their specifications of the designed molecular beam epitaxy chamber.

Reference plane is the plane coincident with the bottom flange. Here, r refers to a rotatable flange, t stands for tapped holes and s indicates special specifications or tolerances, that are noted in the comments below. The flange numbers are shown in the drawings after the table.

#	Flange Name	Flange Size [in]		Tube OD [in]	Focal Point [in]	Focal Length [in]	Polar °	Azimuthal °
A	Bottom Flange	15.25	s[1]	10	$(0, 0, 0)$	0	180	–
B	Top Flange	13.25	s[2]	10	$(0, 0, 0)$	32	0	–
1	Train 1	8	r s[3]	6	$(3.75, 0, 17.7)$	6.75	90	90
2	Train 2	8	r s[3]	6	$(3.75, 0, 17.7)$	6.75	90	270
3	RHEED Gun	4.5	r	2.75	$(0, 0, 24)$	11	93	160
4	RHEED Screen	6	r	4	$(0, 0, 23.1)$	9	90	340
5	Ion Pump	8	r	6	$(0, 0, 6)$	9	90	0
6	TSP	8	r	6	$(0, 0, 6)$	9	90	90
7	Turbo Pump	8	r	6	$(0, 0, 6)$	9	90	180
8	Auger	6	t s[4]	4	$(0, 0.45, 25)$	5.5	90	243
9	Sample Stage	1.33	r	0.75	$(0, 0.64, 24.3)$	11	90	180
10	Sputter Gun	2.75	r	1.75	$(0, 0.45, 25)$	16	155.5	270
11	Microbalance	2.75	r	1.75	$(0, 0, 22.2)$	9	90	20
12	Additional 4.5 in Flange	4.5	r	2.75	$(0, 0, 24)$	15	150	135
13	Additional 4.5 in Flange	4.5	r	2.75	$(0, 0, 24)$	15	150	225
14	Pyrometer	2.75	r	1.75	$(0, 0, 24)$	15	150	315
15	Additional 2.75 in Flange	2.75	r	1.75	$(0, 0, 24)$	15	150	45
16	Train Viewport	6	r	4	$(0, 0, 18.2)$	7.5	90	180
17	Sample Viewport	4.5	r	2.75	$(0, 0, 25)$	9	75	183
18	Backside Viewport	4.5	r	2.75	$(0, 0, 25)$	7	90	45
19	Shutter	1.33	r	0.75	$(0, 0, 19.75)$	7	90	105
20	2.75 in Flange I	2.75	r	1.75	$(0, 0, 29.25)$	7	90	125
21	2.75 in Flange II	2.75	r	1.75	$(0, 0, 24.75)$	7	90	125
22	2.75 in Flange III	2.75	r	1.75	$(0, 0, 21.25)$	7	90	125
23	2.75 in Flange IV	2.75	r	1.75	$(0, 0, 29.25)$	7	90	90
24	2.75 in Flange V	2.75	r	1.75	$(0, 0, 24.75)$	7	90	90
25	Auger Viewport	4.5	r	2.75	$(0, 0, 25)$	8	65	350
26	Additional Shutter I	1.33	r	0.75	$(0, 0, 19)$	7	90	225
27	Additional Shutter II	1.33	r	0.75	$(0, 0, 19)$	7	90	135

[1] actual flange size: 13.25 in, bolt hole at 0° azimuthal angle
[2] bolt hole at 0° azimuthal angle
[3] flanges # 1 and # 2 need to be concentric and parallel
[4] hole pattern: straddle vertical center line, tapped holes; this flange is very critical for focal point and azimuthal angle

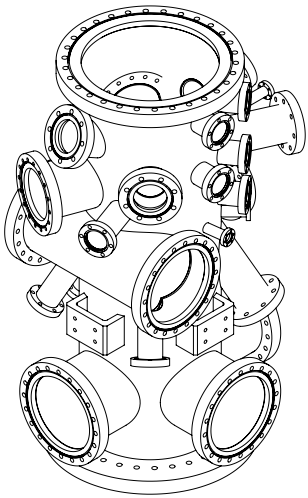

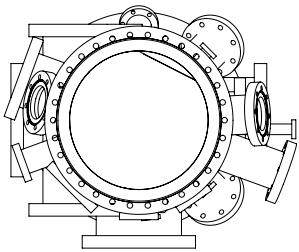

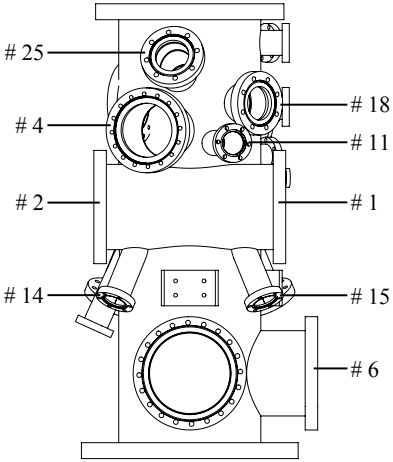
25
4
2
14
18
11
1
15
6

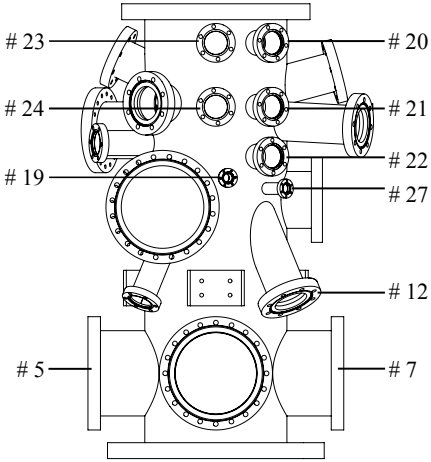
23
24
19
5
20
21
22
27
12
7

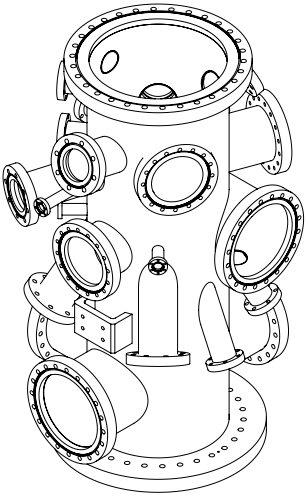

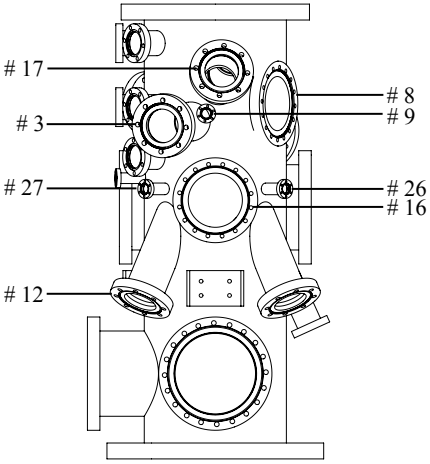
17
3
27
12
8
9
26
16

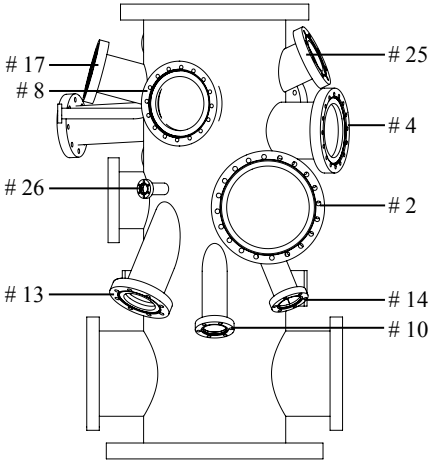
17
8
26
13
25
4
2
14
10

Appendix B

Scanning tunneling spectroscopy fit

We fitted the observed step in dI/dV with the expected inelastic electron tunneling functional form (*24*) to extract the excitation threshold and the step-width. Small differences between the absolute conductance are due to small experimental variations in the height of the tip above the atom. The conductance step is scaled in Figures 3.6 A and 3.7 A, to make the different magnetic field data directly comparable.

The step height, position, step width and vertical offset are fitting parameters. For the smallest AC excitation amplitudes the fitted width for Fe at 0 T is 0.7 mV. This width corresponds to 5.5 $k_{\mathrm{B}}T$ in the case of a thermally broadened transition, resulting in T = 1.5 K. For the Co the width at 0 T is 1.5 mV, which results in T = 3.1 K. Thus the extracted equivalent temperature for both atoms is larger than the 0.6 – 0.7 K measurement temperature. We have excluded the applied AC voltage as a possible broadening source: reducing the rms value does not affect the transition width.

The position of the two separate steps at 4 and 6 T are fitted with the sum of two inelastic electron tunneling functional forms with the same width. Figure

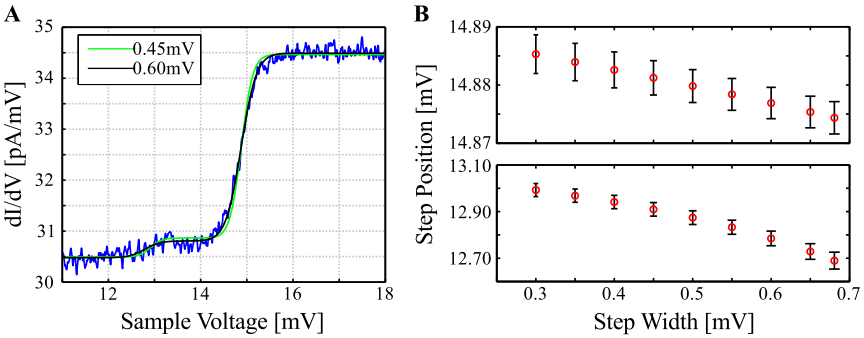

Figure B.1: (**A**) Zoom-in on the Fe's SES step at 6 T (blue) and two fits with a double step of fixed width: of 0.45 meV (green) and 0.6 meV (black). (V = 30 mV, I = 1 nA). (**B**) The position of the low energy (bottom panel) and high energy step (top panel) extracted from the fit to the 6 T data, as a function of fixed SES width.

B.1 A shows how such a fit to the 6 T spectrum of Fe looks like for 2 different width. The heights and position of the steps were allowed to vary independently. Interestingly, the width of the two separate steps at 6 T is 0.65 mV which is smaller than the 0 T step width. For both atoms, the splitting between the two steps in the 2 T data is not sufficiently large to resolve them well.

We ensure that the extracted step positions are robust against changes in the fitting parameters by fitting the double SES step for several different fixed step width ranging from 0.3 to 0.65 mV (0.3 to 1.2 mV) for Fe (Co, respectively). The resulting step positions for Fe are shown in Figure B.1 B. For Fe the position of the smaller step varies by 0.30 mV the one of the higher energy step by 0.01 mV in the given range. For the extracted step used in the main text the fit width employed is 0.3 mV which results in a difference between the two step positions of 1.9$\pm$0.3 mV at 6 T. The error bar is based on the variation in the step position when fitted with different fixed step widths. The same procedure was used for the Co magnetic field dependence and for the Fe and Co current-dependence.

Appendix C

List of free atom wave functions

For the d^2/d^8-configuration we show the free atom wave functions of all multiplets. For all other d^N only the lowest lying multiplet's wave functions are written out, we refer to Slater Vol. II, Appendix 24 (*51*) for additional wave functions.

The wave functions are labeled with their m_{l_i} and m_{s_i} quantum numbers: e.g. $(0^+, 1^-)$ represents the Slater determinant (fully anti-symmetrized wave function) with the first electron having $m_{l_1} = 0$ and $m_{s_1} = +\frac{1}{2} = +$ while the second electron has $m_{l_2} = 1$ and $m_{s_2} = -\frac{1}{2} = -$. Both electrons are in a d state so their m_{l_i} quantum numbers can take the values: $2, 1, ..., -2$, m_{s_i} can be $+$ or $-$. In the example the resulting total quantum numbers are $M_L = 1$ and $M_S = 0$.

C.1 Wave functions of the d^2/d^8-configuration

For the d^2-configuration the following multiplets exist: ^3F, ^3P, ^1G, ^1D and ^1S. The ground state multiplet is the ^3F term. For a d^8-configuration these wave functions represent holes rather than electrons.

M_L	M_S	${}^3F$ wave function
3	1	$(2^+, 1^+)$
3	0	$\frac{1}{\sqrt{2}}((2^+, 1^-) + (2^-, 1^+))$
3	−1	$(2^-, 1^-)$
2	1	$(2^+, 0^+)$
2	0	$\frac{1}{\sqrt{2}}((2^+, 0^-) + (2^-, 0^+))$
2	−1	$(2^-, 0^-)$
1	1	$\frac{1}{\sqrt{5}}(\sqrt{3}(2^+, -1^+) + \sqrt{2}(1^+, 0^+))$
1	0	$\frac{1}{\sqrt{10}}(\sqrt{3}(2^+, -1^-) + \sqrt{3}(2^-, -1^+) + \sqrt{2}(1^+, 0^-) + \sqrt{2}(1^-, 0^+))$
1	−1	$\frac{1}{\sqrt{5}}(\sqrt{3}(2^-, -1^-) + \sqrt{2}(1^-, 0^-))$
0	1	$\frac{1}{\sqrt{5}}((2^+, -2^+) + 2(1^+, -1^+))$
0	0	$\frac{1}{\sqrt{10}}((2^+, -2^-) + (2^-, -2^+) + 2(1^+, -1^-) + 2(1^-, -1^+))$
0	−1	$\frac{1}{\sqrt{5}}((2^-, -2^-) + 2(1^-, -1^-))$
−1	1	$\frac{1}{\sqrt{5}}(\sqrt{3}(-2^+, 1^+) + \sqrt{2}(-1^+, 0^+))$
−1	0	$\frac{1}{\sqrt{10}}(\sqrt{3}(-2^+, 1^-) + \sqrt{3}(-2^-, 1^+) + \sqrt{2}(-1^+, 0^-) + \sqrt{2}(-1^-, 0^+))$
−1	−1	$\frac{1}{\sqrt{5}}(\sqrt{3}(-2^-, 1^-) + \sqrt{2}(-1^-, 0^-))$
−2	1	$(-2^+, 0^+)$
−2	0	$\frac{1}{\sqrt{2}}((-2^+, 0^-) + (-2^-, 0^+))$
−2	−1	$(-2^-, 0^-)$
−3	1	$(2^+, 1^+)$
−3	0	$\frac{1}{\sqrt{2}}((-2^+, -1^-) + (-2^-, -1^+))$
−3	−1	$(-2^-, -1^-)$

M_L	M_S	^3P wave function
1	1	$\frac{1}{\sqrt{5}}(\sqrt{2}(2^+,-1^+)-\sqrt{3}(1^+,0^+))$
1	0	$\frac{1}{\sqrt{10}}(\sqrt{2}(2^+,-1^-)+\sqrt{2}(2^-,-1^+)-\sqrt{3}(1^+,0^-)$ $-\sqrt{3}(1^-,0^+))$
1	−1	$\frac{1}{\sqrt{5}}(\sqrt{2}(2^-,-1^-)-\sqrt{3}(1^-,0^-))$
0	1	$\frac{1}{\sqrt{5}}(2(2^+,-2^+)-(1^+,-1^+))$
0	0	$\frac{1}{\sqrt{10}}(2(2^+,-2^-)+2(2^-,-2^+)-(1^+,-1^-)-(1^-,-1^+))$
0	−1	$\frac{1}{\sqrt{5}}(2(2^-,-2^-)-(1^-,-1^-))$
−1	1	$\frac{1}{\sqrt{5}}(\sqrt{2}(-2^+,1^+)-\sqrt{3}(-1^+,0^+))$
−1	0	$\frac{1}{\sqrt{10}}(\sqrt{2}(-2^+,1^-)+\sqrt{2}(-2^-,1^+)-\sqrt{3}(-1^+,0^-)$ $-\sqrt{3}(-1^-,0^+))$
−1	−1	$\frac{1}{\sqrt{5}}(\sqrt{2}(-2^-,1^-)-\sqrt{3}(-1^-,0^-))$

M_L	M_S	^1G wave function
4	0	$(2^+,2^-)$
3	0	$\frac{1}{\sqrt{2}}((2^+,1^-)-(2^-,1^+))$
2	0	$\frac{1}{\sqrt{14}}(\sqrt{3}(2^+,0^-)-\sqrt{3}(2^-,0^+)+\sqrt{8}(1^+,1^-))$
1	0	$\frac{1}{\sqrt{14}}((2^+,-1^-)-(2^-,-1^+)+\sqrt{6}(1^+,0^-)-\sqrt{6}(1^-,0^+))$
0	0	$\frac{1}{\sqrt{70}}((2^+,-2^-)-(2^-,-2^+)+4(1^+,-1^-)-4(1^-,-1^+)$ $+6(0^+,0^-))$
−1	0	$\frac{1}{\sqrt{14}}((-2^+,1^-)-(-2^-,1^+)+\sqrt{6}(-1^+,0^-)$ $-\sqrt{6}(-1^-,0^+))$
−2	0	$\frac{1}{\sqrt{14}}(\sqrt{3}(-2^+,0^-)-\sqrt{3}(-2^-,0^+)+\sqrt{8}(-1^+,-1^-))$
−3	0	$\frac{1}{\sqrt{2}}((-2^+,-1^-)-(-2^-,-1^+))$
−4	0	$(2^+,2^-)$

M_L	M_S	^1D wave function
2	0	$\frac{1}{\sqrt{7}}(\sqrt{2}(2^+,0^-)+\sqrt{2}(2^-,0^+)-\sqrt{3}(1^+,1^-))$
1	0	$\frac{1}{\sqrt{14}}(\sqrt{6}(2^+,-1^-)-\sqrt{6}(2^-,-1^+)-(1^+,0^-)+(1^-,0^+))$
0	0	$\frac{1}{\sqrt{14}}(2(2^+,-2^-)-2(2^-,-2^+)+(1^+,-1^-)-(1^-,-1^+)$ $-2(0^+,0^-))$
-1	0	$\frac{1}{\sqrt{14}}(\sqrt{6}(-2^+,1^-)-\sqrt{6}(-2^-,1^+)-(-1^+,0^-)$ $+(-1^-,0^+))$
-2	0	$\frac{1}{\sqrt{7}}(\sqrt{2}(-2^+,0^-)+\sqrt{2}(-2^-,0^+)-\sqrt{3}(-1^+,-1^-))$

M_L	M_S	^1S wave function
0	0	$\frac{1}{\sqrt{5}}((2^+,-2^-)-(2^-,-2^+)-(1^+,-1^-)+(1^-,-1^+)$ $+(0^+,0^-))$

C.2 Wave functions of the d^3/d^7-configuration

The d^3/d^7-configuration has the following multiplets: ${}^4F$, ${}^4P$, ${}^2H$, ${}^2G$, ${}^2F$, ${}^2D_1$, ${}^2D_2$ and ${}^2P$. The lowest term is the ${}^4F$ multiplet. Here, only the wave functions for positive M_L and positive M_S are shown.

M_L	M_S	${}^4F$ wave function
3	$\frac{3}{2}$	$(2^+, 1^+, 0^+)$
3	$\frac{1}{2}$	$\frac{1}{\sqrt{3}}((2^+, 1^+, 0^-) + (2^-, 1^+, 0^+) + (2^+, 1^-, 0^+))$
2	$\frac{3}{2}$	$(2^+, 1^+, -1^+)$
2	$\frac{1}{2}$	$\frac{1}{\sqrt{3}}((2^+, 1^+, -1^-) + (2^-, 1^+, -1^+) + (2^+, 1^-, -1^+))$
1	$\frac{3}{2}$	$\frac{1}{\sqrt{5}}(\sqrt{2}(2^+, 1^+, -2^+) + \sqrt{3}(2^+, 0^+, -1^+))$
1	$\frac{1}{2}$	$\frac{1}{\sqrt{15}}(\sqrt{2}(2^+, 1^+, -2^-) + \sqrt{3}(2^+, 0^+, -1^-)$ $+ \sqrt{2}(2^-, 1^+, -2^+) + \sqrt{3}(2^-, 0^+, -1^+)$ $+ \sqrt{3}(2^+, 0^-, -1^+) + \sqrt{2}(2^+, 1^-, -2^+))$
0	$\frac{3}{2}$	$\frac{1}{\sqrt{5}}(2(2^+, 0^+, -2^+) + (1^+, 0^+, -1^+))$
0	$\frac{1}{2}$	$\frac{1}{\sqrt{15}}(2(2^+, 0^+, -2^-) + 2(2^-, 0^+, -2^+)$ $+ 2(2^+, 0^-, -2^+) + (1^+, 0^+, -1^-)$ $+ (1^-, 0^+, -1^+) + (1^+, 0^-, -1^+))$

C.3 Wave functions of the d^4/d^6-configuration

For the d^4/d^6-configuration the following multiplets exist (ordered from lowest to highest energy): ${}^5D$, ${}^3H$, ${}^3G$, ${}^3F_1$, ${}^3F_2$, ${}^3D$, ${}^3P_1$, ${}^3P_2$, ${}^1I$, ${}^1G_1$, ${}^1G_2$, ${}^1F$, ${}^1D_1$, ${}^1D_2$, ${}^1S_1$ and ${}^1S_2$. We only show the wave functions for positive M_L and M_S.

M_L	M_S	${}^5D$ wave function
2	2	$(-1^+, 0^+, 1^+, 2^+)$
2	1	$\frac{1}{2}(-(-1^-, 0^+, 1^+, 2^+) - (-1^+, 0^-, 1^+, 2^+)$
		$- (-1^+, 0^+, 1^-, 2^+) - (-1^+, 0^+, 1^+, 2^-))$
2	0	$\frac{1}{\sqrt{6}}(-(-1^-, 0^-, 1^+, 2^+) - (-1^+, 0^-, 1^-, 2^+)$
		$- (-1^+, 0^+, 1^-, 2^-) - (-1^-, 0^+, 1^-, 2^+)$
		$- (-1^-, 0^+, 1^+, 2^-) - (-1^+, 0^-, 1^+, 2^-))$
1	2	$-(-2^+, 0^+, 1^+, 2^+)$
1	1	$\frac{1}{2}(-(-2^-, 0^+, 1^+, 2^+) - (-2^+, 0^-, 1^+, 2^+)$
		$- (-2^+, 0^+, 1^-, 2^+) - (-2^+, 0^+, 1^+, 2^-))$
1	0	$\frac{1}{\sqrt{6}}(-(-2^-, 0^-, 1^+, 2^+) - (-2^+, 0^-, 1^-, 2^+)$
		$- (-2^+, 0^+, 1^-, 2^-) - (-2^-, 0^+, 1^-, 2^+)$
		$- (-2^-, 0^+, 1^+, 2^-) - (-2^+, 0^-, 1^+, 2^-))$
0	2	$-(-2^+, -1^+, 1^+, 2^+)$
0	1	$\frac{1}{2}(-(-2^-, -1^+, 1^+, 2^+) - (-2^+, -1^-, 1^+, 2^+)$
		$- (-2^+, -1^+, 1^-, 2^+) - (-2^+, -1^+, 1^+, 2^-))$
0	0	$\frac{1}{\sqrt{6}}(-(2^+, 1^+, -1^-, -2^-) - (2^-, 1^-, -1^+, -2^+)$
		$- (2^+, 1^-, -1^+, -2^-) - (2^-, 1^+, -1^-, -2^+)$
		$- (2^-, 1^+ - 1^+, -2^-) - (2^+, 1^-, -1^-, -2^+)$

C.4 Wave functions of the d^5-configuration

The d^5-configuration has the following multiplets: ${}^6S$, ${}^4G$, ${}^4F$, ${}^4D$, ${}^4P$, ${}^2I$, ${}^2H$, ${}^2G_1$, ${}^2G_2$, ${}^2F_1$, ${}^2F_2$, ${}^2D_1$, ${}^2D_2$, ${}^2D_3$, ${}^2P$ and ${}^2S$. Only wave functions with positive M_S are shown.

M_L	M_S	${}^1S$ wave function
0	5/2	$-(-2^+,-1^+,0^+,1^+,2^+)$
0	3/2	$\frac{1}{\sqrt{5}}(-(2^+,1^+,0^+,-1^+,-2^-)-(2^-,1^+,0^+,-1^+,-2^+)$
		$-(2^+,1^-,0^+,-1^+,-2^+)-(2^+,1^+,0^+,-1^-,-2^+)$
		$-(2^+,1^+,0^-,-1^+,-2^+))$
0	1/2	$\frac{1}{\sqrt{10}}(-(2^+,1^+,0^+,-1^-,-2^-)-(2^-,1^-,0^+,-1^+,-2^+)$
		$-(2^+,1^-,0^+,-1^+,-2^-)-(2^-,1^+,0^+,-1^-,-2^+)$
		$-(2^-,1^+,0^+,-1^+,-2^-)-(2^+,1^-,0^+,-1^-,-2^+)$
		$-(2^+,1^+,0^-,-1^+,-2^-)-(2^+,1^+,0^-,-1^-,-2^+)$
		$-(2^+,1^-,0^-,-1^+,-2^+)-(2^-,1^+,0^-,-1^+,-2^+))$

Appendix D

Matrix elements for four-fold symmetric ligand field

D.1 Single electron matrix elements

As derived in the main text, the energy eigenstates for a single electron (the matrix elements) of a certain ligand field potential $V_n^m(\vec{r}_i)$ can be determined by direct integration over the individual wave functions. For the integral, both the single electron wave functions and the ligand field potential are represented as products with spherical harmonics (see main text). The energy eigenstates E_i of a single $3d$ electron are equivalent to the eigenstates of a d^1-configuration with the wave functions $\Psi_i(\vec{r}_i) = R_{n_i}(r_i)Y_{l_i}^{m_{l_i}}(\theta_i, \phi_i)$. They are:

$$\begin{aligned} E_i(n,m) &= -\frac{1}{4\pi\epsilon_0}\ \langle\Psi_i|q_i V_n^m(\vec{r}_i)|\Psi_i\rangle \\ &= -\frac{q_i}{4\pi\epsilon_0}\ \int_0^{2\pi}\int_0^{\pi}\int_0^{\infty} \Psi_i^*(\vec{r}_i)\, r_i^n \gamma_{nm} Y_n^m(\theta_i,\phi_i)\, \Psi_i(\vec{r}_i)\ r_i^2 sin(\theta_i)\ dr_i\, d\theta_i\, d\phi_i \end{aligned} \tag{D.1}$$

The radial and the angular parts of this integral can be separated. The radial part is often not accurately known and it is thus used as a parameter $\langle r^n \rangle = \int_0^\infty R_{n_i}(r_i)^2 r_i^n r_i^2 dr_i$. This parameter is given in several tables, e.g. by Abragam and Bleaney (*31*) (see Table D.1, below). The separation of the radial part leaves the integration over the spherical harmonics when determining the matrix elements of a single electron wave function.

Look-up table for radial part

	$\langle r^2 \rangle$	$\langle r^4 \rangle$
Mn^{2+}	1.548	5.513
Fe^{2+}	1.393	4.496
Co^{2+}	1.251	3.655
Ni^{2+}	1.130	3.003
Cu^{2+}	1.028	2.498

Table D.1: Free ion values of the radial averages for ions on the $3d$-transition metal elements as tabulated by Abragam and Bleaney (*31*). Values are in atomic units a_0 = 0.529 Å.

The following tables show the single electron matrix elements for $3d$ wave functions in a four-fold symmetric ligand field (V_0^0, V_2^0, V_4^0 and V_4^4 potentials). Each entry in the table represents the following integral: $\int_0^{2\pi} \int_0^{\pi} Y_{l_i}^{m_{l_i}*} Y_n^m Y_{l_i}^{m_{l_i}} \, sin(\theta) \, d\theta \, d\phi$.

To obtain the eigenenergies of an atom in a d^1 or d^9 configuration the all elements need to be multiplied by the prefactor $-\frac{q_M}{4\pi\epsilon_0}\langle r^n \rangle \gamma_{nm}$ (as explained in the main text).

l_i, m_{l_i}	2,−2	2,−1	2, 0	2, 1	2, 2
2,−2	$\frac{1}{2}\sqrt{\frac{1}{\pi}}$				
2,−1		$\frac{1}{2}\sqrt{\frac{1}{\pi}}$			
2, 0			$\frac{1}{2}\sqrt{\frac{1}{\pi}}$		
2, 1				$\frac{1}{2}\sqrt{\frac{1}{\pi}}$	
2, 2					$\frac{1}{2}\sqrt{\frac{1}{\pi}}$

Table D.2: Table shows the single electron matrix elements for V_0^0.

l_i, m_{l_i}	2,−2	2,−1	2, 0	2, 1	2, 2
2,−2	$\frac{-1}{7}\sqrt{\frac{5}{\pi}}$				
2,−1		$\frac{1}{14}\sqrt{\frac{5}{\pi}}$			
2, 0			$\frac{1}{7}\sqrt{\frac{5}{\pi}}$		
2, 1				$\frac{1}{14}\sqrt{\frac{5}{\pi}}$	
2, 2					$\frac{-1}{7}\sqrt{\frac{5}{\pi}}$

Table D.3: Table shows the single electron matrix elements for V_2^0.

l_i, m_{l_i}	2,−2	2,−1	2, 0	2, 1	2, 2
2,−2	$\frac{1}{14}\sqrt{\frac{1}{\pi}}$				
2,−1		$\frac{-2}{7}\sqrt{\frac{1}{\pi}}$			
2, 0			$\frac{3}{7}\sqrt{\frac{1}{\pi}}$		
2, 1				$\frac{-2}{7}\sqrt{\frac{1}{\pi}}$	
2, 2					$\frac{1}{14}\sqrt{\frac{1}{\pi}}$

Table D.4: Table shows the single electron matrix elements for V_4^0.

l_i, m_{l_i}	2,−2	2,−1	2, 0	2, 1	2, 2
2,−2					$\frac{1}{7}\sqrt{\frac{70}{\pi}}$
2,−1					
2, 0					
2, 1					
2, 2	$\frac{1}{7}\sqrt{\frac{70}{\pi}}$				

Table D.5: Table shows the single electron matrix elements for V_4^4.

Comments about the matrix elements following from the direct integration:

As done in the previous tables one could determining the matrix elements for other possible V_n^m matrix elements. However, in a four-fold symmetric ligand field the matrix elements shown above are the only non-zero terms in the potential. Thus:

1. All terms of $n > 2l_i$, where l_i is the orbital quantum number of the single magnetic electrons, vanish.

2. Operators of the form Y_n^m have zero matrix elements between two states Φ_{l_1} and Φ_{l_2}, unless $l_1 + l_2 + n =$ even number. This means that within a given configuration, meaning a given l_i, the matrix elements of odd-n terms vanish, however, they could potentially couple different configurations together. For example Y_1^0 can link s to p electrons and p to d and Y_2^0 can link s to d.

3. Operators of the form Y_n^m have zero matrix element between two states $\Phi_{l_1}^{m_{l_1}}$ and $\Phi_{l_2}^{m_{l_2}}$ unless $m = |m_{l_1} - m_{l_2}|$. So the terms Y_n^m will link states with $\Delta L_z = m$.

Note that not all of these remarks are relevant for our particular point charge calculation but they would become relevant if one decided to do calculations similar to the full multiplet calculation.

D.2 Multi-electron matrix elements for a four-fold symmetric ligand field

The ligand field potential acts on each electron individually. Therefore, we can determine the multi-electron matrix elements by summing over the single electron matrix elements. Here we show the multi-electron matrix elements for Ni, Co and Fe, without the prefactor $-\frac{q_M}{4\pi\epsilon_0}\langle r^n\rangle\gamma_{nm}$.

D.2.1 Multi-electron matrix elements for Ni

Here we give a list of the matrix elements for the ${}^3F$ term in the d^2-configuration, which is equivalent to the nickel's d^8-configuration when seen as the hole configuration (in that case, these potentials would need to be multiplied by -1). The prefactor is $\alpha = \frac{1}{14}\sqrt{\frac{1}{\pi}}$, additionally all elements need to be multiplied by $p = -\frac{q_M}{4\pi\epsilon_0}\langle r^n\rangle\gamma_{nm}$ to obtain the energy eigenstates.

M_L	-3	-2	-1	0	1	2	3
-3	14α						
-2		14α					
-1			14α				
0				14α			
1					14α		
2						14α	
3							14α

Table D.6: Table shows the matrix elements for V_0^0 for the ${}^3F$ multiplet in the d^2-configuration.

M_L	-3	-2	-1	0	1	2	3
-3	$-\sqrt{5}\alpha$						
-2		0					
-1			$\frac{3\sqrt{5}}{5}\alpha$				
0				$\frac{4\sqrt{5}}{5}\alpha$			
1					$\frac{3\sqrt{5}}{5}\alpha$		
2						0	
3							$-\sqrt{5}\alpha$

Table D.7: Table shows the matrix elements for V_2^0 for the ${}^3F$ multiplet in the d^2-configuration.

M_L	-3	-2	-1	0	1	2	3
-3	-3α						
-2		7α					
-1			-1α				
0				-6α			
1					-1α		
2						7α	
3							-3α

Table D.8: Table shows the matrix elements for V_4^0 for the ${}^3F$ multiplet in the d^2-configuration.

M_L	-3	-2	-1	0	1	2	3
-3					$-2\sqrt{42}$		
-2						$-2\sqrt{70}$	
-1							$-2\sqrt{42}$
0							
1	$-2\sqrt{42}$						
2		$-2\sqrt{70}$					
3			$-2\sqrt{42}$				

Table D.9: Table shows the matrix elements for V_4^4 for the ${}^3F$ multiplet in the d^2-configuration. The elements in this matrix need to be multiplied by α.

D.2.2 Multi-electron matrix elements for Co

Here we give a list of the matrix elements for the ${}^4F$ term in the d^3-configuration, which is equivalent to the cobalt's d^7-configuration when seen as the hole configuration (thus these potentials would need to be multiplied by -1). The prefactor is $\alpha = \frac{1}{14}\sqrt{\frac{1}{\pi}}$, additionally all elements need to be multiplied by $p = -\frac{q_M}{4\pi\epsilon_0}\langle r^n\rangle\gamma_{nm}$ to obtain the energy eigenstates.

M_L	-3	-2	-1	0	1	2	3
-3	21α						
-2		21α					
-1			21α				
0				21α			
1					21α		
2						21α	
3							21α

Table D.10: Table shows the matrix elements for V_0^0 for the ${}^4F$ multiplet in the d^3-configuration.

M_L	-3	-2	-1	0	1	2	3
-3	$\sqrt{5}\alpha$						
-2		0					
-1			$\frac{-3\sqrt{5}}{5}\alpha$				
0				$\frac{-4\sqrt{5}}{5}\alpha$			
1					$\frac{-3\sqrt{5}}{5}\alpha$		
2						0	
3							$\sqrt{5}\alpha$

Table D.11: Table shows the matrix elements for V_2^0 for the ${}^4F$ multiplet in the d^3-configuration.

M_L	-3	-2	-1	0	1	2	3
-3	3α						
-2		-7α					
-1			1α				
0				6α			
1					1α		
2						-7α	
3							3α

Table D.12: Table shows the matrix elements for V_4^0 for the ${}^4F$ multiplet in the d^3-configuration.

M_L	-3	-2	-1	0	1	2	3
-3					$2\sqrt{42}\alpha$		
-2						$2\sqrt{70}\alpha$	
-1							$2\sqrt{42}\alpha$
0							
1	$2\sqrt{42}\alpha$						
2		$2\sqrt{70}\alpha$					
3			$2\sqrt{42}\alpha$				

Table D.13: Table shows the matrix elements for V_4^4 for the ${}^4F$ multiplet in the d^3-configuration.

D.2.3 Multi-electron matrix elements for Fe

Here we give a list of the matrix elements for the ${}^5D$ term in the d^4-configuration, which is equivalent to the iron's d^6-configuration when seen as the hole configuration (thus these potentials would need to be multiplied by -1). The prefactor is $\alpha = \frac{1}{14}\sqrt{\frac{1}{\pi}}$, additionally all elements need to be multiplied by $p = -\frac{q_M}{4\pi\epsilon_0}\langle r^n\rangle\gamma_{nm}$ to obtain the energy eigenstates.

M_L	-2	-1	0	1	2
-2	28α				
-1		28α			
0			28α		
1				28α	
2					28α

Table D.14: Table shows the matrix elements for V_0^0 for the ${}^5D$ multiplet in the d^4-configuration.

M_L	-2	-1	0	1	2
-2	$2\sqrt{5}\alpha$				
-1		$-1\sqrt{5}\alpha$			
0			$-2\sqrt{5}\alpha$		
1				$-1\sqrt{5}\alpha$	
2					$2\sqrt{5}\alpha$

Table D.15: Table shows the matrix elements for V_2^0 for the ${}^5D$ multiplet in the d^4-configuration.

M_L	-2	-1	0	1	2
-2	-1α				
-1		4α			
0			-6α		
1				4α	
2					-1α

Table D.16: Table shows the matrix elements for V_4^0 for the ${}^5D$ multiplet in the d^4-configuration.

M_L	-2	-1	0	1	2
-2					$-2\sqrt{70}\alpha$
-1					
0					
1					
2	$-2\sqrt{70}\alpha$				

Table D.17: Table shows the matrix elements for V_4^4 for the ${}^5D$ multiplet in the d^4-configuration.

Appendix E

Stevens operator equivalents

In this appendix we would like to demonstrate how to empirically determine the Stevens operator equivalent prefactors B_n^m and how those compare to the original calculation from Stevens and Bleaney (*32*,*57*).

E.1 List of the relevant Stevens operator equivalents

$$\begin{aligned}\hat{O}_2^0 =& 3\hat{L}_z^2 - L(L+1)\\ \hat{O}_4^0 =& 35\hat{L}_z^4 - (30L(L+1)-25)\hat{L}_z^2 + 3L^2(L+1)^2 - 6L(L+1)\\ \hat{O}_4^4 =& \frac{1}{2}(\hat{L}_+^4 + \hat{L}_-^4)\end{aligned} \tag{E.1}$$

E.2 Transformation to Stevens operator equivalents

We show here an empirical determination of the prefactors needed for the Stevens operator equivalents.

$$
\begin{aligned}
B_2^0 =&(\langle r^2\rangle q_M\gamma_{20})p\cdot\frac{V_2^0}{\hat{O}_2^0}=\frac{(\langle r^2\rangle q_M\gamma_{20})p\cdot V_2^0}{(3\hat{L}_z^2-L(L+1))}\\
B_4^0 =&((\langle r^4\rangle q_M\gamma_{40})p\cdot\frac{V_4^0}{\hat{O}_4^0}\\
=&\frac{\langle r^4\rangle q_M\gamma_{40})p\cdot V_4^0}{(35\hat{L}_z^4-(30L(L+1)-25)\hat{L}_z^2+3L^2(L+1)^2-6L(L+1))}\\
B_4^4 =&(\langle r^4\rangle q_M\gamma_{44})p\cdot\frac{V_4^4}{\hat{O}_4^4}=\frac{(\langle r^4\rangle q_M\gamma_{44})p\cdot V_4^4}{(0.5(\hat{L}_+^4+\hat{L}_-^4))}
\end{aligned}
\tag{E.2}
$$

For the transformation one can use any matrix element. Here we show the explicit calculation for each element, using those matrix elements that belong to the largest M_L. We use the Fe atom as base atom and find multiplying factors (x_n) for other transition metal atoms with respect to Fe. The transformation between the two notations is then the following for different elements:

$$
\begin{aligned}
\text{Fe}: B_2^0 =&(\langle r^2\rangle q_M\gamma_{20})p\cdot\frac{2\sqrt{5}\alpha}{6}=(\langle r^2\rangle q_M\gamma_{20})\cdot\frac{p}{42}\sqrt{\frac{5}{\pi}}\\
=&(\langle r^2\rangle q_M\gamma_{20})\cdot a\\
B_4^0 =&(\langle r^4\rangle q_M\gamma_{40})p\cdot\frac{-1\alpha}{12}=(\langle r^4\rangle q_M\gamma_{40})\cdot\frac{-p}{168}\sqrt{\frac{1}{\pi}}\\
=&(\langle r^4\rangle q_M\gamma_{40})\cdot b\\
B_4^4 =&(\langle r^4\rangle q_M\gamma_{44})p\cdot\frac{-2\sqrt{70}\alpha}{\frac{1}{2}24}=(\langle r^4\rangle q_M\gamma_{44})\cdot\frac{-p}{84}\sqrt{\frac{70}{\pi}}\\
=&(\langle r^4\rangle q_M\gamma_{40})\cdot c
\end{aligned}
\tag{E.3}
$$

where a, b and c are the base prefactors used for all elements.

$$\begin{aligned}
\text{Co}: B_2^0 =& (\langle r^2\rangle q_M \gamma_{20}) p \cdot \frac{\sqrt{5}\alpha}{15} = (\langle r^2\rangle q_M \gamma_{20}) \cdot \frac{p}{42}\sqrt{\frac{1}{5\pi}} \\
=& (\langle r^2\rangle q_M \gamma_{20}) \cdot \frac{1}{5} a = (\langle r^2\rangle q_M \gamma_{20}) \cdot a \cdot x_2 \\
B_4^0 =& (\langle r^4\rangle q_M \gamma_{40}) p \cdot \frac{3\alpha}{180} = (\langle r^4\rangle q_M \gamma_{40}) \cdot \frac{p}{5 \cdot 168}\sqrt{\frac{1}{\pi}} \\
=& (\langle r^4\rangle q_M \gamma_{40}) \cdot \frac{1}{5} b = (\langle r^4\rangle q_M \gamma_{40}) \cdot b \cdot x_4 \\
B_4^4 =& (\langle r^4\rangle q_M \gamma_{44}) p \cdot \frac{2\sqrt{70}\alpha}{\frac{1}{2}120} = (\langle r^4\rangle q_M \gamma_{44}) \cdot \frac{p}{5 \cdot 84}\sqrt{\frac{70}{\pi}} \\
=& (\langle r^4\rangle q_M \gamma_{40}) \cdot \frac{1}{5} c = (\langle r^4\rangle q_M \gamma_{40}) \cdot c \cdot x_4
\end{aligned} \tag{E.4}$$

with $x_2 = -x_4 = 1/5$, thus $x_4 = -1/5$.

$$\begin{aligned}
\text{Ni}: B_2^0 =& (\langle r^2\rangle q_M \gamma_{20}) p \cdot \frac{-\sqrt{5}\alpha}{15} = (\langle r^2\rangle q_M \gamma_{20}) \cdot \frac{-p}{42}\sqrt{\frac{1}{5\pi}} \\
=& (\langle r^2\rangle q_M \gamma_{20}) \cdot \frac{-1}{5} a = (\langle r^2\rangle q_M \gamma_{20}) \cdot a \cdot x_2 \\
B_4^0 =& (\langle r^4\rangle q_M \gamma_{40}) p \cdot \frac{-3\alpha}{180} = (\langle r^4\rangle q_M \gamma_{40}) \cdot \frac{-p}{5 \cdot 168}\sqrt{\frac{1}{\pi}} \\
=& (\langle r^4\rangle q_M \gamma_{40}) \cdot \frac{-1}{5} b = (\langle r^4\rangle q_M \gamma_{40}) \cdot b \cdot x_4 \\
B_4^4 =& (\langle r^4\rangle q_M \gamma_{44}) p \cdot \frac{-2\sqrt{70}\alpha}{\frac{1}{2}120} = (\langle r^4\rangle q_M \gamma_{44}) \cdot \frac{-p}{5 \cdot 84}\sqrt{\frac{70}{\pi}} \\
=& (\langle r^4\rangle q_M \gamma_{40}) \cdot \frac{-1}{5} c = (\langle r^4\rangle q_M \gamma_{40}) \cdot c \cdot x_4
\end{aligned} \tag{E.5}$$

with $x_2 = -x_4 = -1/5$, thus $x_4 = 1/5$.

Here, p is the prefactor for the electrostatic potential: $p = -\frac{1}{4\pi\epsilon_0}$, with e the elementary charge and ϵ_0 the electric constant (for SI units) and α is the prefactor used in the transformation from single to multi-electron wave functions of Chapter D ($\alpha = \frac{1}{14}\sqrt{\frac{1}{\pi}}$).

Prefactors as defined by Stevens

Stevens and Bleaney determined the prefactors needed for the transformation between the multi-electron wave function approach and the operator equivalent method as follows (*32*,*56*,*57*):

$$\begin{aligned} B_2^m =& \alpha_J \cdot (Y_2^m - \text{prefactor}) \cdot (\langle r^2 \rangle q_M \gamma_{2m}) \\ B_4^m =& \beta_J \cdot (Y_4^m - \text{prefactor}) \cdot (\langle r^4 \rangle q_M \gamma_{4m}) \end{aligned} \tag{E.6}$$

more specifically for those Stevens operators we are interested in:

$$\begin{aligned} B_2^0 =& \alpha_J \cdot \frac{1}{4}\sqrt{\frac{5}{\pi}} \cdot (\langle r^2 \rangle q_M \gamma_{20}) \\ B_4^0 =& \beta_J \cdot \frac{3}{16}\sqrt{\frac{1}{\pi}} \cdot (\langle r^4 \rangle q_M \gamma_{40}) \\ B_4^4 =& \beta_J \cdot \frac{3}{16}\sqrt{\frac{35}{2\pi}} \cdot (\langle r^4 \rangle q_M \gamma_{44}) \end{aligned} \tag{E.7}$$

where:

$$\begin{aligned} \alpha_J &= \mp \frac{2(2l+1-4S)}{(2l-1)(2l+3)(2L-1)} \\ \beta_J &= \mp \frac{3(2l+1-4S)(-7(l-2S)(l-2S+1)+3(l-1)(l+2))}{(2l-3)(2l-1)(2l+3)(2l+5)(L-1)(2L-1)(2L-3)} \end{aligned} \tag{E.8}$$

a minus sign is used in the first half of the shell and a plus sign is used in the second half of the shell.

Therefore, the element specific factors in Stevens approach are α_J and β_J. To demonstrate that this results in the same prefactor as what is demonstrated in the main text, we will show this with two examples:

$$\begin{aligned} B_2^0(\text{Fe}) =& \alpha_J \cdot \frac{1}{4}\sqrt{\frac{5}{\pi}} \cdot (\langle r^2 \rangle q_M \gamma_{20}) = \frac{-2}{21} \cdot \frac{1}{4}\sqrt{\frac{5}{\pi}} \cdot (\langle r^2 \rangle q_M \gamma_{20}) \\ =& \frac{1}{42}\sqrt{\frac{5}{\pi}} \cdot (\langle r^2 \rangle q_M \gamma_{20}) = a \cdot (\langle r^2 \rangle q_M \gamma_{20}) \\ B_4^0(\text{Co}) =& \beta_J \cdot \frac{3}{16}\sqrt{\frac{1}{\pi}} \cdot (\langle r^4 \rangle q_M \gamma_{40}) = \frac{-2}{315} \cdot \frac{3}{16}\sqrt{\frac{1}{\pi}} \cdot (\langle r^4 \rangle q_M \gamma_{40}) \\ =& \frac{1}{168}\sqrt{\frac{1}{\pi}}\frac{-1}{5} \cdot (\langle r^4 \rangle q_M \gamma_{40}) = b \cdot x_4 \cdot (\langle r^4 \rangle q_M \gamma_{40}) \end{aligned} \tag{E.9}$$

Thus our results are identical with the Stevens approach. Here, the prefactor p for the electrostatic potential $p = \frac{-1}{4\pi\epsilon_0}$ is disregarded.

Appendix F

Tabulated values for point charge model calculation of 3d transition metal atoms

F.1 Radial matrix elements

(a) d^1 - d^4

		$\langle r^2 \rangle$	$\langle r^4 \rangle$
Ti^{3+}	^2D	1.893	7.071
V^{3+}	^3F	1.643	5.447
Cr^{3+}	^4F	1.447	4.297
Mn^{3+}	^5D	1.286	3.446

(b) d^5 - d^9

		$\langle r^2 \rangle$	$\langle r^4 \rangle$
Mn^{2+}	^6S	1.548	5.513
Fe^{2+}	^5D	1.393	4.496
Co^{2+}	^4F	1.251	3.655
Ni^{2+}	^3F	1.130	3.003
Cu^{2+}	^2D	1.028	2.498

Table F.1: Free ion values of the radial averages for ions of the 3d-transition metal elements as tabulated by Abragam and Bleaney (*31*). Values are in atomic units a_0 = 0.529 Å.

F.2 Spin-orbit coupling constants

(a) d^1 - d^4

		λ
Ti^{3+}	^2D	19.71
V^{3+}	^3F	13.14
Cr^{3+}	^4F	11.30
Mn^{3+}	^5D	10.80

(b) d^5 - d^9

		λ
Mn^{2+}	^6S	
Fe^{2+}	^5D	-12.77
Co^{2+}	^4F	-22.07
Ni^{2+}	^3F	-40.17
Cu^{2+}	^2D	-102.91

Table F.2: Spin-orbit coupling constants for ions of $3d$-transition metal elements as tabulated by Abragam and Bleaney (*31*). Values are in meV.

F.3 Element-specific Stevens prefactors

(a) d^1 - d^4

		x_2	x_4
Ti^{3+}	^2D	1	1
V^{3+}	^3F	1/5	$-1/5$
Cr^{3+}	^4F	$-1/5$	1/5
Mn^{3+}	^5D	-1	-1

(b) d^5 - d^9

		x_2	x_4
Mn^{2+}	^6S		
Fe^{2+}	^5D	1	1
Co^{2+}	^4F	1/5	$-1/5$
Ni^{2+}	^3F	$-1/5$	1/5
Cu^{2+}	^2D	-1	-1

Table F.3: Individual prefactors for each ion of the $3d$ transition metals, determined by the empirical method shown in the main text. (Consistent with $x_2 = \frac{\alpha_J}{(-2/21)}$ and $x_4 = \frac{\beta_J}{(+2/63)}$ as determined by Stevens (*31*,*32*,*56*,*57*).)

F.4 Formulas

F.4.1 Gamma

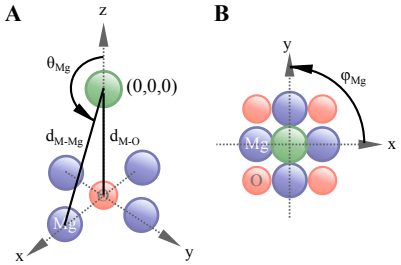

Figure F.1: Side (**A**) and top view (**B**) of the atom arrangement for a single magnetic atom on the four-fold MgO surface. (Identical to Figure 5.6 in the main text.)

$$
\begin{aligned}
\gamma_{20} &= \sum_j \frac{4\pi}{5}\frac{q_j}{R_j^3}Y_2^0(\theta_j,\phi_j) = 4\sqrt{\frac{\pi}{5}}\left(\frac{(3cos^2(\theta_{\text{Mg}})-1)q_{\text{Mg}}}{d^3_{\text{M-Mg}}} - \frac{q_{\text{O}}}{d^3_{\text{M-O}}}\right) \\
\gamma_{40} &= \sum_j \frac{4\pi}{9}\frac{q_j}{R_j^5}Y_4^0(\theta_j,\phi_j) \\
&= \frac{\sqrt{\pi}}{12}\left(\frac{q_{\text{Mg}}}{d^5_{\text{M-Mg}}}(35cos^4(\theta_{\text{Mg}}) - 30cos^2(\theta_{\text{Mg}}) + 3) + \frac{8q_{\text{O}}}{d^5_{\text{M-O}}}\right) \\
\gamma_{44} &= \sum_j \frac{4\pi}{9}\frac{q_j}{R_j^5}Y_4^{-4}(\theta_j,\phi_j) = \frac{q_{\text{Mg}}}{12}\sqrt{\frac{35\pi}{2}}\frac{4sin^4(\theta_{\text{Mg}})}{d^5_{\text{M-Mg}}}
\end{aligned}
\tag{F.1}
$$

Here, for ligand positions on the MgO surface in spherical coordinates (see Figure F.1): O: $(d_{\text{M-O}}, \pi, 0)$, Mg: $(d_{\text{M-Mg}}, \theta_{\text{Mg}}, 0)$, $(d_{\text{M-Mg}}, \theta_{\text{Mg}}, \pi/2)$, $(d_{\text{M-Mg}}, \theta_{\text{Mg}}, \pi)$ and $(d_{\text{M-Mg}}, \theta_{\text{Mg}}, 3\pi/2)$.

F.4.2 Stevens prefactors

$$\begin{aligned} B_2^0 =&(\langle r^2\rangle\gamma_{20}\cdot q_M)\cdot a\cdot x_2, \quad \text{with} \quad a=\frac{p}{42}\sqrt{\frac{5}{\pi}} \\ B_4^0 =&(\langle r^4\rangle\gamma_{40}\cdot q_M)\cdot b\cdot x_4, \quad \text{with} \quad b=-\frac{p}{168}\sqrt{\frac{1}{\pi}} \\ B_4^4 =&(\langle r^4\rangle\gamma_{44}\cdot q_M)\cdot c\cdot x_4, \quad \text{with} \quad c=-\frac{p}{84}\sqrt{\frac{70}{\pi}} \end{aligned} \tag{F.2}$$

where p is the prefactor for the electrostatic potential ($p = -\frac{e}{4\pi\epsilon_0}$), e the elementary charge, ϵ_0 the electric constant and q_M is the charge on the magnetic atom.

F.4.3 Stevens operator equivalents

$$\begin{aligned} \hat{O}_2^0 =&3\hat{L}_z^2 - L(L+1) \\ \hat{O}_4^0 =&35\hat{L}_z^4 - (30L(L+1)-25)\hat{L}_z^2 + 3L^2(L+1)^2 - 6L(L+1) \\ \hat{O}_4^4 =&\frac{1}{2}(\hat{L}_+^4 + \hat{L}_-^4) \end{aligned} \tag{F.3}$$

F.4.4 Full Stevens Hamiltonian

$$\begin{aligned} H_{\text{Stevens}} =&H_{\text{LF}} + H_{\text{SOC}} + H_{\text{Z}} \\ =&B_2^0\hat{O}_2^0 + B_4^0\hat{O}_4^0 + B_4^4\hat{O}_4^4 + \lambda\vec{L}\cdot\vec{S} + (\vec{L}+2\vec{S})\mu_{\text{B}}\vec{B} \end{aligned} \tag{F.4}$$

Appendix G

Energy changes due to atom movements

We show here a simulated increase of the magnetic-atom-to-oxygen distance for both Fe and Co. The changes shown go up to ± 40 pm from the relaxed structure calculated by DFT, which might be an unphysical change: First, because DFT calculations are generally considered very accurate for calculating atom positions. Second, if a position change is caused by the influence of the STM tip, such a large change would potentially only be possible when bonding to the tip occurs, which would change the situation alltogether. However, showing the changes over a large distance here visualizes that our results are quite robust against small changes in the ligand arrangement.

G.1 Energy change due to Fe movement

For the Fe atom we show both the change for the optimized calculation, as used in the main text (Figure G.1 A) as well as for the non-optimized model for completeness (Figure G.1 B). A 5 pm change of the Fe-O distance causes a change of about 1 meV in V_{02} for the optimized model (Figure G.1 C) and

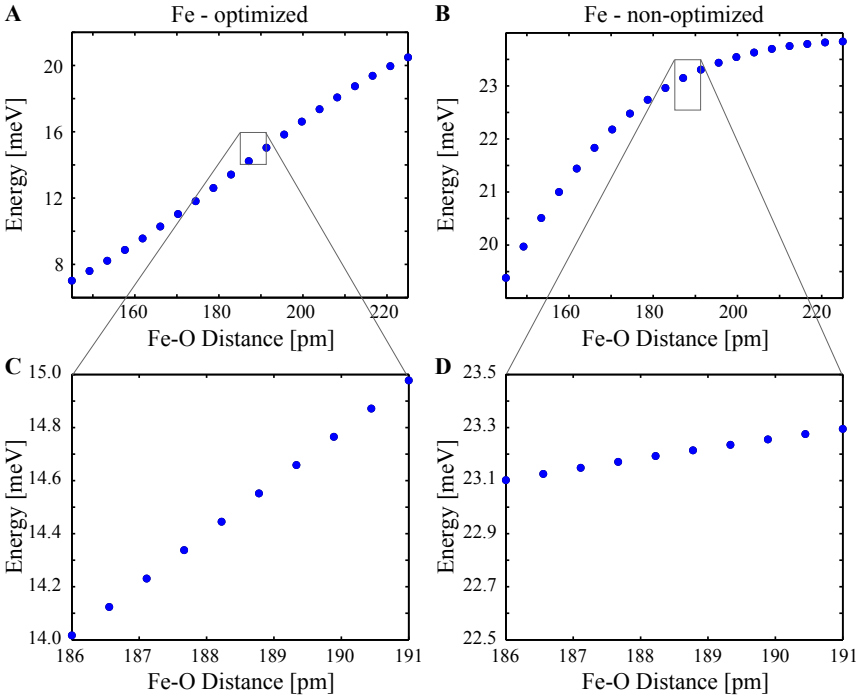

Figure G.1: (**A**) and (**B**) show the changes of the zero-field splitting for Fe in a range of ± 40 pm from the relaxed structure, for both the optimized model (**A**) (see Section 5.3.5) and the non-optimized model (**B**). Panels (**C**) and (**D**) show the energy change starting from the relaxed structure (at 186 pm) and moving the Fe atom further away from the MgO surface. All panels show the changes in $V_{02} = V_{13}$ at 0 T.

a smaller change of only about 0.2 meV for the non-optimized model (Figure G.1 D). In the non-optimized model the calculated energy values are already close to the maximal value possible (which is $\lambda \cdot L \approx 24$ meV (*26*)) and thus the change in energy is smaller than for the optimized model, where the zero-field splitting is far from its maximal value.

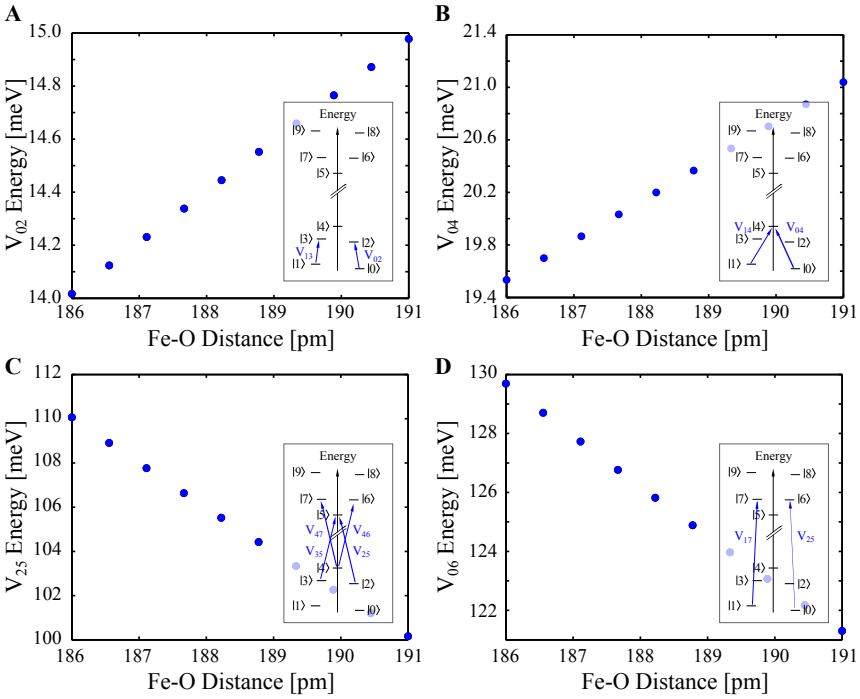

Figure G.2: Energy change due to a 5 pm movement of the Fe atom away from the MgO surface (starting from the relaxed structure calculated from DFT (186 pm)). The transitions shown are (**A**): $V_{02} = V_{13}$, (**B**): V_{04}, (**C**): $V_{25} = V_{35} = V_{46} = V_{47}$ and (**D**): $V_{06} = V_{07} = V_{16} = V_{17}$. All panels show the changes at 0 T obtained from the optimized model.

Changing the Fe-O distance does not only change the $V_{02} = V_{13}$ transition at 0 T but it rather changes all energies. Thus, we show in Figure G.2 other possible transitions, such as V_{04}, $V_{25} = V_{35} = V_{46} = V_{47}$ as well as $V_{06} = V_{07}$. All transitions are affected by a movement of the Fe atom, the ones shown here are potentially observable in STM under certain conditions (e.g. with large enough current or with a spin-polarized tip).

Note that the transitions between different spin-multiplets (change from states 0–4 to states 5–9) are about a factor of 10 larger than transitions within a spin-multiplet.

G.2 Energy change due to Co movement

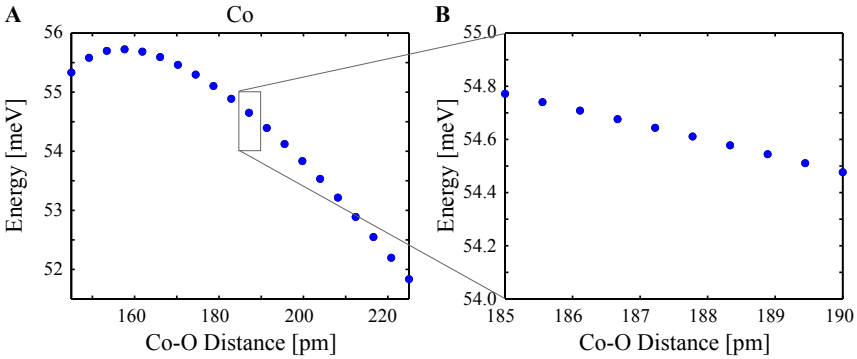

Figure G.3: (**A**) Zero-field energy change ($V_{02} = V_{13}$) of the Co atom due to a change in Co-O distance of $\pm$40 pm. (**B**) The energy changes by 0.2 meV when starting from the relaxed structure as calculated by DFT (185 pm) and moving the Co away from the MgO surface.

Similarly to the Fe atom, we show here for the Co a distance change of $\pm$40 pm (Figure G.3 A). As pointed out in the main text the zero-field splitting of the Co atom is close to the maximal possible value of $\sim$60 meV ($\lambda \cdot L$ (*26*)) and thus the energy change due to a small movement of the magnetic atom is only minimal. A 5 pm change in Co-O distance starting from the relaxed structure (185 pm) has less effect than for the Fe and only causes a change of about 0.2 meV (see Figure G.3).

Appendix H

Master rate equation

H.1 Rate equations

The occupation of each energy level can be described by considering all excitation and deexcitation rates from all other states. The qualitative model described here is the same as used in (*38*) and has the form of a master rate equation. The change in the spin state occupation $n_i(t)$ of each spin state i is given by the difference of the transition rates into and out of each state.

$$\frac{dn_i(t)}{dt} = \sum_j r_{ij} n_j(t) - r_{ji} n_i(t) \tag{H.1}$$

Here, r_{ji} represents the overall transition rate from spin state i to state j. These transition rates consist of induced excitation as well as induced and spontaneous deexcitation. We account for four possible contributions in the model (see schematic 7.4): (i) transitions (excitations and deexcitations) due to electrons tunneling from the tip to the sample ($t \rightarrow s$), (ii) transitions due to electrons tunneling from the sample to the tip ($s \rightarrow t$), (iii) spontaneous deexcitation due to substrate electrons that tunnel through the MgO, interact

with the local spin and tunnel back to the substrate ($s \rightarrow s$) and (iv) spontaneous deexcitation due to tip electrons that tunnel through the vacuum barrier interact with the atom's spin and return to the tip ($t \rightarrow t$).

$$r_{ji} = r_{ji}^{t\rightarrow s} + r_{ji}^{s\rightarrow t} + r_{ji}^{s\rightarrow s} + r_{ji}^{t\rightarrow t} \tag{H.2}$$

The transition rates are described by the conventional model for inelastic electron tunneling (*24*). We account for finite temperature by using the Fermi-Dirac distribution of the occupation of states of both the tip and sample.

$$\begin{aligned}
r_{ji}^{t\rightarrow s} =& \frac{G_{ts}}{e}\int_{-\infty}^{+\infty} F(E)\cdot(1-F(E+eV-\Delta E_{ji}))\cdot P_{ji}^{t\rightarrow s}dE \\
r_{ji}^{s\rightarrow t} =& \frac{G_{ts}}{e}\int_{-\infty}^{+\infty} F(E+eV)\cdot(1-F(E-\Delta E_{ji}))\cdot P_{ji}^{s\rightarrow t}dE \\
r_{ji}^{s\rightarrow s} =& \frac{G_{ss}}{e}\int_{-\infty}^{+\infty} F(E)\cdot(1-F(E-\Delta E_{ji}))\cdot P_{ji}^{s\rightarrow s}dE \\
r_{ji}^{t\rightarrow t} =& \frac{G_{tt}}{e}\int_{-\infty}^{+\infty} F(E)\cdot(1-F(E-\Delta E_{ji}))\cdot P_{ji}^{t\rightarrow t}
\end{aligned} \tag{H.3}$$

These rates depend on the number of electrons per second (and voltage) that interact with the local atom, which is set here by the conductance G per elementary charge e. G_{ts} is given by the tunnel junction impedance, G_{ss}, the substrate conductance, reflects the rate of substrate electrons able to cause transitions, similarly, G_{tt} is the tip conductance. We will derive the relation between these G_{ts}, G_{ss} and G_{tt} in the next Section H.2.

The transition coefficient P is determined from the normalized quantum mechanical transition intensity (Y) including the spin-polarization of the tip. We account for the spin-polarization of the tip by letting the density of up electrons ($\sigma_z = +\frac{1}{2}$) be proportional to $\frac{1+\eta}{2}$, and the one of down electrons ($\sigma_z = -\frac{1}{2}$) be proportional to $\frac{1-\eta}{2}$. The substrate is non-spin-polarized thus

spin-up and spin-down electrons both have a density of states of $\frac{1}{2}$. The transition coefficients are then:

$$
\begin{aligned}
P_{ji}^{t\to s} &= \frac{1}{P_0}\sum_{\sigma_\mathrm{j},\sigma_\mathrm{i}} Y(\Phi_\mathrm{j},\sigma_\mathrm{j},\Phi_\mathrm{i},\sigma_\mathrm{i})\cdot\frac{1}{2}\,(\frac{1}{2}+\eta\sigma_j)\\
P_{ji}^{s\to t} &= \frac{1}{P_0}\sum_{\sigma_\mathrm{j},\sigma_\mathrm{i}} Y(\Phi_\mathrm{j},\sigma_\mathrm{j},\Phi_\mathrm{i},\sigma_\mathrm{i})\cdot\frac{1}{2}\,(\frac{1}{2}+\eta\sigma_i)\\
P_{ji}^{s\to s} &= \frac{1}{P_0}\sum_{\sigma_\mathrm{j},\sigma_\mathrm{i}} Y(\Phi_\mathrm{j},\sigma_\mathrm{j},\Phi_\mathrm{i},\sigma_\mathrm{i})\,\frac{1}{4}\\
P_{ji}^{t\to t} &= P_{ji}^{s\to s}
\end{aligned}
\tag{H.4}
$$

With the normalization constant P_0:

$$
P_0 = Y(\Phi_\mathrm{i},+\frac{1}{2},\Phi_\mathrm{f},+\frac{1}{2})(\frac{1+\eta}{2}) + Y(\Phi_\mathrm{i},-\frac{1}{2},\Phi_\mathrm{f},-\frac{1}{2})(\frac{1-\eta}{2}) \tag{H.5}
$$

We solve these equations for their steady state solution to find the equilibrium population of each state at different voltages.

H.2 Using the rate equations to fit lifetimes

The lifetime as a function of tip height (Figure 8.5) is modeled based on the master rate equation. We use the definition of the lifetime as the $1/e$ relaxation time out of a given state i.

$$
\tau_i = \frac{1}{\sum_j r_{ji}} \tag{H.6}
$$

The spin relaxation can be caused by electrons from either substrate or the tip that interact with the magnetic atom and tunnel back to their original electrode

or across the junction, even in the absence of a tunnel current (*74*). The current corresponding to such tunneling depends exponentially on the distance from these electrodes. For example, the tunnel current across the tunnel junction is proportional to the vacuum barrier as well as the barrier due to the insulating substrate (here MgO):

$$I_{ts} \propto e^{-k_v z_v} e^{-k_s z_s} \tag{H.7}$$

where k is proportional to the inverse decay length of the wave function in either vacuum (v) or the substrate (s) and z represents the corresponding barrier height. Similarly, the current for electrons tunneling back to their original electrodes can be written as two passes through the same barrier:

$$\begin{aligned} I_{ss} &\propto e^{-2k_s z_s} \\ I_{tt} &\propto e^{-2k_v z_v} \end{aligned} \tag{H.8}$$

Thus I_{ts} is proportional to $\sqrt{I_{ss}} \cdot \sqrt{I_{tt}}$, or $I_{tt} \propto I_{ts}^2 \frac{1}{I_{ss}}$.

In the limit of small temperature (as it is the case in our system) we can approximate the Fermi-integral as ΔE which we will use in the following. Additionally, we will focus on a single transition (i.e. from excited state 1 to state 0) and we will use $P_{10} = P^{s \to s}$. Then the rates are:

$$\begin{aligned} r^{t \to s} + r^{s \to t} &= \frac{G_{ts}}{e} \frac{\Delta E}{e} P_{10} \frac{1}{2} \\ r^{s \to s} &= \frac{G_s}{e} \frac{\Delta E}{e} P_{10} \frac{1}{4} \\ r^{t \to t} &= \frac{G_t}{e} \frac{\Delta E}{e} P_{10} \frac{1}{4} = \frac{G_{ts}^2}{G_{ss}} \frac{1}{e} \frac{\Delta E}{e} P_{10} \frac{1}{4} \end{aligned} \tag{H.9}$$

Therefore the lifetime out of the first excited state can be expressed in terms of the tip-sample conductance:

$$\begin{aligned}\tau_{10} &= \frac{1}{\sum r_{10}^{t\to s} + r_{10}^{s\to t} + r_{10}^{s\to s} + r_{10}^{t\to t}} \\ &= \frac{1}{\Delta E \cdot \frac{P_{10}}{4} \cdot \frac{1}{e^2}\left(G_{ss} + 2\,G_{ts} + \frac{G_{ts}^2}{G_{ss}}\right)}\end{aligned} \tag{H.10}$$

In this formula for the lifetime ΔE and P_{10} can be extracted from the point charge model calculation. The only unknown is G_{ss}. For the fit to the experiment in Figure 8.5, we used an additional multiplicative factor for P_{10} ($a \cdot P_{10}$) for a better fit.

References

[1] Thomas, L. *et al.* Macroscopic quantum tunnelling of magnetization in a single crystal of nanomagnets. *Nature* **383**, 145–147 (1996).

[2] Gatteschi, D., Sessoli, R. & Villain, J. *Molecular Nanomagnets* (Oxford University Press, New York, 2006).

[3] Van Vleck, J. H. *The theory of electric and magnetic susceptibilities* (Oxford University Press, Oxford, 1932).

[4] Gambardella, P. *et al.* Giant Magnetic Anisotropy of Single Cobalt Atoms and Nanoparticles. *Science* **300**, 1130–1133 (2003).

[5] Miyamachi, T. *et al.* Stabilizing the magnetic moment of single holmium atoms by symmetry. *Nature* **503**, 242–246 (2013).

[6] Bryan, A. M., Merrill, W. A., Reiff, W. M., Fettinger, J. C. & Power, P. P. Synthesis, Structural, and Magnetic Characterization of Linear and Bent Geometry Cobalt(II) and Nickel(II) Amido Complexes: Evidence of Very Large Spin-Orbit Coupling Effects in Rigorously Linear Coordinated Co^{2+}. *Inorg. Chem.* **51**, 3366–3373 (2012).

[7] Zadrozny, J. M. *et al.* Magnetic blocking in a linear iron(I) complex. *Nat. Chem.* **5**, 577–581 (2013).

[8] Rinehart, J. D. & Long, J. R. Exploiting single-ion anisotropy in the design of f-element single-molecule magnets. *Chem. Sci.* **2**, 2078–2085 (2011).

[9] Klatyk, J. *et al.* Large Orbital Moments and Internal Magnetic Fields in Lithium Nitridoferrate(I). *Phys. Rev. Lett.* **88**, 207202 (2002).

[10] Baumann, S., Rau, I. G., Loth, S., Lutz, C. P. & Heinrich, A. J. Measuring the Three-Dimensional Structure of Ultrathin Insulating Films at the Atomic Scale. *ACS Nano* **8**, 1739–1744 (2014).

[11] Schintke, S. *et al.* Insulator at the Ultrathin Limit: MgO on Ag(001). *Phys. Rev. Lett.* **87**, 276801 (2001).

[12] Brune, H. & Gambardella, P. Magnetism of individual atoms adsorbed on surfaces. *Surface Science* **603**, 1812–1830 (2009).

[13] Arthur, J. R. Molecular beam epitaxy. *Surface Science* **500**, 189–217 (2002).

[14] Eigler, D. M. & Schweizer, E. K. Positioning single atoms with a scanning tunneling microscope. *Nature* **344**, 524–526 (1990).

[15] Heinrich, A. J., Gupta, J. A., Lutz, C. P. & Eigler, D. M. Single-Atom Spin-Flip Spectroscopy. *Science* **306**, 466–469 (2004).

[16] SolidWorks. Dassault Systémes SOLIDWORKS Corp. (2012).

[17] MDC. MDC Vacuum Products, LLC.

[18] Binning, G., Rohrer, H., Gerber, C. & Weibel, E. Surface Studies by Scanning Tunneling Microscopy. *Phys. Rev. Lett.* **49**, 57–61 (1982).

[19] Loth, S., Baumann, S., Lutz, C. P., Eigler, D. M. & Heinrich, A. J. Bistability in Atomic-Scale Antiferromagnets. *Science* **335**, 196–199 (2012).

[20] Khajetoorians, A. A. *et al.* Current-Driven Spin Dynamics of Artificially Constructed Quantum Magnets. *Science* **339**, 55–59 (2013).

[21] Stipe, B. C., Rezaei, M. A. & Ho, W. Single-Molecule Vibrational Spectroscopy and Microscopy. *Science* **280**, 1732–1735 (1998).

[22] Wiesendanger, R. Spin mapping at the nanoscale and atomic scale. *Rev. Mod. Phys.* **81**, 1495–1550 (2009).

[23] Bode, M. Spin-polarized scanning tunnelling microscopy. *Rep. Prog. Phys.* **66**, 523–582 (2003).

[24] Lambe, J. & Jaklevic, R. C. Molecular Vibration Spectra by Inelastic Electron Tunneling. *Phys. Rev.* **165**, 821 (1968).

[25] Hirjibehedin, C. F. *et al.* Large Magnetic Anisotropy of a Single Atomic Spin Embedded in a Surface Molecular Network. *Science* **317**, 1199–1203 (2007).

[26] Rau, I. G. *et al.* Reaching the magnetic anisotropy limit of a 3d metal atom. *Science* **344**, 988–992 (2014).

[27] Tsukahara, N. *et al.* Adsorption-Induced Switching of Magnetic Anisotropy in a Single Iron(II) Phthalocyanine Molecule on an Oxidized Cu(110) Surface. *Phys. Rev. Lett.* **102**, 167203 (2009).

[28] Donati, F. *et al.* Magnetic Moment and Anisotropy of Individual Co Atoms on Graphene. *Phys. Rev. Lett.* **111**, 236801 (2013).

[29] Bryant, B., Spinelli, A., Wagenaar, J. J. T., Gerrits, M. & Otte, A. F. Local Control of Single Atom Magnetocrystalline Anisotropy. *Phys. Rev. Lett.* **111**, 127203 (2013).

[30] Wernsdorfer, W. & Sessoli, R. Quantum Phase Interference and Parity Effects in Magnetic Molecular Clusters. *Science* **284**, 133–135 (1999).

[31] Abragam, A. & Blaeney, B. *Electron Paramagnetic Resonance of Transition Ions* (Clarendon Press, Oxford, 1986).

[32] Stevens, K. W. H. Matrix Elements and Operator Equivalents Connected with the Magnetic Properties of Rare Earth Ions. *Proc. Phys. Soc. A* **65**, 209–215 (1952).

[33] Neyman, K. M., Inntam, C., Nasluzov, V. A., Kosarev, R. & Rösch, N. Adsorption of d-metal atoms on the regular MgO(001) surface: Density functional study of cluster models embedded in an elastic polarizable environment. *Applied Physics A: Materials Science & Processing* **78**, 823–828 (2004).

[34] Otte, A. F. *et al.* The role of magnetic anisotropy in the Kondo effect. *Nat. Phys.* **4**, 847–850 (2008).

[35] Chilian, B. *et al.* Anomalously large g factor of single atoms adsorbed on a metal substrate. *Phys. Rev. B* **84**, 212401 (2011).

[36] Khajetoorians, A. A. *et al.* Itinerant Nature of Atom-Magnetization Excitation by Tunneling Electrons. *Phys. Rev. Lett.* **106**, 37205 (2011).

[37] Hirjibehedin, C. F., Lutz, C. P. & Heinrich, A. J. Spin Coupling in Engineered Atomic Structures. *Science* **312**, 1021–1024 (2006).

[38] Loth, S. *et al.* Controlling the state of quantum spins with electric currents. *Nat. Phys.* **6**, 340–344 (2010).

[39] Thole, B. T., Carra, P., Sette, F. & van der Laan, G. X-ray circular dichroism as a probe of orbital magnetization. *Phys. Rev. Lett.* **68**, 1943–1946 (1992).

[40] Carra, P., Thole, B. T., Altarelli, M. & Wang, X. X-ray circular dichroism and local magnetic fields. *Phys. Rev. Lett.* **70**, 694 (1993).

[41] Chen, C. T. *et al.* Experimental Confirmation of the X-Ray Magnetic Circular Dichroism Sum Rules for Iron and Cobalt. *Phys. Rev. Lett.* **75**, 152–155 (1995).

[42] Gambardella, P. *et al.* Localized Magnetic States of Fe, Co, and Ni Impurities on Alkali Metal Films. *Phys. Rev. Lett.* **88**, 47202 (2002).

[43] Piamonteze, C. *et al.* X-Treme beamline at SLS: X-ray magnetic circular and linear dichroism at high field and low temperature. *J. Synchrotron Rad.* **19**, 661–674 (2012).

[44] de Groot, F. M. F. *et al.* Oxygen $1s$ and cobalt $2p$ X-ray absorption of cobalt oxides. *J. Phys.: Condens. Matter* **5**, 2277 (1993).

[45] Lehnert, A. *et al.* Magnetic anisotropy of Fe and Co adatoms and Fe clusters magnetically decoupled from $Ni_3Al(111)$ by an alumina bilayer. *Phys. Rev. B* **81**, 104430 (2010).

[46] de Groot, F. High-resolution X-ray Emission and X-ray Absorption Spectroscopy. *Chem. Rev.* **101**, 1779–1808 (2001).

[47] de Groot, F. Multiplet effects in X-ray spectroscopy. *Coordination Chemistry Reviews* **249**, 31–63 (2005).

[48] Hund, F. Zur Deutung verwickelter Spektren, insbesondere der Elemente Scandium bis Nickel. *Zeitschrift für Physik* **33**, 345–371 (1925).

[49] McGarvey, B. *Electron spin resonance of transition-metal complexes* (Transition Metal Chemistry Vol. 3, R.L. Carlin (Ed.), Marcel Dekker, 1966).

[50] Bruno, P. Tight-binding approach to the orbital magnetic moment and magnetocrystalline anisotropy of transition-metal monolayers. *Phys. Rev. B* **39**, 865–868 (1989).

[51] Slater, J. C. *Quantum Theory of Atomic Structure* (McGraw-Hill Book Company, Inc, 1960).

[52] Giannozzi, P. *et al.* QUANTUM ESPRESSO: a modular and open-source software project for quantum simulations of materials. *J. Phys.: Condens. Matter* **21**, 395502 (2009).

[53] Blaha, P., Schwarz, K., Madsen, G., Kavasnicka, D. & Luitz, J. *WIEN2k, An Augmented Plane Wave + Local Orbitals Program for Calculating Crystal Properties* (Karlheinz Schwarz, Techn. Universitat Wien, Austria, ISBN 3-9501031-1-2., 2001).

[54] Sgroi, M., Pisani, C. & Busso, M. Ab initio density functional simulation of structural and electronic properties of MgO ultra-thin adlayers on the (001) Ag surface. *Thin Solid Films* **400**, 64–70 (2001).

[55] Cococcioni, M. & de Gironcoli, S. Linear response approach to the calculation of the effective interaction parameters in the LDA+U method. *Phys. Rev. B* **71**, 35105 (2005).

[56] Hutchings, M. T. Point-Charge Calculations of Energy Levels of Magnetic Ions in Crystalline Electric Fields. *Solid State Physics* **16**, 227–273 (1964).

[57] Bleaney, B. & Stevens, K. W. H. Paramagnetic resonance. *Rep. Prog. Phys.* **16**, 108 (1953).

[58] Dai, D., Xiang, H. & Whangbo, M.-H. Effects of spin-orbit coupling on magnetic properties of discrete and extended magnetic systems. *Journal of Computational Chemistry* **29**, 2187–2209 (2008).

[59] Ballhausen, C. J. *Introduction to Ligand Field Theory* (McGraw Hill, New York, 1962).

[60] Gambardella, P. *et al.* Supramolecular control of the magnetic anisotropy in two-dimensional high-spin Fe arrays at a metal interface. *Nat. Mater.* **8**, 189–193 (2009).

[61] George, R. E., Edwards, J. P. & Ardavan, A. Coherent Spin Control by Electrical Manipulation of the Magnetic Anisotropy. *Phys. Rev. Lett.* **110**, 027601 (2013).

[62] Heinrich, B. W., Braun, L., Pascual, J. I. & Franke, K. J. Protection of excited spin states by a superconducting energy gap. *Nat. Phys.* **9**, 765–768 (2013).

[63] Hofer, W. A., Fisher, A. J., Wolkow, R. A. & Grütter, P. Surface Relaxations, Current Enhancements, and Absolute Distances in High Resolution Scanning Tunneling Microscopy. *Phys. Rev. Lett.* **87**, 236104 (2001).

[64] Ternes, M. *et al.* Interplay of Conductance, Force, and Structural Change in Metallic Point Contacts. *Phys. Rev. Lett.* **106**, 016802 (2011).

[65] Lorente, N. & Gauyacq, J.-P. Efficient Spin Transitions in Inelastic Electron Tunneling Spectroscopy. *Phys. Rev. Lett.* **103**, 176601 (2009).

[66] Fernández-Rossier, J. Theory of Single-Spin Inelastic Tunneling Spectroscopy. *Phys. Rev. Lett.* **102**, 256802 (2009).

[67] Loth, S., Lutz, C. P. & Heinrich, A. J. Spin-polarized spin excitation spectroscopy. *New J. Phys.* **12**, 125021 (2010).

[68] Bartels, L., Meyer, G. & Rieder, K.-H. Controlled vertical manipulation of single CO molecules with the scanning tunneling microscope: A route to chemical contrast. *Appl. Phys. Lett.* **71**, 213–215 (1997).

[69] Kahle, S. *et al.* The Quantum Magnetism of Individual Manganese-12-Acetate Molecular Magnets Anchored at Surfaces. *Nano Lett.* **12**, 518–521 (2012).

[70] Delgado, F., Palacios, J. J. & Fernández-Rossier, J. Spin-Transfer Torque on a Single Magnetic Adatom. *Phys. Rev. Lett.* **104**, 26601 (2010).

[71] Brataas, A., Kent, A. D. & Ohno, H. Current-induced torques in magnetic materials. *Nat. Mater.* **11**, 372–381 (2012).

[72] Loth, S., Etzkorn, M., Lutz, C. P., Eigler, D. M. & Heinrich, A. J. Measurement of Fast Electron Spin Relaxation Times with Atomic Resolution. *Science* **329**, 1628–1630 (2010).

[73] Donati, F. *et al.* Magnetism of Ho and Er Atoms on Close-Packed Surfaces. *Phys. Rev. Lett.* **113**, 237201 (2014).

[74] Gauyacq, J.-P., Lorente, N. & Novaes, F. D. Excitation of local magnetic moments by tunneling electrons. *Progress in Surface Science* **87**, 63–107 (2012).

[75] Yan, S., Choi, D.-J., Burgess, J. A. J., Rolf-Pissarczyk, S. & Loth, S. Control of quantum magnets by atomic exchange bias. *Nat. Nanotech.* **10**, 40–45 (2015).

[76] Ernst, K.-H. *et al.* Pasteurs experiment performed at the nanoscale: manual separation of chiral molecules one by one. *Nano Lett.* under review.

[77] IBM. *A Boy and his Atom* (URL: www.ibm.com/madewithatoms, 2013).

[78] Steurer, W., Gross, L. & Meyer, G. Local thickness determination of thin insulator films via localized states. *Appl. Phys. Lett.* **104**, 231606 (2014).

[79] Freund, H.-J. & Pacchioni, G. Oxide ultra-thin films on metals: new materials for the design of supported metal catalysts. *Chem. Soc. Rev.* **37**, 2224–2242 (2008).

[80] Yang, Y., da Costa, R. C., Fuchter, M. J. & Campbell, A. J. Circularly polarized light detection by a chiral organic semiconductor transistor. *Nat. Photon* **7**, 634–638 (2013).

[81] Parschau, M., Fasel, R. & Ernst, K.-H. Coverage and Enantiomeric Excess Dependent Enantiomorphism in Two-Dimensional Molecular Crystals. *Cryst. Growth Des.* **8**, 1890–1896 (2008).

[82] Eriksson, O., Johansson, B., Albers, R. C., Boring, A. M. & Brooks, M. S. S. Orbital magnetism in Fe, Co, and Ni. *Phys. Rev. B* **42**, 2707–2710 (1990).